Measurement of non-linear acoustoelastic effect in steel using acoustic resonance

Simen Eldevik

Dissertation for the degree of philosophiae doctor (PhD)
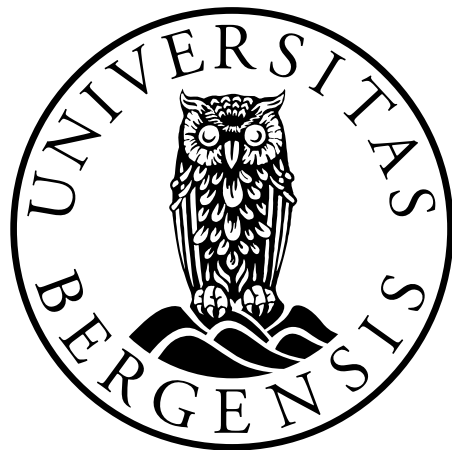University of Bergen, Norway
2014

UNIVERSITY OF BERGEN

Measurement of non-linear acoustoelastic effect in steel using acoustic resonance

Simen Eldevik

Abstract

Non-destructive stress measurements of structures are increasingly valued by the industry. Ultrasonic methods have the advantage that acoustic waves propagate with ease through materials, making it possible to probe the interior of structures.

Classic elastic models predict constant longitudinal and shear sound velocities in a material. However, by including higher order elastic moduli, the acoustoelastic theory indicate that the sound velocities are affected by the current stress state of the material. Experiments on steel plates have confirmed the dependency of speed of sound with stress in the material. This presents a potential method to estimate pipeline wall stress using ultrasound.

Pipeline wall thickness can be measured using resonant ultrasonic signals. The resonant frequencies are linked to the wall thickness via the sound velocity. Thus, equivalently the sound velocities can be estimated when the wall thickness is known.

This study has investigated the possibilty of detecting changes in material properties at very high stress in steel utilising an existing acoustic non-destructive testing (NDT) technique called *Acoustic Resonance Technology* (ART). ART is an ultrasonic technique based on transient acoustic reflections in layer and plates. The technique utilises mainly a pulse-echo method of normally incident longitudinal acoustic signal (pressure waves), recording the longitudinal resonant frequencies across the thickness of a layer. However, it can also be set up to record shear resonant frequencies across the layer thickness by utilising the effect of mode conversion of a slightly off-normal incident pressure wave.

Laboratory experiments utilising ART have been used to measure the change in both longitudinal and shear sound velocities across rectangular steel test

specimens subjected to uniaxial tensional loads. In addtion the acoustoelastic theory have been implemented and used to simulate the change in sound velocities for some steel types reported in the literature for comparison of experimental results and theory. The theoretical investigation and experimental measurements on steel bars performed in this work have shown that the ART methodology is capable of detecting very small changes, in the order of 0.1%, of the sound velocities for test specimens subjected to high levels of stress. In addition, by comparing longitudinal and shear resonance frequencies, ART is capable of measuring an effect of both longitudinal and shear sound velocity changes independent of the thickness of the specimen. This might be highly valuable for potential in-line inspections along several km of pipelines where the wall thickness may vary on a scale approximately two orders of magnitude larger than the measured variation in stress induced sound velocity change.

Folk koma no etter, at Skrotten liksovel maa faa sin Tame (Øvelse) som
Tanken sin. Dette By- og Bokliv, som paa mange Maater gjere folk kloke,
bryte tidt Helsa ned, og gjere Kroppen veik og Tanken turr. Og derfor er
det so klokt gjort, at By- og Bokfolk taka til at tenkje paa Landsens
Arbeid og gamle Leikar.

Aa. O. Vinje: Skiløyping (i Dølen, 1868)

English translation by the author:

It finally dawned on people, that the Body as much needed its exercise as
the Mind. This City- and Book-life, which in many ways make the people
wise, oft break their Health down, and make the Body weak and the Mind
dry. And thus it is so wise, for City- and Book-people to revive the Rural
Work and old Play.

Acknowledgements

To my parents, always.

To my patient and beautiful wife Tonje, my lively and lovely daugther Thale, and to man's best friend Gáisá; I owe a special thanks for your part in breaking up my tedious work on this PhD to excercise other parts of my Mind as well as Body. You all make every day perfect.

Contents

Glossary

Roman Symbols

A, B, C Third order elastic constants (Landau and Lifshitz 1986 [37])

A Area in reference configuration

a Area in current configuration

a_{ij} Third order acoustoelastic coefficients

$\mathbf{a}_{TX}$ Radius of the piezo composite transmitter disk

$\mathbf{B}$ Left Cauchy-Green stretch tensor

$\mathbf{b}$ Body force vector

B Configuration of a continuous body

B_{ijkl} Effective elastic moduli

b_{ij} Fourth order acoustoelastic coefficients

$\mathbf{C}$ Right Cauchy-Green stretch tensor

$\mathbf{c}$ Translation tensor

c Sound velocity / Wave velocity

C_{ijklmn} Third order elastic moduli

C_{ijkl} Second order elastic moduli

c_{IJK} Third order elastic moduli expressed in Voigt's notation

c_{IJ} Second order elastic moduli expressed in Voigt's notation

d Sample thickness

$\mathbf{E}$ Lagrangian strain tensor

$\mathbf{e}$ Eulerian strain tensor

e_i Elongation in one of the principal directions $i \in \{1, 2, 3\}$

$\mathbf{F}$ Deformation gradient

$\mathbf{f}$ Force vector

f Twice continuously differentiable function

F Applied force

f Frequency

$\mathbf{g}$ General vector

g General function

$\boldsymbol{I}$ Incident wave

$\mathbf{I}$ Identity tensor

$\mathfrak{I}$ Interval of time t

I_1, I_2, I_3 Invariants

J Jacobian determinant

k_p Coverage factor corresponding to a certain confidence level

$\mathbf{k}$ Wave number

L Reference length

l Sample length

l, m, n Third order elastic constants (Murnaghan 1951 [83])

l_E, m_E, n_E Third order elastic constants (Ering and Suhubi 1974 [36])

$\mathbf{L1}$ First longitudinal resonance mode

$\mathbf{L2}$ Second longitudinal resonance mode

$\mathbf{m}$ Polarisation unit vector

M_{ijklmn} Combination of second and third order elastic moduli

$\hat{\mathbf{N}}$ Unit direction vector in reference configuration

$\hat{\mathbf{n}}$ Unit direction vector in current configuration

$\mathbf{N}$ Propagation unit vector

n_l Harmonic number (longitudinal wave)

n_s Harmonic number (shear wave)

$\mathbf{O}$ A fixed origin to which $\mathbf{X}$ and $\mathbf{x}$ are referenced to

$\mathbf{P}$ First Piola-Kirchhoff stress tensor

P Material point in reference configuration

p Material point in current configuration

$\bar{q}$ Experimental mean value of measurement quantity q

$\mathbf{Q}_0(\mathbf{n})$ Acoustic tensor

CONTENTS

Q	Material point in reference configuration
q	Measurement quantity
$\boldsymbol{R}$	Reflected pressure wave amplitude
$\mathbb{R}$	Set of all real numbers
$\mathbf{R}$	Proper orthogonal rotation tensor
$r(x_i, x_j)$	Correlation coefficient between measurand x_i and x_j
$r_i = \rho_i c_i$	Characteristic impedance of medium $i \in \{1, 2, 3\}$ for a given sound velocity c (either longitudinal or shear).
$\mathbf{S}$	Nominal stress tensor
S	Surface
$s(\bar{x}_i, \bar{x}_j)$	Experimental estimate of the covariance between measurand x_i and x_j
$s(q)$	Experimental estimate of standard deviation of measurement quantity q
$\mathbf{S2}$	Second shear resonance mode
$\mathbf{S3}$	Third shear resonance mode
$\boldsymbol{T}$	Transmitted pressure wave amplitude
$\mathbf{t}^{(\hat{\mathbf{n}})}$	Stress vector acting on a surface with normal in the $\hat{\mathbf{n}}$-direction
T	Temperature
t	Time
Tr	Transmission coefficient
$\mathbf{U}$	Right stretch tensor. positive definite symmetric translation tensor
$\mathbf{u}$	Displacement vector between reference and current configuration
$\mathbf{u}^{(i)}$	Eigenvectors of right stretch tensor
$u(q)$	Standard uncertainty of quantity q
$\mathbf{V}$	Left stretch tensor. positive definite symmetric translation tensor
$\mathbf{v}^{(i)}$	Eigenvectors of left stretch tensor
V	Volume in reference configuration
v	Volume in current configuration
W	Strain-energy density function
w	Sample width
$\ddot{\mathbf{x}}$	Acceleration vector

$\dot{\mathbf{x}}$	Velocity vector and time derivative of $\mathbf{x}$
$\hat{\mathbf{x}}_i, i = 1, 2, 3$	Cartesian unit base vectors
$\mathbf{X}$	Position vector in reference configuration
$\mathbf{x}$	Position vector in current configuration
x_1	Denoting displacement of Instron machine based on the recorded displacement voltage
Y	Infinitesimal Young's modulus

Greek Symbols

α, β, γ	Third order elastic constants (Bland 1969 [35])
β	Constant
$\boldsymbol{\Gamma}$	Eulerian strain-rate
$\boldsymbol{\sigma}$	Cauchy stress tensor
χ	Mapping function between points in reference and current configuration
δ_{ij}	Kronecker delta
η	Factor to correct for the beam diffraction effect
γ	Constant
κ	Infinitesimal bulk modulus
λ	Lamé's first parameter
λ	Wave length
λ_i	Principal stretch in direction $i \in \{1, 2, 3\}$
μ	Lamé's second parameter, also known as the shear modulus
μ_q	Expectation value of quantity q
ν	Poisson's ratio
ν_1, ν_2, ν_3	Third order elastic constants (Toupin and Bernstain 1961 [18])
ρ	Mass density
σ_q	Standard deviation of measurement quantity q
σ_{ij}	Index representation of $\boldsymbol{\sigma}$
$\sigma_x, \sigma_y, \sigma_z$	Orthogonal normal stresses
$\tau_{xy}, \tau_{xz}, \tau_{yz}$	Orthogonal shear stresses
θ	Incident angle

ξ Linear relation between the slope of two elastic unloading/loading sequences as a function of the intermediate plastic elongation e_1^p

S_{ij} Index representation of $\mathbf{S}$

y^{e_i} Slope from linear regression of the relation between the applied force F and the elastic elongation e_i^e in the principal directions x_i

Superscripts

(0) Denoting displacement from reference to pre-stressed configuration

(1) Denoting displacement from pre-stressed to current configuration

-1 Inverse

e Denoting elastic contribution (e.g. of elongation e_i, $i \in \{1, 2, 3\}$)

$free$ Denoting free length (i.e. length of sample not clamped)

$g1$ Denoting length of sample gripped by upper clamp

$g2$ Denoting length of sample gripped by lower clamp

(i) Index denoting set of eigenvectors, $i \in \{1, 2, 3\}$

$Instron$ Denoting Instron measurement

p Denoting plastic contribution (e.g. of elongation e_i, $i \in \{1, 2, 3\}$)

T Transpose

Subscripts

$, x$ Partial derivative with respect to variable x

α, β Cartesian coordinate direction in current configuration

0 Reference configuration/initial value

6dB -6 dB value

$axial$ Axial direction which in this work corresponds to the x_1-direction

c Denoting combined standard uncertainty

cr Denoting combined relative standard uncertainty

exp Denoting number of experiments / test specimens

i, j Cartesian coordinate direction in current configuration

l Longitudinal waves

$major$ Denoting ARAMIS elongation measurement in x_1-direction

$minor$ Denoting ARAMIS elongation measurement in x_2-direction

$pulse$ Chirp pulse

r Relative change

s Shear waves

t Configuration at time t

th Theory

$transverse$ Transverse direction which in this work corresponds to either the x_2- or x_3-direction

w Water

z Denoting ARAMIS elongation measurement in x_3-direction

Other Symbols

∇ Del operator $= \hat{\mathbf{x}}_1 \frac{\partial}{\partial x_1} + \hat{\mathbf{x}}_2 \frac{\partial}{\partial x_2} + \hat{\mathbf{x}}_3 \frac{\partial}{\partial x_3}$

$\det \mathbf{g}$ Determinant of $\mathbf{g}$

Div $\nabla_{\mathbf{X}} \cdot \mathbf{g}$, the divergence of $\mathbf{g}$ with respect to reference coordinate system

div $\nabla_{\mathbf{x}} \cdot \mathbf{g}$, the divergence of $\mathbf{g}$ with respect to current coordinate system

Grad $\nabla_{\mathbf{X}}\mathbf{g}$, the gradient of $\mathbf{g}$ with respect to reference coordinate system

grad $\nabla_{\mathbf{x}}\mathbf{g}$, the gradient of $\mathbf{g}$ with respect to current coordinate system

$\operatorname{tr}\mathbf{g}$ Trace of $\mathbf{g}$

Acronyms

ARAMIS Photometric measurement system provided by GOM

ASM Angular spectrum method

ART Acoustic Resonance Technology

AS Aksje selskap / Stock company

CNC Computer numerical control

CONTENTS

DAQ   Data acquisition

DSP   Digital signal processing

DNV   Det Norske Veritas

FFT   Fast Fourier transform

FSW   Friction stir welding

GOM   Gesellschaft für Optische Messtechnik - developer and distributer of the ARAMIS system

GUM   Guide to the expression of uncertainty in measurement

MIT FabLab   Massachusetts Institute of Technology fabrication laboratory

NDT   Non-destructive testing

NFR   Norwegian Research Council

P-wave   Pressure or longitudinal wave

p.r.f.   Pulse repetition frequency

PIG   Pipeline inspection gauge

R&D   Research & development

RX   Reciever

SH-wave   Horizontally polarised particle motion of shear wave

SV-wave   Vertically polarised particle motion of shear wave

TOF   Time of flight

TX   Transmitter

UiB   University of Bergen

1

Introduction

1.1 Background / Motivation

As the industry strives to reduce maintenance and repair costs, non-destructive testing (NDT) of structures becomes increasingly valued both in production control and as a means to measure the utilisation and condition of key infrastructure. There are several NDT techniques which measure the stress level of a structure [1] - [3]. Techniques using optical measurements, magnetic measurements, x-ray diffraction, or the deeper penetrating ($<$50 mm) neutron diffraction are all limited to measuring surface or near surface stress or strains. However, for structural integrity the stress/strain state in the interior of the medium is important. Acoustic waves propagate with ease through materials and provide thus a means to probe the interior of structures. An extensive and general account on ultrasonic testing can be found in [4] and [5].

Acoustic Resonance Technology (ART) is an inspection method to measure the wall thickness of steel pipelines that has been developed by *Det Norske Veritas* (DNV) and is currently further developed and commercialised by Halfwave AS [6]. The ART method is mainly used to inspect long pipelines where the inspection tool (also called a Pipeline Inspection Gauge (PIG)) moves through the pipeline from start to finish propelled by the pressure difference. Along the way the tool propagates acoustic signals radially towards the pipeline wall with approximately normal incidence every 2-3 mm in the axial direction. ART is capable of measuring the wall thickness of pipelines transporting both liquids as well as gaseous content. The tool has 192 transducers distributed circumferentially around the inspection tool to be able to cover the entire

1. INTRODUCTION

circumference of the pipeline. The result of such an inspection is an enormous amount of data that can be used to make a detailed map of the wall thickness along the entire length of the pipeline. This can be used to assess if pipelines carrying water, oil, or gas have corroded during operation, and if there are critical areas where the pipeline under operational or accidental pressures can be exposed to loads close to the structural capacity of the steel. The ART method has been explained in more detail in Secs. 2.6 and 3.5.

The ART tool is qualified for several areas of use, such as wall thickness measurements of water, oil, and gas pipelines, and also characterisation of internal materials in the pipeline [7][8][9]. The technology is based on analysis of acoustic half-wave resonance spectra that are directly related to the geometric (i.e. thickness) and material properties of solid state materials like steel (but not limited to such).

The spectrum is created by transmitting a broad-band acoustic signal into the material that is excited into half-wave resonances, which leaks from the structure towards the receiving transducer[10][11]. The latter converts the signal into an electrical time series that is subject to a frequency spectrum analysis, from which the resonance peaks are identified. Knowing the sound velocity in the structure enables the extraction of the thickness of the structure.

Changes in material properties will to some extent change the acoustic properties of the material, and accordingly it might be possible to use ART to detect effects of these changes in the material. It is conceived that the sensitivity to changes in material properties is dependent on the type and amount of material change, and the transducer measurement system.

Where the currently available methods to investigate the stress/strain state of a medium with acoustic waves depend on the careful placement and alignment of one or more acoustic transducers on the surface of the medium, the potential for a non-contact measurement technique would be beneficial for the industry. This work has thus investigated the possibility of utilising the ART method to detect material changes due to high strains in steel materials. This is an important issue for the industry. For example it may enable pipeline operators to quantify the utilisation of the pipeline's strength capacity. Identifying areas where the utilisation is high might give sufficiently early warning to avoid sudden structural failures.

1.2 Objective

The overall objective of this work has been to investigate the possibilities for using a non-contact acoustic measurement system (like ART) to detect changes in material properties at very high elastic stress in steel pipelines.

The proposed approach is to study how the cross-thickness resonance frequencies of both longitudinal and shear waves across a steel plate (simplified substitue for a pipe section) change under the influence of very high static stresses induced in the plate / pipe section, and relate this to changes in the compressional sound wave velocity, c_l, and/or the shear sound wave velocity, c_s, and material properties of the elastic steel material.

The main question to be investigated in this work is whether measured and significant changes in c_l and/or c_s can be a reliable indicator of changes in material properties.

1.3 Scope of work

As stated above, the objective of this work is to investigate the possibility to relate a change in the elastic material properties of steel, due to an induced finite stress state, to a corresponding measured change in sound velocity, and if it is possible to measure this change using the ART methodology. There are two sources of nonlinearity that need to be taken into account when investigating the relation between sound velocity and stress state. The kinematic, or convective, term is independent of the material properties and is related to the nonlinearity of the propagating wave (e.g. effect of a finite amplitude wave) [12, ch. 9.1]. In this work small amplitude stress waves have been used, and it has thus been assumed that they behave linearly to the order of approximation needed. Thus the kinematic non-linearity can be disregarded. The other nonlinearity is related to the inherent physical nonlinearity of the solid. This effect is characterised by the constitutive behavior of the solid, and is called the acoustoelastic effect [12, ch. 9.1]. This effect has been assumed to contribute to the relation between the measured sound velocity and the applied stress state investigated in this work.

This study have thus been divided into two main aspects. The first aspect is how small amplitude acoustic stress waves propagate in a body subjected to a finite pre-stress, i.e. the non-linearity caused by the acoustoelastic effect. The second aspect is how resonant acoustic frequencies can be excited and extracted from layers and plates.

1. INTRODUCTION

The latter is the basis for the ART methodology already used in NDT / inspection of the thickness of steel pipelines. The theory behind the ART method is well known, and relevant literature is introduced in the literature section below (Sec. 1.4) and discussed in Sec. 2.6.

According to classic theory of continuum mechanics a three-dimensional body can sustain both longitudinal and shear waves through its bulk. For elastic isotropic materials these sound velocities are constant for a given material and are related to the second-order elastic moduli of the material as described in [13] (more on this in the literature review in Sec. 1.4). The fore mentioned assumption of a constant sound velocity in a material body is currently utilised by the ART methodology (chosen acoustic NDT equipment in this work) to estimate the wall-thickness of steel pipelines.

The acoustoelastic effect suggest that higher order effects of the constitutive relation introduce variation in the sound velocities as a function of the strain/stress state of the material body. This effect was already theoretically established in 1925 by Brillouin [14], and have later been confirmed and ellaborated on by several authors including Murnaghan (1937) [15], Hughes and Kelly (1953) [16], Truesdell (1961) [17], Toupin and Bernstein (1961) [18], and Thurston and Brugger (1964) [19]. Since the effect of the stress state on the sound velocities was first investigated there have been some controversy as to whether the developed theory is correct or not, and different alternatives have been proposed (see e.g. [20] and [21]). However, this work has based its investigation on the contemporary accepted theory of incremental elasticity, also known as the small-on-large theory. The relevant literature used is briefly introduced in the next section and consists mainly of the works of Ogden [22] [23], Norris [12] [24], and Abiza et al. [25]. It is the more detailed non-linear expansion of the constitutive relation for elastic materials compared to the linear elastic theory already used that may enable ART to assess the stress level of steel pipelines. In addition, the results from this investigation may also contribute to assess the accuracy of current wall-thickness measurements performed by ART.

In addition to the elastic behaviour, knowledge of the failure modes of materials and structures have led to many structures being allowed to plastically deform within some limitations. As the material starts to plastically deform, it is altered on a molecular scale as grain boundaries and dislocations move in response to the applied load, and

the elastic description is no longer valid [26]. This will affect the acoustic properties of the material, and the effect has been called the acoustoplastic effect [27][28].

To be able to consider the acoustoplastic effect, rigorous and exstensive experimental work is needed to establish the plastic properties of any given material. Based on the objective of this study the plastic behaviour and its effect on the acoustic propagation has not been considered in itself. However, the test specimens have been plastically deformed followed by elastic loading and unloading sequences to be able to investigate the elastic behaviour and its influence on the longitudinal and shear sound velocities (denoted c_l and c_s respectively) after the test specimens have been subjected to plastic deformation.

The scope of this work has been limited to investigating whether the acoustic response in a set of tensioned test specimens has a signifiant dependency on the induced stress/strain state, as well as if it is coherent across the number of tests. It has been decided to investigate this by establishing a tension experiment subjecting a set of close to identical steel test specimens to a pre-defined load history, while measuring the acoustic resonance frequency across the thickness of the specimens. To be able to compare the measurment results with theory it has been decided to numerically implement the acoustoelastic theory and simulate the change in sound velocities induced by the applied load history for several steel types previously investigated in the literature.

The relevant literature mainly referred to in this study is introduced in Sec. 1.4 below.

1.4   Literature review

This work has had an experimental focus where the objective has been, as described in Secs. 1.2 and 1.3, to investigate the possibility of estimating the level of stress in a steel sample by investigating how such a stress affects the acoustic sound velocities which can be measured by existing acoustic NDT equipment. This section review the current theoretical knowledge of the relations between longitudinal and shear sound velocities and the stress state of an isotropic hyperelastic solid (e.g. steel or aluminium). Then it continues to investigate the experimental work and studies that have been performed in

1. INTRODUCTION

this field, and which can contribute to the success of the current objective (see Sec. 1.2).

The classic linear behaviour of elastic materials can be found in any text book on continuum mechanics, e.g. [13] or [29] and can be used to establish solutions for the wave equations as done in for example [30]. According to the linear theory of elasticity, the sound velocity for acoustic stress waves in elastic isotropic materials (like steel) is a second order effect of the constitutive relation between the stress state of, and the strain field in, the material body (see Sec. 2.2.2 for details). A three-dimensional body can sustain both longitudinal and shear waves through its bulk. They are, according to linear elastic and isotropic theory, given through any set of two second-order elastic moduli, and are constant for the given material [13]. Classical continuum mechanics and the linear approximation to the elastic wave theory have been regarded as well-established and easily accessible theories and have not been included in this literature review beyond what has been mentioned above.

As early as 1925 Brillouin investigated the effect of a hydrostatic pressure [14] (or more correctly the hystrostatic stress [29, ch. 5.7]) on wave propagation in an elastic medium. He found that the propagation velocity of acoustic waves was dependent on the hydrostatic stress [14], which Tang in his 1967 paper [21] rewrote in a form equivalent to

$$\rho c_l^2 = \lambda + 2\mu - p, \qquad \rho c_s^2 = \mu - p, \tag{1.1}$$

where λ and μ are the Lamé elastic parameters, ρ is the density, and p is a hydrostatic pressure. However, one consequence of this is that sound waves would stop to propagate at sufficiently large pressures (i.e. $c = 0$). This lead to controversy around his theory, and many tried to extend the linear theory of elasticity to a general case for finite strains. Murnaghan presented in 1937 [15] such a theory of finite deformation in elastic isotropic solids where the third-order elastic constants l, m, and n were introduced as a second order expansion of the stress-strain relation (based on the principle of conservation of strain energy), in addition to the second-order elastic moduli λ and μ. The second-order elastic moduli describe what can be regarded as a first-order approximation to the elastic theory, while including the three third-order moduli describes a second-order approximation. Birch applied Murnaghan's theory in his 1938 paper [20] to show that this theory gave stress-strain relations on the same form as the classical theory with elastic parameters depending upon the pressure. He continued to show that the

6

theory agreed well with experimental results for sodium and cesium giving a single-constant formula relating the change in elastic coefficients (and thus also the sound velocity) and the applied pressure. He thus argued that the observed change in sound velocity as a function of an applied pressure was due to a pressure dependency on the elastic constants rather than a difference in the equation of small perturbation motion compared to the equation of motion in the classical elasticity theory as suggested by Brillouin [14]. Biot suggested another theory in his 1940 paper [31] in which he also argued that the the influence of pressure only appears in the elastic coefficients of the material. However, as pointed out by Tang in his 1967 paper [21] the approaches of Birch [20] and Biot [31] can not reproduce the results of Brillouin [14]. Tang showed that the paradoxial result suggested by Brillouin [14] was due to the incorrect assumption that the elastic parameters are not functions of pressure. He argued thus that both the elastic parameters of the material, as well as the equation of a perturbuation motion are influenced by the initial stress state, which can be obtained from Murnaghan's theory [15] of finite deformation.

In 1953 Huges and Kelly [16] used the theories of Brillouin [14] and Murnaghan [15] together with measurements of the longitudinal and shear sound velocities under both hydrostatic and simple compression (homogeneous deformations) to estimate numerical values for the three third-order elastic constants l, m, and n for three different isotropic and elastic materials. They also showed that for small deviations about a hydrostatic pressure an isotropic solid would still act as an isotropic solid where the second-order elastic moduli (e.g. λ and μ) have changed linearly with the applied stress. Huges and Kelly showed that this change in second order moduli could be expressed by the third order elastic moduli l, m, and n.

This has later been regarded as the first confirmation of the acoustoelastic theory. (Note that the term "second-order elastic deformation" used in [16] uses what in this work has been refered to as the "third-order elastic constants". This is due to the fact, as will be further explained in Sec. 2.1.3, that when expanding the constitutive relation between stress and strain there are no first-order elastic constants, which leads to the second-order elastic constants describing the first-order approximation of the stress-strain relation etc.) Bergman and Shahbender also measured the sound velocity of longitudinal and shear sound velocities across a column of aluminium transverse to an applied uniaxial compression [32]. The column was subjected to loads beyond the elastic

1. INTRODUCTION

yield point and all the way until it buckled. The results have been well documented, and the autor refered to the earlier work by e.g. Hughes and Kelly [16] and indicated that the effect was either due to change in density or change in relevant elastic constants. The findings in [32] show in particular that the longitudinal sound velocity (c_l), the shear velocities (c_s) with particle motion polarised parallel and/or perpendicular to the load have different developments as function of the applied stresses. This is also the earliest instance investigating the acoustoplastic effect identified (A review of the literature on the acoustoplastic effect will be presented later in this section).

Early work considered only isotropic hyperelastic materials. In 1961 Toupin and Bernstein presented an extension of Hughes and Kelly's method to determine the third-order elastic constants for istoropic homogeneously deformed materials to materials with arbitrary symmetry [18]. Toupin and Bernstein derived the general equations for small displacements superimposed on a finite deformation of a perfectly elastic material anew, including restrictions on the strain energy function to allow for arbitrary symmetry and compatability with classical elastic theory. Considering isotropic materials they deduced a set of third-order elastic constants which satisfied the invariance of the strain energy function for the orthogonal group of transformations of the natural coordinates. These third-order elastic constants were denoted ν_1, ν_2, and ν_3 and corresponds to the constants l, m, and n presented by Murnaghan in [15]. The different sets of third-order elastic constants are equivalent, but are based on different selection of invariants of the second order tensors used in the strain energy function (see e.g. [29, ch. 3.8]). In 1961 Truesdell wrote a paper [17] expanding and clarifying the expressions derived in the work of Toupin and Bernstein, which was a good summary of contemporary wave theory in finitely deformed elastic materials.

Thurston and Brugger derived in their 1964 paper [19] expressions for what they called the natural sound velocity (i.e. a sound velocities calculated based on the initial Lagrangian, or natural, state of the material) and their stress derivatives. The advantage of such a natural velocity is that it is more easily obtained from experiments than actual velocities which must be corrected for change in path length due to the applied stress. At this time most sound velocity measurements where done by measuring time-of-flight, or its inverse, the repetition frequency, of a round trip between opposing faces of the test specimens. In 1965 Thurston expanded the theory and introduced the term effective elastic coefficient [33]. These effective elastic coefficients where defined in such a way

8

that the formulas for wave propagation would not change under hydrostatic pressure when expressed in terms of them. He also introduced wave-propagation coefficients which were more convenient when discussing wave propagation. An important note is that for all other stress states than a hydrostatic pressure the full symmetry commonly expected of elastic coefficients is lost, even for isotropic materials which essentially experience an anisotropic stress.

At this stage the theory of acoustoelasticity has been developed to a level which describes the effect of stress on the acoustic velocities sufficiently for the purpose of the current proposed work. A good review can be found in the paper by Pao and Gamer from 1985 [34]. Without going into the work of all the different authors who have specialised in different aspects and applications of the acoustoelastic effect in detail, the works which this study have been directly based on have been presented in the following.

Although there are several equivalent theories on the acoustoelastic effect, they differ mainly by the selection of invariants of the strain energy density function, and thus resulting in different constants describing the elastic properties of a material (i.e. from the constitutive relation between stress and strain). The theoretical background used to predict and compare the measurements of this study is mainly based on the thorough account of the theory of finite elasticity presented by Ogden in 1997 [22], supplemented by the works of Norris in 1998 [12, ch. 9], and by Ogden and Norris in 2007 [23], [24] respectively, and with the relevant special case applicable for the experimental setup used here outlined by Abiza et al. in 2012 [25]. Norris notes that there are many notations used for the third-order elastic moduli to describe an isotropic hyperelastic material. In addition to the two sets derived by Murnaghan [15], and Toupin and Bernstein [18] mentioned above, Norris notes three other sets. One derived by Bland in 1969 [35], one by Eringen and Suhubi in 1975 [36], and finally the set derived by Landau and Lifshitz in 1959 [37] (this work refers to the 3rd edition published in 1986). All of these sets of three third-order elastic coefficients are spescial cases for a hyperelastic isotropic material. The general third-order elastic coefficients can of course also be expressed by the standard tensor notation C_{ijklmn} [22], or using Voigt's notation C_{IJK} [12]. The Landau and Lifshitz coefficients [37] are denoted A, B, and C, and are the set used throughout this work and the main works refered to ([12],[22],[23], [24], [25]). These works will be

discussed further when presenting the relevant theory for this work in Ch. 2.

Having presented the main literature leading up to the acoustoelastic theory applied in this work, the next part will look into the history of experimental work done to corroborate the theory. As already mentioned Hughes and Kelly confirmed the acoustoelastic theory experimentally by determining the third-order elastic moduli of three different elastic materials by measuring sound velocities in the material under hydrostatic and simple compression already in 1953 [16], while Bergman and Shahbender measured acoustic velocity in an aluminium bar under uniaxial compression well outside the elastic limit in 1958 [32]. Many authors have since investigated the effect of stress on the acoustoelastic velocities in different types of materials. Since this work investigates the applicability of a non-fixed-contact acoustic measurement technique (like ART) on highly stressed steel, not all historic acoustoelastic measurement techniques or results have been deemed appropriate to be included here.

In 1962 Crecraft reported measured variation of both longitudinal and shear sound velocities induced by stress for waves with frequencies in the MHz region in stressed nickel steel [38]. In his 1967 paper [39] he also compares acoustoelasticity (or sono-elasticity as he termed it) to the theory of photoelasticity based on the similar behaviour of the polarised shear waves in a stressed solid to that of polarised light in a transparent and stressed solid. He also gives a reasonable account of the different contemporary measurement methods for determining the sound velocity available. A pulse-echo technique, as applied by Hughes and Kelly [16], lacks precision. A refinement was introduced by Bergman and Shahbender [32] comparing the pulse-echo going through the specimen with a simultaneously transmitted pulse going through a delay line matching the unstressed delay time of the specimen. This increased the resolution of the relative velocity change measured in a 4 inches thick aluminium specimen to 0.01 %. Espoinola and Waterman presented in 1958 [40] an ultrasonic interferometer to measure temperature induced sound velocity change with a resolution of $5 \cdot 10^{-5}$ in fused silica and alkali halide crystals. A technique described by Cedrone and Curran [41] called the "sing-around" method used a recieving transducer to retrigger the transmitter, and thus creating a pulse "singing-around" the system at some pulse repetition frequency (p.r.f.). In this method the period of the signal is adjusted to match an integer multiple of the transit time, and thus making it possible to apply different interference schemes to

estimate the sound velocity. Crecraft [39] [42] used this sing-around method to measure the sound velocity change of both longitudinal and shear waves with polarised particle motion across the center of bars that were uniaxially stressed. He investigated three different materials, nickle-steel, copper, and aluminium, and estimated the third-order elastic constants based on the sound velocity measurements. The measured relative change in sound velocities of waves propagating perpendicular to the applied uniaxial compressive stress for the nickle-steel reported by Crecraft was $-8.7 \cdot 10^{-5}$ per MPa for the longitudinal wave, $-2.9 \cdot 10^{-5}$ per MPa for the shear wave with particle motion perpendicular to the applied stress, and $-8.2 \cdot 10^{-4}$ per MPa for the shear wave with particle motion in parallel to the applied stress (converted from the original units in [39] by the author of this work). The nickle-steel is sufficiently simlar to the steel used in this work, and has thus been included in the simulations described in Ch. 4 of this work. Crecraft also noted that for longitudinal waves (and for the individual shear waves) measurements of the path length to within 0.01 % would be needed to detect even large stresses, and would not give any information on the principal stress directions [39]. On the other hand, for the birefringence effect of the shear waves with particle motion polarised perpendicular to and in parallel with the applied stress, the difference in the two principal shear wave velocities would indicate the magnitude of the stress while their particle motion polarisation would indicate the principal stress axis. Thus it would be imperative to measure these principal shear waves [39]. However, Crecraft also identified practical problems in relation to exciting and alignment the particle polarisation direction of the shear waves with the principal stress directions and at the same time ensuring the shear waves seeing the same path length to remove the need of accurate measurements of this [39]. The ideas presented by Crecraft in [39] have been important for the selection of relevant measurement quantities in this work as described in Sec. 2.7 and Sec. 3.5. Crecraft [39] also discussed his results in light of a preferred orientation (elastic anisotropy) and further increase of this effect by plastic deformation. He refers to [43] and notes that

> (. . .) strain in the order of 50 % is necessary to cause appreciable change in preferred orientation (. . .)

Since the maximum strain applied in this work is in the order of 4.5 % « 50 % that any measured relative change in sound velocities as a function of plastic strain is most

likely due to dislocation movement alone (as suggested by Crecraft [39]). It is noted with this in mind that the objective of this work relates to measurements in the elastic region, but that the test specimens have been deformed plastically to investigate the elastic behaviour after such plastic deformation.

Smith et al. have in their 1966 paper [44] measured stress induced sound velocity change for polycrystalline materials. [44] described an acoustic measurement method applying interference of shorter pulses passing through the test specimen with a longer carrying pulse that do not propagate through the specimen (both with a frequency of 5 MHz). The inerference between the two signals can be used to measure changes in sound velocity with a resolution of approximately $2 \cdot 10^{-6}$. They have measured the change in sound velocity for waves propagating perpendicular to the applied compressive uniaxial load, both for longitudinal waves and shear waves polarised parallel and perpendicular to the applied load. Based on these measurements they then estimated the third-order moduli using the theory of Thurston and Brugger [19]. 5 of the 15 investigated materials were steels. All these 5 steel types have been included in the simulations performed in this work to be able to compare the behaviour of the currently used steel to that of other similar steels reported in the literature (see Ch. 4). Note that the setup used for the measurements in [44] consists of identical quartz transducers acting as transmitters and receivers bonded directly to the test specimens (X-cut quartz were used to excite longitudinal waves, while oriented Y-cut quartz where used to excite the respective polarised shear waves). It is also worth noting that Smith in 1963 [45] looked at other authors' measurements and their reported behaviour of the acoustoelastic effect together with own measurements on nickle-steel. Here he shows that the birefringence of the two shear waves with particle motion polarised parallel and perpendicular to the applied tension behaved linearly and identically in the elastic regions both before and after appreciable plastic deformation. The birefringence of the shear waves was measured to be in the order of 0.1 % relative to the unstressed shear sound velocity for the entire elastic region of the tested nickle-steel [45]. He also showed that the plastic strain and dislocations had negligible effect in polycrystalline materials (like aluminium and steel) [45].

In 1976 Egle and Bray [46] presented experimental results of the stress-induced changes in acoustic wave velocity in steels typically used in railroad rails. They measured the five unique wave velocities that according to Hughes and Kelly [16] can be

determined for a state of uniaxial stress. These five wave velocities are of two waves propagating in the direction parallel to the applied stress (one longitudinal and one shear wave), and three waves propagating perpendicular to the applied stress (óne longitudinal, and two shear waves polarised in parallel and perpendicular to the applied stress). Egle and Bray [46] conclude that their measurements agree with the second-order theory of Hughes and Kelly [16] within the limits of the measurement accuracy. Based on the five velocity measurements done on two samples of the rail steel, the Murnaghan constants [15] where estimated. The applied uniaxial tension was varied between compressive and tensional loads deforming the specimens elastically between -0.09 % and 0.09 % strain. This resulted in the relative change in sound velocities of waves propagated perpendicular to the applied stress for one of the test specimens of approximately 0.03 % per 1 % strain for the longitudinal wave, -0.15 % per 1 % strain for the shear wave with particle motion in parallel with the applied stress, and 0.006 % per 1 % strain for the shear wave with particle motion perpendicular to the applied stress [46]. The estimated third order elastic constants from this work have also been included in the simulations described in Ch. 4.

These three works ([39],[44],[46]) give a reasonable spread in third order elastic constants for various steels to be able to compare the measurements of change in sound velocities performed in this work with the theoretically predicted behaviour of other steel types investigated in the literature. Thus, even though there may be relevant measurement data found in the literature of other authors, this work has limited its scope to the above mentioned relevant steel types.

Guz et al. started in the early 1970s to investigate both theoretically and experimentally the possibility of determining bi-axial stress states by measuring the propagation velocity of shear waves polarised in the direction of the two principal stresses, given the third-order elastic constants [47], [48]. Based on this work Gushcha and Makhort showed a good correspondence between acoustic measurements and theoretical equations of residual stresses produced by spot welding at the center of an aluminium alloy sample in their paper from 1976 [49]. Bach and Askegaard discussed in 1979 [50] a method to investigate the difference in residual principal stresses of a bi-axial stress field based on the difference in relative velocity change of the polaraised shear waves using a 45° transducer method and the theory of Hughes and Kelly [16]. This method

is also reffered to as acoustoelastic birefringence, and simplifies the acoustoelastic theory by introducing the proportionality factor between the above mentioned difference in relative shear sound velocities and between the biaxial stresses. This proportionality factor has been called the stress-acoustic constant, and can be expressed by the second and third-order elastic constants as done by Bach and Askegaard [50]. Using this simplified version of the acoustoelastic effect (or similar variations with different proportionality factors utilising changes in either the shear wave velocities or longitudinal wave velocities), several authors have estimated the residual stress state of different material samples (see e.g. [51], [52], [53], [54], [55]). More recent work based on the work of Guz et al. can be found in Nikitina's 2006, 2007 and 2010 papers [56], [57], [58].

In 1981 Johnson presented a generalised acoustoelastic theory which included the effect of plastic deformation [59] based on his work [60] that the assumption of a constant sound velocity during plastic deformation might not be applicable for all materials. His approach was to include arbitrary functions of the plastic strain and work-hardening parameter in the strain-energy formulation. In the 1987 paper of Daami et al. [61] they investigated the effect of plastic deformation on several materials. They concluded that in order to estimate stress levels in plastically deformed material it is necessary to survey the relevant material to determine the acoustic response caused by the plastic deformation, and that the un-modified acoustoelastic method would only give a good measure of the stresses in the materials in which the acoustic response is unaffected by plastic strain (much in line with the work of Johnson [59]).

Kobayashi has also studied the effect of plastic deformation on the propagation velocity of acoustic waves both theoretically and experimentally in e.g. [27] and [62], and more recently in [63]. This extension of the acoustoelastic theory has also been termed acoustoplasticity. For the acoustoplastic theory it is common that the parameters describing the plastic behaviour need to be, in most cases, experimentally determined, and may be quite diverse for materials with similar elastic behaviour. The objective of this work focus on the elastic behaviour which should be sufficient for many industrial applications where the material is not intended to deform plastically. This work has thus deemed it to be too cumbersome to include this effect in a study of a suitable NDT application for industry steel types which might have similar elastic behaviour, but very different plastic behaviour. The test specimens used in this work have however been

subjected to plastic deformation to investigate the elastic behaviour after such plastic deformation as mentioned earlier. This has been discussed in more detail in Secs. 2.5 and 2.5.2.

It is deemed unecessary to go into historical detail on all the different methods and materials investigated in the literature as many of these have established that it is possible to measure a linear acoustoelastic effect when a test specimen has been subjected to an applied stress state, some works are worth noting. In a recent method applied by Gachi et al. in 2009 [64], they performed a simple uniaxial test to calibrate the acoustoelastic effect for the current test specimen material. Then they estimated the residual stress across the heat-affected zone of two aluminium sheets joined by friction stir welding (FSW). The residual stress was also estimated by X-ray diffraction, and the comparison showed good correlation of the results from the two different methods. This is an approach that seems promising also for the non-contact measurement technology ART used in this work (i.e. by establishing the relation of the acoustoelastic effect for a relevant steel type by a uniaxial tension and then using this relation when performing the actual acoustic measurements).

As presented in this literature review the theoretical basis for stress estimates based on measurment of acoustic velocities are sufficiently mature, which is also reflected by many successful experimental measurements of various stress states utilising the acoustoelastic effect. It is however recognised that plastic deformations may render the acoustoelastic theory insufficient for the purpose of estimating stress states. acoustoplastic theory needs specific experimentally determined properties for each relevant material, and has thus been regarded as too specialised for the purpose of the current investigation. However, the acoustoelastic theory may possibly yield good estimates of the stress level with the group of materials where the relevant level of plastic deformation does not affect the acoustic response to applied stresses. Therefore the current work has also investigated the acoustic response to plastic deformation for the currently used steel.

The currently used measurement technology utilise transient acoustic scattering from layers and plates which has been described in the papers by Maze et al. in 1985 and 1986 [65], [10], and by Guyott and Cawley in 1988 [11], and will be further discussed in Sec. 2.6.1. The actual measurement system (ART) is detailed in the patents [7] and [8]. In addition, the ART method utilize common digital signal processing theory to extract

the excited resonance frequencies. This theory can be found in any signal processing text book, for example [66] by Smith.

Looking at the experimental setups described in the literature to measure the sound velocity across a stressed test specimen most utilise transducer setups that comprise one or more transducers bonded directly to the test specimen (see e.g. Daami et al. 1987 [61] and Sato et al. 1993 [67] using opposing transducers on either side of the specimen, or Gachi et al. 2009 [64] using a setup of one transceiver and two receivers on the same side of the specimen). This is related to the fact that fluids do not carry shear waves [13], and thus to be able to measure changes in shear wave velocities it has historically been convenient to use transducers exciting shear waves bonded directly to the test specimen. The work of Scott et al. [52] mentioned above apply longitudinal waves propagating through water, and base their results on the measurement of longitudinal waves only. However, as shown by Kim and Hong in their 2009 paper [68] it is possible to measure change in sound velocities both for longitudinal and shear waves through mode conversion / refraction (see [69, ch. 9]). Kim and Hong used in [68] a pulse-echo method of longitudinal waves that impigning on a bounded test specimen at an oblique angle to excite both longitudinal and shear waves in the test specimen. They also showed that they could measure a relative change in the ratio of two mode-converted waves (one based on the time-of-flight of only longitudinal waves and one based on the time-of-flight of both longitudinal and shear waves) of approximately $2 \cdot 10^{-6}$ per MPa.

The currently selected measurement method consist of a broad band pulse-echo transducer with a frequency dependent beam angle. The target will thus be excited by longitudinal waves with a distribution of incident angles around the normal, and thus exciting both longitudinal and shear waves in the test specimen. This has been done by e.g. Maze et al. in their 1985 paper [65] for an unloaded plate. However, the author is not aware of any other work applying this method to measure the relative change in sound velocity for both longitudinal and shear waves with the intent of studying the acoustoelastic effect. One of the main benefits of being able to measure the change in both longitudinal and shear sound velocity through a fluid coupling medium is that the measurement equipment can easily move along or across a test specimen and measure at several locations without the rigorous work of bonding and detaching it between measurements. During the current work it has been shown that the ART methodology

is capable of measuring resonance frequencies of different wave types (longitudinal and shear), and thus indirectly the sound velocity of these waves. Another limitation of transducer setups that depend on more than one transducer is that they are very much dependent on knowledge of the path length of the acoustic waves which may change significantly under high loads and stresses (see elastic deformation in e.g. [13, ch. 1.3] and plastic deformation in e.g. [70]). For a pulse-echo setup where all the waves excite approximately the same area of the test specimen and propagate close to perpendicularly across the test specimen, different waves can be combined to remove/minimize the thickness dependency as mentioned in [39] and shown by Kim and Hong in their 2009 paper [68] using time-of-flight measurements. The current work have also shown how this is possible by using resonance frequencies. This method has been presented in Secs. 2.7, and is one of the main contributions of this study.

Preliminary results from the current work have been presented at conferences as paper [71], poster [72] and presentation [73].

1.5   Outline of thesis

This thesis has been divided into seven main chapters, and this section briefly describes the content of each chapter.

Chapter 1 gives a short introduction to why this study was initiated, the background for it and its objective. A proposed scope of work for this study has been presented as well as a review of the current knowledge and application of the acoustoelastic effect found in literature with a more specific overview of the relevant literature applied in this study. Finally the introduction chapter gives a brief outline of the thesis.

In chapter 2, the relevant theory used in this work is presented. The theory related to the deformation of the steel test specimen has been divided into two parts. The first part describes the mechanics of a continuum subjected to finite strains and the constitutive relation between strains and stresses. This can be thought of as the mathematical description of the steel pipeline when subjected to stresses caused by for example internal pressure, referred to as the "large" pre-stress state. The second part is related to the

1. INTRODUCTION

response of a pre-stressed steel subjected to an additional, but much smaller, dynamic deformation in the form of an acoustic pressure signal. This is also known as the acoustoelastic effect.

The theory of elastic continuum mechanics can be derived with focus on different aspects, and as such equivalent theories can be described by different sets of parameters. Some of the different descriptions found in the literature have briefly been mentioned for the reader to be able to relate the results of this work in light of other well used parameters.

The theory presented in the first sections of chapter 2 is only applicable under the assumption of elastic deformation. Steel is a ductile material and can sustain large plastic deformations. A discussion of plastic deformation and how elastic and plastic contributions can be separated has been presented.

Finally the underlying theory for the ART measurement technique is presented, followed by some suggestions on relevant measurement quantities to better be able to extract the necessary dependency of the sound velocity on the applied stress state.

Chapter 3 describes the experimental setup and measurement methods chosen to investigate measurements of the acoustoelastic effect by ART. It consists of four main parts. First we have the actual steel test specimen for which we want to investigate the acoustoelastic effect. Then we have the tension machine which subject the test specimen to a "large" finite strain, which puts the test specimen in a pre-stressed state. The third component is the ART equipment which is applied to generate an acoustic signal propagating through the test specimen in the pre-stressed state. This is the actual measurement which reveal the acoustoelastic effect in the test specimen. In addition a fourth element is added to be able to quantify and take into account the geometrical change the test specimen experience during the load history.

In chapter 4, 8 different sets of second- and third-order elastic constants for common steels reported in the literature have been presented, and the corresponding input values for numerical simulation of the acoustoelastic theory presented in Ch. 2 is collected.

Chapter 5 presents the experimentally obtained measurement results and any relevant estimate of derived results in an order which corresponds to the order of the

presented experimental setup in chapter 3. At the end the relevant results are compared with the theory presented in chapter 2. The main results are presented in figures and tabulated data inline with the text, however, supporting data is also presented in figures and tables in appendix C and D.

The uncertainties of the obtained measurement results are then discussed and described and tabulated in chapter 6. Each result presented in chapter 5 is treated in the consequtive order of chapter 5. The estimation of uncertainty and the theory of propgation of theory is based on the *Guide to the expression of uncertainty in measurement* (GUM)[74]. Parts of this document is referenced and presented in line with the discussion of uncertainty in the results where it first becomes relevant. Figures and tabulated data used to document the uncertainties are presented in appendix C and D.

Finally the discussion of the results together with the conclusions of the study and recommendations for further work are collected in chapter 7 and 8.

Detailed derivations that did not fit naturally in to the main part of the thesis have been included in App. A. Calibration certificate for the tension machine have been included in App. B. App. C include additional figures which supports the condensed results presented in the main part of the thesis. A large table of initial geometrical measurements of the test specimens is included in App. D.

1. INTRODUCTION

2

Theory

The objective of this work has been to investigate the possibility to relate a change in the elastic material properties of steel, due to an induced finite stress state, to a corresponding measured change in sound velocity. When studying waves in solids nonlinear effects must be taken into account. Norris states in [12, ch. 9.1] that:

> "Two general sources of nonlinearity can be recognised: the kinematic, or convective, nonlinearity that is independent of the material properties, and the inherent physical nonlinearity of the solid, as characterised by its constitutive behavior."

The current experimental setup has been divided into two separate features. The first one is to apply a "large" uniaxial deformation to the steel test specimens which introduce the prestress. The relation between the deformation and resulting prestress is determined by the characteristic constitutive relation for the relevant steel and include the inherent physical nonlinearity of the solid as described by Norris above. This effect will be presented in detailed in this chapter. The second feature is to apply a "small"-amplitude acoustic sinusoidal stress perturbation to the already applied prestressed state. In this work it has been assumed that the acoustic stress perturbation can be regarded as linear. The nonlinear effects related to the kinematics, also called the convective effect, are thus assumed to be negligible in this work. Further reading on the nonlinear effects related to the kinematis can be found in [12, ch. 9.1].

The prestress of the steel has been induced by fixing a rectangular test specimen in a tension machine and deforming it through displacment- or load-controlled deformation. A transducer has then been used to propagate a sinusodial acoustic signal through water

as coupling medium towards the center of the face of the test specimen. The propagated signal exert a dynamic acoustic pressure field at the surface of the test specimen, which introduces a stress perturbation propagating across the thickness of the test specimen. This allows us to measure how fast the stress perturbation propagates through the test specimen, and consequently estimates the average sound velocity across its thickness at the current applied prestress. The details of the mechanical and acoustic experimental setups are described in Secs. 3.3 and 3.5 respectively.

In accordance with these two aspects of how the sound velocity is measured and how it relates to the applied stress state, the theoretical backround is ordered correspondingly. Sec. 2.1 describes the theoretical stress state of a known finite motion (i.e. finite stress and strain), or its specialization; a known static deformation. Then Sec. 2.2 examines the problem of a superimposed incremental motion on the known finite motion (i.e. an infinitesimal acoustic amplitude). This is also known as the theory of "Small-on-Large" [24]. These two sections first define the stress and strain state of a body, the relation between applied stress and resulting strain known as an elastic constitutive law. Based on this relation, the subsequent sound velocity and its dependence on the stress/strain state of the body is derived. The terminology and nomenclature of this work has been aligned with those used in [22], [23] and [25]. Depending on different choices of parameters the elastic moduli of an elastic body can be presented in slightly different forms. Sec. 2.4 summarises the some of the common alternatives found in the literature and how they relate.

The theory presented in Secs. 2.1 and 2.2 are approximations valid for elastic deformations. However, when a specimen is strained so far that the elastic approximation no longer holds and the material starts to plastically deform, an approach to account for the plastic deformation is needed. Sec. 2.5 describes plastic deformation and how it is included in this work.

After establishing the theory of the stress/strain state of a deformed body in Secs. 2.1 to 2.5, this chapter continues to describe the theory behind the measurement technique used to measure the sound velocity in Sec. 2.6. Finally other relevant measurement quantities are described in Sec. 2.7.

It should be noted that some of the figures presented in this chapter have been made to fit the terminology and nomenclature used, but are inspired by figures in the two textbooks used as the main references [22, ch. 2] and [29, ch. 5,6,10], as well as the

article [10], while Fig. 2.10 was obtained through personal communication with other authors [75] and [76].

2.1   Large elastic deformation - prestress

This section describes the theory of continuum mechanics needed to establish the theoretical stress/strain field of a deformed body, which in this case will represent the test specimen and the prestress as it is deformed in the tension machine. It is important to establish this basis to understand the conditions under which the superimposed acoustic stress field propagates.

The basic physics of the infinitesimal deformation of a continuum can be found in any continuum mechanics textbook (see for example [29]), or more specific for this work on finite deformation in textbooks on non-linear elastic deformations [22]. This work tries to closely follow the terminology and nomenclature used in [23] and [25] which are based on [22].

Contact forces, body forces, or temperature changes within the body result in a stress field which may cause a deformation. This deformation can be described by the relative displacement of points within the body, also called a strain field. The relation between applied stresses and induced strains are expressed by constitutive equations and suitable relations will be presented in this section. Note that the setting is assumed to be isothermal, and thus no thermodynamic effects have been included in this theoretical framework [22, ch. 3].

A deformation of a continuous solid can be categorised depending on whether the deformation process is reversible or not. If the original configuration can be recovered by removing the stress field the deformation is elastic. On the other hand, if the original configuration can not be recovered by removing the stress field the deformation is plastic, or irreversible. This occurs after a material is subjected to stresses above a certain threshold value. Above this threshold value, called yield stress, the material undergos changes on the atomic lattice level. Slips or dislocations between neighbouring atoms, or groups of atoms, in the atomic lattice is generally not reversible, and the final configuration after the stress field is removed will thus be different than the original configuration [29, ch. 10.5]. This chapter will mainly consider elastic deformations, but

will also include some aspects of plastic deformation in Sec. 2.5.

2.1.1   Deformation and strain

The first step to gain theoretical understanding of the behaviour of any elastic material is to establish a framework to be able to describe a material body, its behaviour as a whole, and the behaviour of any point within its boundaries. The aim of this section is to introduce and show the mathematical framework for a suitable measure of deformation that can be used to describe the deformation of the test specimen. Although the following theory is applicable to an arbitrarily chosen material body, it is in this text also related to the chosen configuration of the steel test specimens used in this work. Thus, if not otherwise specified, the framework can be used for any arbitrarily chosen elastic material body even though the test specimen is refered.

The test specimen can be treated as a collection of points in a connected open subset of a three-dimensional Eucledian space, which is refered to as the configuration of a continuous body B [22, ch. 2.1.2]. This is illustrated by the gray area denoted B_0 in Fig. 2.1 where the subscript 0 denotes the reference configuration (i.e. initial or undeformed configuration). Although arguably a material body consists of discrete points of atoms, continuum mechanics treats the body as a continuum of material points.

The position of a material point P within the reference configuration B_0 can be given by the position vector $\mathbf{X}$ relative to a fixed origin $\mathbf{O}$. Note that vectors and tensors are denoted by bold symbols throughout this text. A transformation of a body from a reference configuration (B_0 in Fig. 2.1) to another configuration B_t, where subscritp t denotes the configuration at time $t \neq 0$ (i.e. current or deformed configuration), can be decomposed into two components. The first is a rigid-body displacement which consist of a translation and/or a rotation of the body. This rigid-body displacement does not change the size or shape of the body [22, ch. 2.1.4]. The second component consist of a deformation of the body. This happens when the shape and/or the size of the body change, and occurs if there is a relative displacement between the material points within the body [22, ch. 2.2]. After a rigid body motion and/or a deformation the new position of the same material point is indicated by p with position vector $\mathbf{x}$ relative to the same fixed origin $\mathbf{O}$ in the current configuration B_t.

Note that the coordinate system and its origin, which the material points are referenced to, can be arbitrarily chosen. For convenience **O** has been selected to be the origin and have been defined at the same point in space for all the coordinate systems used in this thesis. The coordinate systems used are cartesian coordinates where the same orientation with the unit base vectors $\hat{\mathbf{x}}_i$, $i = 1, 2, 3$ as shown in Fig. 2.2 have been used for all configurations (e.g. for B_0 and B_t, or any other configuration). Note also that the convention that a capital variable signify a Lagrangian reference frame (i.e. with respect to the reference configuration) while a lower case variable signify a Eulerian reference frame (i.e. with respect to the current configuration) is used throughout this work. Thus the Lagrangian coordinates are denoted by **X**, while the Eulerian coordinates are denoted by **x** .

The motion and deformation of the body can be represented by a mapping function χ which takes points **X** in B_0 to points **x** in B_t such that

$$\mathbf{x} = \chi(\mathbf{X}, t) \tag{2.1}$$

and vica verca (under the assumption that the Jacobian determinant $J \neq 0$, which will be justified below)

$$\mathbf{X} = \chi^{-1}(\mathbf{x}, t) \tag{2.2}$$

[22, ch. 2.1.2-3].

This mapping function represents thus the displacement field, consisting of the displacement vectors $\mathbf{u}(\mathbf{X}, t)$ of all the material points. Note that this is a mathematical function describing the displacement of each material point from one configuration to another, thus it does not consider any properties of the relevant material. The displacement of a material point P can thus be defined as the point difference

$$\mathbf{u} = \mathbf{x} - \mathbf{X} \tag{2.3}$$

or equivalently

$$\mathbf{u}(\mathbf{X}, t) = \chi(\mathbf{X}, t) - \mathbf{X} \tag{2.4}$$

as shown in Fig. 2.1 [22, ch. 2.1.2-3].

Fig. 2.2 shows how two neighbouring particles P and Q in the reference configuration move in relation to each other during deformation. This local deformation at a material point **X** is described by the deformation gradient tensor defined as [77]

$$\mathbf{F} = \nabla_{\mathbf{X}} \mathbf{x} = \nabla_{\mathbf{X}} \chi(\mathbf{X}) \tag{2.5}$$
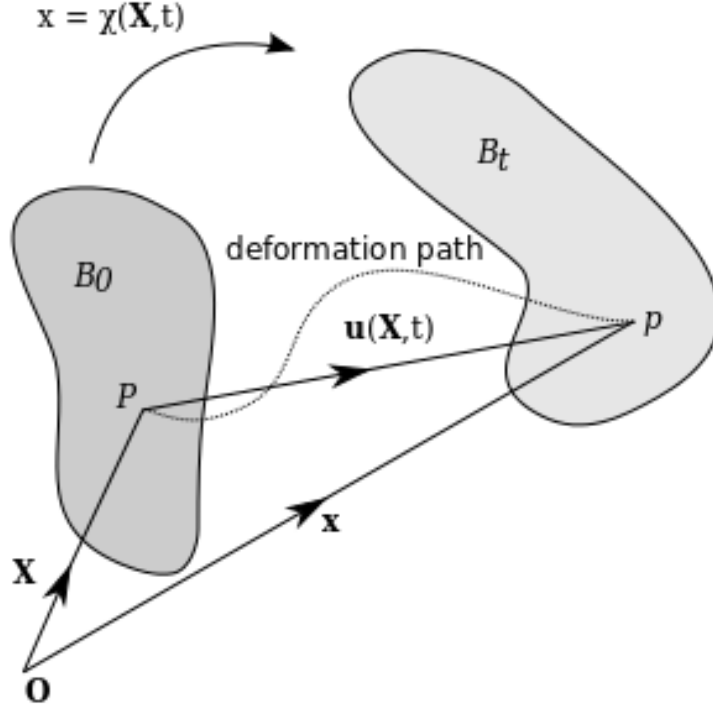
Figure 2.1: Displacement and deformation of a continuum body

where $\mathbf{F}$ is a second order tensor with the components $F_{i\alpha} = \frac{\partial x_i}{\partial X_\alpha}$, and $i, \alpha \in \{1, 2, 3\}$ signifies the cartesian coordinate directions in the deformed current (B_t) and undeformed reference (B_0) configuration respectively. If not otherwise stated index notation and the summation convention over repeated indices is used in this thesis (see [22, ch. 1] for details on index notation and the summation convention). In the following the Del operator ∇ will be replaced with the textual grad or div denoting the use as a gradient or divergence operator respectively, and with the capitalisation of the first letter denoting which configuration the operator is applied with respect to (i.e. $\text{Grad}\, g = \nabla_{\mathbf{X}} g$, $\text{grad}\, g = \nabla_{\mathbf{x}} g$, while $\text{Div}\, \mathbf{g} = \nabla_{\mathbf{X}} \cdot \mathbf{g}$, and $\text{div}\, \mathbf{g} = \nabla_{\mathbf{x}} \cdot \mathbf{g}$).

It should be noted that although the tensor A is independent of the coordinate sytem, the matrix $\mathbf{A}$ can be used to describe the tensor A in a given coordinate system [29, ch. 3.7]. Since only óne coordinate system is used in this work it is thus for convenience
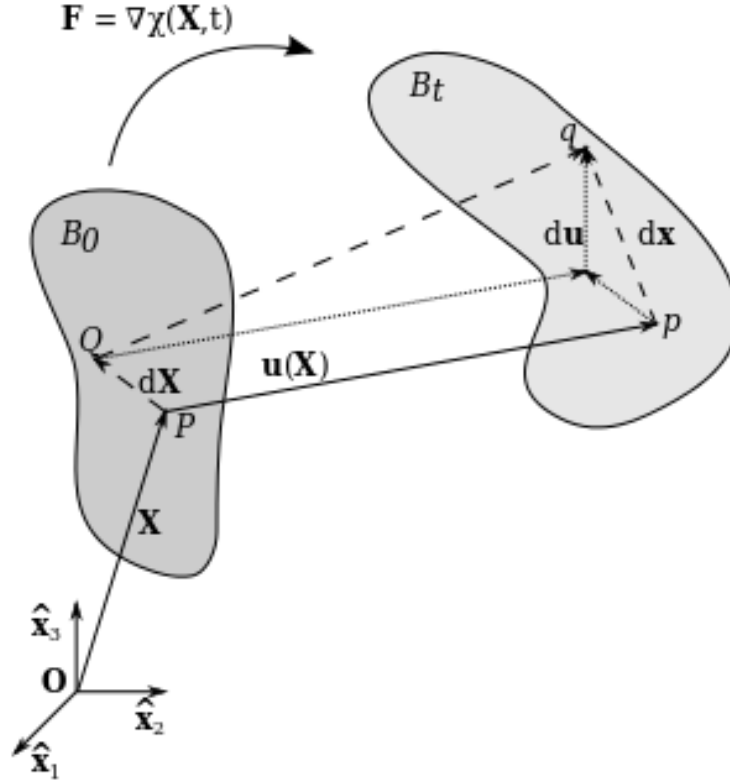
Figure 2.2: Movement of two neighbouring particles (P and Q) within a continuum body during deformation

possible to employ both matrix notation and direct tensor notation to describe tensors. The matrix notation have been chosen over the direct tensor notation throughout this text while component/index notation also have been used when convenient.

The Jacobian is defined as [29, ch. 7.2]

$$J \equiv \det F = \begin{vmatrix} \frac{\partial x_1}{\partial X_1} & \frac{\partial x_1}{\partial X_2} & \frac{\partial x_1}{\partial X_3} \\ \frac{\partial x_2}{\partial X_1} & \frac{\partial x_2}{\partial X_2} & \frac{\partial x_2}{\partial X_3} \\ \frac{\partial x_3}{\partial X_1} & \frac{\partial x_3}{\partial X_2} & \frac{\partial x_3}{\partial X_3} \end{vmatrix} > 0 \tag{2.6}$$

and is a local measure of change in material volume. It also is a part of the mass conservation equation $\rho_0 = J\rho_t$, or conversely $J = \frac{\rho_0}{\rho_t}$, where ρ is the mass density with subscripts 0 and t denoting the reference or current configuration respectively [29, ch. 7.2]. The additional restriction $J > 0$ is imposed by the physical interpretation that $J = 0$ would imply either a zero density in the reference configuration or that the

current density is infinite. This also justifies the assumption made in Eq. (2.2) that $J \neq 0$ [29].

The polar decomposition theorem [22, ch. 2.2.4] states that the deformation gradient tensor $\mathbf{F}$ can be decomposed into a proper orthogonal tensor and a positive definite symmetric tensor as

$$\mathbf{F} = \mathbf{RU} = \mathbf{VR} \tag{2.7}$$

where $\mathbf{R}^T = \mathbf{R}^{-1}$ and $\det\mathbf{R} = +1$ is a proper orthogonal second order tensor representing a rotation, while $\mathbf{U} = \mathbf{U}^T$ and $\mathbf{V} = \mathbf{V}^T$ are positive definite symmetric second order tensors [22, ch. 2.2.4] . The superscripts T and -1 denotes a transpose and the inverse of the tensor. $\mathbf{U}$ and $\mathbf{V}$ are called the right and left stretch tensors respectively [22, ch. 2.2.4] (see below for definition of stretch). The rotation and stretch tensors and their combination to form the deformation gradient $\mathbf{F}$ are illustrated in Fig. 2.3 and helps interpret the deformation gradient tensor geometrically. Here the decomposition of the deformation gradient tensor $\mathbf{F}$ is illustrated by either a pure stretch by the right stretch tensor $\mathbf{U}$ followed by a pure rotation (described by rotation tensor $\mathbf{R}$), or the opposite sequence of a pure rotation ($\mathbf{R}$) followed by a pure stretch described by the left stretch tensor $\mathbf{V}$.

The positive definite right and left stretch tensors can be decomposed using the unit eigenvectors $\mathbf{u}^{(i)}$ and $\mathbf{v}^{(i)}$ of $\mathbf{U}$ and $\mathbf{V}$ respectively together with the principal stretches (or eigenvalues) $\lambda_i > 0, i \in \{1, 2, 3\}$ as:

$$\mathbf{U} = \sum_{i=1}^{3} \lambda_i \mathbf{u}^{(i)} \mathbf{u}^{(i)T}, \qquad \mathbf{V} = \sum_{i=1}^{3} \lambda_i \mathbf{v}^{(i)} \mathbf{v}^{(i)T} \tag{2.8}$$

where $\lambda_i \equiv l_i / L_i$ is the stretch ratio between the current length l_i and reference length L_i in the principal directions $\hat{x}_i$ [23],[25]. Note that $\mathbf{u}$ and $\mathbf{v}$ are the Lagrangian (reference configuration- or body-frame) and Eulerian (current cofiguration- or lab-frame) principal axes respectively [23].

A rotation followed by its inverse rotation leads to no change ($\mathbf{RR}^T = \mathbf{R}^T\mathbf{R} = \mathbf{I}$, where $\mathbf{I}$ is the identity tensor). Together with the fact that the determinant $\det\mathbf{I} = 1$, and thus $\det\mathbf{R} = \pm 1$ [29, ch. 2.1], the above restriction on the Jacobian J, and that positive definite tensors have positive eigenvalues [29, ch. 2.5]; The Jacobian can be expressed by [23]:

$$J = \det\mathbf{F} = \det\mathbf{U} = \det\mathbf{V} = \lambda_1 \lambda_2 \lambda_3 \tag{2.9}$$
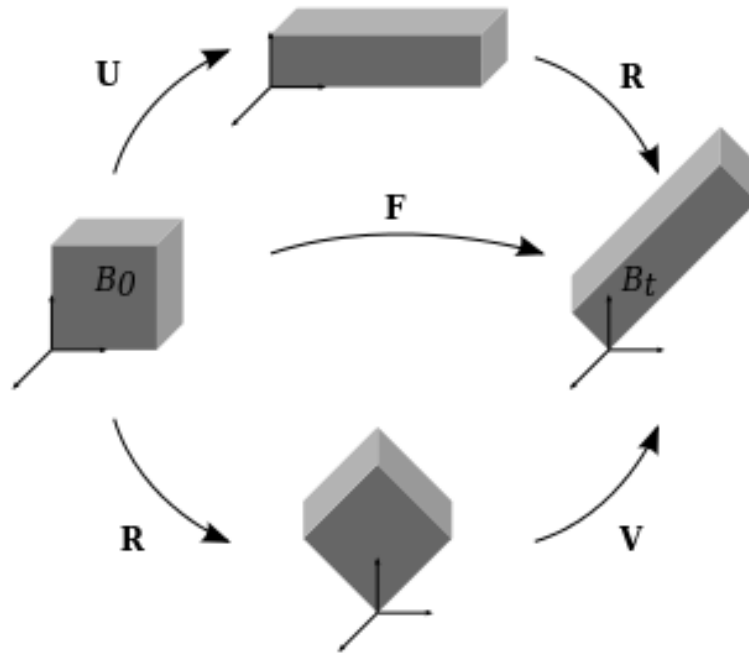
Figure 2.3: Polar decomposition of the deformation gradient tensor

For a rigid-body motion [22, ch. 2.2.6]

$$\mathbf{x} = \mathbf{R}\mathbf{X} + \mathbf{c}, \tag{2.10}$$

where $\mathbf{R}\mathbf{X}$ is a rigid-body rotation and $\mathbf{c}$ is a rigid-body translation, the deformation gradient tensor is $\mathbf{F} = \mathbf{R}$ through use of Eq. (2.5). The deformation gradient tensor $\mathbf{F}$ is thus dependent on rigid motion through rotation but not through translation. Although the general deformation gradient tensor $\mathbf{F}$ is important in the analysis of deformation it is not a suitable measure of deformation in itself since it is dependent on rigid motion through rotation (i.e. $\mathbf{F}$ may include both ridgid motion rotation $\mathbf{R}$ as well as deformation ($\mathbf{U}$ or $\mathbf{V}$) through the polar decomposition theorem in (2.7)). It is thus convenient to use rotation-independent measures of deformation. The rotational part of $\mathbf{F}$ can be exluded by multiplying it with its transpose as [22, ch. 2.1.4, 2.2.1],

2. THEORY

[29, ch. 6.4]

$$\mathbf{C} = \mathbf{F}^T \mathbf{F} = \mathbf{U}^2, \qquad \mathbf{B} = \mathbf{F}\mathbf{F}^T = \mathbf{V}^2. \tag{2.11}$$

$\mathbf{C}$ and $\mathbf{B}$ is known as the right and left Cauchy-Green deformation tensors respectively.

The principal invariants of both $\mathbf{C}$ and $\mathbf{B}$ are defined by [23]

$$I_1 = \text{tr}(\mathbf{C}) \qquad I_2 = \frac{1}{2}\left[I_1^2 - \text{tr}(\mathbf{C}^2)\right] \qquad I_3 = \det(\mathbf{C}) \tag{2.12}$$

where tr() is called the *trace* and is the sum of elements on the main diagonal (i.e. $\text{tr}(\mathbf{C}) = C_{ii} = C_{11} + C_{22} + C_{33}$). Recall also the convention used in this work to represent tensors by their matrix in the current coordinate system yielding $\mathbf{C}^2 = C_{ik}C_{kj}$ [29, ch. 3.8]. Expressed with the principal stretches λ_i of Eq. (2.8) they are [23]

$$I_1 = \lambda_1^2 + \lambda_2^2 + \lambda_3^2 \qquad I_2 = \lambda_2^2\lambda_3^2 + \lambda_1^2\lambda_3^2 + \lambda_1^2\lambda_2^2 \qquad I_3 = \lambda_1^2\lambda_2^2\lambda_3^2 \tag{2.13}$$

These invariants do not change with rotation of the coordinate system, and are thus useful when establishing constitutive relations in Sec. 2.1.3.

For a rigid-body motion the deformation gradient tensor is $\mathbf{F} = \mathbf{R}$ as mentioned above. This leads to

$$\mathbf{C}(\mathbf{F} = \mathbf{R}) = \mathbf{R}^T \mathbf{R} = \mathbf{I}, \tag{2.14}$$

and hence $\mathbf{C}$ has the constant value $\mathbf{I}$ throughout a rigid-body motion. Similarly $\mathbf{B} = \mathbf{I}$ for rigid-body motion as well. Since there is no material deformation for a rigid-body motion it is thus convenient to define the Lagrangian and Eulerian finite strain tensors, $\mathbf{E}$ and $\mathbf{e}$ respectively, such that $\mathbf{E} = \mathbf{e} = \mathbf{0}$ for such rigid-body motion [29, ch. 6.4]. They will thus be a measure of the relative change between two neighbouring material points with respect to the reference configuration[1] and the current configuration[2] respectively

$$\mathbf{E} = \frac{1}{2}\left(\mathbf{C} - \mathbf{I}\right), \qquad \mathbf{e} = \frac{1}{2}\left(\mathbf{I} - \mathbf{B}^{-1}\right), \tag{2.15}$$

or in index notation using Eq. (2.3) [29, ch. 6.4]

$$E_{\alpha\beta} = \frac{1}{2}\left(\frac{\partial u_\alpha}{\partial X_\beta} + \frac{\partial u_\beta}{\partial X_\alpha} + \frac{\partial u_k}{\partial X_\alpha}\frac{\partial u_k}{\partial X_\beta}\right), \tag{2.16}$$

$$e_{ij} = \frac{1}{2}\left(\frac{\partial u_i}{\partial x_j} + \frac{\partial u_j}{\partial x_i} - \frac{\partial u_k}{\partial x_i}\frac{\partial u_k}{\partial x_j}\right). \tag{2.17}$$

---

[1]$\mathbf{E}$ is the Lagrangian description which describe the relative change in length between neighbouring points with respect to the reference configuration.

[2]$\mathbf{e}$ is the Eulerian description which describes the relative change in length between neighbouring points with respect to the current configuration.

The details of the derivation of these expressions can be found in App. A.1.

These two forms of finite deformation strain tensors are suitable measures of the deformation independent of any rigid-body motion. Both will be further used when establishing constitutive relations for the steel test specimen in Sec. 2.1.3 and when deriving the stress state dependency of the sound velocities in Sec. 2.2.2 and 2.3. The reason for the use of both the Lagrangian and Eulerian descriptions is that some relations are more easily obtained for one than the other. This will be specified where it is relevant.

Recall the convention applied in this work where a capital variable signify a Lagrangian reference frame (i.e. with respect to the reference configuration) while a lower case variable signify a Eulerian reference frame (i.e. with respect to the current configuration).

Note also that both the Lagrangian and Eulerian finite strain tensors are functions of the principal stretches λ_i defined in Eq. (2.8), which relate the current length l_i with the reference length L_i in the principal directions $\hat{x}_i$. They are thus both a measure of what is also known as the principal engineering strains e_i which can be expressed by the principal stretches as $e_i = l_i/L_i - 1 = \lambda_i - 1$ (see Sec. 2.3 for definition and [78] for a good account on engineering strains under uniaxial extension).

2.1.2 Stress

The next step is to understand the forces acting on the body under investigation (i.e. the test specimen), and how they act on its internal parts. This section aims to introduce and show the mathematical concepts describing how the applied forces act on the body and how it introduces stress between adjacent parts of the body, as well as presenting suitable measure quantities for this stress which will be used together with the deformation measure presented in Sec. 2.1.1 to construct constitutive relations describing the properties of the relevant material (in this case steel).

The configuration of a body B may be subjected to external influences which are independent of the frame of reference, which exert forces on the body. These forces are refered to as *applied* forces and consist of body forces acting on all material points (i.e. gravity), and contact forces acting only on the surface of the body while affecting all material points by transmission across surfaces [22, ch. 3.2]. Note that forces related

to thermodynamic effects and other influences like electromagnetic radiation, chemical behavior, etc. are disregarded as insignificant effects in the current application.

Stress is a measure of force $\mathbf{f}$ acting on a surface S between adjacent parts of the body. The stress vector can then be expressed as $\mathbf{t}^{(\hat{\mathbf{n}})} = d\mathbf{f}/dS$, where $\hat{\mathbf{n}}$ is the unit-length direction vector normal to the surface dS [29, ch. 5] (See Fig. 2.4 for illustration). The SI unit of the stress is $[Pa = N/m^2]$. Different stress tensors can be defined depending on the reference configuration, and have different applicability. The stress tensors needed to develop the constituive relations as well as the stress dependency of the sound velocities in Sec. 2.1.3 and 2.2.2 respectively are presented in this section.
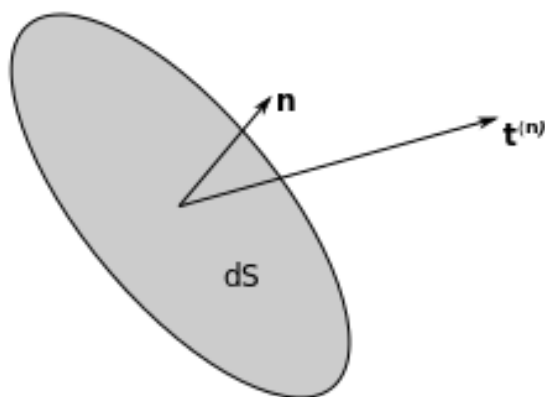
Figure 2.4: Stress vector on an arbitrary surface between adjacent parts of a body

The most commonly used stress tensor is the Cauchy stress tensor $\boldsymbol{\sigma}$. It is defined through the Cauchy's stress theorem as the linear relation between the stress vector
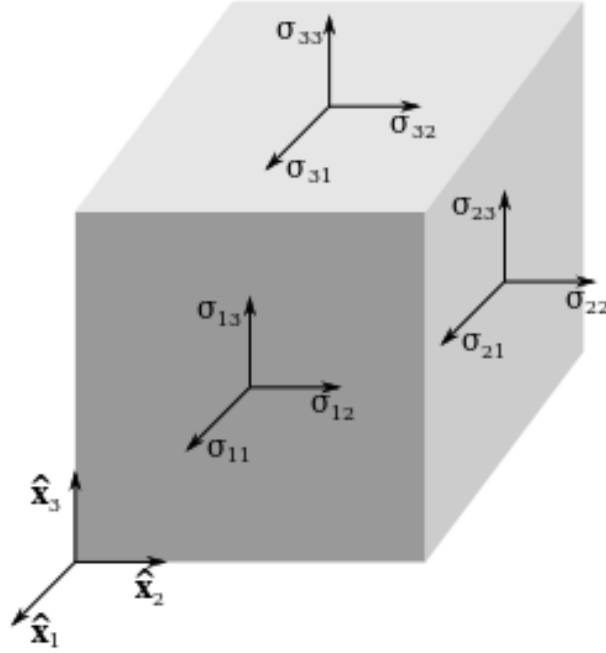
Figure 2.5: Cauchy stress components on the surface of an infinitesimal cube within the body

$\mathbf{t}^{(\hat{\mathbf{n}})}$ and the normal unit vector $\hat{\mathbf{n}}$ of an arbitrary selected surface dS in the current configuration. Decomposing the stress vector $\mathbf{t}^{(\hat{\mathbf{n}})}$ into three new stress vectors $\mathbf{t_i}$ acting on mutually orthogonal surface areas with unit normal vectors $\hat{\mathbf{n}}_i$ oriented in the $\hat{\mathbf{x}}_i$-direction of the current configuration ($i = 1, 2, 3$), the relation between the stress vectors $\mathbf{t}_i$ and the Cauchy stress tensor $\boldsymbol{\sigma}$ can be written on matrix form independent of $\hat{\mathbf{n}}$ as [29, ch. 5.2-3]

$$\begin{bmatrix} \mathbf{t}_1 \\ \mathbf{t}_2 \\ \mathbf{t}_3 \end{bmatrix} = \begin{bmatrix} \sigma_{11} & \sigma_{12} & \sigma_{13} \\ \sigma_{21} & \sigma_{22} & \sigma_{23} \\ \sigma_{31} & \sigma_{32} & \sigma_{33} \end{bmatrix} \begin{bmatrix} \hat{\mathbf{x}}_1 \\ \hat{\mathbf{x}}_2 \\ \hat{\mathbf{x}}_3 \end{bmatrix} \tag{2.18}$$

where the components of stress are illustrated in Fig. 2.5. In index notation this becomes

$$\mathbf{t}_i = \sigma_{ij}\hat{\mathbf{x}}_j. \tag{2.19}$$

It can be shown that the components of the finite stress vector $\mathbf{t}^{(\hat{\mathbf{n}})}$ can then be found by [22, ch. 3.3], [29, ch. 5]:

$$\mathbf{t}^{(\hat{\mathbf{n}})} = \hat{\mathbf{n}} \cdot \boldsymbol{\sigma}. \tag{2.20}$$

The diagonal elements of the Cauchy stress $\delta_{ij}\sigma_{ij}$ (where δ_{ij} is the Kronecker delta) are called the orthogonal normal stresses and are often denoted $\sigma_x, \sigma_y, \sigma_z$, where subscripts x, y, z corresponds to the base vector directions $\hat{x}_1, \hat{x}_2, \hat{x}_3$. The off-diagonal elements $(1 - \delta_{ij})\sigma_{ij}$ are called the orthogonal shear stresses and are often denoted $\tau_{xy}, \tau_{xz}, \tau_{yz}$. These stresses are relative to the chosen coordinate system. By transforming the coordinate system and aligning it with the principal stress directions it is always possible to get a stress tensor where the shear stresses are zero ($\tau_{ij} = 0$) and the diagonal elements (normal stresses) equals what is known as the principal stresses.

In addition, through conservation of rotational momentum, it can be shown that the Cauchy stress tensor is symmetric [22, ch. 3.3], [29, ch. 5.5], i.e.

$$\sigma_{ij} = \sigma_{ji}. \tag{2.21}$$

As mentioned when defining the Cauchy stress tensor $\boldsymbol{\sigma}$ it is defined relative to an arbitrary surface in the current configuration B_t and are thus an Eulerian description [1]. The deformation gradient and the right and left Cauchy-Green deformation tensors $\mathbf{F}, \mathbf{C}$, and $\mathbf{B}$, however, describe the deformation relative to the reference configuration B_0 and combine Lagrangian and Eulerian description as shown in Sec. 2.1.1. These type of tensors which have variables in both Lagrangian and Eulerian coordinates are called two-point tensors [22, ch. 2.4]. Thus it is convenient to introduce the nominal stress tensor $\mathbf{S}$ which relates the forces in the current configuration with surface areas of the reference configuration[2]. It is expressed through [23]

$$\mathbf{S} = J\mathbf{F}^{-1}\boldsymbol{\sigma}, \tag{2.22}$$

where $\mathbf{F}^{-1}$ is the inverse of the deformation gradient tensor defined in Eq. (2.5) and J is as defined in Eq. (2.6). This also relates the reference and current configurations

---

[1] $\boldsymbol{\sigma}$ is the Eulerian description of the force acting on a surface area in the current configuration. It is also known as the true stress tensor (see [78] for definition of true stress). Its 1D equivalent describing the acting force over the current cross sectional area is referred to as true stress or Cauchy stress in this work.

[2] $\mathbf{S}$ is a two-point tensor description of the current force acting on a surface area in the reference configuration. Its 1D equivalent which describes the acting force across the reference cross section area is referred to as engineering stress in this work [78].

and is thus a two-point tensor. $\mathbf{S}$ is in general not necessarily symmetric [23], however, symmetry conditions will be further discussed in Sec. 2.2.2. It should also be noted for reference that the nominal stress tensor $\mathbf{S}$ is the transpose of the first Piola-Kirchhoff stress tensor defined as [22, ch. 3.4]

$$\mathbf{S} = \mathbf{P}^T.$$
(2.23)

However, this work have consistently used the nominal stress tensor $\mathbf{S}$.

2.1.3 Constitutive relations

Secs. 2.1.1 and 2.1.2 have set up the mathematical framework to describe both the finite strain and the internal stress in a body, both with respect to either of the reference and/or current configurations, B_0 and B_t respectively. This is however insufficient to describe the mechanical behaviour of a specific material. To be able to specify the mechanical properties of any material, constitutive laws relating the stress in a body to the strain is needed [22]. The material under investigation in this work is a common construction steel, "Bright rectangular steel bar S235JRG2C+C" [79], which in this respect will be regarded as a uniform, homogeneous, isotropic, and hyperelastic material (Defenition of these terms are explained where they become relevant in the text). This section will thus present the constitutive relations relevant for such a material. It is noted that steel will start to plastically deform if it is subjected to stresses larger than the initial yield point [29, ch. 10.5]. This will however not be a concern of this section, but will be addressed seperately in Sec. 2.5.

An elastic material is defined as a material where the state of stress at each material point in the current configuration is solely determined by the state of deformation of this configuration to an arbitrary choice of reference configuration. More specific it is independent of the rate at which the deformation occurs, and the path of deformation joining the two configurations [22, ch. 4.1.2]. This implies that for a closed loop deformation path the stress state returns to the initial stress state, i.e. the deformation is reversible (see Eqs. (2.1) and (2.2)).

A material is considered uniform if all the material points of the body are mutually isomorphic. That is, two materialpoints X and X' are said to be isomorphic if the neighbourhood around each point has the same uniform density (i.e. $\rho_0 = \rho'_0$), and that

the mechanical properties of X and X' are indistinguishable (i.e. that the material in the neighbourhood of X and X' responds in the same way when subjected to the same deformation gradient history $\mathbf{F}(t)$). In addition, if the response of each material point of the body is the same relative to the deformation χ, the body is said to be homogeneous [22, ch. 4.1.3].

If there exists at least one reference configuration of a material where the mechanical response of the material does not exhibit a preferred direction, characterising isotropy, the material is said to be an isotropic elastic material [22, ch. 4.2.4]. The steel used in this work is assumed to have this property in its unstressed configuration.

To arrive at a constitutive relation between stress and strain we need to establish the mechanical energy balance-, or conservation of power-, equation. Taking the scalar product of Cauchy's first law of motion [22, ch. 3.3.2]

$$\mathrm{div}\boldsymbol{\sigma}^T + \rho_t\mathbf{b} = \rho\ddot{\mathbf{x}} \tag{2.24}$$

with the particle velocity $\dot{\mathbf{x}}$, and using the symmetry of $\boldsymbol{\sigma}$, can together with integration over the current configuration B_t (i.e. Eulerian description) and use of the divergence theorem and conservation of mass give the mechanical energy balance equation as [22, ch. 3.5.1]

$$\int_{B_t}\rho_t\mathbf{b}\cdot\dot{\mathbf{x}}dv + \int_{\partial B_t}\mathbf{t}\cdot\dot{\mathbf{x}}da = \frac{\partial}{\partial t}\int_{B_t}\frac{1}{2}\rho_t\dot{\mathbf{x}}\cdot\dot{\mathbf{x}}dv + \int_{B_t}\mathrm{tr}(\boldsymbol{\sigma}\boldsymbol{\Sigma})dv. \tag{2.25}$$

In the above two equations $\mathbf{b}$ is the body forces acting on the volume element dv of B_t, $\dot{\mathbf{x}}$ is the particle velocity of material points $\mathbf{x}$, and $\mathbf{t}$ is the contact forces acting on the surface elements da on ∂B_t, which is the surface of B_t. $\boldsymbol{\Sigma} = \frac{1}{2}(\boldsymbol{\Gamma} + \boldsymbol{\Gamma}^T)$ is called the Eulerian strain-rate tensor, and is the symmetric part of the Eulerian velocity gradient tensor $\boldsymbol{\Gamma} = \mathrm{grad}\,\dot{\mathbf{x}}$ [22, ch. 2.3.1]. The Eulerian strain-rate tensor $\boldsymbol{\Sigma}$ is derived by taking the Lagrangean time derivative (i.e. the material derivative) of the Green strain tensor $\mathbf{E}$ in Eq. (2.15) as $\dot{\mathbf{E}} = \mathbf{F}^T\boldsymbol{\Sigma}\mathbf{F}$ [22, ch. 2.3.1]. Note however that it is not necessarily expressible as either the Lagrangian or Eulerian time derivative of a strain tensor, and is thus not a rate of strain. However, it is a measure of the rate at which line elements of material change length - i.e. the motion of the material body is rigid only if $\boldsymbol{\Sigma} = \mathbf{0}$ [22, ch. 2.3.1].

A dotted variable will in this work signify the derivative of a variable with respect to time, i.e. $\dot{\mathbf{x}} = \partial/\partial t(\mathbf{x})$. Partial time derivative $\partial/\partial t$ at fixed $\mathbf{X}$ is referred to as the Lagrangian time derivative (also known as the material derivative), and for fixed $\mathbf{x}$ it is called the Eulerian time derivative. The relation between the Lagrangian and Eulerian time derivative can be expressed by using the chain rule and the relation in Eq. (2.1) as

$$\left.\frac{\partial}{\partial t}\right|_{\mathbf{X}} = \left.\frac{\partial}{\partial t}\right|_{\mathbf{x}} + \dot{\mathbf{x}} \cdot \text{grad}. \tag{2.26}$$

To make the notation more compact and to avoid confusion the Lagrangian (or material) derivative $\partial/\partial t|_{\mathbf{X}}$ at fixed $\mathbf{X}$ will in this work be denoted by d/dt such that

$$\frac{d}{dt} = \left.\frac{\partial}{\partial t}\right|_{\mathbf{X}} = \left.\frac{\partial}{\partial t}\right|_{\mathbf{x}} + \dot{\mathbf{x}} \cdot \text{grad} \tag{2.27}$$

if not otherwise stated.

Eq. (2.25) can also be expressed using the Lagrangian description as [22, ch. 3.5.1]

$$\int_{B_0} \rho_0 \mathbf{b}_0 \cdot \dot{\boldsymbol{\chi}} dV + \int_{\partial B_0} (\mathbf{S}^T \hat{\mathbf{N}}) \cdot \dot{\boldsymbol{\chi}} dA = \frac{d}{dt} \int_{B_0} \frac{1}{2} \rho_0 \dot{\boldsymbol{\chi}} \cdot \dot{\boldsymbol{\chi}} dV + \int_{B_0} \text{tr}(\mathbf{S}\dot{\boldsymbol{F}}) dV. \tag{2.28}$$

Here $\mathbf{b_0}$ is the body forces acting on the volume element dV of B_0, $\hat{\mathbf{N}}$ is the unit (outward) normal vector to the area element dA of the boundary surface ∂B_0 of B_0, and the short form $\dot{\boldsymbol{\chi}} = \frac{\partial \chi}{\partial t}(\mathbf{X}, t)$ is introduced. The left-hand sides of Eqs. (2.25) and (2.28) represent thus the rate of change of mechnaical work of the applied forces on the body in configuration B_t or B_0 respectively. The first term on the right-hand side

$$\frac{\partial}{\partial t} \int_{B_t} \frac{1}{2} \rho_t \dot{\mathbf{x}} \cdot \dot{\mathbf{x}} dv, \qquad \text{or} \qquad \frac{d}{dt} \int_{B_0} \frac{1}{2} \rho_0 \dot{\boldsymbol{\chi}} \cdot \dot{\boldsymbol{\chi}} dV \tag{2.29}$$

represent the rate of change of the kinetic energy of the body where $\frac{1}{2}\rho\dot{\mathbf{x}} \cdot \dot{\mathbf{x}}$ and $\frac{1}{2}\rho_0 \dot{\boldsymbol{\chi}} \cdot \dot{\boldsymbol{\chi}}$ are the kinetic energy densities with respect to configurations B_t or B_0 respectively. The second term

$$\int_{B_t} \text{tr}(\boldsymbol{\sigma}\boldsymbol{\Sigma}) dv, \qquad \text{or} \qquad \int_{B_0} \text{tr}(\mathbf{S}\dot{\mathbf{F}}) dV \tag{2.30}$$

is the rate of work done on the body by the stresses, also known as the stress power.

From Eq. (2.30) it is clear that $\boldsymbol{\sigma}$ and $\boldsymbol{\Sigma}$ are a pair of stress and strain tensors which can be used to describe the Eulerian stress power. Equivalently the pair $\mathbf{S}$ and $\dot{\mathbf{F}}$ can be used to describe the Lagrangian stress power.

Energy is in general not conserved during the motion of a continuum, and the rate of stress powers of Eq. (2.30) incorporate both dissipative (i.e. energy losses)

and conservative (i.e. stored internal energy) contributions. However, in the special case where the material response is elastic, and where an elastic strain-energy density function exist, mechanical energy is conserved (i.e. any dissipative processes can be neglected) [22, ch. 3.5.1]. Assuming now that the right-hand side of Eq. (2.28) can be expressed as the rate of change of the total mechanical energy of the body results in the mechanical energy balance under conservation of energy as [22, ch. 4.3.1]

$$\int_{B_0} \rho \mathbf{b}_0 \cdot \dot{\boldsymbol{\chi}} \, dV + \int_{\partial B_0} \left(\mathbf{S}^T \hat{\mathbf{N}} \right) \cdot \dot{\boldsymbol{\chi}} \, dA = \frac{d}{dt} \int_{B_0} \left(\frac{1}{2} \rho \dot{\boldsymbol{\chi}} \cdot \dot{\boldsymbol{\chi}} + W \right) dV, \qquad (2.31)$$

where, as before, $\frac{1}{2} \rho_0 \dot{\boldsymbol{\chi}} \cdot \dot{\boldsymbol{\chi}}$ represent the kinetic energy density, while W is the internal energy density which under the above assumption of elastic response becomes a measure of the stored internal elastic energy. W is better know as the strain-energy density function, and is the terminology adopted in this work [22, ch. 4.3.1]. Note also that W is defined per unit volume in this work [22, ch. 4.3.1].

To be able to do the transformation from the Lagrangian mechanical energy balance in Eq. (2.28) to Eq. (2.31) expressed with the strain energy W, we need to impose the restriction on W that [22, ch. 4.3.1]

$$\dot{W} = \text{tr}(\mathbf{S}\dot{\mathbf{F}}) \qquad (2.32)$$

Pairs of stress and strain tensors where the (Lagrangian or material) time derivative of the strain tensor can be coupled to give the stress power density as in Eq. (2.32) is said to be conjugate pairs of stress and strain tensors [22, ch. 3.5.2]. The Eulerian strain-rate $\boldsymbol{\Sigma}$ can not in general be expressed as the Lagrangian time derivative over some strain tensor, and therefor the stress and strain tensor pair $\boldsymbol{\sigma}$ and $\boldsymbol{\Sigma}$ in the stress power term in the Eulerian mechanical energy balance (Eqs. (2.25) and (2.30)) is not a conjugate pair such as $\mathbf{S}$ and $\dot{\mathbf{F}}$ in Eq. (2.32) [22, ch. 3.5.2]. This is also the reason why the Lagrangian form of the stress power is used to further develop the constitutive relation between stress and strain.

A constitutive relation between the nominal stress tensor $\mathbf{S}$ and the deformation gradient tensor $\mathbf{F}$ is assumed to be expressed by some material response function $\mathbf{G}$ for an unconstrained material as [22, ch. 4.2]

$$\mathbf{S} = \mathbf{G}(\mathbf{F}) \qquad (2.33)$$

For an unconstrained hyperelastic material (see below for definition), which we assume can describe the behaviour of the currently used steel, certain restrictions on $\mathbf{G}$ can be imposed [22, ch. 4.2-3].

Assuming that W exist and that it is a scalar function of $\mathbf{F}$, Eq. (2.32) can through Eq. (2.33) be written as [22, ch. 4.3.1]

$$\dot{W} = \text{tr}(\mathbf{G}(\mathbf{F})\dot{\mathbf{F}}) \tag{2.34}$$

If a function $W(\mathbf{F})$ exist such that the above relation in Eq. (2.34) holds then through use of the chain rule

$$\dot{W} = \text{tr}\left(\frac{\partial W}{\partial \mathbf{F}}(\mathbf{F})\dot{\mathbf{F}}\right) \tag{2.35}$$

also holds. If such a strain-energy density function exist for an elastic material, this material is called a Green-elastic or hyperelastic material [22, ch. 4.3.1]. Comparing Eqs. (2.33) to (2.35) it is evident that for such an unconstrained material the constitutive relation, or stress-deformation relation, is simply

$$\mathbf{S} = \frac{\partial W(\mathbf{F})}{\partial \mathbf{F}}. \tag{2.36}$$

Including the condition that the elastic stored energy should be unaffected by a super-posed rigid-body motion (as defined in Eq. (2.10)) after the deformation leads to [22, ch. 4.3.1]

$$W(\mathbf{R}\mathbf{F}) = W(\mathbf{F}) \tag{2.37}$$

for all proper orthogonal $\mathbf{R}$ and arbitrary deformation gradients $\mathbf{F}$. Using this in combination with the polar decomposition theorem of Eq. (2.7) it is clear that W is a function of $\mathbf{U}$ alone [22, ch. 4.3.1], i.e.

$$W(\mathbf{F}) = W(\mathbf{R}^T\mathbf{F}) = W(\mathbf{R}^T\mathbf{R}\mathbf{U}) = W(\mathbf{U}). \tag{2.38}$$

For the special case of an isotropic hyperelastic material where the material response does not have a preferred direction the elastic stored energy is not affected by a rigid-body motion before the deformation. Thus in the same manner as the previous relation it is clear that W is a function of $\mathbf{V}$ alone as well [22, ch. 4.3.4].

$$W(\mathbf{F}) = W(\mathbf{F}\mathbf{R}^T) = W(\mathbf{V}\mathbf{R}\mathbf{R}^T) = W(\mathbf{V}). \tag{2.39}$$

Based on these two conditions it can be shown that W is an isotropic scalar function of $\mathbf{U}$ or $\mathbf{V}$, and consequently a symmetric function of their eigenvalues the principal stretches λ_i [22, ch. 4.3.4]

$$W(\mathbf{U}) \equiv W(\mathbf{V}) = W(\lambda_1, \lambda_2, \lambda_3). \tag{2.40}$$

It can also be shown that the constituive relation of an unconstrained hyperelastic material in Eq. (2.36) can be expressed in terms of the Lagrangian strain $\mathbf{E}$ as [22, ch. 5.1][12][24]

$$\mathbf{S} \quad = \quad \frac{\partial W}{\partial \mathbf{F}}(\mathbf{F}) = \frac{\partial W}{\partial \mathbf{E}}(\mathbf{E})\mathbf{F}^T. \tag{2.41}$$

The detailed derivation of this relation is presented in App. A.2.

This concludes the general mathematical description of the mechanical behaviour the current test specimen experiences as it is prestressed/deformed in the tension machine. The next section will investigate the effect of a small elastodynamic (wave) deformation superimposed on the established prestress of this section.

2.2 Small dynamic (acoustic) deformation

This section will investigate small dynamic (time dependent) disturbances introduced by an acoustic signal travelling in a test specimen already subjected to an initial stress state induced by an imposed deformation in a tension machine. First it will present the elastodynamic, or wave, equations governing the propagation of an acoustic signal in an elastic material. Then it will go on to investigate the combination of a prestressed configuration with an additional acoustic signal. Finally it will use this in combination with the constitutive relation of Eq. (2.36) presented in Sec. 2.1.3 to develop the dependency of the acoustic velocities on the magnitude of the prestress, looking specifically into the case of an applied uniaxial tension as prestress. This section is mainly aligned with-, and based on-, the work of Ogden [22][23] and Norris [12][24].

2.2.1 Elastodynamic equations

In parallel to the elastostatic derivation above, B_0 denotes a time independent reference configuration of the body. Letting $t \in \mathcal{I} \subset \mathbb{R}$ denote time, where $\mathcal{I}$ is an appropriate

interval of time, the current (or deformed) configuration B_t can be parametrizied by t. Assuming that the current configuration B_t evolves continuously with t, the collection of configurations $\{B_t : t \in \mathfrak{I}\}$ is the motion of the body [23]. As before a point of the body within the reference configuration has the position vector $\mathbf{X}$, while $\mathbf{x}$ is the position within the current configuration. Including the time dependence of the elastodynamic deformation the mapping function in Eq. (2.1) takes the form [23]

$$\mathbf{x} = \chi(\mathbf{X}, t) \qquad \text{for all } \mathbf{X} \in \mathbf{B_0}, \, \mathbf{t} \in \mathfrak{I} \tag{2.42}$$

The velocity $\dot{\mathbf{x}}$ and acceleration $\ddot{\mathbf{x}}$ of a material point are defined through the Lagrangian (or material) time derivative (see Eq. (2.27)) by

$$\dot{\mathbf{x}} \equiv \dot{\boldsymbol{\chi}} = \frac{d}{dt}\chi(\mathbf{X}, t) \tag{2.43}$$

and

$$\ddot{\mathbf{x}} = \ddot{\boldsymbol{\chi}} = \frac{d^2}{dt^2}\chi(\mathbf{X}, t) \tag{2.44}$$

where a dotted variable is the notation for the partial derivative with respect to the variable t, and $\mathbf{X}$ and t are the independent variables (i.e. Lagrangian description) [23].

Based on the equation of linear momentum balance [22, ch. 3.2] together with the assumption that ρ_0, $\mathbf{b}_0$ and $\ddot{\mathbf{x}}$ are continuous, and that $\mathbf{S}$ is continuously differentiable; The governing equation of motion for a continuum in terms of the nominal stress can be expressed by the relation [22, ch. 3.3.2]

$$\text{Div}\,\mathbf{S} + \rho_0\mathbf{b}_0 = \rho_0\ddot{\boldsymbol{\chi}}, \tag{2.45}$$

also known as the Lagrangian form of the Cauchy's first law of motion. In the current setup the only body-force acting is that of the gravity. This force is constant throughout the experiments, and is also insignificant compared to the applied tensional load. Thus, disregarding the body-force term, Eq. (2.45) becomes

$$\text{Div}\,\mathbf{S} = \rho_0\ddot{\boldsymbol{\chi}}. \tag{2.46}$$

This relation will be used further when looking at small incremental motions superimposed on a finite motion in the next section "Small-on-Large".

2.2.2   Small-on-large - The acoustoelastic effect

The acoustoelastic effect describes how the sound velocity of small amplitude waves in elastic bodies depend on the stress state of the body in which they travel. To investigate the theoretical explanation of this effect we need to destinguish between three different states and their coordinates. First a material point in the reference, or un-stressed, state/configuration B_0 have the coordinate vectors $\mathbf{X}$. Secondly the static initial (deformed) stress state B_t, corresponding to the state after the tension machine has deformed the test specimen, has the coordinate vectors $\mathbf{x}$. This corresponds to the two states discussed in Secs. 2.1.1 and 2.1.2. The third state B' is the current state where a materialpoint experience a small dynamic displacement in addition to the larger static deformation of B_t (small-on-large) and has the coordinate vectors $\mathbf{x}'$. Note that these positions are all relative to the same origin and with the same orientation of the coordinate systems. The total displacement of the material points can thus be described by [24]

$$\mathbf{u} = \mathbf{u}^{(0)} + \mathbf{u}^{(1)} = \mathbf{x}' - \mathbf{X}, \tag{2.47}$$

where

$$\mathbf{u}^{(0)} = \mathbf{x} - \mathbf{X}, \qquad \mathbf{u}^{(1)} = \mathbf{x}' - \mathbf{x}, \tag{2.48}$$

is the displacements describing the static deformation (consequently defining the static stress and strain state according to Secs. 2.1.1 and 2.1.2), and the small-on-large additional dynamic displacement (Sec. 2.2.1) added to the static deformation, respectively. The objective of this section is thus to derive the equation of motion for the additional disturbance $\mathbf{u}^{(1)}$ in terms of the intermediate deformation $\mathbf{u}^{(0)}$ assuming that the small-on-large assumption

$$|\mathbf{u}^{(1)}| \ll |\mathbf{u}^{(0)}| \tag{2.49}$$

holds.

It is noted that this latter assumption may not be valid for those parts of the load history where the applied displacement goes to zero (see Sec. 3.3). However, in these load states approaching zero stress it is assumed that the propagation of acoustic stress waves can be described by ordinary linear elastic theory for unstressed materials (i.e. the acoustic disturbance is assumed to always be linear and only non-linearity due to the applied pre-stress has been considered here [12]). Thus, the considerations of this section is obsolete as the applied stress is reduced towards zero. As soon as a tension is

applied to the system it is assumed that the resulting static stress field is much larger than the acoustically induced dynamic stress field, making the above assumption valid.

Assuming that the scalar strain energy W can be expressed as a power series in the total strain $\mathbf{E}$ (i.e. both for the static pre-stress and dynamic acoustic stress), that the elastic stored energy is unaffected by a rigid body motion, and that it both has a minimum, and is zero at the unstressed/undeformed state, it follows that there is no linear term in the expansion of W in powers of E_{ij} [13, ch. 1.3]. Thus [12][24]

$$W = \frac{1}{2!}C_{ijkl}E_{ij}E_{kl} + \frac{1}{3!}C_{ijklmn}E_{ij}E_{kl}E_{mn} + \cdots ,\qquad(2.50)$$

where C_{ijkl} and C_{ijklmn} are contant components of a fourth order and a sixth order tensor respectively. Note that the use of greek subscripts to denote Lagrangian components has been dropped. The symmetry of $\mathbf{E}$, $E_{ij} = E_{ji}$, together with the assumption that W is a scalar implies through Eq. (2.50) that the second order moduli C_{ijkl} have the following symmetry

$$C_{ijkl} = C_{jikl} = C_{ijlk}.\qquad(2.51)$$

The strain energy power expansion in Eq. (2.50) implies also that for hyperelastic material the addition symmetry

$$C_{ijkl} = C_{klij}\qquad(2.52)$$

is applicable [22, ch. 6.1.6][29, ch. 8.3]. These symmetries reduce the number of independent components of C_{ijkl} from 81 to 21 at most. Similarly the third order moduli C_{ijklmn} also have symmetries such that both C_{ijkl} and C_{ijklmn} can be expressed by the Voigt's notation [12]. That is;, $C_{ijkl} = C_{IJ}$ and $C_{ijklmn} = C_{IJK}$, where $i,j,k,l,m,n \in \{1,2,3\}$ and $I,J,K \in \{1,2,3,4,5,6\}$, and the relationship $ij = 11,22,33,23,31,12 \leftrightarrow I = 1,2,3,4,5,6$ [12][24]. The second order moduli C_{ijkl} has at most 21 independent components, while the third order moduli C_{ijklmn} have at most 56 [12]. These reduce in the presence of material symmetri. See [80] for a thorough account of elastic symmetries. It should be noted that this work uses the full index notation. However, the Voigt's notation has been used when relating other representations of elastic moduli for isotropic solids (see Table 2.1).

2. THEORY

Introducing the displacement gradient

$$\mathrm{Grad}\,\mathbf{u} = \mathrm{Grad}\,\mathbf{x}' - \mathrm{Grad}\,\mathbf{X} = \mathbf{F} - \mathbf{I}, \qquad (2.53)$$

from Eq. (2.47), which in component form can be rearranged to

$$F_{i\alpha} = \frac{\partial u_i}{\partial X_\alpha} + \delta_{i\alpha}, \qquad (2.54)$$

the power expansion of Eq. (2.50) togheter with the symmetries of Eqs. (2.51) and (2.52) enables the constitutive relation of Eq. (2.41) to be expanded as [12]

$$\begin{aligned}
S_{\beta q} &= \frac{\partial W}{\partial E_{\alpha\beta}} F_{\alpha q} = \frac{\partial W}{\partial E_{\alpha\beta}} \left(\frac{\partial u_\alpha}{\partial X_q} + \delta_{\alpha q} \right) \\
&= \left(\frac{\partial u_\alpha}{\partial X_q} + \delta_{\alpha q} \right) \left[C_{\alpha\beta kl} E_{kl} + \frac{1}{3!} \left(C_{\alpha\beta klmn} E_{kl} E_{mn} + \right. \right. \\
&\qquad\qquad \left. \left. C_{ij\alpha\beta mn} E_{ij} E_{mn} + C_{ijkl\alpha\beta} E_{ij} E_{kl} \right) + \cdots \right]
\end{aligned} \qquad (2.55)$$

Using $E_{\alpha\beta}$ expressed by displacement gradients as in Eq. (2.16) and the symmetries of both C_{ijkl} and E_{ij}, Eq. (2.55) can be written as [12][24] (see App. A.3.3 for details)

$$S_{ji} = C_{ijkl} \frac{\partial u_k}{\partial X_l} + \frac{1}{2} M_{ijklmn} \frac{\partial u_k}{\partial X_l} \frac{\partial u_m}{\partial X_n} + \frac{1}{3} M_{ijklmnpq} \frac{\partial u_k}{\partial X_l} \frac{\partial u_m}{\partial X_n} \frac{\partial u_p}{\partial X_q} + \cdots \qquad (2.56)$$

where

$$M_{ijklmn} = C_{ijklmn} + C_{ijln} \delta_{km} + C_{jnkl} \delta_{im} + C_{jlmn} \delta_{ik}, \qquad (2.57)$$

and third- and higher order terms in $\partial u_i / \partial X_j$ have been neglected [12][24]. [12][24] also note that $M_{ijklmn} \neq M_{jiklmn}$, and that the non-symmetry of $\mathbf{S}$ is thus an effect of the second order terms in $\partial u_i / \partial X_j$.

It is also noted for later reference that for small deformations/strains where second and higher order terms in strain measure $\partial u_i / \partial X_j$ are much less than the first order term, and Eq. (2.56) can be linearised to

$$S_{ji} \approx C_{ijkl} \frac{\partial u_k}{\partial X_l}. \qquad (2.58)$$

This is one alternative of a Lagrangian description of the generalised Hooke's law where S_{ji}, the nominal stress tensor, is a measure of stress and $\partial u_k / \partial X_l$ is a measure of strain, which are related by a linear homogeneous equation. [13, ch. 1.3].

Using the chain rule, and changing the variable through Eqs. (2.47) and (2.48), partial derivatives with respect to X_j can be expanded in x_j as [24] (see App. A.3.2 for details)

$$\frac{\partial}{\partial X_j} \quad = \quad \frac{\partial}{\partial x_j} + u_{k,j}^{(0)}\frac{\partial}{\partial x_k} + \cdots \tag{2.59}$$

where the short form $u_{k,j}^{(0)} \equiv \partial u_k^{(0)}/\partial x_j$ has been used [24]. Thus the divergence of S_{ij} (the left hand side of the Lagrangian equation of motion from Eq. (2.46)) can be expanded using the relation in Eq. (2.56) as [24] (see App. A.3.4 for details)

$$
\begin{aligned}
\frac{\partial S_{ji}}{\partial X_j} &\approx \frac{\partial S_{ji}}{\partial x_j} + u_{p,j}^{(0)}\frac{\partial S_{ji}}{\partial x_p} \\
&\approx C_{ijkl}\left(\frac{\partial^2 u_k}{\partial x_j \partial x_l} + u_{q,l}^{(0)}\frac{\partial^2 u_k}{\partial x_j \partial x_q} + u_{q,lj}^{(0)}\frac{\partial u_k}{\partial x_q}\right) \\
&\quad + u_{p,j}^{(0)}C_{ijkl}\left(\frac{\partial^2 u_k}{\partial x_p \partial x_l} + u_{q,l}^{(0)}\frac{\partial^2 u_k}{\partial x_p \partial x_q} + u_{q,lp}^{(0)}\frac{\partial u_k}{\partial x_q}\right) \\
&\quad + \frac{1}{2}M_{ijklmn}\left\{\left(\frac{\partial^2 u_k}{\partial x_j \partial x_l} + u_{q,l}^{(0)}\frac{\partial^2 u_k}{\partial x_j \partial x_q} + u_{q,lj}^{(0)}\frac{\partial u_k}{\partial x_q}\right)\left(u_{m,n} + u_{r,n}^{(0)}u_{m,r}\right) \right. \\
&\quad \left. + \left(u_{k,l} + u_{q,l}^{(0)}u_{k,q}\right)\left(\frac{\partial^2 u_m}{\partial x_j \partial x_n} + u_{r,n}^{(0)}\frac{\partial^2 u_m}{\partial x_j \partial x_r} + u_{r,nj}^{(0)}\frac{\partial u_m}{\partial x_r}\right)\right\} \\
&\quad + u_{p,j}^{(0)}\frac{1}{2}M_{ijklmn}\left\{\cdots\right\} \\
&\quad + \cdots
\end{aligned}
\tag{2.60}
$$

Assuming that the static initial deformation $\mathbf{u}^{(0)}$ of configuration B_t is in equilibrium yields from Eq. (2.46)

$$\text{Div}\,\mathbf{S}^{(0)} = \mathbf{0}, \qquad \mathbf{u}_{,tt}^{(0)} = \mathbf{0}, \tag{2.61}$$

where the superscript $^{(0)}$ denote the part of given variable related to the configuration of static pre-stress, and correspondingly the superscript $^{(1)}$ will denote the part of a variable related to the additional dynamic acoustic disturbance. Eq. (2.60) can the be used to deduce a linear equation (disregarding higher order terms in $u_{m,n}^{(0)}$) for the additional disturbance $\mathbf{u}^{(1)}(\mathbf{x}, t)$ based on the Lagrangian equation of motion in Eq. (2.46) as [24] (see App. A.3 for details)

$$B_{ijkl}\frac{\partial^2 u_k^{(1)}}{\partial x_j \partial x_l} = \rho_0\frac{\partial^2 u_i^{(1)}}{\partial t^2} \tag{2.62}$$

where

$$B_{ijkl} = C_{ijkl} + \delta_{ik}C_{jlqr}u_{q,r}^{(0)} + C_{rjkl}u_{i,r}^{(0)} + C_{irkl}u_{j,r}^{(0)} + C_{ijrl}u_{k,r}^{(0)} + C_{ijkr}u_{l,r}^{(0)} + C_{ijklmn}u_{m,n}^{(0)}. \tag{2.63}$$

is the effective elastic moduli, and comprise terms of order zero and one in the applied deformation $u_{m,n}^{(0)}$. The assumption that the initial stress and strain are uniform implies that the coefficients B_{ijkl} are constants [24]. Eq. (2.62) is thus an equation of motion for the additional disturbance $\mathbf{u}^{(1)}$ in terms of the initial static deformation $\mathbf{u}^{(0)}$ as sought (i.e. B_{ijkl} being a function of the initial disturbance $\mathbf{u}^{(0)}$ as $B_{ijkl}(\mathbf{u}^{(0)})$).

2.2.2.1 Plane wave

Considering a plane wave of the form [23]

$$\mathbf{u}^{(1)}(\mathbf{x}, t) = \mathbf{m}f(\mathbf{N} \cdot \mathbf{x} - ct), \tag{2.64}$$

where $\mathbf{N}$ is a Lagrangian unit vector in the direction of propagation (i.e. normal to the phase front), $\mathbf{m}$ is a unit vector referred to as the polarisation vector (describing the direction of particle motion), c is the phase velocity of the wave, and f is a twice continuously differentiable function (e.g. a sinusodial function) [22, ch. 6.4]. Inserting this plane wave into Eq. (2.62) yields

$$\mathbf{Q}(\mathbf{N})\mathbf{m} = \rho_0 c^2 \mathbf{m} \tag{2.65}$$

where $\mathbf{Q}(\mathbf{N})$ is introduced as the acoustic tensor, and depends on $\mathbf{N}$ as [22, ch. 6.4][24]

$$[\mathbf{Q}(\mathbf{N})]_{ij} = B_{ijkl}N_jN_l. \tag{2.66}$$

Eq. (2.65) is called the propagation condition, and determines for a given propagation direction $\mathbf{N}$ the velocity and polarisation of possible waves corresponding to plane waves. The wave velocities can be determined by the characteristic equation [22, ch. 6.4]

$$\det\left(\mathbf{Q}(\mathbf{N}) - \rho_0 c^2 \mathbf{I}\right) = 0. \tag{2.67}$$

For a hyperelastic material $\mathbf{Q}(\mathbf{N})$ is symmetric, and thus its eigenvalues are real, but not necessarily positive. For the wave velocities c to be real, the eigenvalues $\rho_0 c^2$ must be positive. If this is the case, from Eq. (2.67) it is clear that three mutually orthogonal

real plane waves exist for the given propagation direction $\mathbf{N}$. From Eq. (2.65) and (2.66) the characteristic wave velocities can be expressed as:

$$\rho_0 c^2 = \mathbf{Q}(\mathbf{N})\mathbf{m} \cdot \mathbf{m} = B_{ijkl} N_j N_l m_i m_k. \tag{2.68}$$

The inequality relation

$$B_{ijkl} N_j N_l m_i m_k > 0 \tag{2.69}$$

is called the strong ellipticity condition for all non-zero vectors $\mathbf{N}$ and $\mathbf{m}$ [22, ch. 6.2.7]. Thus, if the strong ellipticity condition holds then $\rho_0 c^2 > 0$ for all propagation and polarisation directions $\mathbf{N}$ and $\mathbf{m}$. For a strongly elliptic system it is thus guaranteed that the speeds of homogeneous plane waves are real. [22, ch. 6.2.7][22, ch. 6.4]

If the propagation direction is along one of the Eulerian principal directions (i.e. $\mathbf{N} = \mathbf{u}^{(i)}$, where $i = 1, 2, 3$, the polarisation directions for an unconstrained material satisfying Eq. (2.65) are simply $\mathbf{u}^{(i)}$. The polarisation $\mathbf{m} = \mathbf{N}$ corresponds to a longitudinal wave where the particle motion is parallel to the propagation direction, also referred to as compressional wave. The two other polarisations where $\mathbf{m} \cdot \mathbf{N} = 0$ corresponds to transverse waves with the particle motion orthogonal to the propagation direction, also refered to as shear waves. [22, ch. 6.4]

2.2.2.2 Isotropy

As this work limits the investigation to isotropic hyperelastic materials, the strain energy expansion of Eq. (2.50) can be rewritten in terms of the invariants of the second order tensor $\mathbf{E}$. Such second order tensors have the invariants $\mathrm{tr}\,\mathbf{E}^k$ where $k \in \{1, 2, 3\}$ [29, ch. 3.8]. Thus $W(\mathbf{E}) = W(\mathrm{tr}\,\mathbf{E}^k), k \in \{1, 2, 3\}$, and Eq. (2.50) can for an isotropic hyperelastic material be rewritten as [12]

$$W = \frac{\lambda}{2}(\mathrm{tr}\mathbf{E})^2 + \mu\,\mathrm{tr}\mathbf{E}^2 + \frac{C}{3}(\mathrm{tr}\mathbf{E})^3 + B(\mathrm{tr}\mathbf{E})\mathrm{tr}\mathbf{E}^2 + \frac{A}{3}\mathrm{tr}\mathbf{E}^3 + \cdots, \tag{2.70}$$

Thus, by combining the two expressions for the strain energy function in Eqs. (2.50) and (2.70) the second- and third order elastic moduli can be expressed by [12]

$$\begin{aligned} C_{ijkl} &= \lambda\delta_{ij}\delta_{kl} + 2\mu I_{ijkl}, \tag{2.71}\\ C_{ijklmn} &= 2C\delta_{ij}\delta_{kl}\delta_{mn} + 2B(\delta_{ij}I_{klmn} + \delta_{kl}I_{mnij} + \delta_{mn}I_{ijkl})\\ &\quad + \frac{1}{2}A(\delta_{ik}I_{jlmn} + \delta_{il}I_{jkmn} + \delta_{jk}I_{ilmn} + \delta_{jl}I_{ikmn}), \tag{2.72} \end{aligned}$$

where $I_{ijkl} = \frac{1}{2}(\delta_{ik}\delta_{jl} + \delta_{il}\delta_{jk})$, and where λ, μ are the second order elastic moduli (also known as the Lamé parameters) and A, B, C are the third order elastic moduli introduced by [37] and used by [22][12] and more specific for the following section by [25]. In the following isotropy will be assumed if not otherwise stated.

Note also from Eq. (2.68) that the characteristic wave velocities $c(\mathbf{N}, \mathbf{m})$ are functions of the effective elastic moduli B_{ijkl} and the propagation and polarisation directions $\mathbf{N}$ and $\mathbf{m}$ respectively. Recalling from Eq. (2.63) that the effective elastic moduli B_{ijkl} is a function of the second and third order elastic moduli (C_{ijkl} and C_{ijklmn}, or correspondingly λ, μ, A, B, and C for an isotropic hyperelastic material) and the initial static deformation $\mathbf{u}^{(0)}$, it can be shown through Eqs. (2.8), (2.11), (2.15) and (2.16) that B_{ijkl} is a function of the principal stretches $\lambda_1, \lambda_2, \lambda_3$ [22, ch. 6.4]. Thus the characteristic sound velocities are also a function of the principal stretches. This will be further investigated for the special case of a uniaxial initial static displacement in Sec. 2.3 below.

2.3 Acoustoelasticity for uniaxial tension

This work has concentrated on a uni-axial tension with the propagation of sound perpendicular to the direction of tension. This choice has been made based on the similarity with a pipeline inspection tool travelling along the inside of a steel pipeline probing the wall thickness perpendicularly to the direction of the hoop stress, which is the dominating and load bearing stress of a pressurised pipeline. Uniaxial tension is specifically handled in [25], and the current work is thus based on the expressions presented therein.

A cuboidal sample of a compressible solid in an unstressed reference configuration can be described by the Cartesian coordinates $X_i \in [0, L_i], i = 1, 2, 3$, where the geometry is aligned with the natural coordinate system, and L_i is the length of the sides of the cuboid (similar to the current test specimen shown in Fig. 3.1). Assume then that the cuboid is subjected to a uniaxial tension in the x_1-direction so that it deforms with a pure homogeneous strain such that $x_1 = \lambda_1 X_1$, $x_2 = \lambda_2 X_2$, $x_3 = \lambda_3 X_3$, which gives the elongation

$$e_i \equiv l_i/L_i - 1 = \lambda_i - 1, \qquad i \in \{1, 2, 3\} \tag{2.73}$$

in the x_i-direction. Here l_i signifies the deformed length of the cuboid side i in the pre-stressed configuration, and where the ratio between the length of the sides in the pre-stressed and reference configuration are denoted by

$$\lambda_i \equiv l_i/L_i \qquad (2.74)$$

and called the principal stretches. Note that in this work both the terms strain and elongation will be used. Strain will be used as the general term, while elongation denotes the principal strains measured by strain gauges in the x_1-, x_2-, and x_3-direction of the uniaxial tension setup described in Sec. 3.3. This corresponds for an isotropic material to a deformation gradient without any rotation (i.e. from Eq. (2.7) $\mathbf{F} = \mathbf{U} = \mathbf{V}$ with $\mathbf{R} = \mathbf{I}$) which can be described by the principal stretches as eigenvalues $\lambda_i \equiv l_i/L_i$ as shown in Eq. (2.8) [25], or equivalently by the elongations (Eq. (2.73)) in the three principal directions x_i.

The Jacobian in Eq. (2.9)

$$J = \lambda_1\lambda_2\lambda_3 = \frac{l_1l_2l_3}{L_1L_2L_3} \qquad (2.75)$$

can be regarded as a measure of the volume change when the material is subjected to elongation/compression in one or more directions. Correspondingly the relation

$$\frac{J}{\lambda_1} = \frac{l_2l_3}{L_2L_3} \qquad (2.76)$$

can be regarded as a measure of change in the cross-section area in the x_2-x_3-plane.

For an uniaxial tension in the x_1-direction we assume that $e_1 = \lambda_1 - 1$ increase by some amount. If the lateral faces are free of traction, which is ensured if Eq. (2.36) for the pre-stressed conditions satisfy [25]

$$S_{22} = S_{33} = \frac{\partial W}{\partial \lambda_2} = \frac{\partial W}{\partial \lambda_3} = 0, \qquad (2.77)$$

the lateral elongations $e_2 = \lambda_2 - 1$ and $e_3 = \lambda_3 - 1$ are limited to the range $e_2, e_3 \in (-1, 0]$. This contraction in the x_2- and x_3-direction when applying a tension in the x_1-direction is also know as the Poisson-effect [13, ch. 1.3]. For isotropic materials the lateral elongation (or rather contraction) must also be equal (i.e. $e_2 = e_3$), and the range corresponds to the range from total lateral contraction ($e_2 = e_3 = -1$, which is non-physical), and to no change in the lateral dimensions ($e_2 = e_3 = 0$). It is noted that

theoretically the range could be expanded to values larger than 1 corresponding to an increase in lateral dimensions as a result of increase in axial dimension. However, very few materials exhibit this property [81][82] and it has not been relevant for this work.

Recalling the expansion of S_{ij} in Eq. (2.56) in terms of partial derivatives of the displacement $\partial u_i / \partial X_j$ (Eq. (2.48)) can for such an uniaxial deformation, with use of the elastic moduli in Eqs. (2.71) and (2.72), be expressed as [13, ch. 1.3]

$$S_{ij} = (\lambda \delta_{ij} \delta_{kl} + \mu(\delta_{ik} \delta_{jl} + \delta_{il} \delta_{jk})) \frac{\partial u_k}{\partial X_l} + \cdots . \tag{2.78}$$

Note that the superscript $^{(0)}$ to denote the initial deformation of state B_t has been dropped in the following. For a homogeneous uniaxial deformation the partial derivative will only have non-zero elements along its diagonal, and it can thus be expressed by the principal stretches λ_i, or conversley the elongations e_i, as

$$\delta_{kl} \frac{\partial u_k}{\partial X_l} = \delta_{kl} \frac{\partial x_k}{\partial X_l} - \delta_{kl} = \lambda_k - 1 = e_k \tag{2.79}$$

The restriction imposed by Eq. (2.77) leads thus to [25]

$$S_{22} = \lambda(e_1 + 2e_2) + 2\mu e_2 = 0, \tag{2.80}$$

which, when rearranged, gives the relation between the applied elongation e_1 and the resulting elongation $e_2 = e_3$ as

$$-\frac{e_2}{e_1} = \frac{\lambda}{2(\lambda + \mu)} \equiv \nu, \tag{2.81}$$

which is known as the Poisson's ratio [13, ch. 1.3] (see Sec. 2.4).

Note that Eq. (2.80) only includes terms of order one in the applied deformations $u_{i,j}^{(0)}$. By including higher order terms from Eq. (2.56) the contraction e_2 can up to second order in e_1 be written as [25]

$$e_2 = -\nu e_1 - \beta e_1^2 \tag{2.82}$$

where ν is defined in Eq. (2.81) above, and [25]

$$\beta = \frac{3\kappa\lambda}{8(\lambda + \mu)^2} + \frac{\lambda^2 A}{8(\lambda + \mu)^3} + \left[\frac{\lambda(\lambda - 2\mu)}{2(\lambda + \mu)^2} + 1 \right] \frac{B}{2(\lambda + \mu)} + \frac{\mu^2 C}{2(\lambda + \mu)^3}, \tag{2.83}$$

where

$$\kappa = \lambda + \frac{2}{3}\mu \tag{2.84}$$

is the infinitesimal bulk modulus [13, ch. 1.3].

Using the relation between Cauchy- and nominal-stress in Eq. (2.22) and the constitutive relation for a homogeneous and uniaxial deformation in Eqs. (2.36), (2.70) yields the relation [22, ch. 4.3.4][25]

$$S_{11} = \frac{J}{\lambda_1}\sigma_{11} = \frac{\partial W}{\partial \lambda_1}, \tag{2.85}$$

where J/λ_1 is the change in x_2-x_3 cross section area over which the tension is applied (see Eq. (2.76)) By substituting the expansion of e_2 from Eq. (2.82) into Eq. (2.85) the relation between the pre-stress and pre-strain up to the second order in $e1$ can be found, which [25] have shown to be

$$\sigma_{11} = \frac{3\kappa\mu}{\lambda + \mu}e_1 + \gamma e_1^2 \tag{2.86}$$

where

$$\gamma = \frac{3\kappa\mu(5\lambda + 3\mu)}{2(\lambda + \mu)} + \left[1 - \frac{\lambda^3}{4(\lambda + \mu)^3}\right]A + \frac{3\mu(3\lambda^2 + 4\lambda\mu + 2\mu^2)}{2(\lambda + \mu)^3}B + \frac{\mu^3}{(\lambda + \mu)^3}C. \tag{2.87}$$

Note that $3\kappa\mu/(\lambda + \mu) = Y$ is the infinitesimal Young's modulus. We will come back to alternative descriptions of the elastic moduli in Sec. 2.4, but will mainly focus on the Lamé second order elastic moduli and third order elastic moduli of Eq. (2.71) and (2.72). Conversely, it is possible to expand the pre-strain up to the second order of pre-stress, which [25] have shown to yield

$$e_1 = \frac{\lambda + \mu}{3\kappa\mu}\sigma_{11} + \left(\frac{\lambda + \mu}{3\kappa\mu}\right)^3\gamma\sigma_{11}^2. \tag{2.88}$$

For a load applied in the x_1-direction, we take the acoustic propagation direction (see Sec. 2.2.2.1 to be in the x_3-direction (i.e. $\mathbf{N} = [0, 0, 1]$). Selecting an orthonormal set of polarisation vectors (i.e. describing the direction of particle motion) as

$$\{\mathbf{m}\} = \begin{cases} \mathbf{m}_1 = \hat{\mathbf{x}}_1 = [1, 0, 0] & \parallel \text{to applied tension} \\ \mathbf{m}_2 = \hat{\mathbf{x}}_2 = [0, 1, 0] & \perp \text{to applied tension} \\ \mathbf{m}_3 = \hat{\mathbf{x}}_3 = [0, 0, 1] & \parallel \text{to } \mathbf{N} \end{cases} \tag{2.89}$$

leads, through Eq. (2.68), to the three sound velocities [25]

$$\rho_0 c_{33}^2 = B_{3333}, \qquad \rho_0 c_{31}^2 = B_{1313}, \qquad \rho_0 c_{32}^2 = B_{2323}, \qquad (2.90)$$

where c_{33} is the sound velocity of the longitudinal wave (also denoted c_l) where the particle motion is parallel with the propagation direction, c_{31} is the sound velocity of the transverse wave with particle motion polarised parallel to the direction of tension, and c_{32} is the sound velocity of the transverse wave with particle motion polarised perpendicular to the direction of tension (also denoted c_s or c_{sk} where subscript k signify polarisation direction of the particle motion). Including the elongation e_1 in the effective elastic moduli B_{ijkl} of Eq. (2.63), the sound velocities can be expressed as [25] (see App. A.4 for details on the expansion and the relevant values of B_{ijkl})

$$\rho_0 c_{33}^2 = \lambda + 2\mu + a_{33}e_1, \qquad \rho_0 c_{3k}^2 = \mu + a_{3k}e_1, \quad k = 1, 2 \qquad (2.91)$$

where

$$a_{33} = -\frac{2\lambda(\lambda + 2\mu) + \lambda A + 2(\lambda - \mu)B - 2\mu C}{\lambda + \mu} \qquad (2.92)$$

$$a_{31} = \frac{(\lambda + 2\mu)(4\mu + A) + 4\mu B}{4(\lambda + \mu)} \qquad (2.93)$$

$$a_{32} = -\frac{\lambda(4\mu + A) - 2\mu B}{2(\lambda + \mu)} \qquad (2.94)$$

are the acoustoelastic coefficients related to effects from third order elastic constants. Abiza et al. [25] have also shown that acoustoelastic coefficients, b_{ij}, related to fourth order elastic constants may also be important for some cases. Although they have not been applied in this work, they have been included in App. A.4 for completeness.

The sound velocitys can also be expressed in terms of the corresponding pre-stress σ_{11} up to second order as [25]

$$\rho_0 c_{33}^2 = \lambda + 2\mu + a_{33}^* \sigma_{11} + b_{33}^* \sigma_{11}^2, \qquad \rho_0 c_{3k}^2 = \mu + a_{ik}^* \sigma_{11} + b_{ik}^* \sigma_{11}^2, \quad k = 1, 2 \quad (2.95)$$

Using the relation in Eq. (2.88) to determine a_{ij}^* and b_{ij}^* as [25]

$$a_{ij}^* = \left(\frac{\lambda + \mu}{3\kappa\mu}\right) a_{ij}, \qquad b_{ij}^* = \left(\frac{\lambda + \mu}{3\kappa\mu}\right) \left(b_{ij} - \frac{\lambda + \mu}{3\kappa\mu}\gamma a_{ij}\right) \qquad (2.96)$$

To be able to compare theoretical values of the sound velocities with experimental data the following three sound velocities have been implemented in numerical computation algorithms (see Sec. 4 for details) based on Eq. (2.91) and the acoustoelastic constants in Eqs. (2.92), (2.93), and (2.94).

$$c_{33} = \sqrt{\frac{\lambda + 2\mu + a_{33}e_1}{\rho_0}} \tag{2.97}$$

$$c_{31} = \sqrt{\frac{\mu + a_{31}e_1}{\rho_0}} \tag{2.98}$$

$$c_{32} = \sqrt{\frac{\mu + a_{32}e_1}{\rho_0}} \tag{2.99}$$

The second index k in c_{3k} indicate as before the polarisation direction of the particle motion (i.e. $k = 3$ signifies a longitudinal wave, while $k = 1$ and $k = 2$ signify shear waves with direction of the particle motion polarised in the x_1- and x_2-direction respectively). Note that for $e_1 = 0$ this corresponds to $c_{31} = c_{32}$ (i.e. no difference in propagation velocity for shear waves with particle motion in the x_1- or x_2-direction in the unstressed configuration, as expected for an isotropic material [30, ch. 2.10]).

2.4 Alternative descriptions of elastic moduli

2.4.1 Second order elastic moduli

For a hyperelastic isotropic material the second order elastic moduli C_{ijkl} relating the stress and strain can be expressed by two constant parameters λ and μ as shown in Sec. 2.2.2.2 Eq. (2.71). These two parameters are called Lamé's first and second parameter. μ is also known as the shear modulus as it is a suitable measurand relating the shear stress to the shear strain (i.e. $S_{ij} = \mu\, u_{i,j}$ where $i \neq j$). Another suitable measurand is the bulk moduls κ (Eq. (2.84)) which is connected to the dilatational part of the strain ($S_{ij} = \kappa\, u_{i,j}$ where $i = j$) which can be measured under hydrostatic pressure [13, ch. 1.3]. The linear part (dependent on the second order elastic moduli) of the constitutive relation in Eq. (2.56) can thus be expressed by [22, ch. 6.1.6]

$$S_{ij} = 2\mu u_{i,j} + \lambda u_{i,j}\delta_{ij}. \tag{2.100}$$

By dividing the strain measure into a dilatational part describing the constitutive relation under influence of normal stresses only as [22, ch. 6.1.6]

$$S_{ij}\delta_{ij} = \kappa u_{i,j}\delta_{ij} \tag{2.101}$$

and a distortional part describing the constitutive relation when the contribution from the dilatational part is removed as [22, ch. 6.1.6]

$$S_{ij} - S_{ij}\delta_{ij} = 2\mu(u_{i,j} - \frac{1}{3}u_{i,j}\delta_{ij}) \tag{2.102}$$

the bulk modulus κ defined in Eq. (2.84) can be seen to have a direct relation to the normal stresses (i.e. $S_{ij}\delta_{ij}$). For physical reasons both the bulk and shear modulus must be positive [22, ch. 6.1.6]

$$\kappa > 0, \qquad \mu > 0 \tag{2.103}$$

Young's moduls can be used as a convenient measure of the elasticity a linear elastic material which for of a long thin rod subjected to a uniaxial stress behaves according to the generalised Hooke's law (see definition given in relation to Eq. (2.58)) such that [13, ch. 1.3]

$$Y \equiv \frac{S_{axial}}{e_{axial}} \tag{2.104}$$

where subscript *axial* denotes the uniaxial direction of the applied tension and coaxial resulting strain (e.g. the experimental setup in Sec. 3.3 apply a uniaxial tension in the x_1-direction and under the assumption that the resulting deformation is homogeneous $Y = S_{11}/u_{1,1} = S_{11}/e_1$, where e_1 is the elongation as defined in Sec. 2.3). Under such a uniaxial deformation where the material is unconstrained in the other principal (transverse) directions it usually tends to expand or contract depending on whether the applied uniaxial stress is positive or negative respectively. The Poisson's ratio ν is a measure of how much the material deforms in the transverse direction when a long thin rod is subjected to an axial load [13, ch. 1.3]

$$\nu \equiv -\frac{e_{transverse}}{e_{axial}} \tag{2.105}$$

where subscript *transverse* denotes either of the two principal directions orthogonal to the *axial* direction in which the stress is applied (e.g. for the current experimental setup in Sec. 3.3 this yields $\nu = -u_{2,2}/u_{1,1} = -u_{3,3}/u_{1,1} = -e_2/e_1 = e_3/e_1$). It is

noted that Y and ν are bulk material properties describing the elastic response of a solid [13, ch. 1.3]. It should thus be independent of the geometry of the solid. However, when estimating these elastic properties from the results of a tension test effects of the geometry will affect the outcome based on deviations from ideal conditions (e.g. that the test specimen is not ideally straight, has impurities, the accuracy of measurements, etc., which will be further discussed in Sec. 3.6).

Selecting the axial and transverse directions in one of the principal directions of the coaxial S_{ij} and $u_{i,j}$ of Eq. (2.100) gives the relation between Young's modulus and Poisson's ratio and the Lamé parameters as [13, ch. 1.3]

$$Y = \frac{\mu\,(3\lambda + 2\mu)}{\lambda + \mu}, \qquad \nu = \frac{\lambda}{2\,(\lambda + \mu)} \tag{2.106}$$

The linear elastic properties of a homogeneous isotropic hyperelastic material can be described by combination of any two of these elastic moduli. And conversely, given any two of the elastic moduli enables the calculation of the other.

Note also that from Eq. (2.91) the unstressed longitudinal and shear sound velocities (i.e. $e_1 = S_{11} = 0$) are related through the second order elastic moduli. More specifically the ratio between the longitudinal and shear sound velocity can be expressed by

$$\frac{c_l}{c_s} = \sqrt{\frac{\lambda}{\mu} + 2} = \sqrt{\frac{2\,(1 - \nu)}{(1 - 2\nu)}}. \tag{2.107}$$

The elastic moduli of 8 steel samples are presented in Table 4.4 in Ch. 4, and based on the Lamé parameters of these steel types the relation between the longitudinal and shear sound velocities in an unstressed material can be approximated by

$$c_l \approx 1.83 c_s, \qquad \text{or} \qquad c_s \approx 0.55 c_l. \tag{2.108}$$

2.4.2 Third order elastic moduli

The acoustoelastic effect describing the shift in sound velocities of acoustic waves propagating in a body subjected to a finite pre-stress have been explained by the meticulous consideration of higher order expansion of the constitutive relation and strain energy of a material (see Sec. 2.1.3). Parts of this theory was already established correctly back in 1925 by Brillouin [14], and later confirmed by Huges and Kelly [16] in 1953. The third order elastic constants for an isotropic hyperelastic material A, B, C used in this thesis is ascribed Landau & Lifshitz in 1986 [37]. However, based on the selected

grouping of expanded terms different authors have proposed different sets of third order constants. Norris [12] has summarised the most widely used in table form, and this is reproduced here in Table 2.1.

Table 2.1: Relations between third order elastic constants for isotropic solids

Landau and Lifshitz [37] 1986	Toupin and Bernstein [18] 1961	Murnaghan [83] 1951	Bland [35] 1969	Eringen and Suhubi [36] 1974		Standard C_{IJK} [12]
A	$\nu_1 = 2C$	$l = B + C$	$\alpha = \frac{1}{3}C$	$l_E = \frac{1}{3}A + B + \frac{1}{3}C$	$C_{123} = 2C$	$C_{111} = 2A + 6B + 2C$
B	$\nu_2 = B$	$m = \frac{1}{4}A + B$	$\beta = B$	$m_E = -A - 2B$	$C_{144} = B$	$C_{112} = 2B + 2C$
C	$\nu_3 = \frac{1}{4}A$	$n = A$	$\gamma = \frac{1}{3}A$	$n_E = A$	$C_{456} = \frac{1}{4}A$	$C_{166} = \frac{1}{2}A + B$

Reproduced from [12]

2.5 Plastic deformation

Many materials behave elastically when subjected to moderate stresses. However, if subjected to stresses above a certain limit they acquire a permanent deformation that do not dissapear when the stress is removed (i.e. the deformation is not reversible). For crystalline materials like steel where the stress depends on previous deformation, but not the rate of deformation, this phenomenon is called plasticity [29, ch. 10.5].

Looking at a typical stress-strain curve for a uniaxial tension applied to a typical steel we note several points of interest (see Fig. 2.6). Point O represents the unstressed state, while point A is called the point of initial yield. Within the section OA the material is said to deform elastically, and a complete removal of the stress will return the deformation of the material to its initial configuration [29, ch. 10.5]. The behaviour of the material in this section is to a good approximation, that of the elastic theory presented in Sec. 2.1. The slope of the curve OA is a good approximation of the Young's modulus Y defined in Eq. (2.104) [13, ch. 1.3]. Increasing the stress to values above S_{11}^{A} the slope of the curve will change. This change may be abrupt or more gradual, it may include a drop or a plateau, and is a signature of how a specific material deforms plastically. If the force is removed after the material has been subjected to a stress S_{11}^{B} at point B the unloading follows the curve BC, which to a good approximation is parallel to AB. When the stress is completely removed there is a remaining residual strain OC which corresponds to the plastic deformation the material has experienced.
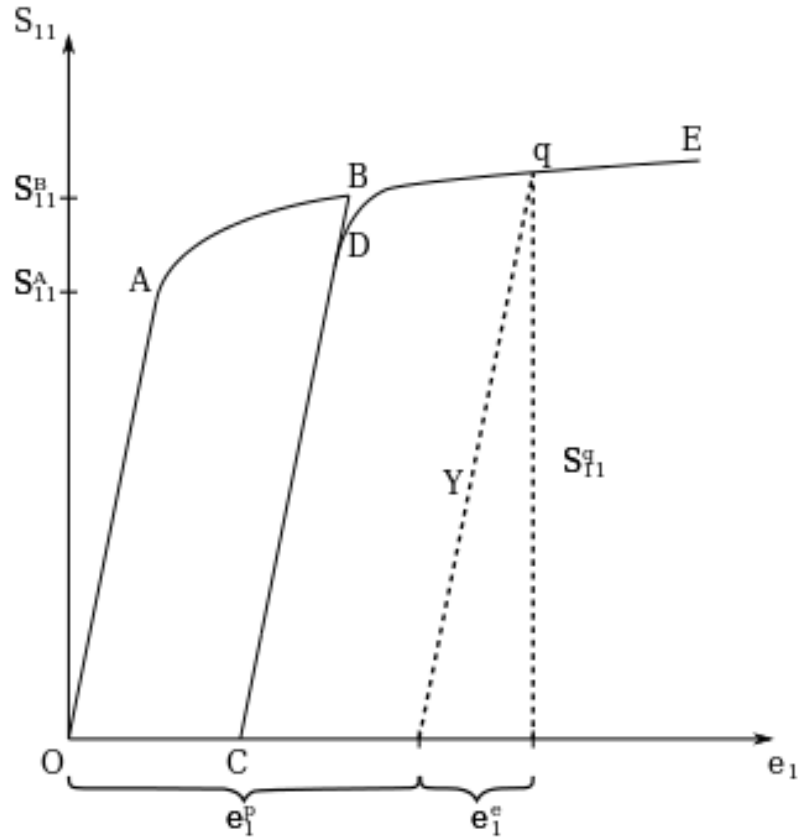
Figure 2.6: Typical stress-strain curve for a plastic solid

On reloading the path will follow CB closely up to point D, where it will gradually return to continue the curve OAB towards point E. It should be noted that the value of S_{11} at point D where the slope depart from the elastic slope is generally larger than at the first loading S_{11}^{A} [29, ch. 10.5].

Materials that follow this type of stress-strain curve are usually crystalline solids. Elastic deformation is explained on microscopic scale as small recoverable displacements of the atoms in the crystal lattice. Or in other words that the distance between individual atoms change slightly, but that the lattice structure is mainly not changed. Plastic deformation on the other hand is assumed caused mainly by permanent slip between neighbouring planes of atoms, deforming the structure of the lattice, which is not recoverable [29, ch. 10.5].

This study will not investigate the basic theoretical influence of plastic deformation on the stress dependence of the acoustic velocity in a material. This is mainly because of the diversity of plastic responses within the group of materials that behaves similarly in the elastic regime, and will thus introduce the need to develop specific yield criteria, yield functions, and plastic stress-strain relations for each material even though their elastic properties may be very similar [70][84][85]. The parameters describing the plastic behaviour need in most cases to be experimentally determined, and are thus to cumbersome to be suitable in an industrial NDT setting. However, this work has measured the acoustoelastic effect well in to the plastic region, and also in the elastic unloading and loading after plastic deformation. To be able to compare the measured result with the theory of acoustoelasticity two different approaches have been investigated. The first approach has been to simply diregard the plastic contribution to the deformation and comparing the measured effect with the theoretical effect of the corresponding elastic deformation. Details on how this has been done can be found in Sec. 2.5.1. The other approach was to compare the measured effect with a theory developed to include the plastic effects. This has been evaluated as outside the scope of this work, however the discussion around the approach has been included in Sec. 2.5.2.

2.5.1 Elastic and plastic strain

Although the previous sections have argued the case of a non-linear relation between stress and strain for a hyperelastic material the assumption of a linear relation between the applied tension and the resulting *elastic* strain is still a good approximation after plastic deformation if one make the distinction between the resulting *elastic* and *plastic* strain. This section will apply the nomenclature of a homogeneous uniaxial deformation as described in Sec. 2.3, however, the more general description can also be applied. The generalised Hooke's law (see Eq. (2.58)) can be expressed as $S_{11} = Y\, e_1^e$ for the applied uniaxial stress S_{11} and corresponding uniaxial homogeneous elastic elongation e_1^e (see Eq. (2.73) and Fig. 2.6), where Y is the Young's mouduls as defined in Eq. (2.104) and the superscript e denote the elastic part of the total elongation. Assuming that stresses above the yield limit S_{11}^A will plastically deform the material as shown in Fig. 2.6, and that any unloading will follow a path parallel to the initial slope of the stress-strain curve, it is possible to estimate the elastic elongation e_1^e at any point on the stress-strain

curve given by the stress S_{11} at that point as [29, ch. 10.5][70]

$$e_1^e = \frac{S_{11}}{Y} \tag{2.109}$$

Thus, the plastic elongation $e^p(e_1, S_{11})$ can be estimated as the difference between the total elongation e_1 and the elastic elongation e_1^e (i.e. e_1^p is the remaining elongation when the stress is completely removed, $S_{11} = 0$) [29, ch. 10.5][70].

$$e_1^p = e_1 - e_1^e = e_1 - \frac{S_{11}}{Y} \tag{2.110}$$

Superscript ^{e} and ^{p} denote elastic and plastic deformation respectively.

As mentioned above this estimate of elastic and plastic strains are only valid if the slope of the elastic unloading does not change when the material is plastically deformed (i.e. that Y is constant). However, as will be shown in the result chapter (Ch. 5) the slope of the linear unloading sequences after plastic deformation are not parallel to the initial loading sequence. In the case of a different slope it has in this work been assumed that the change in slope, or correspondingly change in Y, has a linear dependence on the induced plastic strain (i.e. Y need to be continuous and differentiable to avoid discontinuities in the both the elastic e_1^e and plastic e_1^p elongations, and a linear dependence is a first approximation used between the three unloading sequences applied in this work). Thus, between the current and previous unloading sequence the change in Y is described by the linear relation

$$Y^{CB} = Y^{OA} + \xi e_1^p \tag{2.111}$$

where ξ is the linear increase or decrease in Y for a given plastic strain e_1^p between the linear loading sequences OA and BC.

A more generic way to extract the plastic and elastic contributions for all the principal directions is to use the force-strain relation in the same way as the stress-strain relation together with the Young's modulus have been used above. Replacing the stress with the force $F = S_{11}A_0$, where A_0 is the unstressed cross section area (which change under plastic deformation), and using the slope of the applied force versus elastic strain represented by $y^{ei} = \frac{F}{e_i^e} = \frac{S_{11}A_0}{e_i^e} = A_0 Y$ for all the principal elongations instead of the Young's modulus Y, Eq. (2.109) becomes

$$e_i^e = \frac{F}{y^{ei}}. \tag{2.112}$$

Estimating the "remaining" strain if the current force F is reduced to 0 along the linear slope of the elastic force-elongation relation ($F = y^{ei}e_i^e$). The plastic contribution then becomes

$$e_i^p = e_i - e_i^e = e_i - \frac{F}{y^{ei}} \tag{2.113}$$

The slope y^{ei} can be estimated from linear regression, and if the slope changes between different unloading sequences, a linear relation between the two slopes can be used as described above in Eq. (2.111). This has been used to estimate a plastic strain between unloading sequences based on linear regression of the actual slopes y^{ei} of the measured force-elongation curves as shown in Fig. 5.8 in Sec. 5.3.

After the measured elastic strains have been estimated using this approach they can be implemented in the acoustoelastic theory of Sec. 2.3 to compare the theory with the actual measured acoustoelastic effect. More on the setup of numerical calculations can be found in Ch. 4.

2.5.2 Acoustoplasticity

Acoustoplasticity is an extension of the acoustoelastic theory presented in Sec. 2.2.2 to also include the effect of plastic deformation on the acoustic propagation velocities. Several authors have investigated this effect [59] [61] [86] [87] [27]. However, the plastic stress-strain relations are complex and difficult to establish. The linear-elastic properties of a hyperelastic material, in our case steel, can be obtained through an uniaxial tension test. Arguing that the non-linear elastic properties of a hyperelastic material are due to non-linear effects in how the spacing of atoms in the crystal lattice change under elastic loads[88, ch. 4,5] [70, ch. 2.2], it might be reasonable to assume that the third order elastic constants of materials consisting of mainly the same type of atoms and with the same type of crystal structure will be of similar magnitude [88, ch. 4,5]. The elastic constants presented in Table 4.4 also suggest that this might be a reasonable assumption. However, plastic behaviour depends on much more than the deformation that can be ascribed to the interaction between single neighbourhoods of atoms. Some of the mechanisms attributed to plasticity in polyctrystalline aggregates (e.g. composed of large numbers of grains which individually has the structure of a simple crystal) are explained in [88, ch. 4,5] [70, ch. 2.2], and it is evident that a thorough experimental examination of each individual material (as well as a representative number of tests from different spatial locations) is needed to establish a good material model for the plastic

behaviour for any given material. This is outside the scope of this study, and as argued by Smith in his 1963 paper [45] where he argues that plastic strain and dislocations has negligible effect in polycrystalline materials (like aluminium and steel). Thus this has thus not been further investigated in this work. For some of the latest developments in acoustoplastic research the reader is referred to [55] and [63], which also are good sources on further reading.

2.6 Sound velocity measurement

There are currently several methods to assess the sound velocity with high accuracy (see [4] [5]). This work has used the ART [7][8][9] developed by DNV to assess the possibility of measuring the stress state of steel pipelines with the technology and methodology of this existing tool.

2.6.1 Acoustic resonance

The ART methodology is based on transient acoustic reflections from layers and plates (e.g. across the wall thickness of a pipeline) [65][10][11]. A broad band signal (e.g. a linear chirp) is produced by a transducer which propagate a longitudinal pressure signal through a coupling medium towards a plate at close to normal incidence. Assuming that the radiated acoustic beam signal can be represented by a plane wave decomposition of the incoming pressure field, the signal impinging on the plate can be described by a set of plane waves with a distribution of incident angles around the normal incidence. Some part of the energy will be reflected from the front interface (reflection $R_i, i = 0, 1, 2, \ldots$ in Figs. 2.7 and 2.8). The rest of the energy will through mode conversion be propagated through the plate as both longitudinal pressure waves (P-waves) and vertically polarised shear waves (SV-waves) [69]. These waves will both be reflected and transmitted (transmitted waves $T_i, i = 0, 1, 2, \ldots$ in Fig. 2.7) at the back interface. This is illustrated in Fig. 2.7 for a steel plate immersed in water where R_i signify reflected pressure wave amplitudes and T_i signify transmitted pressure wave amplitudes. The multiple reflections within the steel (Layer 2) will transmit some of its energy both back toward the direction of the incoming signal in Layer 1 as well as away from the incoming signal in Layer 3. If the thickness of Layer 2 is sufficiently small, the transmitted amplitude from the internal reflections R_i where $i > 0$, will overlap with

the amplitude R_0 of the initial reflection from interface between Layer 1 and Layer 2. This is illustrated in Fig. 2.8 where t_{pulse} is the duration of the pulse and $2t_d$ is the time it takes for the signal to travel the thickness of Layer 2 twice. The characteristic acoustic impedance of the water in Layer 1 and Layer 3 is approximately

$$r_1 = r_3 = \rho_w c_w \approx 1000\,\text{kg/m}^3 \cdot 1500\,\text{m/s} = 1.5\,\text{Mrayl}, \tag{2.114}$$

while for the steel in Layer 2 it is approximately

$$r_{2l} = \rho_0 c_l \approx 7850\,\text{kg/m}^3 \cdot 6000\,\text{m/s} = 47.1\,\text{Mrayl}. \tag{2.115}$$

$$r_{2s} = \rho_0 c_s \approx 7850\,\text{kg/m}^3 \cdot 3300\,\text{m/s} = 25.9\,\text{Mrayl}. \tag{2.116}$$

where ρ_w and ρ_0 are the mass density of water and steel respectively, and c_w is the longitudinal sound velocity of water, while c_l and c_s are the longitudinal and shear sound velocities of steel respectively. Thus

$$r_{2l} > r_{2s} > r_1 = r_3. \tag{2.117}$$

Thus the first reflection R_0 will be in phase with the incoming pulse I at the surface boundary between Layer 1 and Layer 2. All the consecutive transmissions (R_i^{sl} or R_i^{ll}, where $i > 0$) of the internal reflections within Layer 2 into Layer 1 will have a phase that has been shifted $180°$ at the surface boundary between Layer 2 and Layer 3 [69][89]. The superscripts ^{ll}, ^{ls}, and ^{ss}, or other combinations (i.e. ^{lsll} etc.) in Fig. 2.7 denotes whether the internal reflected signal has propagated through mode conversion as longitudinal and/or shear waves before it is transmitted back into Layer 1 or Layer 3 as a longitudinal pressure wave.

For plane wave theory and normal incidence the frequencies where an integer multiple of the half wave length $\lambda/2$ of either the longitudinal or shear waves matches the thickness of the plate d (see Fig. 2.9), the internal reflections will interfere constructively with each other and their collective amplitude can thus be called resonant. This collective amplitude of several resonant internal reflections will, because of the phase shift, interfere destructively with the initial reflection R_0 when it is transmitted back into Layer 1 (R_i, $i > 0$). However, after the first reflection has passed, the total amplitude of internal resonant reflections will be transmitted as a tail dominated by the frequencies which have accumulated the largest constructive interference. These frequencies will hence forth be referred to as the resonance frequencies f^n (superscript n
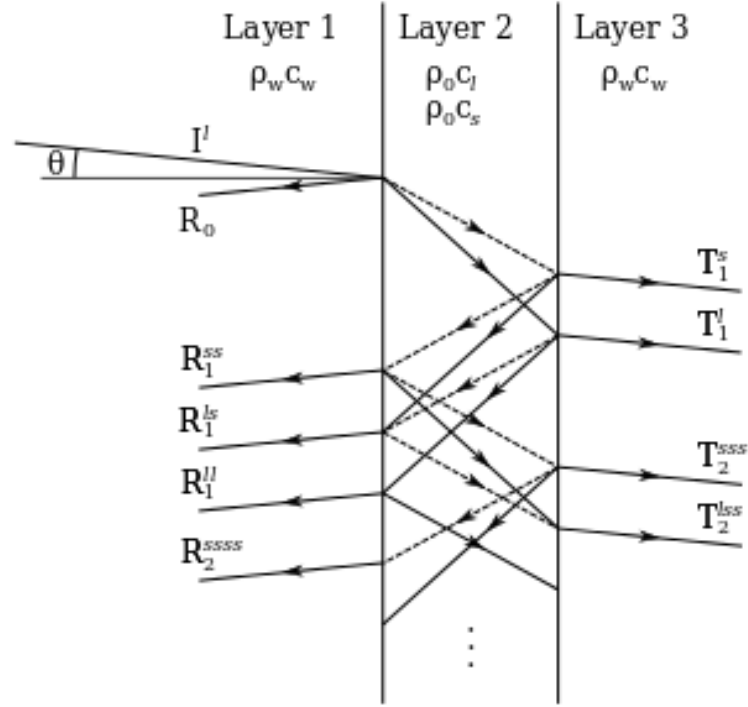
Figure 2.7: Multiple reflections from a solid layer (layer 2) imbedded within two half-space fluid layers (layer 1 and layer 3). Solid and dashed lines represent longitudinal (^{l}) and shear (^{s}) waves respectively, and R_i and T_i signify the reflected and transmitted pressure wave amplitudes respectively.

denotes the integer harmonic number of matching half wave lengths). If the duration of the incoming signal is significantly larger than the time it takes for the pulse to cross Layer 2 twice, the signal have time to excite internal resonances, and the signal will be reflected back into Layer 1 as a main echo followed by a lower amplitude tail which mainly consists of these half-wave resonance frequencies [7][10][11]. Note that shear waves would not be excited at normal incidence, and that the incoming signal must have a component impinging at an oblique angle to excite shear waves [69]. The experimental setup applied in this work have such an oblique component because of the effective beam angle of the transducer used, and thus both longitudinal and shear waves may be excited.
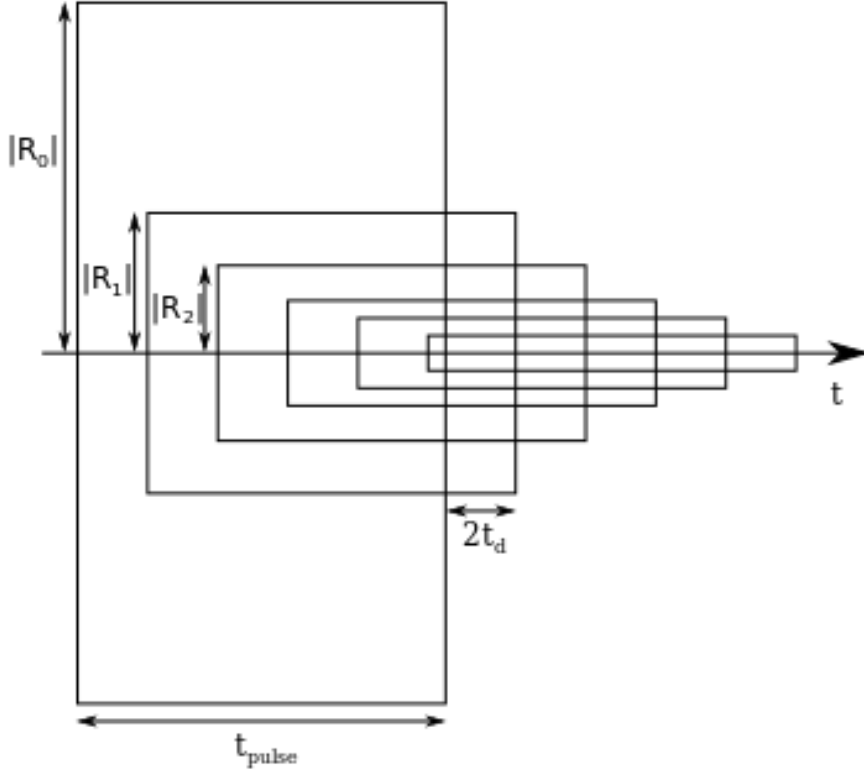
Figure 2.8: Amplitude of overlapping reflections R_i (not including interference)

The resonant frequencies f_n are found where an integer number n of half the wavelengths $\lambda_l^{(n_l)}$ or $\lambda_s^{(n_s)}$ matches the thickness d of the layer as [7][4]

$$n_l \frac{\lambda_l^{(n_l)}}{2} = d, \qquad n_s \frac{\lambda_s^{(n_s)}}{2} = d, \qquad n_l, n_s = 1, 2, 3, \ldots, \tag{2.118}$$

where subscript $_l$ or $_s$ signifies a longitudinal or shear wave respectivly, and where the superscripts $^{(n_l)}$ and $^{(n_s)}$ signify the integer number for the respective longitudinal and shear wave. The shear waves can also be decomposed into two orthogonal polarisations of its particle motion [69][4]. The relation between the frequency f, wave length λ, and the sound velocity c [4],

$$f = \frac{c}{\lambda}. \tag{2.119}$$

gives thus the longitudinal and shear resonance frequencies as

$$f_{\text{th}}^{(n_l)} = \frac{n_l}{2} \frac{c_l}{d}, \qquad \text{and} \qquad f_{\text{th}}^{(n_s)} = \frac{n_s}{2} \frac{c_s}{d}, \qquad n_l, n_s = 1, 2, 3, \ldots \tag{2.120}$$
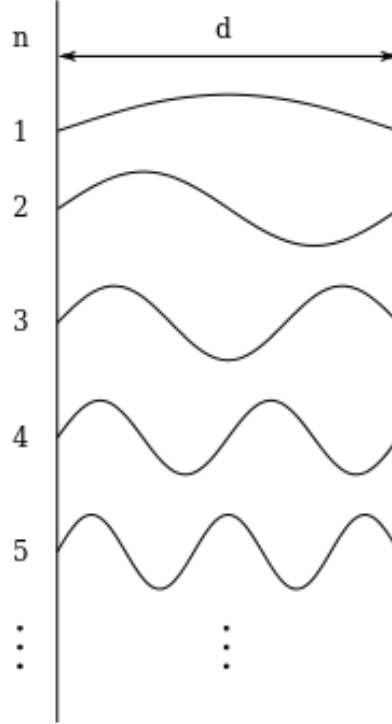
Figure 2.9: Sketch of an integer number n half waves matching the thickness d of a layer.

respectively, where the subscript $_\text{th}$ denotes plane wave theory, or conversely the longitudinal and shear sound speed as

$$c_l = 2d\frac{f_\text{th}^{(n_l)}}{n_l}, \qquad \text{and} \qquad c_s = 2d\frac{f_\text{th}^{(n_s)}}{n_s}, \qquad n_l, n_s = 1, 2, 3, \ldots \tag{2.121}$$

Note that these relations are only a theoretical approximation according to plane wave theory. First it is noted that for normal incidence no propagating shear waves will be excited [69, ch. 9.D]. For incident angle $\theta > 0$ shear waves will be excited, however their resonance frequencies will be a function of the distance traveled by the wave, and thus a function of the thickness d and the incident angle $\theta > 0$ (see Fig. 2.7). The effect of oblique incidence caused by the beam width of the transducer is discussed further in Sec. 2.6.2. Based on the measured resonance frequency and the thickness of the test specimen (distance traveled) it is thus possible to calculate the average sound velocity across the test specimen through Eq. (2.121).

2.6.2 Beam effects

The theory presented in Sec. 2.2.2 is derived using plane waves. This is one method to develop a relation between the sound velocities of a material and the deformation produced by the pre-applied stress to the material body. However, the description of acoustic waves as plane waves is a choice of mathematical convenience, and other wave representations can be used. The acoustic signal produced by the transducer in the experimental setup is not a single plane wave when impinging at the interface of the test specimen. In-house characterisation of the transducer produced by PCT [90] used in this work has shown that the transmitter disk of the transducer has a beam angle ($\theta_{6\text{dB}}$ - see Sec. 3.5) varying between $\sim 5°$ at 800 kHz, $\sim 7°$ at 550 kHz, and $\sim 13°$ at 300 kHz [91], see Sec. 3.5 for details. Assuming that the radiated acoustic beam signal can be represented by a plane wave decomposition of the incoming pressure field on the first interface between Layer 1 and Layer 2 [92][93], the signal propagating through the test specimen (Layer 2) can thus be regarded as a superposition of the transmitted plane waves from the set of incoming decomposed waves. Recent work by Lohne et al. [93], Aanes et al. [94] [95] [96], and Waag et al. [97] have compared the transmission of actual acoustic beams with that of plane waves impigning at a layer immersed in a fluid. Fig. 2.10 shows the absolute value of the transmission coefficient Tr for plane waves (i.e. ranging from 0 (white) to 1 (black)) for the frequencies in the applied linear chirp signal (300-800 kHz) excited by the transducer as a function of the incident angle θ and the frequency of the plane wave. The black lines denoted L1, S2, S3, L2 corresponds to the first and second symmetrical and second and third antisymmetrical leaky Lamb-modes (S_i and A_i, $i = 0, 1, 2, \ldots$, in standard leaky Lamb-mode notation [93][94]). The reason for using the notation L1, L2, S1, S3, etc. in this work has been to heighten the awareness of the reader as to whether the observed resonance mode is dominated by the longitudinal sound velocity (L1, L2, etc.) or the shear sound velocity (S1, S2, etc.) at normal incidence. The dashed line in Fig. 2.10 shows a smoothed curve between the three characterised beam angles at 300, 550, and 800 kHz. At normal incidence ($\theta = 0$) L1 and L2 corresponds to the cross-thickness longitudinal resonance modes in Eq. (2.120) (i.e. $f^{(n_l)}$ for $n_l = 1, 2$ respectively). At normal incidence the shear resonance modes are not excited, however, for small angles of incidence the S2 and S3

Table 2.2: Input to transmission coefficient plot

Material	Density	Sound velocity		Layer thickness
	ρ [kg/m^3]	c_l [m/s]	c_s [m/s]	d [m]
Water	1000	1500	-	∞
Steel	7500	6000	3300	$7.5 \cdot 10^{-3}$

Typical values for steel and water based on values given in [4]

leaky Lamb-modes approach the cross-thickness shear resonance modes of Eq. (2.120) (i.e. $f^{(n_s)}$ for $n_s = 2, 3$ respectively) [69][93][94][96][97].

Fig. 2.10 has been produced by implemented algorithms developed by Aanes et al. [96] and Waag et al. [97] and recieved by personal communications courtesy of these authors [76][75] (2013). The input to their plane-wave models was tentative characteristic values for water and steel presented in Table 2.2.

As can be seen from Fig. 2.10 the resonance frequencies depend on the incident angle [92] [75], and the resonance frequencies measured by the ART method should thus be a superposition of a collection of plane waves impinging on the test specimen with an angular distribution dictated by the beam angle of the transducer. This frequency shift at normal alignment of the transducer towards the plate was shown through experiments published by Lohne et al. in 2008 [92], and was indicated to be an effect of a finite beam angle in the sound field of the applied transducer. This beam effect can be decomposed into a spectrum of plane waves impinging on the steel plate with a distribution of incidence angles. The beam effect and its influence on the measurement of thickness and sound velocities in plate was discussed and theoretically explained and confirmed by the angular spectrum method (ASM) in [93]. Others have later investigated this effect as earlier mentioned [94] [95] [96] [97]. The result of this effect has been further discussed in Sec. 3.5.1.

The fact that the propagated acoustic signal impinging on the test specimen has a distribution of incident angles around the normal incident is thus the reason why shear waves are excited in the test specimen [69][4, ch. 2.4].

2.7 Relevant measurement quantities

The sound velocities c_l and c_s measured through the relations in Eq. (2.121) are of course relevant measurement quantities. However, as the theory of acoustoelasticity
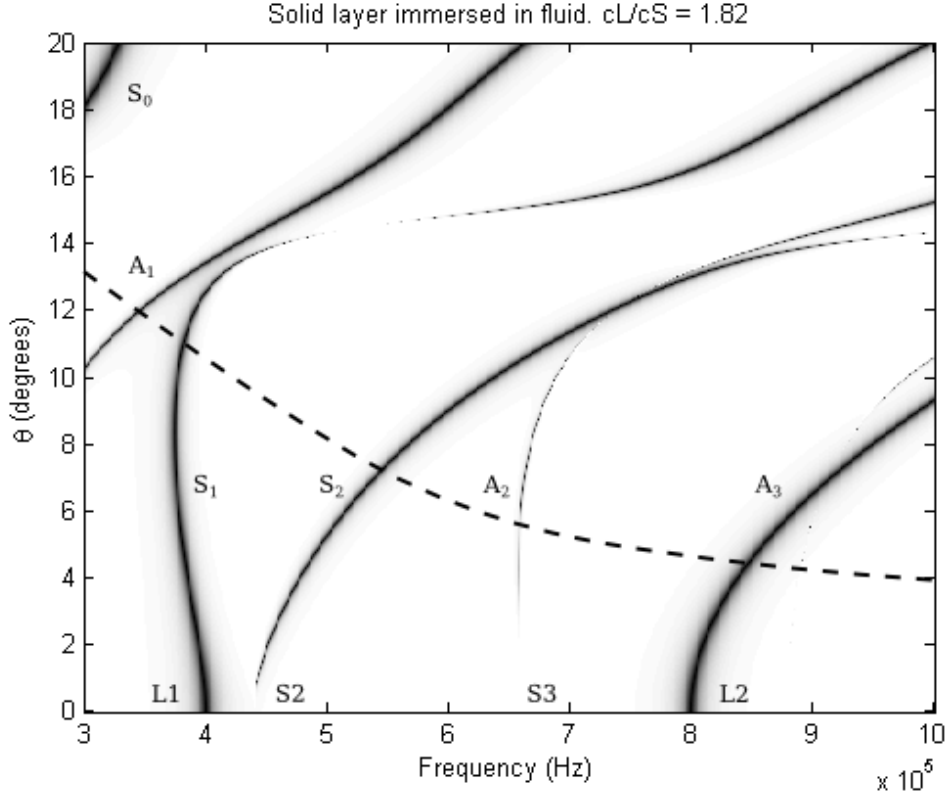
Figure 2.10: Transmission coefficients of plane waves impigning on a steel layer immersed in water. Courtesy of Waag [75] and Aanes [76]. L1, L2, S2, S3 denotes the leaky Lamb-modes that corresponds to the 1st and 2nd cross-thickness resonance modes dominated by the longitudinal sound velocity and 2nd and 3rd cross-thickness resonance modes dominated by the shear sound velocity respectively. The dashed line indicates the -6dB beam angle of the transducer used in this work.

presented in Sec. 2.2 shows, the magnitude of change in sound velocities as a function of applied tension are small compared to the magnitude of the individual sound velocities. It may thus be more appropriate to investigate the relative sound velocity changes. The relative sound velocity change Δc_r can be expressed as

$$
\begin{aligned}
\Delta c_r \equiv \frac{\Delta c}{c_0} &= \frac{c - c_0}{c_0} = \frac{c}{c_0} - 1 = \frac{l_3 f^{(n)}}{L_3 f_0^{(n)}} - 1 = \frac{\cancel{L_3}(1 + e_3) f^{(n)}}{\cancel{L_3} f_0^{(n)}} - 1 \\
&= \frac{(1 + e_3) f^{(n)}}{f_0^{(n)}} - 1,
\end{aligned} \tag{2.122}
$$

where subscript 0 denotes the reference values measured at zero loading, c can be either c_l or c_s, $f^{(n)}$ is either $f^{(n_l)}$ or $f^{(n_s)}$ (note that these frequencies are measured quantities and do not have the subscript $_{\text{th}}$ denoting resonance frequencies based on plane wave theory), and where l_3 is the thickness which can be calculated as

$$l_i = L_i(1 + e_i) \qquad (2.123)$$

for $i = 3$ where e_3 is the measured elongation in the thickness-, or x_3-, direction. The notations $\Delta q = q - q_0$ and $\Delta q_r = (q - q_0)/q_0$ have also been used for other relevant measurement quantities q (e.g. f, c, etc.).

The relative sound velocity change Δc_r is dependent on thickness and frequency measurements at both the zero loading- and current state. Thus the uncertainty in the relative sound velocity change will be dependent on the uncertainty in all of these parameters (see Ch. 6 for details on uncertainty calculation and propagation). Assuming that thickness variation between test specimens, the uncertainty in the actual thickness, and in the thickness development measurements are a significant portion of the total uncertainty it would be convenient to remove the uncertainty related to the thickness measurements. By comparing the ratio between the calculated relative sound velocity change of waves which have different dependency on the applied stress this can be achieved. A variant of this has been presented by Kim and Hong in their 2009 paper [68] where they presented the linear relation between the ratio of time of flight (TOF) measurements of a longitudinal wave and the TOF of a mode converted longitudinal-shear wave and an applied tensile stress in the test specimen. This approach is similar but based on a different measurement technique than the method applied here. For the measured longitudinal and shear resonance frequencies measured in this work the larger the difference in gradient of sound velocity change is, the larger the resulting relative ratio change will be on increasing magnitude of the applied stress. As can be shown on use of Eq. (2.91) and the elastic constants for steel in Table 4.4 the longitudinal and shear modes have different, and sometimes opposite, gradients of their respective sound velocity change and the ratio may thus enhance the measured change. The ratio between longitudinal and shear sound velocities and/or resonance frequencies can be calculated as

$$\frac{c_l}{c_s} = \frac{n_s}{n_l} \frac{f^{(n_l)}}{f^{(n_s)}} \qquad (2.124)$$

where n_l and n_s signifies the harmonic number of the longitudinal and shear modes respectively. The relative change in this ratio is then

$$\Delta \left(\frac{c_l}{c_s}\right)_r \equiv \frac{\Delta\left(c_l/c_s\right)}{c_{l0}/c_{s0}} = \frac{c_l/c_s}{c_{l0}/c_{s0}} - 1 = \frac{f^{(n_l)}/f^{(n_s)}}{f_0^{(n_l)}/f_0^{(n_s)}} - 1 \equiv \Delta \left(\frac{f^{(n_l)}}{f^{(n_s)}}\right)_r \qquad (2.125)$$

which does not depend on any thickness measurements, and thus reduce the uncertainty in the sound velocity change measurements. The different measurements and derived results are presented in Ch. 5 together with comparison with theoretical simulations.

3

Experimental setup and measurement methods

This chapter describes the experimental setup and measurement methods that have been used in this work. While most other techniques to measure the sound velocity in a steel sample needs careful placement of the acoustic measure equipment, it has been a goal of this study to investigate the possibility of using the existing Acoustic Resonance Technology (ART) method with a transducer that is not in physical contact with the test specimen (i.e. normal incidence and liquid coupling). Other works [7][9] have shown that the ART method can be used without physical contact between the transducer and test specimen both in pressurised gas and atmospheric air. Although it is possible to measure in atmospheric air, for convenience, water has been used as a coupling medium to reduce the acoustic energy loss between the transducer and the test specimen to get good pulse-echo recordings.

The different instruments used in the experimental part of this work have been summarised in Table 3.1 in Sec. 3.1, and are discussed in more detail in the appropriate sections in this chapter.

3.1 Instruments

Table 3.1: Instruments

Instrument	Make	Type	Function
Test specimen, initial geometry Sec. 3.2			
Micrometer screw	Mitutoyo	0-25mm Cone	Used to measure thickness of test specimen.
Digital caliper	Sylvac	S_cal_{pro}	Used to measure width of test specimen.
Steel ruler	-	-	Used to measure length of test specimen.
Calibration blocks	Mitutoyo	Set no. BM1-103-0, Serial no. 111276	Used to calibrate readings of the micrometer screw, digital caliper, and steel ruler.
Tension test Sec. 3.3			
Tension machine	Instron [98]	8502	Tension machine with a load capacity of 300 kN in tension
Control unit	MessTek [99]	Mobile control and acquisition unit	Controlunit to control the load cell through displacement or load
Acoustic measurements Sec. 3.5			
DAQ	National Instruments	NI PXIe-1062Q	Digital to Analog controller pc
DAQ	National Instruments	NI PXI-5421	Digital to Analog signal converter
DAQ	National Instruments	NI PXI-5922	Analog to Digital signal converter
RF amplifier	Electronics & Innovation	model 2100L	Power amplifier between signal generator and electronic matching circuit
Electronic transformer / matching circuit	Halfwave	Custom made electronic [100]	Electronic up-transformation of voltage signal and matching of transducer impedance
Electronic gain circuit	Halfwave	Custom made electronic [100]	Electronic 23dB gain for received voltage signal by RX ring
PCT TX disk	PCT [90]	Custom made transducer	Exciting acoustic pressure signal

| Instrument	Make	Type	Function
PCT RX ring	PCT [90]	Custom made transducer	Receiving acoustic pressure signal
Thermometer	Hanna	HI 93530	Thermometer, K-type thermoelement
Geometric measurements Sec. 3.6			
Strain gauge	TML [101]	YFLA-2	2 mm x 1.8 mm strain gauge with a strain limit of 15-20 %
Strain gauge	TML [101]	YFLA-5	5 mm x 2 mm strain gauge with a strain limit of 15-20 %
ARAMIS	GOM [102]	5M ARAMIS system	Photometric strain measurement system
Tension machine	Instron [98]	8502	Applied displacement voltage reading

3. EXPERIMENTAL SETUP AND MEASUREMENT METHODS

3.2 Test specimen

This work examines the ability of ART to measure the slight change of both longitudinal and shear sound velocities predicted by the theory presented in Ch. 2. A common construction steel has been used for the testing. The geometry of the test specimen has been selected to reduce unwanted acoustic disturbances (e.g. thickness variation and acoustic reflections from edges and/or other geometrical features). The simplest geometry for measuring thickness resonance is that of an infinite plate. However, since the specimen is also to be subjected to a homogeneous uniaxial stress, and the tension machine has limitations with respect to the size of the specimen, a rectangular specimen has been selected with dimensions 600 mm x 50 mm x 7.5 mm (length (L_1) x width (L_2) x thickness (L_3)) in the x_1-, x_2-, x_3-direction respectively as shown in Fig. 3.1. Based on these considerations several bars of a common construction steel "Bright rectangular steel bar S235JRG2C+C" [79] from one production batch was procured. The density ρ of the bars was 8000 kg/m^3 [79], while the dimensions were (L_1 x L_2 x L_3) 4000 mm x 50 mm x 8 mm [79], which has been cut in 600 mm lengths and CNC machined down to a thickness of 7.5 mm with an accuracy of a few hundredths of a mm (more on the accuracy of the dimensions in the Sec. 6.4.1.1). The pre- and post-test test specimen dimensions (length, width, and thickness) was measured with a micrometer screw, a digital caliper and a steel ruler respectively. The specimens were machined on both sides to reduce any initial stresses. It is noted that heat treatment of the test specimens after machining could have removed the stresses. Because of little experience and lack of control with any furnace and heating processes which would have needed to be outsourced, it has been deemed more appropriate to keep control of the geometry of the specimens. The geometry has a direct effect on the measured resonance frequencies, and it is expected that the levels of initial stresses are already low. Using the tentative un-stressed sound velocity estimates given in Table 2.2 and the relation in Eq. (2.120) gives an estimate of the longitudinal and shear harmonic frequencies that can be expected to be measured over the thickness of the test specimen. The four lowest harmonics are presented in Table 3.2.

The coordinate system used in this work has been aligned with the test specimen such that the length-, width-, and thickness-dimensions are in the x_1-, x_2-, and x_3- directions respectively as shown in Fig. 3.1. The specimen dimensions will thus in the
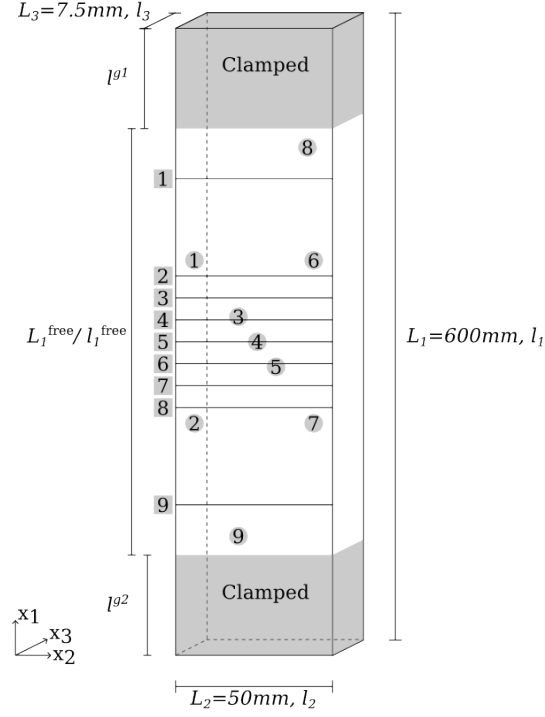
Figure 3.1: **Rectangular specimen including aligned coordinate system and showing measurement location of length (l_1), width (l_2), and thickness (l_3)**

Table 3.2: Tentative typical values for longitudinal and shear resonance frequencies based on steel values in Table 2.2

n_l, n_s	Longitudinal modes $f^{(n_l)}$ (kHz)	Shear modes $f^{(n_s)}$ (kHz)
1	400	220
2	800	440
3	1200	660
4	1600	880

following be referred to by the length in the aligned coordinate system (i.e. $l = l_1$ in the x_1-direction, $w = l_2$ in the x_2-direction, and $d = l_3$ in the x_3-direction).

3. EXPERIMENTAL SETUP AND MEASUREMENT METHODS

The initial geomety of each test specimen is important when comparing the different deformation paths and acoustic resonances. Thus, the dimensions of each test specimen where measured by hand both before and after it was used in a test.

The measurements where taken in approximately the same area for each test specimen and Fig. 3.1 indicates the locations. The numbered circles in Fig. 3.1 show the location of micrometer caliper measurements of the thickness measured both before and after each test run (denoted L_3 and l_3 in App. D, Table D.1). The numbered squares show the location of caliper measurements of the width measured before and after each test (denoted L_2 and l_2 in Table D.1). Finally L_1 and l_1 are the total length of the test specimen measured before and after each test, l_1^{g1} denotes the length of the test specimen that was gripped by the upper wedged clamp, while l_1^{g2} corresponds to the length gripped by the lower clamp. Assuming that l_1^{g1} and l_1^{g2} are not subjected to any lengthwise deformation the free length of the test specimen before and after the test (denoted L_1^{free} and l_1^{free} respectively in Table D.1) can be calculated as the difference between L_1 or l_1 and the sum of l_1^{g1} and l_1^{g2} respectively.

$$L_1^{free} = L_1 - (l_1^{g1} + l_1^{g2}) \qquad l_1^{free} = l_1 - (l_1^{g1} + l_1^{g2}). \tag{3.1}$$

This method to determine the free length has been done because of difficulties in measuring this while the test specimens were clamped fixed in the tension machine. Note that l_1^{free} is the free length of the specimen that may deform during the test. Thus the relationship between the current free length and the initial free length can be calculated according to Eq. (2.123) as

$$l_1^{free} = L_1^{free}(1 + e_1) \tag{3.2}$$

For each test Table D.1 thus include 5 lines where line 1 is the thickness measurements before the test (L_3), and line 2 is the thickness measurements after the test (l_3) were performed. Correspondingly line 3 and 4 are respectively the width measurements before (L_2) and after (l_2) the test. Line 5 consist of four length measurements L_1, l_1, l_1^{g1} and l_1^{g2}, and two calculated lenghts L_1^{free} and l_1^{free} (see Fig. 3.10). In addition the calculated mean, standard deviation and relative standard deviation have been included for the relevant measurements. The first column also include the test specimen number, and whether ART, ARAMIS, and/or strain gauges (denoted sg) measurements have been performed during the test (when no type is specified the test have been done

76

without ART, ARAMIS or strain gauge measurments - i.e. only MessTek recording Instron displacement and force).

3.3   Tension test configuration

The test specimens have been tensioned in an Instron 8502 [98] tension machine with a load capacity of 300 kN in tension. The Instron machine use two sets of wedged clamps with a clamping pressure of 55 MPa and serrated clamping faces to fixate the flat test specimens. An overview of the experimental setup is shown in Fig. 3.2, with close-ups of the watertank with transducer and test specimen and the wedged clamp shown in Fig. 3.3. A schematic of the tension setup including the acoustic measurement system is shown in Fig. 3.6b. A control unit from MessTek [99] were used to control the applied loadhistory during the tests.

To be able to investigate the acoustic behaviour of the steel subjected to a uni-axial tension, a specific sequential load history has been selected to be able to compare acoustic results from many test specimens. The load history should consist of loading and unloading sequences in both the elastic and the plastic deformation range to be able to investigate both regimes. As steel starts to deform plastically the elongation can increase rapidly without a corresponding increase in the applied force. To be able to control the deformation the loading sequences were done with the MessTek control unit in *displacement control* mode, while the unloading sequences to an unstressed state (0 kN) were done under *force control*. The MessTek unit measured continuously both the displacement and force throughout each test.

The Instron tension machine operates with better accuracy during dynamic loading compared to a static loading. This is because the control unit will cause the tension machine to fluctuate around a given set-point and thus create an additional uncertainty to the applied load/displacement reading. On the other hand, during a dynamic loading the uncertainty will be closer to the uncertainty related to the actual measurement reading only. The duration where each of the acoustic measurements interact with the steel will also influence the uncertainty. This duration is approximately 90 μs.

The selected load history comprises three displacement-controlled loading sequences with an approximately displacement velocity of 6 mm/min, and three intermittent load-controlled unloading sequences with an approximately unloading velocity of -500

kN/min. The average displacement history over the 37 specimens tested is shown in Fig. 3.4 plotted against 306 predefined bins spanning approximately 1s each. The reason for grouping measurments in predefined bins are discussed in Sec. 3.4. The average force history is similarly shown in Fig. 3.5. Combining these two plots yields the force-displacement history shown in Fig. 5.3 in Sec. 5.2. The displacement and force history for the 37 individual test specimens have been included in Figs. C.1 and C.2 in App. C.1. The duration of each test was approximately 300 seconds, or 5 minutes.

The first loading sequence is marked in Figs. 3.4 to 3.5 by the start point denoted A and the endpoint denoted B, which for simplicity has been referred to as the load sequence AB. The first unloading was done before the material reached the yielding limit (i.e. before the specimen started to plastically deform) at 1.5 mm displacement and is shown as the unloading sequence BA in Figs. 3.4 to 3.5. The second loading sequence is then denoted AC, while the second unloading is marked CD and was done well into the plastic region at 10 mm displacement. The last load/unloading sequences is thus marked as DE and EF respectively, and deformed the test specimens close to collapse of the material at a total displacement of 20 mm (point E). After the last unloading EF the test specimens was permanently deformed with a plastic deformation of approximately 17.4 mm. The combination of displacement and force measurements are presented in Sec. 5.2.

The output force F from the Instron machine has been callibrated according to the calibration certificate in App. B. However, the displacement output is not callibrated since it is dependent on the relevant test specimen and the response of the wedged clamps. Thus the displacement reading have only been used to control the displacement history and to correlate different measurement quantities as discussed in Sec. 3.4.

Based on the measured force F and the initial dimensions described in Sec. 3.2 the engineering stress S_{11} can be calculated according to Eqs. (2.85) and (2.76) in Sec. 2.3 for a uniaxial load.

$$S_{11} = \frac{l_2 l_3}{L_2 L_3}\sigma_{11} = \frac{a}{A_0}\sigma_{11} = \frac{F}{A_0} \tag{3.3}$$

where $F = \sigma_{11}a$ is the applied force, $A_0 = L_2 L_3$ denotes the original cross section area. L_2 is the width of the test specimen and L_3 is the thickness of the test specimen, both measured in the reference configuration. $a = l_2 l_3$ is the current cross section area, where l_2 is the current width and l_3 is the current thickness. The elongation $e_1^{instron}$ can be calculated according to Eq. (2.73) from the original free length L_1^{free} of the

test specimen (i.e. the length of the test specimen not gripped by the clamping wedges that is free to deform, see Fig. 3.1) and the applied deformation Δx_1 (i.e. recorded displacement of Instron machine corresponding to change in free length of the test specimen) in the x_1-direction as

$$e_1^{Instron} = \frac{\Delta x_1 - 0}{L_1^{free}} \tag{3.4}$$

The results are presented in Sec. 5.2. Note that the elongation calculated based on the displacement recording of the Instron machine have been denoted by the superscript ^{Instron} to ensure that it is not confused with the elongations measured by strain gauges or the ARAMIS system. This distinction is necessary because the recorded displacement of the Instron machine is not calibrated, and depends on the response of the test specimen and the wedged clamps as described in Sec. 3.3. Thus the elongation $e_1^{Instron}$ may deviate from the actual elongation of the test specimens, and has thus not been used for any other purpose than visualising the load history. The elongations measured by strain gauges described in Sec. 3.6.1 are in comparison local estimates over the extent of the strain gauges.

It should be noted that the test specimens have been subjected to destructive plastic deformation and have thus only been used once. In total 41 tests were run on an equal number of individual test specimens. However, because of erroneous mounting of some of the instruments and/or wrong load history applied for 4 test specimens, these have been excluded from result pool, thus reducing the number of tests and test specimens with valid results to 37 .

## 3.4 General measurement considerations

One challenge when combining results from different measurement systems to calculate a final measurement quantity is to ensure that corresponding values are used in the calculations. The different measurement setups sample their respecitve measurands at different frequencies based on physical limitations and practicallity. This results in large differences in the number of measurements over the applied load history. Each test was run with the same pre-programmed load history as described in Sec. 3.3, which ran in approximately 300 s, or 5 min. For the force and displacement recorded by the MessTek control unit and the strain gauge measurements the sampling frequency was set to 10

Figure 3.2: Experimental setup overview. a) acoustic setup, b) tension machine, c) control unit, d) water tank
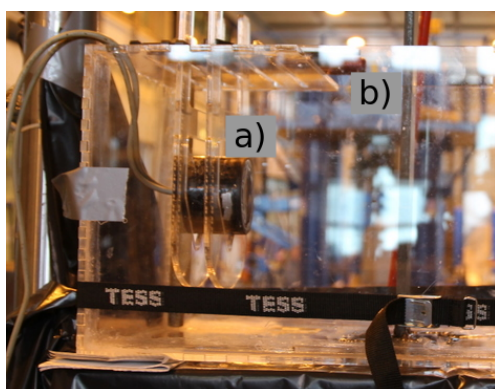
(a) Transducer (a) and test specimen (b) in watertank

(b) Upper clamping wedge
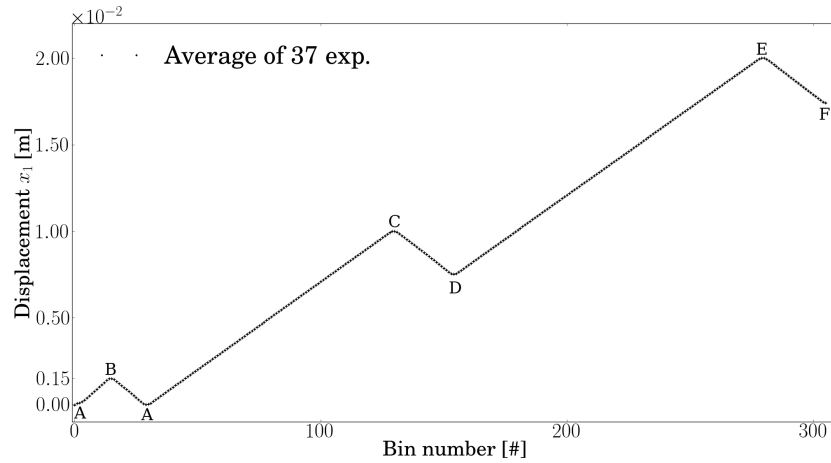
Figure 3.3: Close up of experimental setup

Figure 3.4: Displacement (Δx_1 from the Instron machine) history for the 37 test specimens. 1 bin spans approximately 1s
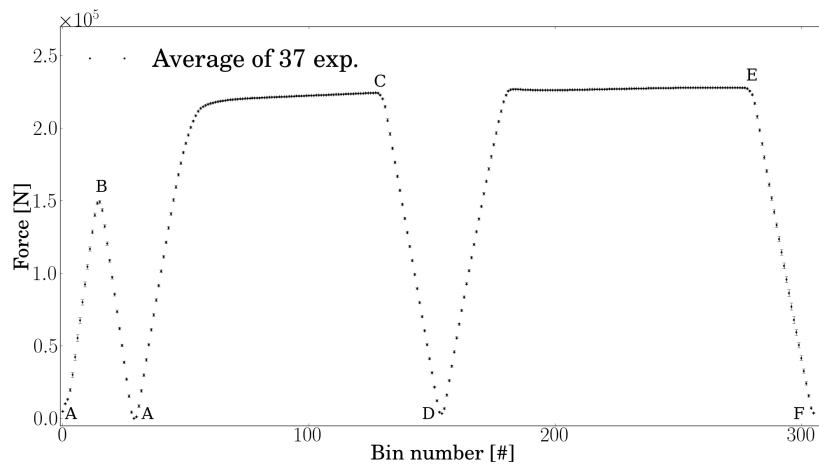

Figure 3.5: Load history (F from the Instron machine) for the 37 test specimens. 1 bin spans approximately 1s

81

Table 3.3: Measurement types and number of measurements per test

Type	Number of measurements/test
Instron displacement	$\sim$ 3000
Instron force	$\sim$ 3000
Strain gauges	$\sim$ 3000
ARAMIS	$\sim$ 300
ART	$\sim$ 12000

Hz, which resulted in just above 3000 measurements over the duration of each test (see Sec. 3.3 and 3.6.1. For the ARAMIS photometric measurement system (Sec. 3.6.2) the amount of computation time needed to process each measurement where significant, and thus it was decided to measure every 1 s. This resulted in just above 300 measurements for each test, or one measurement for every 10 reading of force, displacement or strain gauge.

As this investigation looks into the change in sound velocity at different stress states the acoustic measurements have on the other hand been done as fast as the hardware and experiment setup has allowed to avoid interference between individual measurements during the dynamic loading of the test specimen. To be sure to capture the echo the recording takes 500 μs, and is together with the latency in the data acquisition unit (DAQ) and electronics the limiting factor on how often samples can be recorded. The system was for practical reasons set up to continuously shoot and record 1000 chirp pulses followed by a 1 s delay before the next group of 1000 pulses was recorded, and so onward until the end of the loading sequence. This has yielded approximately 12 000 recordings for each ART test, which corresponds to 4 acoustic measurements per force, displacement, or strain gauge reading, or 40 acoustic measurements per ARAMIS measurement. A summary of the number of measurements for each measurement type is shown in Table 3.3.

Because of the different sampling frequencies, latency between groups of samples, difference in initiation time of the measurement cycles, and the fact that many of the measurements have been performed on different test specimens, it has been important to find a way to combine the different types of measurements with corresponding values of other measurements and other tests. To be able to correlate the different measurements, a common measurand which behave in a predictable and linear fashion is needed. Time is such a linear common measurand. However, the change in time is constant for all

the different stages of the load history, and it has thus not been possible to determine the current load state by time alone. The load history was displacement controlled with a constant displacement velocity for all the loading sequences, while the resulting displacement velocity for the load controlled unloading sequences were also very close to constant. Thus, the displacement measurements changed linearly for the whole load history (see Figs. 3.4 and 3.5, which is based on the underlying data of the 37 tests shown in Figs. C.1 and C.2 in App. C.1). Note that for a small period of time where the loading change from displacement controlled to load controlled, or vice versa, the displacement were constant to the degree of accuracy in the MessTek [99] control unit. This makes the displacement measurement an ideal measurand to be able to correlate different types of measurements. Thus, the displacement voltage has been measured simultaneously for all the measurements, and because of its linear behaviour it has thus been possible to interpolate to get corresponding values for the measurands where the sampling frequencies were different.

Another challenge is the large amount of data per test and how to combine relevant values from these data sets with corresponding data across the number of tests. To ensure that the measurements used in further calculations correspond with resonable reliability each loading/unloading sequence have been divided into a set number of bins which have been used to represent one specific state of deformation. The bins have been arranged across each loading/unloading sequence so that each bin includes an equal number (different for each measurement type) of measure points for the particular measurement. Each measurement type have been sampled at regular time intervals, and the number of bins of the different load sequences have been chosen so that they span approximately 1s, or correspondingly approximately 0.1 mm displacement. The benefit of grouping measurements into predefined bins which are equally spaced throughout each load sequence is that one gets estimated values that correspond with eachother across the different measurement setups. In addition, for measurements with few measurement points across the total number of experiments, this binning can reduce the effect of minor observation uncertainties and produce a representative value within each bin. This reduces the number of evaluated states to a manageble number, however, it also introduces a variation in the measurands because they might be measured at sligtly different states. The uncertainties introduced by this has been further discussed and analysed in Ch. 6.

Table 3.4: Result bins

Sequence		Number of bins [-]	Displacement	
			start [mm]	end [mm]
1. loading	AB	15	0.0	1.5
1. unloading	BA	15	1.5	0.0
2. loading	AC	100	0.0	10.0
2. unloading	CD	25	10.0	7.5
3. loading	DE	125	7.5	20.0
3. unloading	EF	26	20.0	17.4
Total		306		

Because of the regular sampling frequency the mean of the measurements within each bin have been used as an estimated value of the particular measurement in the range of states covered by the bin size. This has then been combined with similar and corresponding mean values of other measurement quantities. All plots presented in this thesis are of this type of binned data if not otherwise stated.

During the elastic loading/unloading each bin corresponds to approxiemetly a span of 8 kN. The loading sequences with the number of bins and approximate start and end displacement limits are summarised in Table 3.4. As an example the 2nd unloading is divided into 25 bins, and starts when the tension machine has displaced the sample 10 mm (see Fig. 3.4 point C, bin #130). It then reduces the applied force to zero as shown in Fig. 3.5 segment CD, bin #130-155 . The displacement is correspondingly reduced to approximately 7.5 mm at point D which is a permanent deformation (Fig. 3.4 point D, bin #155).

3.5   Acoustic measurements

The acoustic measurement configuration was comprised of a custom built piezo composite transducer from PCT [90] where the specimen under investigation is placed approximately 11 cm from the transducer and the system is aligned with an approximate normal angle of incidence. It also included a water tank, a function generator, a data acquisition (DAQ) unit, both transmitting and receiving electronics, and a computer with software to control the function generator and process the recorded acoustic data. A box model is shown together with a schematic of the setup in Fig. 3.6. The instruments used are listed in Table 3.1.

(a) ART box model

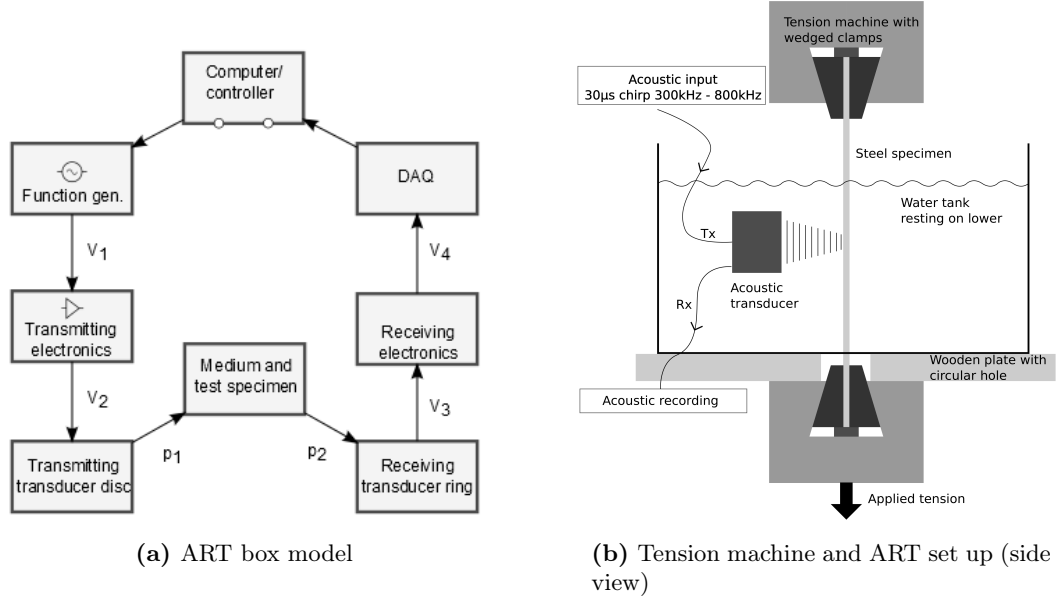(b) Tension machine and ART set up (side view)

Figure 3.6: ART measurement set-up

The transducer was custom built by PCT Ltd [90] and consist of a transmitter (TX) disk with radius a_{TX} of 12.5 mm with a receiver (RX) ring placed outside the TX disk with an outer radius of 50 mm. Both the TX and RX is operable in the frequency band 300-800 kHz [91]. For the frequency f spanning from 300 kHz to 800 kHz this corresponds to ka_{TX} values ranging from 15.7 to 41.9 for the TX respectively, where $k = \omega/c$ is the wave number defined by the angular frequency $\omega = 2\pi f$ and the sound velocity c in the coupling medium water (see Table 2.2 for values used). Assuming an axial response of the TX similar to that of a plane circular piston in a stiff baffle the axial limit of strong interference is assumed to be at the axial distance $r = a_{TX}^2/\lambda - \lambda/4$ [89], which corresponds to the range 3.1 cm to 8.3 cm for the respective frequency range. Thus it is assumed that the specimen placed at ~11 cm has been placed outside the range of strong interference. In-house characterisation of the transducer produced by PCT [90] used in this work has shown that the transmitting piezo composite disk of the transducer has a beam angle ($\theta_{6\text{dB}}$ - the angle from axial direction to where the peak to peak recorded voltage level is reduced by 6dB) varying between 4.6° at 800 kHz, 6.7° at 550 kHz, and 12.7° at 300 kHz [91].

The transducer was aligned perpendicularly to the x_1, x_2 plane such that the axial

direction of the transducer was in the thickness (x_3) direction of the test specimens (normal incidence). Placing the transducer approximately 11 cm from the test specimen will with the specified beam angles result in an acoustic footprint (-6dB) of approximately 2.5 cm at 300 kHz and down to approximately 0.9 cm at 800 kHz on the face of the test specimen.

In this work a 30 μs chirp signal with linear frequency sweep from 300 kHz to 800 kHz has been used to excite transient standing half-wave acoustic harmonics across the thickness of the test specimen under investigation as described in Sec. 2.6.1. From the computer controller the signal generator generates the chirp signal which is passed through the matching electronic circuit and the TX part of the transducer. This excites a propagating acoustic wave which propagates from the transducer to the test specimen, interacts with the testspecimen, and finally propagates back towards the transducer. The interaction with the test specimen is described in Secs. 2.6.1 and 2.6.2. It has been assumed that the water-tank has large enough dimensions that any energy that is not directly reflected from the test specimen back toward the receiving part of the transducer leaves the system and can thus be neglected from further considerations. When the energy of the reflected echo, consisting of a main echo and a transient tail, propagates back toward the transducer, it is received by the ring RX and the receiving electronics. The DAQ hardware and software records the recieved acoustic pressure signal. It is noted that the only signal processing other than what is described in Sec. 3.5.1 is an electronic matching circuit on the transmitter side and a gain circuit on the receiving side (see Table 3.1) [100]. No additional filtering has been used except a lower limit of 300 kHz and an upper limit of 1200 kHz on the FFT. The upper limit is set higher than the upper range of the chirp (800 kHz) to make sure to include one of the resonance frequencies that is predicted at 800 kHz (see Table 3.2).

The propagation velocity in the coupling medium (water) is approximately 1500 m/s, and with a distance between the transducer and the test specimen of 11 cm, the propagation time for the round trip transducer - test specimen is approximately 150 μs. The DAQ records the acoustic pressure measured by the RX ring from the time when the chirp pulse is produced by the TX disk and for ~ 500 μs to be sure that the echo is recorded. The resonance frequencies are then extracted from the transient tail behind the main reflected echo. The tail used in this study has a length twice the

lenght of the original pulse. The applicable interaction time in this setup have thus been approximaetly 90 μs.

As the test specimen is placed close to the finite transducer the generated acoustic signal will impinge the water/steel interface with a distribution of incident angles. If a longitudinal wave impinge with an incident angle on the surface of the layer, vertically polarised shear waves (SV) (named based on their component of particle motion in the same "vertical" direction as the impigning longitudinal wave) can be excited through mode conversion. Horizontally ploarised shear waves (SH) have no coupling to the impigning longitudinal wave and will thus not be excited [69, ch. 9]. It has been assumed that the acoustic field around the acoustic axis of the transducer has a circular symmetry around the normal incidence. Thus SV waves with polarisation directions (in this context the polarisation directions refer to the component of shear wave particle motion in plane of incidence and the "horizontal" direction of the layer surface (see [69, ch. 9] for details)) in all the directions of the surface plane should be excited. Based on this assumption the SV waves excited in the test specimen should have an approximately equal distribution of waves with particle motion in parallell as well as perpendicular to the applied tension. Thus, both longitudinal and shear waves will be excited in the steel layer. Both the shear and longitudinal waves inside the steel layer will in turn excite longitudinal waves propagating away from the steel layer through the water half-spaces. This enables the system to record both longitudinal and shear resonance frequencies within the steel, even though the shear waves will not propagate through water (see Sec. 2.6.2 for details).

The thickness of the test specimen has been selected in such a way that the frequency range of the PCT transducer excites both a shear and a longitudinal harmonic resonance that is easily distinguishable. From Table 3.2 and Fig. 3.9 the 3rd shear harmonic at approximately 660 kHz and the 2nd longitudinal harmonic at approximately 800 kHz is such a pair.

As mentioned in Sec. 3.3, a dynamic displacement velocity of approximately 6 mm/min and an unloading of -500 kN/min have been used for the loading and unloading sequences respectively. Combining this with the interaction time of 90 μs yields a displacement of approximately 9 μm per acoustic shot, or conversely -0.75 N per acoustic shot. This is below the accuracy of the static load control, and also much less than the applied pre-load. Thus it has been assumed that this effect is insignificant for the

overal acoustic behaviour for the purpose of this study. Each acoustic shot will give a result which can be regarded as the mean over the range of the relevant displacement. The uncertainties related to the acoustic shots will be further discussed in Sec. 6.2.

Of the total 37 test specimens, 16 were performed including acoustic measurements. The remaining test specimens were tested with other measurement systems to characterise the geometrical change of the specimens during loading (See Sec. 3.6).

3.5.1 Signal processing

The resonance frequencies are extracted from the acoustic signal by digital signal processing (DSP) techniques that can be found in any textbook on the subject (e.g. [66]). Mainly it entails a routine to cross-correlate the input signal with the recorded echo (shown in Fig. 3.7) [66, ch. 7] to pinpoint the main echo in the reflected signal, thus enabling the extraction of the constructively resonating tail signal as shown in Fig. 3.8. Then a Fast Fourier Transform (FFT)[103] and its corresponding frequency spectrum have been computed by applying a Hanning window [66, ch. 7-12] to the tail of the echo. The sampling frequency F_s of the signal was 15 MHz while the length T of the FFT was 60 μs corresponding to $N = TF_s = 900$ samplepoints, which yields a spectral frequency resolution of the FFT of 16.7 kHz (see [66, ch. 9]) which should be sufficient to distinguish the resonance modes presented in Table 3.2. However, this resolution is not good enough to distinguish the potential separation of shear resonance modes due to the effect of polarised particle motion as explained in Sec. 2.3, Eqs. (2.98) and (2.99). This will be discussed further in Secs. 6.2, 6.3, and 7.6.1.

The signal processing has been performed utilising the Python 2.7 [104] programming language, and more specifically the numerical computational libraries NumPy and SciPy [103]. The peaks of the FFT spectrum corresponding to the resonance frequencies have been found using a peak-detection algorithm and the maximum of a spline interpolation around each peak. The peaks have then been categorised according to whether they fit a longitudinal or shear resonance mode by comparing an estimated tentative harmonic number n_l or n_s from Eq. (2.120) with the resonance frequencies for longitudinal and shear resonance modes based on the tentative data in Table 2.2. A measured peak has been accepted as a resonance peak if the measured resonance frequency was within 5 % of any of the estimated shear resonance frequencies and 10 % of any of the longitudinal resonance frequencies given in Table 3.2. The acceptance criteria for

the longitudinal resonance frequencies has been increased compared to the shear modes because of the shift in resonance frequency caused by the beam effect discussed below and explained in Sec. 2.6.2.

The FFT spectrum of the recorded tail signal of Fig. 3.8 is shown in Fig. 3.9, where the resonance frequencies according to plane wave theory for both longitudinal and shear sound waves (Eq. (2.120) with updated estimates of the sound velocities estimated in Sec. 5.6 and presented in Table 5.5) have been plotted as vertical dotted and dashed lines and denoted L1, L2, S2, S3 for the 1st and 2nd longitudinal, and 2nd and 3rd shear resonance frequencies respectively. The discrepancy between the theoretical and measured resonance frequency of Fig. 3.9 are due to the beam effect explained in Sec. 2.6.2. The resonance peaks in Fig. 3.9 should, according to the beam effect, be dependent on the superposition of a collection of plane waves impigning on the test specimen with an angular distribution dictated by the beam angle of the transducer. Comparing the resonance peaks in the FFT spectrum (Fig. 3.9) and the leaky Lamb modes in Fig. 2.10 it is clear that for a distribution of plane waves with incidence angle less than the -6dB beam angle of $< 13°$ for frequencies around 300 kHz that the combined response of such waves would shift the measured resonance peaks slighly down in frequency as seen in Fig. 3.9. Correspondingly a distribution of plane waves with incidence angles less than the beam angle of $< 7°$ for frequencies around 550 kHz, and $< 5°$ for 800 kHz, suggest that the combined response for both the S2 and L2 mode would be shifted up in the frequency spectrum. From Fig. 2.10 in Sec. 2.6.2 the S3 mode is not affected by the angle of incidence before it is approximately $6°$. Thus it is reasonable to assume that this mode is not as much affected by the beam effect as the other modes presented. The shifts seen in the FFT (Fig. 3.9) corresponds qualitatively well with the above discussed beam effect, and is thus assumed related to the directivity of the transducer. Because the angle between the acoustic axis of the transducer and the face of the test specimen does not change during testing it has been assumed in this work that the observed shift is close to constant throught each individual test.

3.5.2 Temperature

The sound velocities in steel are dependent on the temperature [105]. Thus the temperature in the water tank has been measured before and after the acoustic measurements were performed. The test specimens and water tank weere installed into the tension

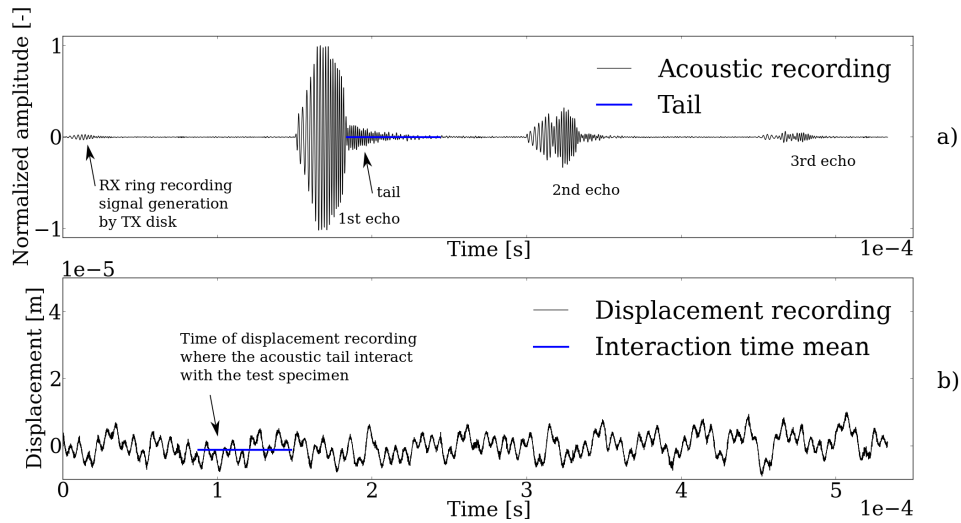**Figure 3.7:** a) Recorded signal showing acoustic echos reflected from the test specimen and b) simultaneously recorded displacement voltage signal from the Instrom machine. Variations in the diplacement voltage relates to random variations / noise in the recorded voltage and not actual displacement.
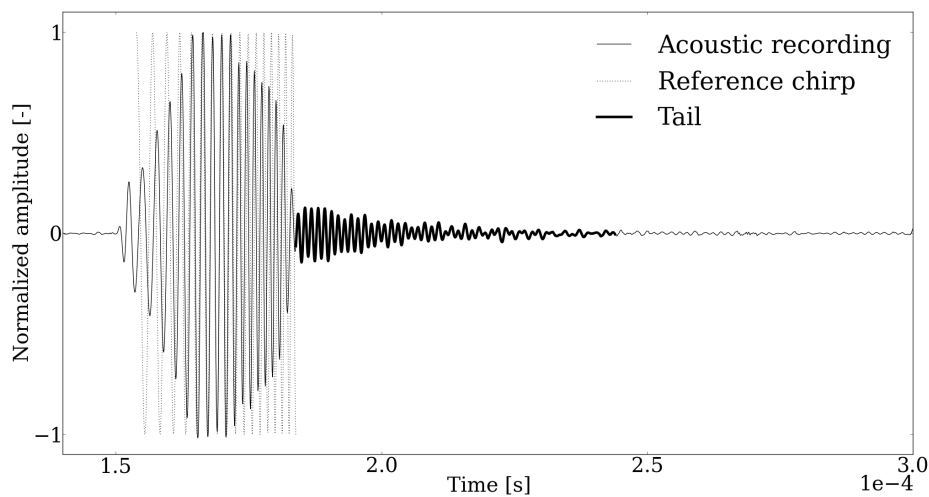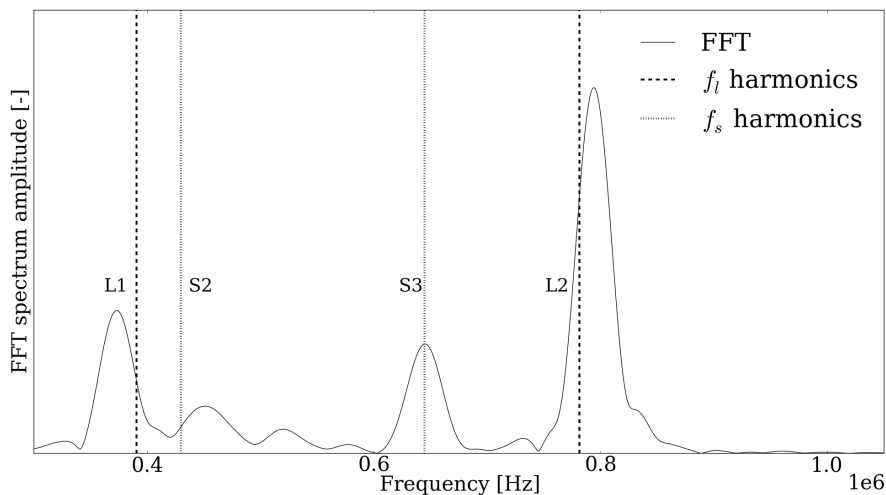

Figure 3.8: Zoomed in on 1st echo in Fig. 3.7 a) with the reference pulse (linear chirp) overlaid and the extracted tail

Figure 3.9: Calculated FFT spectrum of extracted tail with 1st and 2nd longitudinal, and 2nd and 3rd shear resonance frequencies denoted L1, L2, S2, and S3 respectively.

machine before the test specimen was fixed in the bottom clamp and the orifice through the bottom of the water tank was sealed shut. Then the water tank was filled with tap water and the system was set to reach the equilibrium temperature while the rest of the rig was prepared (approximately 10-20 minutes). The temperature of the water was measured just before the tension test was initiated and just after the test finished. The results have been presented in Table 5.4 in Sec. 5.4.

3.6 Geometrical measurement configuration

As the load was applied in the x_1-direction (see Figs. 3.1, 3.6b) the Poisson effect reduces the thickness of the test specimen [13, ch. 1.3]. From Eq. (2.120) it is clear that a negative relative change in thickness will have the same effect on the measured resonance frequencies as a corresponding positive relative change in sound velocity. The contribution owing to thickness change can be removed by comparing the resonance frequencies of different harmonics as described in Sec. 2.7. However, to consolidate the results and to measure the strains which are used as input to the theoretical calculations (see Sec. 2.3 and Ch. 4), two methods have been used to measure the geometrical change of the test specimen during loading. In addition to the effect on the measured frequency,

the theory presented in Sec. 2.3 uses strain in its calculation of the acoustoelastic effect. Thus the strains (or equivalently the elongation for a unaxial test) in the principal directions are needed, both as input to the acoustoelastic theory, and to calculate the true stress, or Cauchy stress σ_{11}, (applied force per actual cross section area).

As mentioned in Sec. 2.4 the measured uniaxial stress and strain from an uniaxial tension test can also be used to estimate both the Young's modulus Y and the Poisson's ratio ν. Y and ν is directly related to the other second order elastic constants as described in Sec. 2.4, Eq. (2.106), and are thus a convenient measure to be able to compare the elastic properties of the current steel with other reported steels found in the literature. The estimate is done under the ideal assumption that all the stress is used to elongate the test specimen in the uniaxial direction. The ideal geometry for such a measurement is that of a long, thin, and straight bar. However, when the bar is not ideally straight some of the initial applied stress will be used to straighten the test specimen. Also, if the fixation points are not ideally aligned it will also introduce a slight shearing in the test specimen. Such deviations from the ideal setup will affect the accuracy of estimates of the elastic properties. For estimates of the Poisson's ratio the thin bar introduce an additional inaccuracy as it is also more difficult to measure the contraction of a thin bar with high accuracy compared to the elongation in the axial direction. This is because it is more difficult to align e.g. strain gauges in parallel with the short transverse directions compared to the long axial direction. The test specimens used in this study have been CNC-machined with a high geometric accuracy as described in Sec. 3.2, and any deviation from a straight sample is less than visually detectable when put on a plane surface (i.e. it is not possible to visually see gaps between the test specimen and the plane surface if it lays flat on top of the surface). The alignment of the test specimen in the tension machine have been done using a vertical leveling instrument, and thus it has been assumed that the initial strain/stress used to "straighten" or "shearing" the sample have been small compared to the overall applied stress/strain level. The measured stress and strain can then with good approximation be used to estimate the linear elastic properties. This has been explained in Sec. 3.6.3.

The principal strains have been monitored throughout the tests using two independent measurement systems. Strain gauges have been bonded directly on to the surface of the test specimens in different locations with different principal orientations, while the ARAMIS system have measured relative displacement (strains) between points in

a spraypainted stochastic pattern on the surface of the x_1-x_2-plane. The ARAMIS sofware have, based on photometric analysis of the development of this stochastic pattern, calculated the principal x_1, x_2, and x_3-strains. The two different methods have been described in Secs. 3.6.1 and 3.6.2 respectively, and the principal strains (or correspondingly principal elongations in the uniaxial setup used in this work) in the x_1-, x_2-, x_3-direction have been named e_1, e_2, e_3 respectively for the strain gauges and e_{major}, e_{minor}, e_z for the ARAMIS measurements to be able to distinguish them. The two methods described above are local measurements giving estimates at some relevant positions on the test specimens. In addtion a global estimate in the axial (x_1-direction) has been based on the uniaxial displacement of the Instron tension machine recorded by the MessTek control unit as described in Sec. 3.3.

3.6.1 Strain gauge

The most common method of geometrical measurements is the strain gauge. This is small strips of electric conductors that were bonded to the test specimen in such a fashion that they follow the local deformation of the specimen (see Eq. (2.73) where L_i is the original length of the strain gauge and l_i is the current length of the strain gauge). When they are elongated or compressed the resistance over the conductor change, which allows measurements of the elongation/compression of the strips. The strain gauges used in this setup were of the type YFLA-2 and YFLA-5 produced by TML - Tokyo Sokki Kenkyujo Co., Ltd., with a strain limit of 15-20 % strain [101]. The strain gauges yields good measurements over the area where they are placed, however because of their limited physical extension (2 mm x 1.8 mm for the YFLA-2 and 5 mm x 2 mm for the YFLA-5 [101]) they can not give a distributed strain field over the test specimen. In addition, small variations in the alignment of the strain gauges also affect the measured strains. They would also have introduced an uncertainty in the acoustic measurements if they were present at a location in which it could influence the acoustic signal. Thus, for the test specimens including acoustic measurements the strain gauges have been placed in the area just below the upper wedged clamp (see Fig. 3.6b), away from the acoustic footprint to mitigate any influence on the acoustic signal. Because of a limited number of strain gauges, not all tests have been run with strain gauges. To get a statistical representation of relevant elongation for those tests run without strain gauges, the placement of the strain gauges have been varied between combinations of

placement and alignment on selected test specimens. Both with and without acoustic measurements (described in Sec. 3.5), and with and without the geometrical ARAMIS measurements (described in Sec. 3.6.2). Note that only a limited number of strain gauges (41) have been available for this work, and the number of strain gauges per test specimen, where they have been included, has been varied between 1 and 6. Strain in the x_1- and x_2-direction, or for the principal directions applied in this work referred to as elongation $e_i, i = 1, 2, 3$, have been measured at either the front or/and the back plane of the specimen, while the x_3-direction has been measured across the thickness on either the left or/and right side of the specimen. In addition some tests have been run without acoustics where the strain has been measured at the center, where the acoustic signal has been focused. The statistical average over all of these measurements (as described in Ch. 5) have been used where applicable. The locations of placements are indicated in Fig. 3.10. The strain gauges indicated at the front and back of the middle of the test specimen have not been included when acoustic measurements have been performed as it is located at the acoustic footprint.

Note also that the elongation measured by strain gauges is denoted by e_i, while the axial elongation estimated based on the applied displacement recorded by the Instron tension machine and MessTek control unit is labeled $e_1^{Instron}$ (Eq. (3.4)).

Of the total 37 tests, 18 were performed including strain gauges.

3.6.2 ARAMIS photometric measurement

To be able to get a more distributed strain measurement, a photometric measurement system called ARAMIS developed by "Gesellschaft für Optische Messtechnik" (GOM) [102],[106],[107] has been used. This system uses two digital cameras to obtain a stereo image of a stochastic pattern sprayed on the test specimen. These stereo images can then be used to calculate displacement and strain fields for the imaged area. According to the system description the accuracy can be as good as 0.01 % strain [107]. A sketch of the ARAMIS measuring system and a strain distribution calculated by the ARAMIS software is shown in Figs. 3.11a and 3.11b (Note that the overlayed image in Fig. 3.11b is not of the test specimens used in this work, but of a similar steel specimen including two u-shaped notches on each short side to create strain consentrations). The 2D strain field measured by ARAMIS on the surface of the specimen can, according to [107], be used to calculate a thickness reduction strain (i.e. e_z), under the assumption
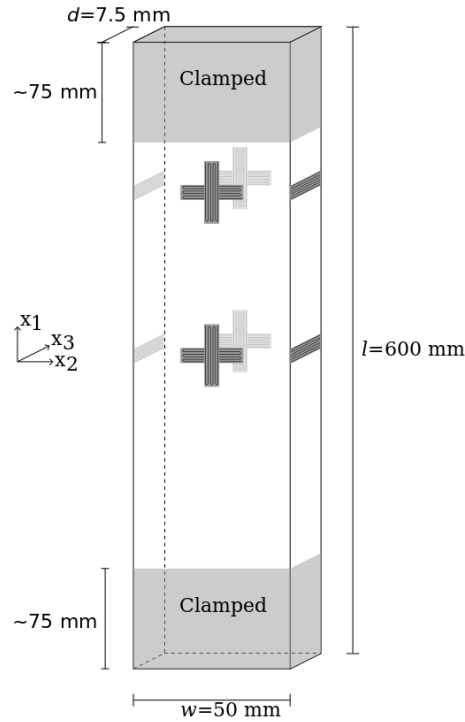
Figure 3.10: Rectangular specimen with illustration of the strain gauge placements used. Different combinations of placements with different number of gauges have been used for different test specimens.

of material volume constancy. The applicability of this statement has not been verified, but the ARAMIS measurement results have been compared with the corresponding strain gauge measurements, and the result of this is discussed further in Sec. 5.3.1. The ARAMIS measurements give results distributed over a region of the specimen, e.g. where the acoustic beam is focused. Unfortunately the ARAMIS system can not be operated through the water tank of the ART setup. Therefore the ARAMIS measurements have been done on a set of separate test specimens to create a distribution of strain measurements throughout the load history. Because of processing time the delay between each photometric measurement was set to 5 s.

Of the total 37 tests, 15 were performed including the ARAMIS measurement sys-

tem.

(a) ARAMIS schematic
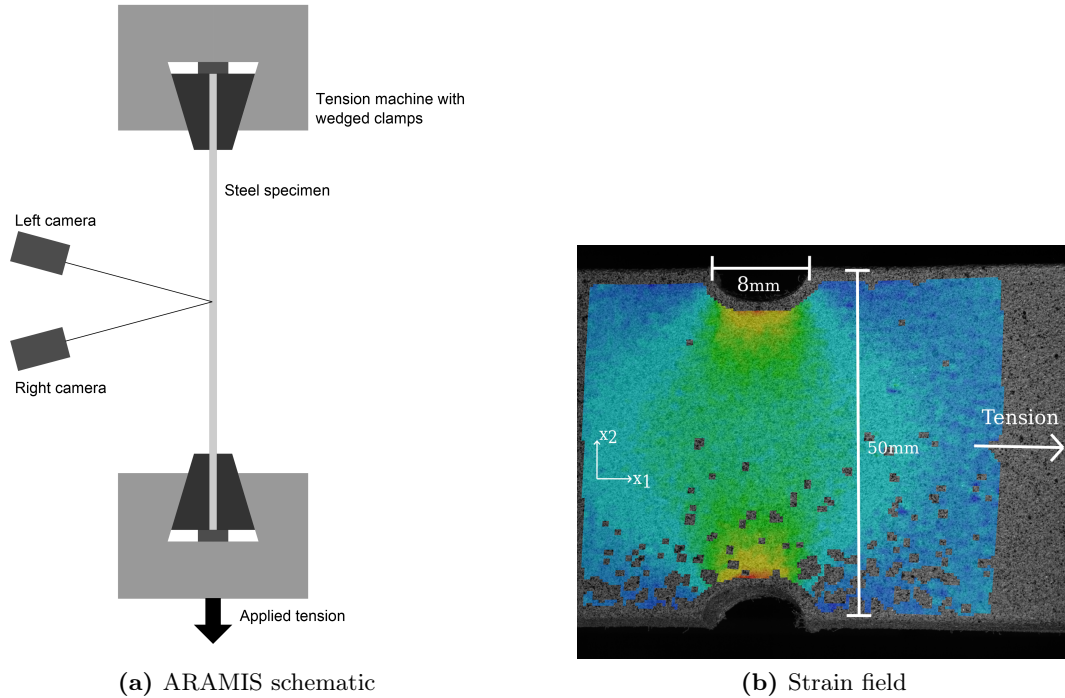
(b) Strain field

Figure 3.11: ARAMIS system with example of stochastic pattern and estimated strain field of a notched test specimen (blue indicate low leveles of strain while red indicate higher levels of strain)

3.6.3 Strain derivatives

The challenge of measuring the geometric deformation simultaneously and at the same location as the acoustic response has been best solved by placing strain gauges across the thickness (i.e. x_3-direction) at the center of the test specimen. As described in Sec. 2.6.2 the width and length of the test specimen is assumed to be so large that no effect of reflections from the edges interferes with the cross thickness resonance modes. Thus it is also assumed that strain gauges placed on the edge at the center of the test specimen measuring across the thickness does not affect the acoustic signal significantly.

3.6.3.1 Sound velocity

Even though the thickness dependency can be removed as described in Sec. 2.7, the measurements can be used to corroborate the results by visualising the relative change

in the actual sound velocities (Eq. (2.121) including d as the reduced thickness in Eq. (2.123)) for comparison with theory, and not just their ratio.

When estimating the absolute magnitude of the sound velocities it is important to evaluate contributions from the beam effect described in Sec. 2.6.2, this shift of the L1 and L2 mode will produce a similar discrepancy in calculated longitudinal sound velocity. We have the relations (from Eq. (2.108)) for a common unstressed steel

$$\frac{c_l}{c_s} \approx 1.83, \tag{3.5}$$

which together with Eq. (2.121) leads to the relation

$$\frac{c_l}{c_s} = \frac{n_s}{n_l} \frac{f_{0,th}^{(n_l)}}{f_{0,th}^{(n_s)}} \approx 1.83. \tag{3.6}$$

Now, looking at the stressed longitudinal velocity based on plane wave theory we get through Eqs. (2.121) and (2.123)

$$
\begin{aligned}
c_l &= \frac{2l_3}{n_l} f_{th}^{(n_l)} = \frac{2L_3(1+e_3)}{n_l} f_{th}^{(n_l)} = \frac{2L_3(1+e_3)}{n_l} \frac{f_{th}^{(n_l)}}{f^{(n_l)}} f^{(n_l)} \\
&= \frac{2L_3(1+e_3)}{n_l} \eta^{(n_l)} f^{(n_l)},
\end{aligned}
\tag{3.7}
$$

where l_3 and L_3 is the current and initial thickness (d) respectively, subscript $_{th}$ denotes plane wave theory, and $f_l^{(n_l)}$ is the measured n_l resonance frequency mode. Correspondingly the same relation can be developed for the plane wave theory shear wave velocity and the measured n_s resonance frequency modes as

$$c_s = \frac{2l_3}{n_s} f_{th}^{(n_s)} = \frac{2L_3(1+e_3)}{n_s} \eta^{(n_s)} f^{(n_s)}. \tag{3.8}$$

In the above two equations

$$\eta^{(n_l)} \equiv \frac{f_{th}^{(n_l)}}{f^{(n_l)}} \qquad \text{and} \qquad \eta^{(n_s)} \equiv \frac{f_{th}^{(n_s)}}{f^{(n_s)}} \tag{3.9}$$

has been introduced as a correction factor of the beam diffraction effect for the longitudinal n_l and n_s-modes.

To correct for the beam diffraction effect the unstressed longitudinal frequencies have been estimated based on the relation between the measured unstressed longitudinal and shear sound velocities of Eq. (3.6) and the assumption that the S3 mode ($n_s = 3$) does

not experience any shift for the relevant incident angles. This latter assumption has been based on the relative constant location of the S3 mode at ~ 660 kHz observed for a beam angle $< 6°$ in Fig. 2.10 which then yields the relation

$$\eta^{(n_s=3)} \equiv \frac{f_{th}^{(n_s=3)}}{f^{(n_s=3)}} \approx \frac{f_{0,th}^{(n_s=3)}}{f_0^{(n_s=3)}} \approx 1. \tag{3.10}$$

Thus the correction factor for the n_l-modes become

$$\eta^{(n_l)} \equiv \frac{f_{th}^{(n_l)}}{f^{(n_l)}} \approx \frac{f_{0,th}^{(n_l)}}{f_0^{(n_l)}} = \frac{1.83 n_l}{3} \frac{f_{0,th}^{(n_s=3)}}{f_0^{(n_l)}}$$

$$\approx \frac{1.83 n_l}{3} \frac{f_0^{(n_s=3)}}{f_0^{(n_l)}}, \tag{3.11}$$

where $f_{s0}^{(n_s=3)}$ is the measured unstressed S3 ($n_s = 3$) resonance mode, while $f_{l0}^{(n_l)}$ is the measured unstressed n_l resonance mode. It is noted that the same methodology and equations can be used to establish an estimate of the correction factor for shear resonance modes as well by substituting the subscript $_l$ with $_s$ denoting longitudinal and shear waves respectively.

Assuming also that the beam diffraction effect is constant throughout each test (argued in Sec. 3.5.1) this leads to the plane wave theory frequency used when estimating the magnitude and development of the longitudinal sound velocity based on both the L1 and L2 resonance mode as

$$f_{0,th}^{(n_l)} \approx \eta^{(n_l)} f_0^{(n_l)}, \tag{3.12}$$

and the S3 resonance mode as

$$f_{0,th}^{(n_s=3)} \approx f_0^{(n_s=3)}. \tag{3.13}$$

Note that this adjustment has only been used when estimating the absolute longitudinal sound velocities based on the measured frequencies of the L1, L2, and S3 resonance modes presented in Fig. 5.17. For all other measurements this correction is either not relevant, or it cancels out as is the case for relative measurements.

3.6.3.2 Stress

When presenting results involving stress it has been decided to use the Cauchy stress σ_{11} instead of the nominal stress S_{11}. The two stresses are related through the deformation

as seen in Eqs. (2.76) and (2.85). The reason for this selection is based on Cauchy stress giving a more intuitive representation of the relation between the applied deformation and the needed force / current cross section area to achive this deformation.

Stress is generally a second order tensor field. However, in this work an uniaxial load has been applied and the stress can thus be described by a stress tensor ($\boldsymbol{\sigma}$) with the only non-zero component aligned with the direction of the applied force (in this case the x_1-direction), i.e. $\sigma_{11} = F/a$ where F is the applied force and $a = l_2 l_3$ is the current cross section area of the test specimen. All the other stress components is assumed to be zero, i.e. $\sigma_{ij} = 0$ for $i, j = 1, 2, 3$ where $i = j \neq 1$. When the term stress is used in the following, this non-zero component in the x_1-direction is implied if not otherwise stated.

To calculate the change in cross sectional area two approaches have been used. The straight forward approach is where both elongation in the x_2- and the x_3-direction (e_2 and e_3 respectively) are available for a given test specimen. The Cauchy stress can then be found by (Eqs. (2.76) and (2.85))

$$\sigma_{11} = J^{-1}\lambda_1 S_{11} = \frac{S_{11}A_0}{a} = \frac{F}{l_2 l_3} = \frac{F}{L_2(1 + e_2)L_3(1 + e_3)}, \qquad (3.14)$$

where $F = S_{11}A_0$ is the applied force, $a = l_2 l_3$ denotes the current cross sectional area, l_2 is the current width (w) of the test specimen, and l_3 is the current thickness (d) of the test specimen, and $A_0 = L_2 L_3$ is the initial unstressed cross section. The relation between the initial and current width or thickness is given by the same equation as used for the reduced thickness in Eq. (2.123). The subscript 0 signifies a measurement at the initial unstressed state, and e_2 is the measured elongation in the width- (x_2-) direction and e_3 is the measured elongation in the thickness- (x_3-) direction. If, however, only one of the e_2 or e_3 is available, the cross section area can be calculated under the asumption that for an isotropic solid an elongation in the x_1-direction will induce a relative contraction equal in both the x_2- and x_3-direction (see the Poisson's effect in Eq. (2.105)). Thus the current cross section area can be found by applying Eq. (2.85) as

$$\sigma_{11} = \frac{F}{a} = \frac{F}{l_2 l_3} = \frac{F}{L_2 L_3(1 + e_2)^2} = \frac{F}{L_2 L_3(1 + e_3)^2}. \qquad (3.15)$$

These two methods will give slightly different values for the estimated σ_{11} based on the difference in the measured e_2 and e_3. To evaluate how large this difference is the

relative difference has been calculated as

$$\frac{\sigma_{11}(e_2)}{\sigma_{11}(e_2, e_3)} - 1, \qquad \text{or} \qquad \frac{\sigma_{11}(e_3)}{\sigma_{11}(e_2, e_3)} - 1. \tag{3.16}$$

The results have been discussed in Sec. 5.3.

3.6.3.3 Linear elastic moduli

The linear elastic properties Young's modulus Y and Poisson's ratio ν can also be estimated based on stress-strain measurements as described in Sec. 2.4.1. Young's modulus Y can be estimated from Eq. (2.104) as the gradient of the Lagrangian stress-strain relation in the x_1-direction for the linear elastic region. The Poisson's ratio ν can be estimated from Eq. (2.105) as the negative ratio between the measured elastic elongation in the x_2- or x_3-direction and in the x_1-direction for the linear elastic region as

$$\nu = -\frac{e_2^e}{e_1^e} = -\frac{e_3^e}{e_1^e} \tag{3.17}$$

As the Young's modulus is defined through the Lagrangian nominal stress S_{ij} relative to the initial, unstressed, cross section area (see Sec. 2.1.2). The Youngs's modulus after plastic deformation should thus be estimated with respect to the Lagrangian nominal stress relative to the current, plastically deformed, unstressed cross section area (see Sec. 2.5). Thus the Young's modulus has been calculated through the relation (Eqs. (2.104) and (3.14))

$$Y \equiv \frac{S_{11}}{e_1^e} = \frac{F/A_0}{e_1^e} \tag{3.18}$$

which yields

$$Y(e_1^p > 0) = \frac{F/a^p}{e_1^e} = \frac{S_{11} A_0}{e_1^e a^p} = \frac{S_{11}}{e_1^e} \frac{1}{(1 + e_2^p)(1 + e_3^p)}, \tag{3.19}$$

where e_i^e is the elastic part of the total strains ($i = 1, 2, 3$, see Eq. (2.109)), e_i^p is the plastic part of the total strain (see Eq. (2.110)), and $a^p = A_0(1 + e_2^p)(1 + e_3^p)$ is the plastic part of the total deformed cross section area $a = A_0(1 + e_2)(1 + e_3)$ (i.e. corresponding to the unstressed cross section area after the test specimen has experienced plastic deformation, $a(e_2^e = 0, e_3^e = 0, e_2^p, e_3^p)$). The equivalent expression using the Cauchy stress is

$$Y = \frac{\sigma_{11}}{e_1^e} \frac{a}{a^p} = \frac{\sigma_{11}}{e_1^e} \frac{(1 + e_2)(1 + e_3)}{(1 + e_2^p)(1 + e_3^p)}. \tag{3.20}$$

The former of the equivalent expressions (Eq. (3.19)) is recognised as the slope of the measured nominal stress - elongation curve in the elastic loading and unloading regions. The average Young's modulus and Poisson's ratios in these linear elastic regions can thus be estimated based on the slope of linear regression of the stress-elongation relation, and Eq. (3.19) has thus been used in this work. The resulting estimates have been presented in Sec. 5.3.1.

3. EXPERIMENTAL SETUP AND MEASUREMENT METHODS

4

Numerical simulation set-up

This work investigates the applicability of ART used as a method of NDT to measure and monitor the stress/strain state of offshore pipelines. As a variety of steel types is used in the offhsore industry this work has limitited its scope to investigate the measurement capability of the ART equipment/method, and has not tried to establish the third order elastic moduli of any steel types used in the industry. However, to be able to compare the measured acoustoelastic effect with the current development of theory, third order elastic constants for different types of steel found in the literature [44][39][46] have been used to calculate the theoretical sound velocity change predicted by the theory presented in Sec. 2.3. A list of these steels have been collected in Table 4.1. Although this is not ideal because of the lack of knowledge of third order elastic moduli for the specific steel used in this work, it should give a good idea of the variability of the acoustoelastic effect in different but common types of steel. The elastic moduli for 5 different types of steel is presented in [44] and is reproduced in Table 4.2. One type of steel is presented in [39] while [46] present the moduli of two different samples of the same type of steel, all of which are reproduced in Table 4.3. These values are reported using the notation of Tupin and Bernstein [18] and Murnaghan [83] respectively. To be able to use them in the formalism adopted in this work the conversion between the different notations of Table 2.1 have been used and the resulting constants in the Landau and Lifshitz [37] notation is presented in Table 4.4. To be able to easily compare the second-order elastic constants (Lamé parameters) of the different steel types with easily obtained experimental values, the conversion to Young's modulus and Poisson's ratio using Eq. (2.106) is presented in Table 4.5. Note that [44][39][46] have not reported

the confidence level of their reported uncertainties, thus this work has treated it as a standard uncertainty with a confidence level of approximately 68.3 % [74].

The sound velocities presented in Eqs. (2.97) to (2.99) from the acousto-elastic theory in Sec. 2.3 have been implemented using the programming language Python 2.7 [104] and the numerical computational libraries NumPy and SciPy [103]. The sound velocities have then been simulated using all of the second- and third-order elastic moduli presented in Table 4.4 together with the measured uniaxial elastic elongation from strain gauges as input. The results of these simulations have been presented in Sec. 5.7.

Table 4.1: List of steels with determined third-order elastic moduli found in literature

Material	Composition [%]	Density ρ [kg/m^3]	Source
Hecla 37 (0.4 % C)	C, 0.4; Si, 0.3; Mn, 0.8	7823	[44]
Hecla 37 (0.6 % C)	C, 0.6; Si, 0.2; Mn, 0.8	7825	[44]
Hecla 138A	C, 0.4; Cr, 0.6; Mo, 0.5; Ni, 2.5	7843	[44]
Rex 535 Ni steel	Not known	7065	[44]
Hecla ATV austenitic	Ni, 36; Cr, 10; Mn, 1	8065	[44]
Nickle-steel S/NTB	Not known	Not known*	[39]
Rail steel	C, 0.67-0.80; Si, 0.10-0.25; Mn, 0.70-1.00; P, <0.04; S, <0.05	7800 ± 23	[46]
Compared with steel used in this PhD			
S235JRG2C+C	C, <0.17; Si, 0.15-0.30; Mn, <1.40; P, <0.045; S, 0.020-0.045	8000	[79]

*Where the density is not known a value of 7850 has been used in the numerical simulations where applicable

Table 4.2: Lamé and Toupin and Bernstein constants in GPa

Material	Lamé constants		Toupin and Bernstein constants		
	λ	μ	ν_1	ν_2	ν_3
Hecla 37 (0.4 % C)	111 ± 1	82.1 ± 0.5	-358 ± 70	-282 ± 30	-177 ± 8
Hecla 37 (0.6 % C)	110.5 ± 1	82.0 ± 0.5	-134 ± 20	-261 ± 20	-167 ± 6
Hecla 138A	109 ± 1	81.9 ± 0.5	-323 ± 50	-265 ± 30	-177 ± 10
Rex 535 Ni steel	109 ± 1	81.8 ± 0.5	-175 ± 50	-240 ± 50	-169 ± 15
Hecla ATV austenitic	87 ± 2	71.6 ± 3	34 ± 20	-552 ± 80	-100 ± 10

Reproduced from [44]

Table 4.3: Lamé and Murnaghan constants in GPa

Material	Lamé constants		Murnaghan constants		
	λ	μ	l	m	n
Nickle-steel S/NVT	109.0 ± 1	81.7 ± 0.2	-56 ± 20	-671 ± 6	-785 ± 7
Rail steel sample 1	115.8 ± 2.3 %	79.9 ± 2.3 %	-248 ± 2.8 %	-623 ± 4.1 %	-714 ± 2.7 %
Rail steel sample 4	110.7 ± 2.3 %	82.4 ± 2.3 %	-302 ± 2.8 %	-616 ± 4.1 %	-724 ± 2.7 %

Reproduced from [39][46]

Table 4.4: Lamé and Landau and Lifshitz constants in GPa for the constants of Tables 4.2 and 4.3 using the conversion in Table 2.1

Material	Lamé constants		Landau & Lifshitz constants		
	λ	μ	A	B	C
Hecla 37 (0.4 % C)	111 ± 1	82.1 ± 0.5	-44.3 ± 2.0	-282 ± 30	-179 ± 35
Hecla 37 (0.6 % C)	110.5 ± 1	82.0 ± 0.5	-41.8 ± 1.5	-261 ± 20	-67.0 ± 10
Hecla 138A	109 ± 1	81.9 ± 0.5	-44.3 ± 2.5	-265 ± 30	-162 ± 25
Rex 535 Ni steel	109 ± 1	81.8 ± 0.5	-42.3 ± 3.8	-240 ± 50	-87.5 ± 25
Hecla ATV austenitic	87 ± 2	71.6 ± 3	-25.0 ± 2.5	-552 ± 80	17.0 ± 10
Nickle-steel S/NVT	109.0 ± 1	81.7 ± 0.2	-785 ± 7.0	-279 ± 6.9	-223 ± 21
Rail steel sample 1	115.8 ± 2.6	79.9 ± 1.8	-714 ± 19	-266 ± 27	18.0 ± 28
Rail steel sample 4	110.7 ± 2.5	82.4 ± 1.9	-724 ± 20	-254 ± 27	48.0 ± 28

Table 4.5: Lamé parameters converted to Young's modulus and Poisson's ratio

Material	Young's modulus [GPa] Y	Poisson's ratio [-] ν
Hecla 37 (0.4 % C)	211.4 ± 1.1	0.287 ± 0.001
Hecla 37 (0.6 % C)	211.1 ± 1.1	0.287 ± 0.001
Hecla 138A	210.5 ± 1.1	0.285 ± 0.001
Rex 535 Ni steel	210.3 ± 1.1	0.286 ± 0.001
Hecla ATV austenitic	182.5 ± 6.9	0.274 ± 0.006
Nickle-steel S/NVT	210.1 ± 4.7	0.286 ± 0.003
Rail steel sample 1	207.1 ± 4.3	0.296 ± 0.004
Rail steel sample 4	212.1 ± 4.4	0.287 ± 0.004

5

Experimental and theoretical results

In this chapter the results from the tensional deformation history of 37 individual test specimens have been presented. The pool of results from the 37 tension tests are comprised of 16 tests where ART measurements was included (Sec. 3.5), 18 tests including strain gauges (Sec. 3.6.1), and 15 tests including the ARAMIS measurement system (Sec. 3.6.2), where the former measures the resonance frequency across the specimen thickness as described in Sec. 3.5, while the latter two are tests to measure the geometrical change as described in Sec. 3.6. Strain gauges have been used on a selected set of test specimens both alone and toghether with ART or ARAMIS measurements. In addition both the displacement and force of the Instron tension machine has been recorded for all the test by the MessTek control unit.

Note that for some of the experiments some of the measured data may be missing, or has been deemed to be obviously erroneous. In these cases the missing/erroneous measurements have been removed from the result pool. Although some of the data might be missing/erroneous, the data that was deemed useful has been included in the result pool. E.g. if a strain gauge was not correctly fitted to the test specimen, giving obviously erroneous measurements, this data set was removed from the result pool. However, independent measurements (e.g. acoustic measurements or other strain gauges) from the same test have been included. A short overview of the excluded data has been presented in Table 5.1

5. EXPERIMENTAL AND THEORETICAL RESULTS

Table 5.1: Measurements removed from the result pool

Test number	Setup	Measurement	Reason
1	Tension	All except initial geometry	Wrong load history
4, 6, 8, 9	Tension	Strain e_1,e_3	The strain gauge in x_1- and x_3-direction did not produce any ouput (zero-readings).
16, 26, 27, 28, 29, 30	ARAMIS	Strain	Bad accuracy in ARAMIS data.
14, 17	ARAMIS	e_{minor} strain	Inability of developed algorithm to devide the measurement into the appropriate elastic and plastic loading sequences.
23	ART	Acoustics	Missing corresponding displacement reading. Not possible to associate the resonance frequency with applied stress or strain.
31, 36	ART	Acoustics	Large jumps in both acoustic resonance and corresponding displacement. Might be an effect of the processing routine.
34, 39	ART	Upper strain region	The samples experienced significantly more plastic deformation close to the upper clamp at the end of the load history.

When the test specimens were clamped into the tension machine small variations in the initial position and tension force may have been introduced (in the order of 1 mm and 5 kN respectively). To align the measurements to better be able to compare them the position measurement (either displacement or measured strain) has been transposed to correct the measurement offset so that the endpoint of the first unloading was at zero displacement/strain where the applied unloaded force was zero (point A after the specimen have deformed along ABA in Figs. 3.4, 3.5 or 5.2). This has been justified by the fact that the first loading sequence was elastic (displacement $\lessapprox$ 1.5 mm, see Table 3.4 and Figs. 3.4 and 3.5) and does not induce plastic deformation. The target setpoint for the first unloading was at zero applied force, thus returning the specimen to its unstressed state. The same argument can be made for those measurement types where the measurement value has been expected to be zero when the first unloading has brought the specimen to a state of zero applied force. This is relevant for the measured

force, and thus the stress, and any relative change measurements (i.e. measurements on the form $\Delta x / x_0$, where $\Delta x = x - x_0$ is the difference of the current measurement x and the reference measurement x_0 at the zero force state). For any absolute measurements (e.g measurement of the resonance frequencies) the actual measurement values have been used without any alignment of the first unloaded zero force state.

Finally, all plotted result data in this work has been presented with the experimental standard uncertainty (grey error bars - describing a variation of the spread in outcome of any given measurement series) and/or the experimental standard uncertainty of the mean (black error bars - describing a variation in spread of the estimated mean of several measurement series) as described in Ch. 6, if not otherwise stated. The confidence level of the standard uncertainties used throughout this work is approximately 68.3 %, corresponding to $\pm$ one standard deviation of a standard normal distribution [74]. The resulting combined standard uncertainties have been presented in Ch. 6 and discussed in Ch. 7.

Only the main results have been included in this chapter, intermediate and supporting results have been included in App. C.

5.1   Test specimen

The initial dimensions of each test specimen where measured by hand before it was used in the tension machine as described in Sec. 3.2. The dimensions where also measured after the tension test and the results have been presented in Table D.1 in App. D.1.

The variation in dimensions between the test specimens both before and after the tension test can help indicate how much of the uncertainty in the desired result quantities can be ascribed to variations in the actual test specimen geometry. This has been discussed in Sec. 6.4.1.1.

5.2   Engineering stress and displacement elongation

The basis for the experiment results has been the loading and displacement pattern of each individual test. It has been important that the load history and displacement pattern are equivalent across the test specimens to ensure comparable results. Fig. 5.1 shows force versus displacement development for 37 test specimens where each measurement set (from individual test specimens) has been divided into 306 bins as explained in

Sec. 3.4. Thus each of the 37 series in Fig. 5.1 consist of 306 points with representative bin values, representing one individual test specimen. In Fig. 5.2 each of the binned values from the 37 tests have been combined across the 37 tests and averaged to give a representative value over all the experiments for the load state of the relevant bin. Note that this way of presenting results for individual experiments and average values over several experiments, respectively, have been used throughout this work. Note also that the flat part of the displacement force curve (between the yield point (somewhat above point B) and point C, and between point C and E) corresponds to where the test specimen deforms plastically. Fig. 5.2 is the combination of the individual displacement and force histories shown in Figs. 3.4 and 3.5. Fig. 3.5 shows that for a constant applied displacement velocity (corresponding to the linear increase in displacemen seen in Fig. 3.4), the force needed to achieve the target displacement stops following the initial linear relation (corresponding to the linear stress-strain relation of the generalised Hooke's law). These parts of the load history are thus recognised as regions of plastic deformation.

Using the estimated free length L_1^{free} the calculation of the elongation $e_1^{Instron}$ and engineering stress S_{11} can be done as described in Sec. 3.3. Fig. 5.3 shows S_{11} versus $e_1^{Instron}$.

The legend in Fig. 5.1 signifies that the plot includes results from 37 experiments (exp. for short) performed on individual test specimens. This short form has been used in some plots to avoid cluttered legends and it denotes the number of experiments / test specimens the presented plot is based on. A plot of the 37 individual tests which Fig. 5.3 is based on is shown in App. C.1, Fig. C.3.

5.3 Strain, stress and plastic deformation

The acoustoelastic theory presented in Sec. 2.3 has been derived with respect to elastic strain and stress. Measurements of these quantities have thus been required to be able to compare the measured sound velocity change with equivalent estimates based on the theory presented in Sec. 2.3. The results of strain, or elongation, and stress measurements described in Sec. 3.6 have been presented in this section, together with the extraction of both the elastic and plastic contributions (see Sec. 2.5.1). The three
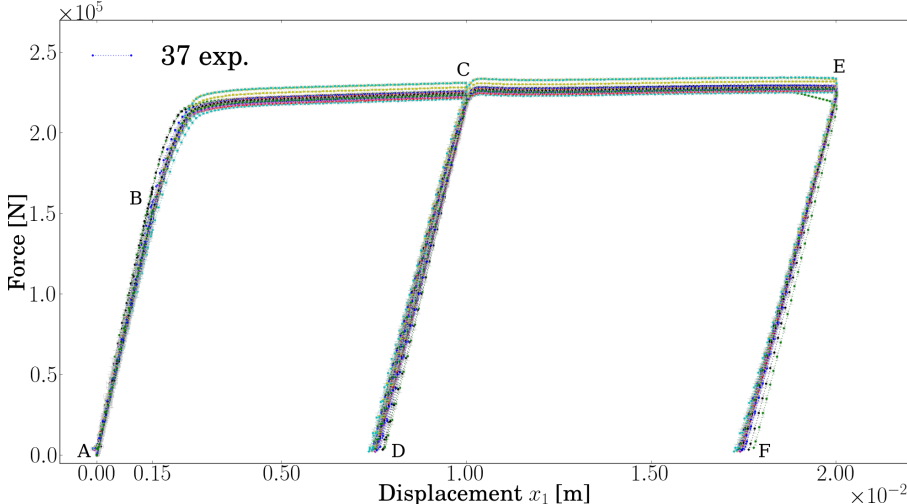
Figure 5.1: Displacement x_1 and force recordings in 306 predefined bins for the 37 test specimens
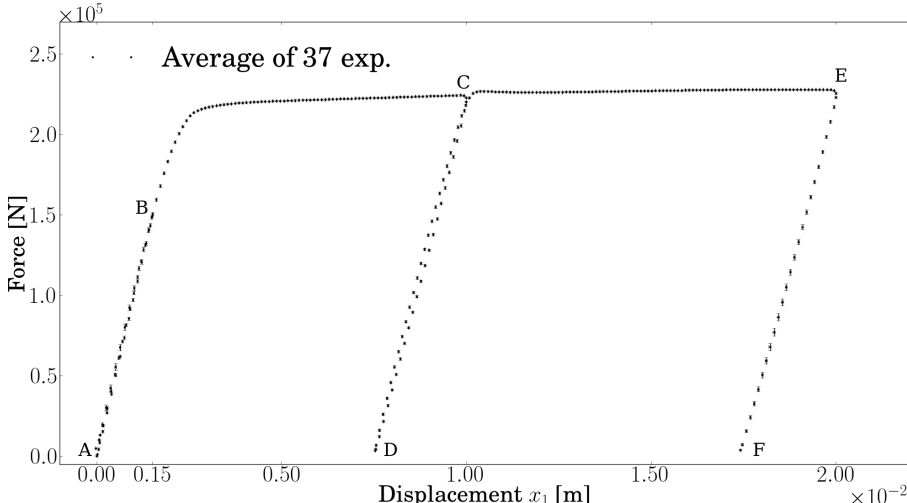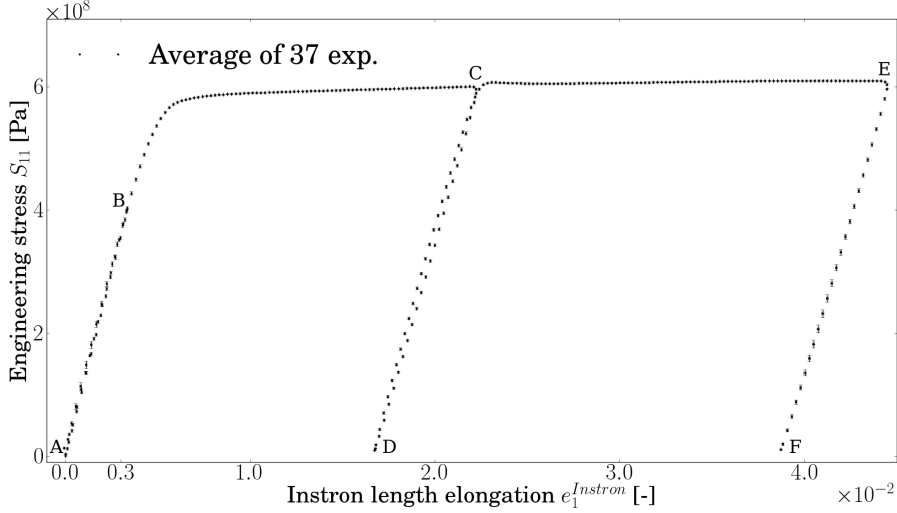

Figure 5.2: Average of x_1 displacement and force over 37 test specimens

Figure 5.3: Average of engineering stress S_{11} and elongation $e_1^{Instron}$ based on the recorded Instron displacement x_1 over 37 test specimens

principal elongations e_i for the uniaxial deformation used in this work have all been plotted against the estimated Cauchy stress (σ_{11}) as described in Sec. 3.6.3, Eqs. (3.14) or (3.15). Note in the following that from the 41 only 27 have been included in the result pool presented here. The reason for the significant number of strain gauges measurements not included is described in Table 5.1 under "Test number" 4, 6, 8, 9, 34, and 39.

Elongation in the x_1-direction (e_1) is important as the main input to the theory of calculating the sound velocity change in this uniaxial tension setup. The average measured values presented in Fig. 5.4 are based on 7 strain gauges placed on 6 test specimens. The 7 strain gauges have been placed at one or two of the different locations described in Sec. 3.6.1, Fig. 3.10, for each of the 6 test specimens. Note the increase in uncertainty of the measured elongation e_1 between the different loading/unloading sequences AB, CD, and EF, i.e. as the test specimen deforms plastically. Fig. 5.4 is the average over the 7 individual strain gauge measurements presented in App. C.2.1, Fig. C.4. Looking at the individual measurements it is evident that the increase in uncertainty is not related to increasing uncertainty within each measurement series, but rather differences in how the strain gauges and/or the test specimens respond to the applied displacement. These variations have been discussed further in Sec. 6.4.1.2,

and are also evident for the e_2 and e_3 measurements presented below.
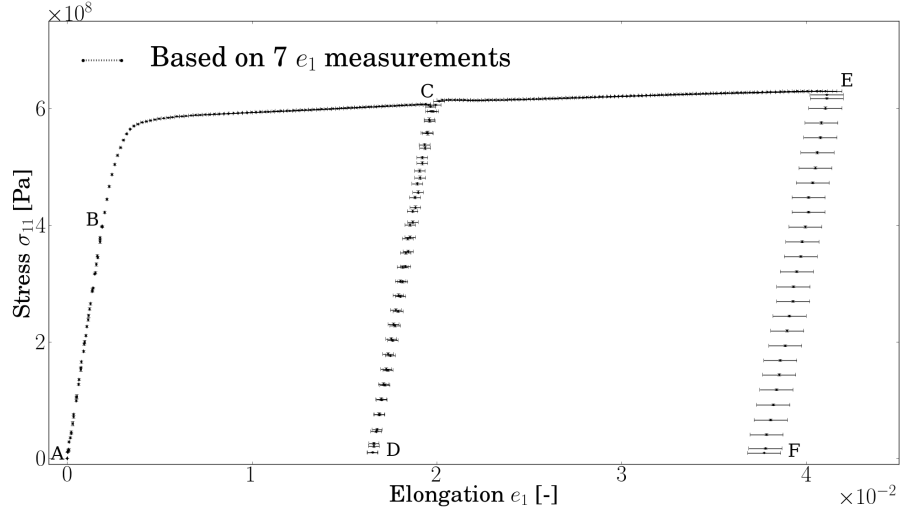
Figure 5.4: Average of e_1 elongation over 7 strain gauges on 6 test specimens plotted against σ_{11}

The e_2 elongation in the x_2-direction is not used directly in calculating the change in sound velocity, but it can be used to measure the change in cross section area of the test specimens, and thus be a part of the estimation of true stress (see Eqs. (3.14) and (3.15)). The average measured values of e_2 presented in Fig. 5.5 are based on 3 strain gauges placed at one or two of the different locations described in Sec. 3.6.1, Fig. 3.10, on 2 test specimens.

Elongation in the x_3-direction (e_3) is directly relevant when calculating the sound velocity change based on cross-thickness resonance frequencies as can be seen from Eqs. (2.121) and (2.123) where the thickness d is a function of the e_3 elongation. In addition it is also used to calculate the change in the cross section, and thus also relevant for the calculation of the true stress. The average measured values presented in Fig. 5.6 are based on 16 strain gauges placed both in the center, at the top, and on the left and right side of 13 test specimens.

The results of the individual strain gauges have been included in Figs. C.4 to C.6 in App. C.2.1.

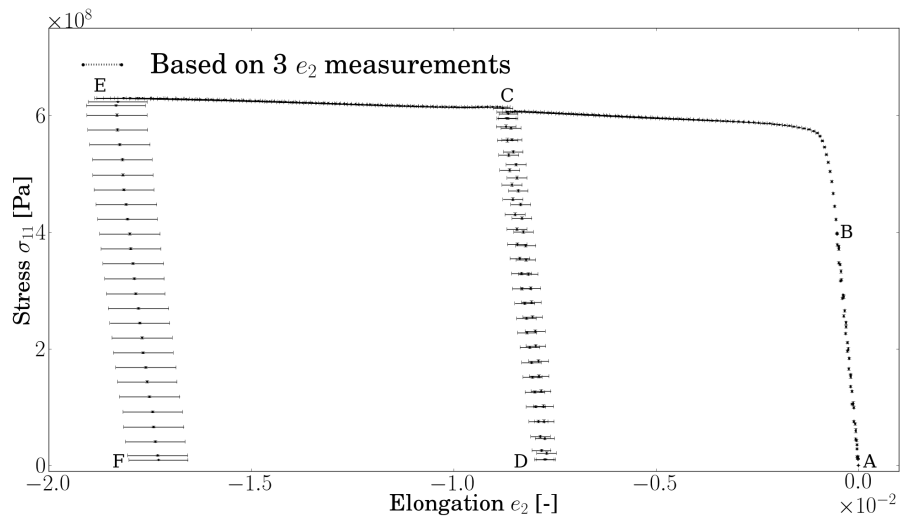Based on the measured force F and the elongations presented above it is possible

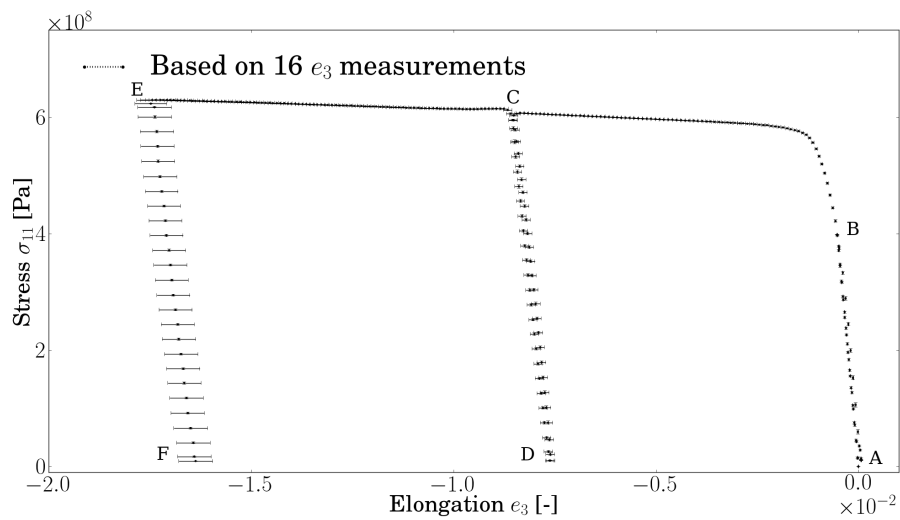Figure 5.5: **Average of e_2 elongation over 3 strain gauges on 2 test specimens plotted against σ_{11}**

Figure 5.6: **Average of e_3 elongation over 16 strain gauges on 13 test specimens plotted against σ_{11}**

to estimate the Cauchy stress σ_{11}. Cauchy stress has been selected as a convenient measurand (see Sec. 3.6.3.2) to visualize the load history as done above. As mentioned in Sec. 3.6.3 the estimated σ_{11} can vary slightly based on whether it is calculated using both e_2 and e_3 measurements, or only one of them under the assumption that the Poisson's ratio is valid in both lateral directions for an isotropic material (see Sec. 3.6.3). The results of the comparison between these two methods have been presented in App. C, Fig. C.7, for the strain gauge measurements. The relative difference in values estimated by the two methods is less than 0.25 %, which has been considered to be sufficiently low to give reasonable estimates of the stress level from both methods.

The estimated stress shown in Fig. 5.7 have been based on estimation of $\sigma_{11}(e_2, e_3)$ (Eq. (3.14)), and $\sigma_{11}(e_2)$ and $\sigma_{11}(e_3)$ (Eq. (3.15)) based on the measured e_2 and e_3 elongations and plotted against the measured e_1 elongation. It should be noted that this estimated Cauchy stress σ_{11} is the same stress as have been used when plotting the different strain components in Figs. 5.4 to 5.6 above.
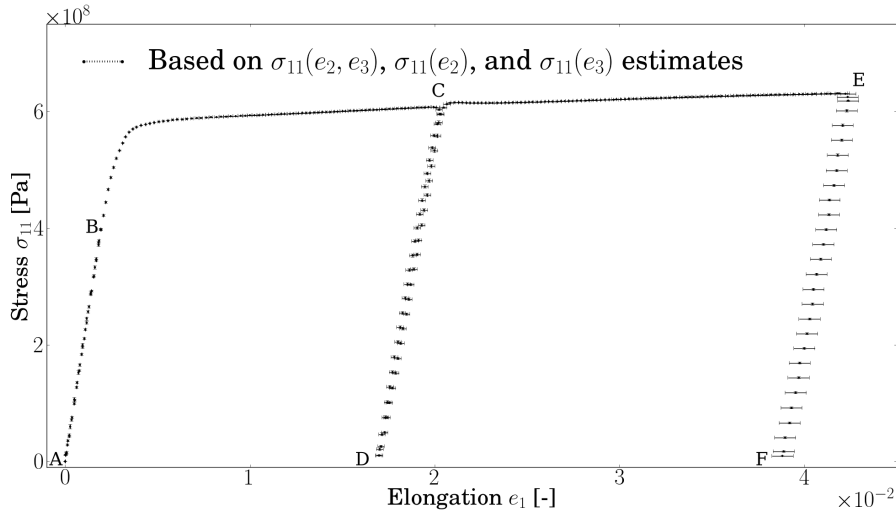

Figure 5.7: Average of σ_{11} stress and e_1 elongation based on measured contraction elongations e_2 and/or e_3

To be able to estimate the Young's modulus Y and Poisson's ratio ν the elastic and plastic contributions of the elongations need to be extracted as described in Sec. 3.6.3. The elastic contribution is also needed as input to the acoustoelastic theory to be

able to compare the predicted change in sound velocity to the estimated change based on the acoustic measurements done in this work. In Fig. 5.8, the black curve is the measured elongation e_1 plotted against itself. The blue curve is the elastic contribution e_1^e calculated from the relation in Eq. (2.112), where the elastic loading and unloading sequences can be recognised as the sequences AB, CD, and EF as before. The red curve is the plastic strain e_1^p calculated according to Eq. (2.113), and the sum of the elastic and plastic contribution reproduce the original total elongation e_1 (black curve). Note how each elastic region have a corresponding horizontal region in the plastic contribution, indicating no plastic deformation while the test specimens were subjected to elastic loading or unloadeding. Similar plots of the elastic and plastic contributions for the measured elongations e_2 and e_3 have been included in App. C.2.1, Figs. C.8 and C.9. The Young's modulus Y and Poisson's ratio ν estimated based on the measured elongations as described in Sec. 3.6.3.3 have been presented in Sec. 5.3.1.
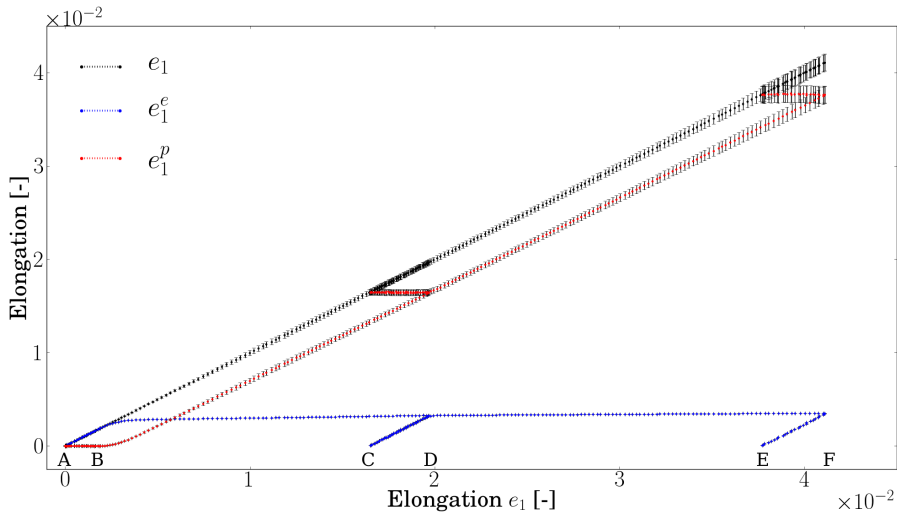
Figure 5.8: Elastic and plastic elongations (e_1^e, e_1^p) plotted against total measured elongation e_1

The same quantities as presented for the strain gauge measurements above have also been measured using the ARAMIS photometric measurement system (Sec. 3.6.2), which result in corresponding results based on the ARAMIS elongations e_{major}, e_{minor}, and e_z. As will be explained in Sec. 5.3.1 the ARAMIS results have not been used in

Table 5.2: Estimated Young's modulus and Poisson's ratio based on average over strain gauge measurements

Sequence	Young's modulus Y [GPa]	Poisson's ratio $\nu(e_2)$ [-]	$\nu(e_3)$ [-]
1. loading	209	0.28	0.31
1. unloading	212	0.29	0.28
2. loading (elastic)	208	0.28	0.28
2. unloading	185	0.31	0.29
3. loading (elastic)	186	0.30	0.28
3. unloading	179	0.31	0.30

further evaluations in this work and have thus only been included in App. C.2.2 for reference.

5.3.1 Young's modulus and Poisson's ratio

The Young's modulus and Poisson's ratio have been estimated based on the slope of a linear regression of the stress strain relation in the linear elastic regions as described in Sec. 3.6.3, Eq. (3.19), for the strain gauge measurements (see Sec. 3.6.1) and the ARAMIS strain measurements (see Sec. 3.6.2). The results have been presented in Table 5.2 and 5.3. As will be further discussed in Ch. 7, the strain measurements based on strain gauges provides the best comparison with measurements done by other authors (e.g. by comparing the estimated Young's modulus Y and Poisson's ratio ν with the values for common steels presented in Table 4.5). The values of $\nu(e_3) > 0.5$ estimated based on the ARAMIS estimated e_3-elongation are in fact unphysical since $\nu \in \{-1, 0.5\}$ [13]. Thus, in the following, where strain measurements are relevant for the estimated results, only the results based on strain gauge measurements have been presented. The ARAMIS results are thus only included in this section for reference and to support the estimated reduction in Young's modulus with increasing plastic deformation which have been discussed in more detail in Sec. 7.8. Note that only the nominal values have been presented here while the uncertainties related to these estimates will be discussed in Sec. 6.4.2.

Table 5.3: Estimated Young's modulus and Poisson's ratio based on average over ARAMIS photometric measurements

Sequence	Young's modulus	Poisson's ratio	
	Y [GPa]	$\nu(e_2)$ [-]	$\nu(e_3)$ [-]
1. loading	237	0.22	0.81
1. unloading	255	0.19	0.88
2. loading (elastic)	288	0.29	0.98
2. unloading	179	0.31	0.66
3. loading (elastic)	182	0.27	0.67
3. unloading	165	0.24	0.64

5.4 Temperature

The sound velocity in a body is dependent on the temperature of the body. A temperature change in the test specimen during the tests will thus affect the measured resonance frequencies. Some data on the temperature dependency of steel can be found in [105]. The data presented therein shows a change in sound velocity for both longitudinal and shear waves of less than 1 (m/s)/°C. This corresponds to an approximate relative sound velocity change of 0.02 %/°C for longitudinal waves ($c_l \approx 6000$ m/s) and 0.03 %/°C for shear waves ($c_l \approx 3300$ m/s). The data in [105] have been measured on an alloy steel, which is not the same as the construction steel used in this work. However, it is assumed that the properties are sufficiently similar to be a relevant approximation of the sound velocity contribution from any change in the temperature in this work.

The temperature measurements performed before and after the acoustic tests have been presented in Table 5.4. The measured temperature differences was in the order of the resolution of the digital thermometer. Combining this with the approximate dependency yields a sound velocity change based on temperature of approximately 0.002 % and 0.003 % for longitudinal and shear sound velocities respectively. This has been included in the uncertainty analysis in Ch. 6, and has been judged to be negligible compared to other uncertainties.

5.5 Acoustic resonance

The sound velocity across the test specimens is related to the thickness of the specimen and the resonance frequencies as described in Sec. 2.6.1. The ART measures the acoustic resonance frequencies across the thickness of the specimens, and the result

Table 5.4: Temperature measurements

Test specimen	Temperature [°C]			
	Room	Water tank		
		Start	End	Δ
21	23.3	-	31.6	-
22	27.5	30.3	30.4	0.1
23	23.8	33.1	32.7	-0.4
24	23.2	33.4	33.4	0.0
25	25.7	34.5	-	-
31	22.6	11.8	11.9	0.1
32	25.4	11.6	-	-
33	26.1	13.2	13.2	0.0
34	-	12.7	12.8	0.1
35	25.4	-	-	-
36	21.4	13.2	13.2	0.0
37	21.5	13.2	13.2	0.0
38	22.8	12.8	-	-
39	23.4	12.8	12.8	0.0
40	24.0	12.9	-	-
41	23.7	12.9	12.9	0.0

of these measurements have been presented in this section. Note that the resonance frequencies presented here are the extracted FFT peaks from the recorded acoustic signal (see Sec. 3.5.1), not correcting for the beam diffraction effect (Sec. 2.6.2 and 3.6.3.1). This correction has been done in relation with the estimated sound velocities presented in Sec. 5.6.

After processing and categorising each acoustic shot from all the ART tests as described in Sec. 3.5, the development of the resonance frequency responses of the first and second longitudinal modes and the third shear mode have shown good coherence throughout the tests withouth large erratic noise. Fig. 5.9 shows the extracted frequencies based on the L2 resonance peaks throughout 13 different acoustic tests (as extracted from the recorded acoustic signal - see Sec. 3.5.1). Remember from Sec. 3.4 that each series represent one test, and that each point (306 in total) represent the average value over each predefined bin. Grey error bars indicate the standard deviation within each bin. However, for the L2 resonance in Fig. 5.9 the standard deviation within each bin is so small that the error bars are hard to see. As also can be seen in Fig. 5.9, the development of the L2 resonance frequency appear to be similar, however with a varia-

tion in the initial unstressed frequency at point A. Some of this variation is assumed to be caused by slight variations in thickness between different test specimens and maybe slight differences in temperature etc. at the unstressed condition (e.g. a 5 kHz difference for the L2 resonance $f^{(n_l=2)}$ corresponds to a difference in thickness d of approximately 0.05 mm, Eq. (2.120)). Fig. 5.10 shows the average over corresponding bins for the 13 test specimens. Here the black error bar shows the experimental standard deviation of the mean for the 13 test specimens (see Eq. (6.2) in Ch. 6). This is how results over several test specimens have been presented in the following if not otherwise stated. The presented uncertainties have been estimated and propagated using the numerical computational library *Uncertainties: a Python package for calculations with uncertainties* [108]. The input to these calculations have been discussed and presented in relevant sections in Ch. 6.

Recalling the load history described by the sequence A-B-A-C-D-E-F as presented in Sec. 3.3 the same notation have been used in this section to visualise the loading and unloading sequences.
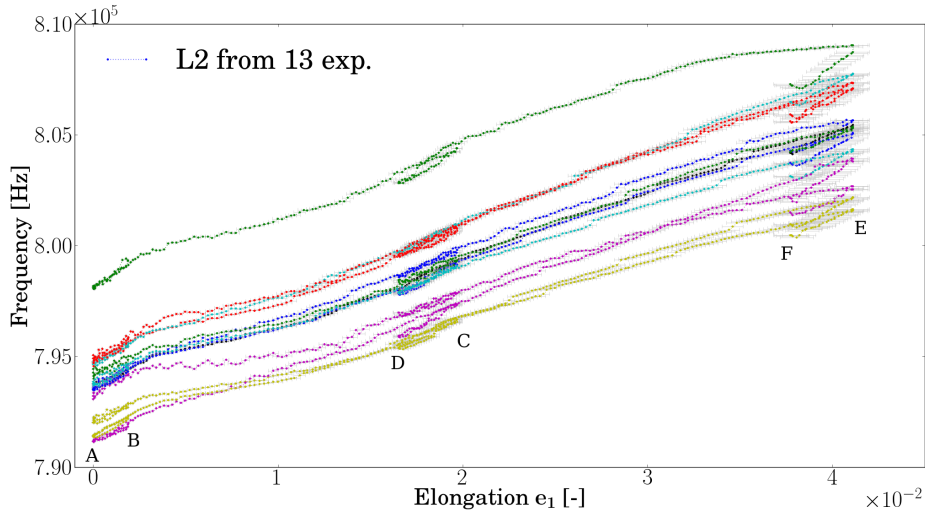
Figure 5.9: Frequency development of the measured L2 resonance mode ($f^{(n_l=2)}$) for 13 test specimens

When the test specimens have been uniaxially deformed in the x_1-direction, the thickness d over which the acoustic resonance has been measured has decreased (see Sec. 2.3). According to Eq. (2.120) a reduction in thickness d will induce an increase in
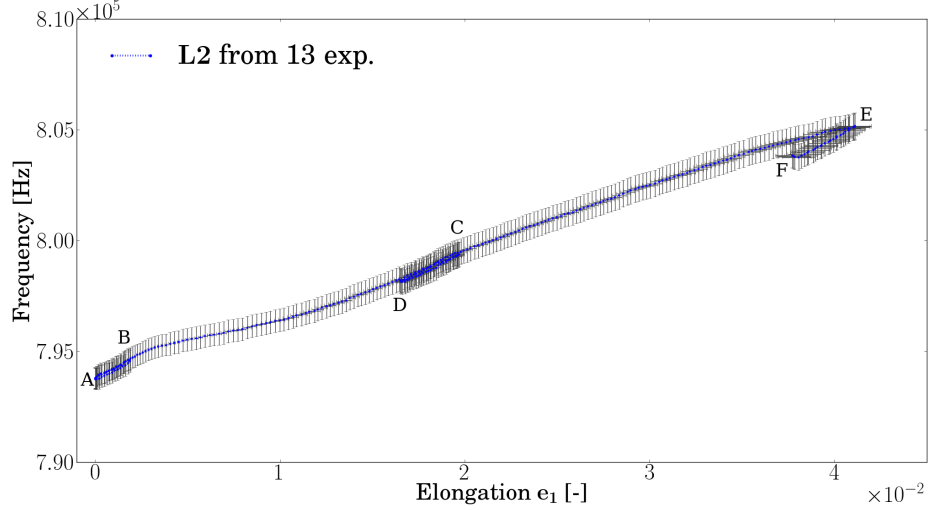
Figure 5.10: Average of frequency development of the measured L2 resonance mode ($f^{(n_l=2)}$) over 13 test specimens shown in Fig. 5.9

measured resonance frequencies f. This behaviour is clearly seen in Fig. 5.10 all the way from point A (unstressed) to point E (largest applied deformation). Correspondingly during the relaxation of the applied uniaxial tension (sequence BA, CD, and EF) the thickness d increase and the measured frequency decrease as expected. Based on this observation it has not been possible to say if any of the observed frequency change were due to a change in longitudinal sound velocity c_l or if it was solely a result of the change in thickness d. Similar results have been observed for the L1 resonance mode shown in Fig. 5.11.

However, for the shear mode S3 which depends on the shear sound velocity, one property observed in Fig. 5.12 differ significantly from the behaviour of the L1 and L2 longitudinal modes. Looking at the elastic loading and unloading sequences AB, BA, AB, CD, DC, and EF it is obvious that the frequency $f^{(n_s=3)}$ (mode S3) decrease as the thickness d also decrease. From Eq. (2.120) this is not physically possible if not the sound velocity c_s also decrease under uniaxial increased deformation. This indicate that the sound velocity of longitudinal and shear propagation modes behave very differently when the test specimens were subjected to elastic uniaxial tension. The effect that longitudinal and shear waves change with opposite and different magnitudes when an isotropic hyperelastic material is subjected to either compression or tension
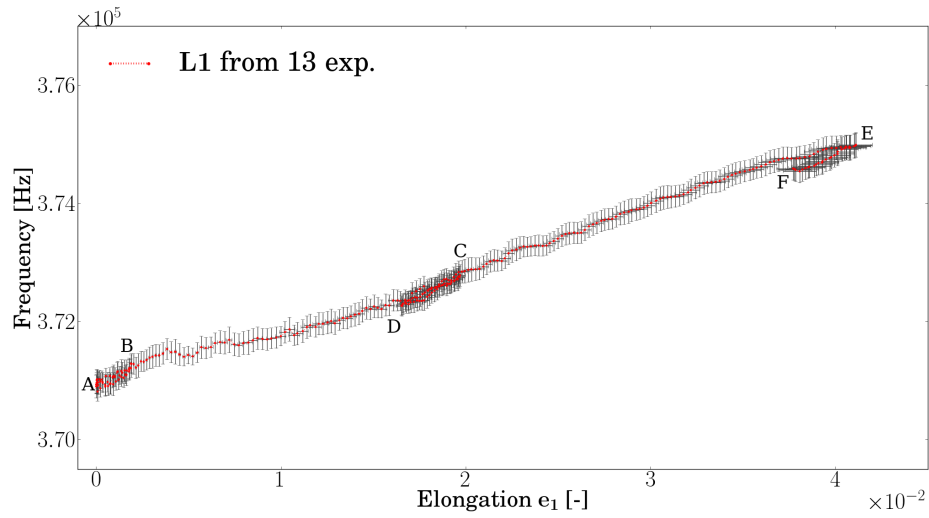
Figure 5.11: Average of frequency development of the measured L1 resonance mode ($f^{(n_l=1)}$) over 13 test specimens shown in Fig. C.21
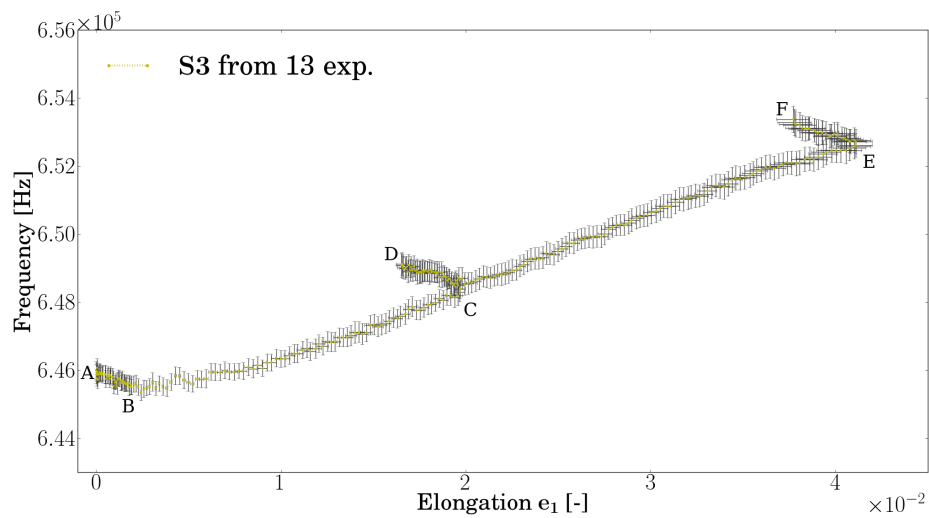

Figure 5.12: Average of frequency development of the measured S3 resonance mode ($f^{(n_s=3)}$) over 13 test specimens shown in Fig. C.22

was shown as early as 1958 by [32] in Aluminium, by Smith et al. [44] in 1966 for several polycrystalline materials, by Crecraft [39] in 1967 for both aluminium and steel, and later confirmed by several other authors (see Sec. 1.4 for a more detailed account). Note however that the theoretically predicted separation of the shear sound velocities for shear waves polarised parallel and perpendicular to the applied tension (shown by e.g. [32], [44], and [39]) have not been observed for the recorded S3 shear resonance mode. Because of the frequency separation resolution of the FFT of 16.7kHz (see Sec. 3.5.1), which corresponds to a sound velocity resolution in the unstressed test specimen of approximately 3.8 %, it is not possible to detect different resonance frequencies with less separation in the frequency domain than this. The frequency, or sound velocity, separation resolution is more than one order of magnitude larger than the observed and predicted relative frequency change. Thus the measured S3 resonance mode should consists of the combined contribution from shear waves propagating with both parallel and perpendicular particle motion polarisation.

The individual results from the 13 test specimens making the basis for both the L1 and S3 modes in Figs. 5.11 and 5.12, have been included in App. C.3, Figs. C.21 and C.22 respectively.

Because of small variations in inital thickness of the test specimens, and possible other factors like difference in tempereature between tests etc., the unstressed resonance frequencies can vary with large absolute values between the different tests. This effect can clearly be seen for the resonance modes in Figs. 5.9, C.21 and C.22. Because this work is concerned with the changes caused by the stress state of the steel, one way to circumvent this effect is to look at the relative change of the measured quantity and to transpose the measurements so that the unstressed state of the first unloading is aligned for all the tests. This has been done by estimating a reference frequency at the un-stressed / zero loading state as described in the introduction of Ch. 5. The frequency value in the last bin of the first unloading (see Table 3.4) is a convenient choice of reference frequency since the applied force for this bin has been load controlled to 0 kN. This alignment has been done for the L2 mode in Fig. 5.13. (Corresponding figures for the L1 and S3 modes can be found in Figs. C.23 and C.24 in App. C.3). The different resonance modes and their experimental mean of relative frequency change have been plotted and compared in Fig. 5.14, where red is the L1 mode, blue is the L2 mode and

yellow is the S3 mode as in the previous plots of the individual resonance modes.
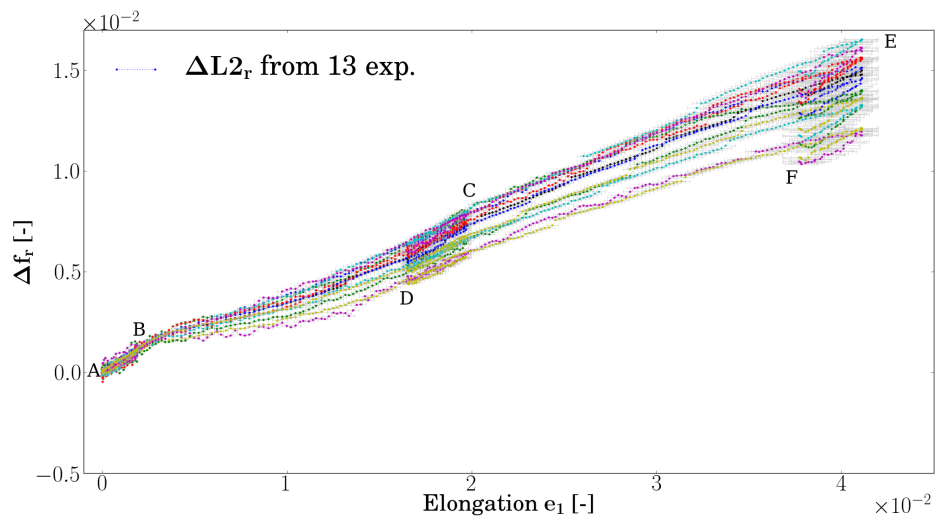
Figure 5.13: Relative frequency development of the L2 resonance mode for 13 test specimens shown in Fig. 5.9
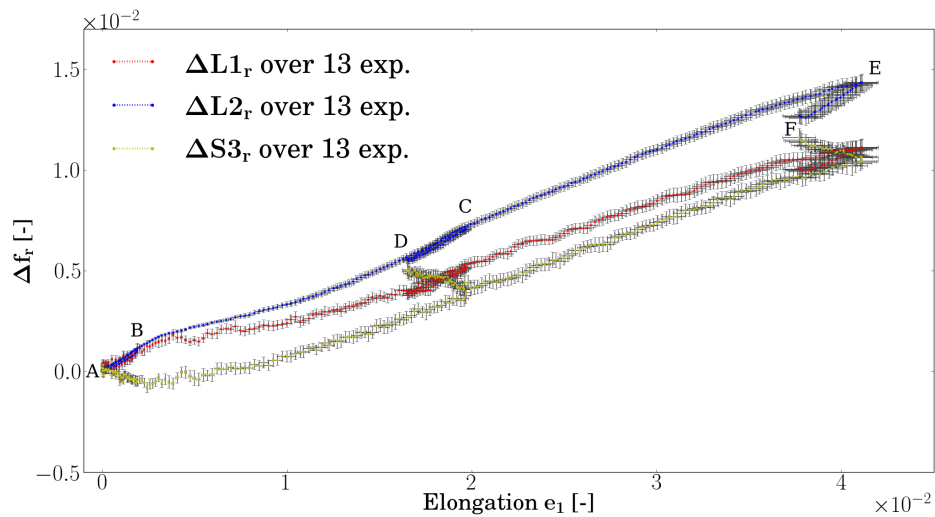
Figure 5.14: Average of relative change in resonance frequency for the L1, L2, and S3 modes based on the results presented in Figs. C.23, 5.13, and C.24 respectively

5.6   Sound velocity change

5.6.1   Thickness dependent estimates

The sound velocity can be calculated based on the measured resonance frequencies and the measured thickness change according to Eqs. (2.121) and (2.123). Combining the frequencies from the L1, L2 and S3 modes with the original measured thickness L_3 and the thickness elongation (e_3) based on strain gauge measurements yields the absolute and relative sound velocity changes.
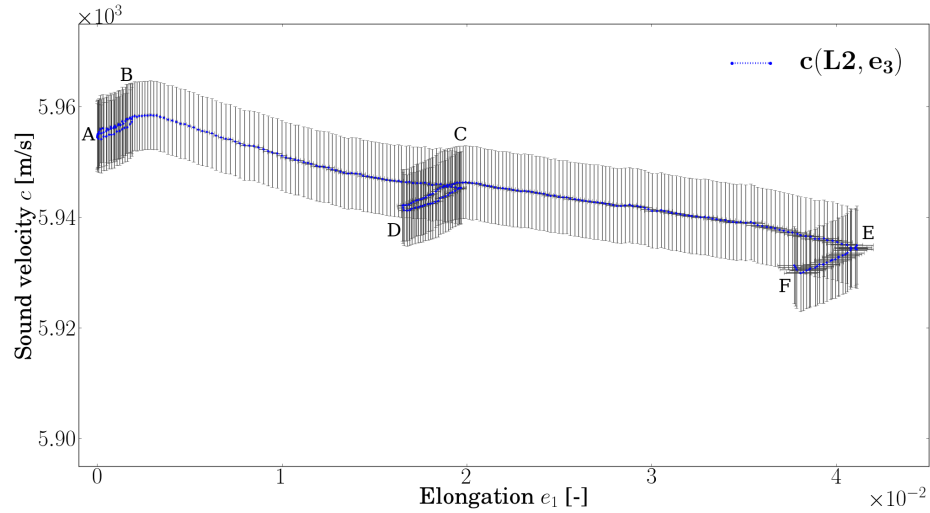
Figure 5.15: Sound velocity c_l based on the L2 mode including thickness reduction compensation (e_3), but not the beam diffraction correction

Fig. 5.15 shows the longitudinal sound velocity $c_l^{(n_l=2)}$ based on the L2 resonance mode presented in Fig. 5.10, including the measured thickness reduction (e_3), but not including the beam diffraction correction described in Sec. 3.6.3.1 (this will be included in Fig. 5.17). Similarly to the frequency development of the L2 mode, the elastic regions AB, CD, and EF shows an increase in the estimated sound velocity for increasing applied deformation. It is also possible to visually observe that the longitudinal sound velocity have similar slopes of change in the elastic regions. However, contrary to the continued increase in frequency as the test specimens have deformed plastically (region BC and CE), the estimated sound velocity shows a decrease in the sound velocity. Although it is recognised that the observation of the magnitude of change in sound velocity may

be an effect of systematical inaccuracies in the thickness measurements, it is clear that there exist a relation between the applied deformation e_1 and the longitudinal sound velocity c_l, and that this relation is different under elastic and plastic deformation. The large error bars seen in Fig. 5.15 are mainly due to the same effect as described for the L2 resonance frequencies, e.g. slight variation in initial thickness and temperature of the test specimens leads to variation in the estimated initial sound velocity. These effects are effectively removed by comparing relative change of the sound velocity as will be presented in Fig. 5.19.

Figure 5.16: Sound velocity c_l based on the L1 mode including thickness reduction compensation (e_3), but not the beam diffraction correction
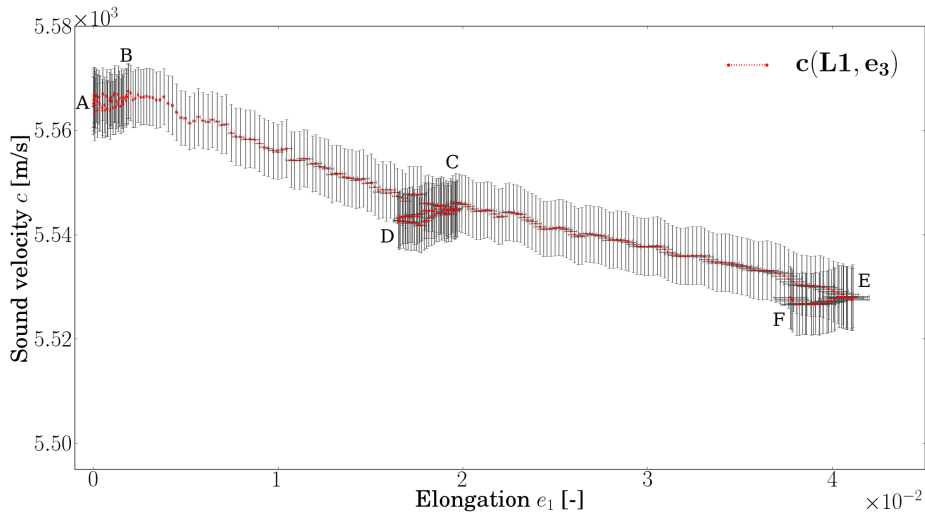
In Fig. 5.16 the longitudinal sound velocity estimations $c_l^{(n_l=1)}$ based on the L1 resonance mode of the same 13 acoustic tests with the same approach as for the L2 mode are shown. A very similar development of the sound velocity can be seen in both these figures. However, one distinct difference is noted. The initial unstressed longitudinal sound velocity is estimated to be ~ 5563 m/s and ~ 5954 m/s based on the L1 and L2 resonance modes respectively. This difference in the order of 7 % is much larger than the standard uncertainty in the order of 0.1 % for the sound velocities based on each of the resonance modes from several test specimens (see Sec. 6.3. As have been explained in Sec. 3.6.3 this large difference is thus probably related to the beam effect described in Sec. 2.6.2. To correct for this beam effect the estimated longitudinal

sound velocities have been adjusted according to Eq. (3.7) and plotted in Fig. 5.17. For the 13 test specimens the correction factor $\eta_{n_l=1}$ have varied between 1.050 and 1.062 (i.e. an underprediction of approximately 5-6 %), while for $\eta_{n_l=2}$ varied between 0.982 and 0.989 (i.e. an overprediction of approximately 1-2 %). After the adjustment the estimated longitudinal sound velocities based on both the L1 and L2 mode have an initial unstressed magnitude of $\sim$ 5872 m/s. The development of both estimates can be seen in Fig. 5.17. The initial unstressed longitudinal sound velocities have been corrected for the beam diffraction effect and the development shows very similar behaviour. However, these two estimated developments should theoretically have been the same. The discrepancy between the longitudinal sound velocity estimated based on the measured frequencies of the L1 and L2 resonance modes might thus be an effect of the probable erroneous assumption that the beam diffraction effect (see Sec. 2.6.2, Fig. 2.10) is constant throughout each test run. This discrepancy will be further discussed in Sec. 7.4.1. Note also that the uncertainties related to the measured frequencies, unstressed thickness, and thickness reduction have been propagated to the calculated sound velocities using a numerical computational library as described in Sec. 6.1. This has also been done for any other calculated estimates based on measurements in the following if not otherwise stated.
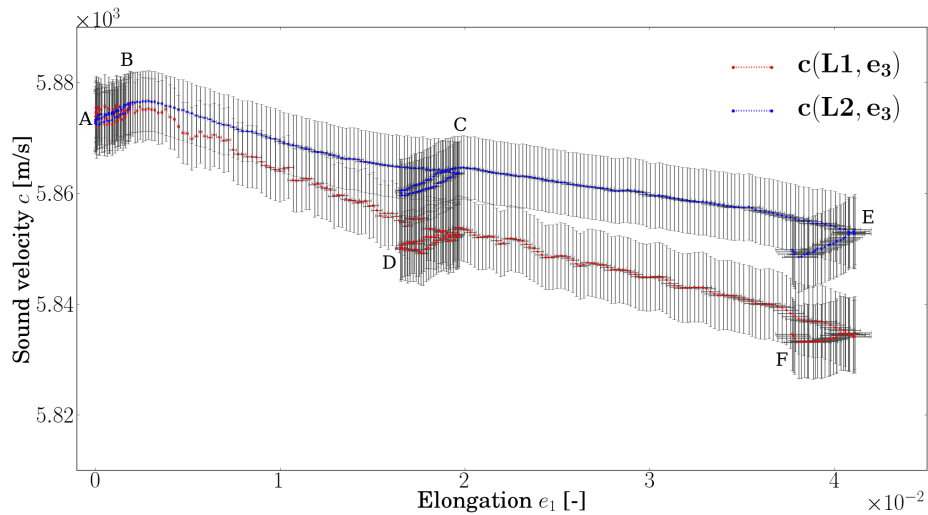
Figure 5.17: Sound velocity based on the L1 and L2 modes including thickness reduction compensation (e_3), including the beam diffraction correction

5. EXPERIMENTAL AND THEORETICAL RESULTS

The last sound velocity estimated has been the shear sound velocity based on the S3 resonance frequencies using Eqs. (3.7) and (3.9). This has been presented in Fig. 5.18. This plot shows the opposite sound velocity development for the shear sound waves compared to the elastic regions of the longitudinal sound velocity in Fig. 5.17. This is as predicted for the elastic regions by the corresponding decrease in measured frequency for the S3 resonance mode in Fig. 5.12, and is a combination of the change in sound velocities for shear waves with particle motion polarised in parallel to or perpendicular to the applied tension (see Secs. 5.5 and 3.5.1). The estimated initial unstressed magnitude of the shear sound velocity is ~ 3229 m/s.
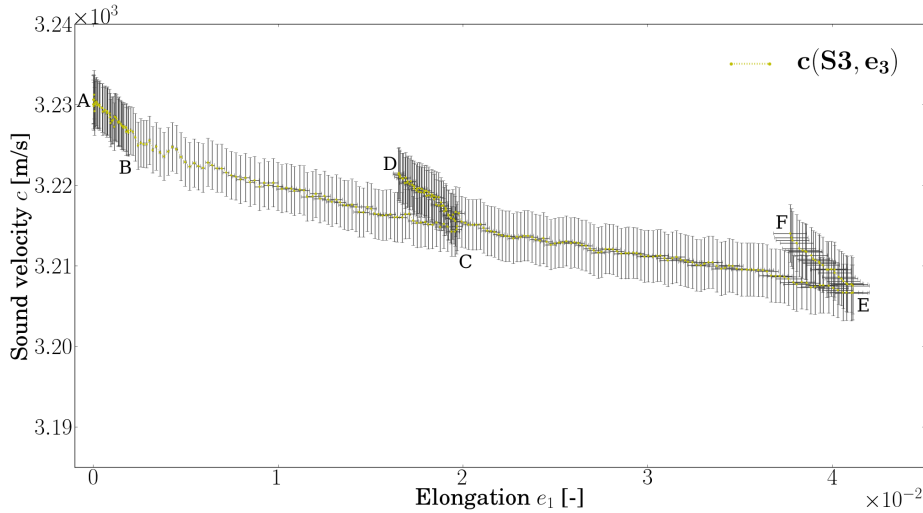
Figure 5.18: Sound velocity based on the S3 mode including thickness reduction compensation (e_3), and the beam diffraction correction $\eta^{(n_s=3)} \approx 1$.

Removing the uncertatainty related to variation across test specimens by calculating the relative sound velocity change (see Sec. 2.7, Eq. (2.122)), and plotting the three different estimates together results in the plot shown in Fig. 5.19. When calculating the relative change the beam correction factor is on combination of Eq. (2.122) and (3.7) canceled out and is thus not needed.

As can be visually seen from Fig. 5.19 the longitudinal sound velocity estimated based on both the L1 and L2 resonance mode have similar development in the elastic regions with aproximately the same gradient of change in estimated sound velocity with respect to applied strain, both in magnitude and sign. However when the test
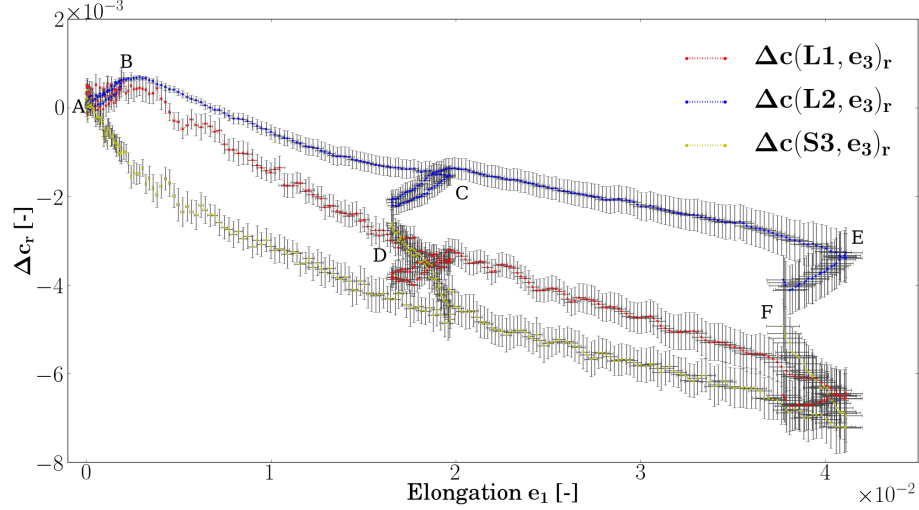
Figure 5.19: Average of relative change in estimated sound velocity based on resonance frequencies of the L1, L2, and S3 mode including thickness reduction compensation (e_3). Note that the beam diffractin correction falls out for relative measurements.

specimen deforms plastically the magnitude of the velocity gradient is slightly different as mentioned above. When it comes to the shear sound velocity estimated based on the S3 resonance mode the development and its gradient with respect to applied strain has opposite sign, and as mentioned in Sec. 5.5 the opposite negative development of the shear sound velocity can only be an effect of actual sound velocity change and not an effect of innsuficiently good measurements of the thickness development. It is possible that the negative trend of all the curves in the plastic regime (from point B to C and from C to E) might be an effect of change in second order elastic constants, or it might be an effect of unknown systematic uncertainties in the e_3 measurement (see Eq. (2.122)). The potential change in linear elastic moduli is estimated in Sec. 5.6.1.1. To remove the uncertainty introduced by the thickness change measurements and avoid that problem the ratio between either of the two estimated longitudinal sound velocities and the shear sound velocity have been calculated according to Sec. 2.7 and presented in Sec. 5.6.2.

Table 5.5: Estimated linear elastic moduli based on unstressed sound velocity estimates including beam diffraction correction

Based on mode	Sound velocities c_l [m/s]	c_s [m/s]	Lamé constants λ [GPa]	μ [GPa]	Young's modulus Y [GPa]	Poisson's ratio ν [-]
Unstressed reference configuration (point A)						
L1,L2,S3	5872±6	3229±3	109.0±1.1	83.4±0.9	214.1±2.2	0.283±0.001
Unstressed configuration after 1st plastic deformation (point D)						
L1,S3	5848±6	3221±3	107.7±1.1	83.0±0.8	212.8±2.2	0.282±0.001
L2,S3	5858±6	3221±3	108.6±1.1	83.0±0.8	213.0±2.2	0.283±0.001
Unstressed configuration after 2nd plastic deformation (point F)						
L1,S3	5831±6	3212±4	106.9±1.2	82.5±0.8	211.6±2.2	0.282±0.001
L2,S3	5846±6	3212±4	108.3±1.2	82.5±0.8	211.9±2.2	0.284±0.001

$\rho_0 = 8000 \pm 1\% \text{ kg/m}^3$[79]

5.6.1.1 Linear elastic moduli based on sound velocity

Recalling the relation between the sound velocity and the Lamé moduli presented in Eq. (2.91) it is possible to estimate the linear elastic moduli λ and μ (Lamé constants) based on the measured unstressed sound velocities c_l and c_s, and to further estimate the Young's modulus Y and Poisson's ratio ν through the relations in Eq. (2.106) respectively. This has been done by including the adjustment of the unstressed longitudinal resonance frequencies with respect to the beam effect (see Sec. 3.6.3.1). The results have been presented in Table 5.5 for the three unstressed configurations (point A, D, and F). As can be seen from the results in Table 5.5 the potential change in the Young's modulus based on observed change in sound velocities is in the order of -0.5 % and -1 % at point D and F respectively. Note that the uncertainty related to the beam diffraction correction of the frequencies have not been included in the reported uncertainties. This has been discussed in Sec. 6.3.

5.6.2 Ratio of longitudinal and shear resonance frequencies

As described in Sec. 2.7, for two sound velocities which have opposite sound velocity response when subjected to a deformation, the ratio between the two will enhance the measured difference as well as remove any thickness dependence. The relative change of the ratios between the measured frequencies of the L2 and S3, and the L1 and S3, resonance modes have been calculated according to Eq. (2.125), where the beam

diffraction correction cancels out as described in relation with the relative sound velocity change presented in Fig. 5.19. In addition the relative change of the ratio between the two longitudinal modes L1 and L2 have also been calculated, and the relative change in the three frequency ratios (or equivalently the relative change in the sound velocity ratios) have been presented in Fig. 5.20. Plots of the individual ratios per test specimen have been included in Figs. C.25 to C.27 in App. C.3.
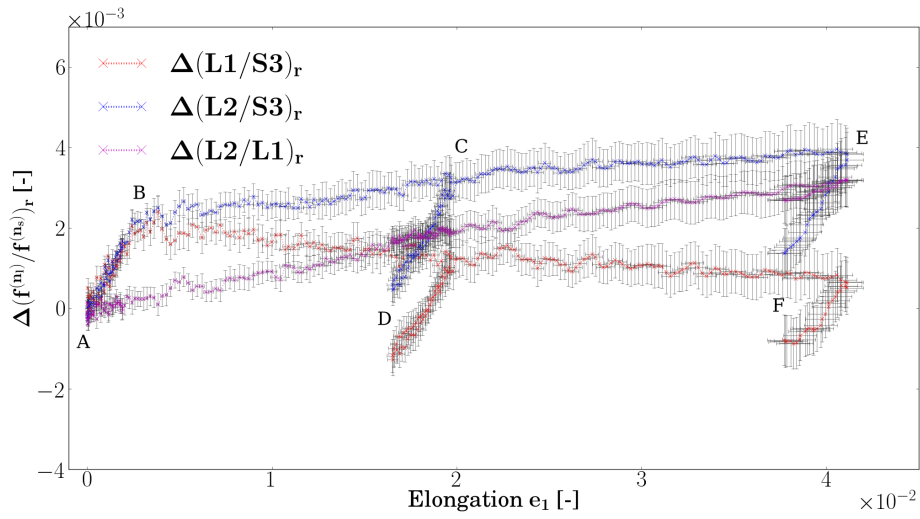
Figure 5.20: Average of relative change in ratio of resonance frequency modes L1/S3, L2/S3, and L2/L1. Note that both the need for thickness reduction compensation and beam diffraction correction falls out as described in Secs. 2.7 and 3.6.3.1

Since both the longitudinal modes L1 and L2 are dependent on the same physical longitudinal sound veloctiy both should experience the same amount of change. Thus the relative change of the ratio L2/L1 should give a theoretical relative change equal to zero. As can be seen from Fig. 5.20 this is evidently not the case. However, recalling the beam effect described in Sec. 2.6.2 the L1 mode is measured slightly below the theoretical plane wave value, while the L2 mode is measured slightly above the theoretical plane wave value. It is possible that the observed increase in the relative L2/L1 ratio is related to a thickness dependence of the beam effect. The effect of this has been further discussed in Sec. 7.4.1. For the L1/S3 and L2/S3 ratios it is apparent that the slope of the relative change in the elastic regions (AB, CD, EF) all have linear dependencies on the applied uniaxial elongation which are similar.

131

In the plastic regions however, the observed relative change in sound velocity ratios are significantly less. In fact, the dependence of the sound velocity ratios on the plastic strain are opposite for the L2/S3 and L1/S3 ratio. As discussed above this is probably related to the beam effect not beeing constant throughout the tests (i.e. a possible thickness dependence). This has been further discussed in Sec. 7.4.1.

5.7 Simulation of acoustoelastic theory

As described in Ch. 4 the theoretical expressions relating the longitudinal sound velocity c_{33} (Eq. (2.97)), and the shear sound velocities c_{31}, and c_{32} (Eqs. (2.98) and (2.99)) to the elastic part (e_1^e) of the applied uniaxial elongation e_1 (see Sec. 2.5.1) have been implemented and simulated based on the two second order elastic constants λ and μ, and the three third order elastic constants A, B, and C for the 8 steels found in literature and presented in Table 4.4. Remember from Sec. 2.3 that the subscripts c_{33} signify a longitudinal wave propagating perpendicular to the applied tension, c_{31}, and c_{32} signifying a shear wave propagating perpendicular to the applied tension, but with polarisation respectively in parallel to- and perpendicular to- the applied tension.

Note that the theory presented in Sec. 2.3 is limited to the elastic regime, while the test specimens have been deformed well in to the plastic regime. To be able to compare the measured sound velocity change after the test specimens have been plastically deformed, the elastic part e_1^e of the total elongation e_1 has been extracted as shown in Fig. 5.8, where the blue curve represents the elastic contribution e_1^e and the black curve is the corresponding total measured elongation e_1. Any plastic contribution has been ignored in the simulations (see argumentation in Sec. 2.5.2). Thus the theoretical simulation in this section shows the predicted sound velocities of the acoustoelastic theory with the extracted elastic elongation e_1^e (blue curve in Fig. 5.8) as input to the simulations, while the simulated results have been plotted against the total measured elongation e_1 to be able to compare it with actual measured results.

5.7.1 Absolute magnitude of sound velocities

Fig. 5.21 shows the simulation of the 8 steels in Table 4.4. Examining Eq. (2.97) it is clear that the magnitude of the initial unstressed sound velocity is determined by the density ρ_0 and the elastic constants λ and μ (i.e. $e_1 = 0$), and thus the location

of the different series representing the absolute magnitude of the sound velocities for the 8 steels might be widely separated based on variations in these parameters. This spread in absolute magnitudes will not be relevant when investigating the relative sound velocity change presented in Sec. 5.7.2. Note also that the plot of the magnitude of the theoretical sound velocities presented here are of nominal values without uncertainties included. The relevant uncertainties have been investigated in the following sections.
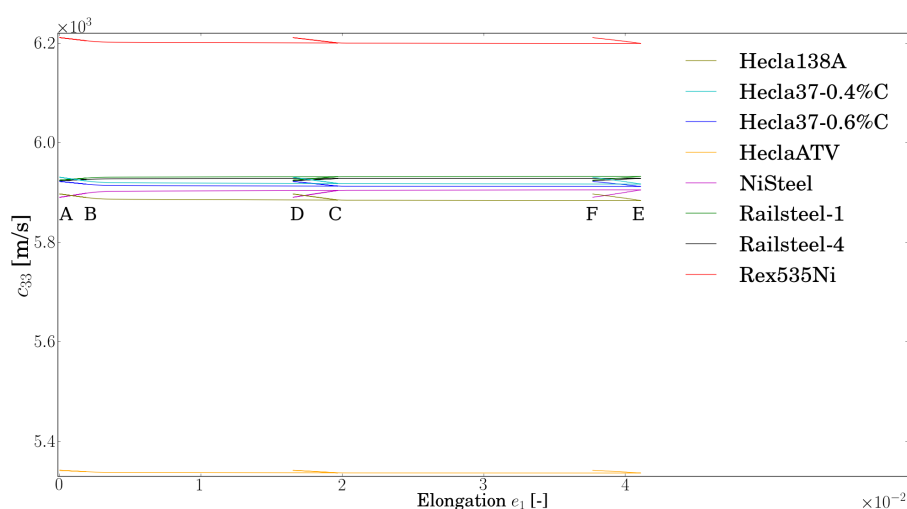
Figure 5.21: Simulated sound velocity development (c_{33}) of longitudinal waves propagating perpendicular to the applied stress based on elastic properties given in Table 4.4

It is noted that 6 of the steels have an unstressed longitudinal sound velocity c_{33} of approximately 5900 m/s, while one is as low as ~ 5300 m/s and one is as high as ~ 6200 m/s. The elastic loading and unloading sequences are also visible as slight gradients and is marked previously by AB, CD and EF. It is difficult to investigate details of the development of the sound velocities from the absolute magnitudes in Fig. 5.21, and thus the more relevant relative change of the sound velocities have been investigated below.

The magnitude of the shear sound velocities c_{31} and c_{32}, and their development have also been plotted and are included in Figs. C.28 and C.29 respectively in App. C.4. It is noted for reference that 6 of the steels (the same as above) have an unstressed shear sound velocity of approximately 3200 m/s, while the lowest is just below 3000 m/s, and the highest is at approximately 3400 m/s. Comparing the simulations with

the estimated longitudinal and shear sound velocity presented in Sec. 5.6 of 5870 m/s and 3230 m/s respectively, shows a representative agreement with the simulated values of the 6 steels above. The development of the simulated sound velocities will be compared to the estimated sound velocities presented in Sec. 5.6 in Sec. 5.7.4. It is noted that the density of the Nickle-Steel, denoted NiSteel, was not reported in the literature, thus the simulations have assumed a density of 7850 kg/m^3 for this steel, which is a reasonable value compared to the other reported steels (see Table 4.2). Note also that the effect of the density is canceled out according to Eq. (2.91) when investigating the relative change of the sound velocities as will be done in the following section.

5.7.2 Relative change of simulated sound velocities

The relative development of the longitudinal sound velocity have been calculated based on the simulations and has been presented in Fig. 5.22. This figure shows that the simulated relative change of the longitudinal sound velocity migth both be positive and negative, depending on the variation in both the elastic constants λ and μ, and the acousto elastic coefficients A, B, and C (see Eqs. (2.97) to (2.99) and (2.92) to (2.94) for the relations). Three steels have a positive development of the relative change in c_{33} (Railsteel-1, Railsteel-4, and NiSteel) spanning from approximately 0.05 % to 0.3 %. The other five steels have a negative development of the relative change in c_{33} spanning from appoximately -0.05 % to -0.25 %. Note also that the reported uncertainty in the second order elastic constants (λ, μ) and the third order elastic constants A, B, and C from Table 4.4 have been propagated to the simulated results by the numerical computation library *Uncertainties: a Python package for calculations with uncertainties* [108]. The uncertainties have been further discussed in Sec. 6.5.

Fig. 5.23 shows in the same manner as above the relative change in the simulated shear sound velocity with a polarisation parallel to the applied tension, c_{31}. The relative changes of the simulated c_{31} do also vary significantly across the 8 steels, however, here all the steels exhibit a negative development as a function of applied elongation. Four of the steels exhibit a maximum negative relative change between 0 and 0.05 % (Hecla138A, Hecla37-0.4 % C, Hecla37-0.6 % C, and Rex535Ni), while the other four (Hecla ATV, Railsteel-1, Railsteel-3, and NiSteel) have a maximum negative relative change between -0.3 % and -0.6 %.
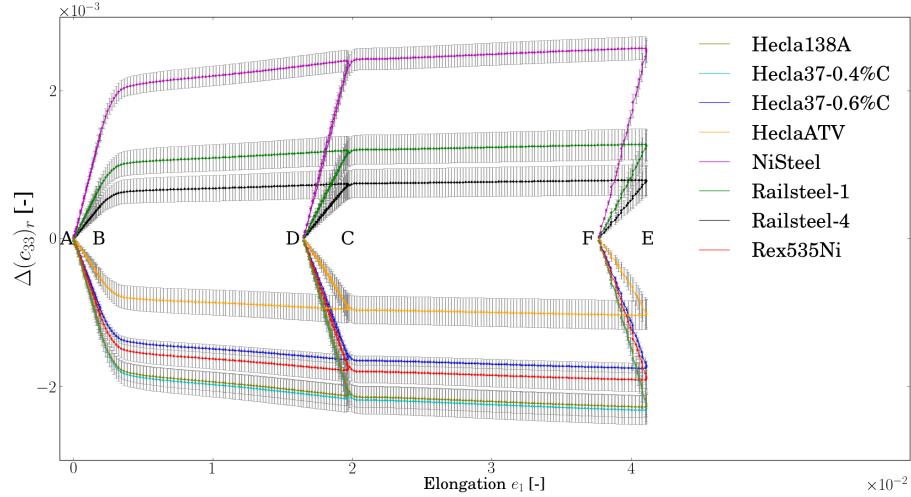
Figure 5.22: Simulated relative sound velocity development of longitudinal waves propagating perpendicular to the applied stress (c_{33}) based on elastic properties given in Table 4.4

For the shear sound velocity c_{32} polarised perpendicular to the applied tension, the simulated results based on the 8 steels have been presented in Fig. 5.24. In Fig. 5.23 showing the plot of the shear waves polarised parallel to the applied tension it can be seen that the three steels with the largest maximum negative c_{31} change (Railsteel-1, Railsteel-3, and NiSteel), are the three steels with the least maximum absolute change for the c_{32} sound velocity (between 0 and 0.05 %), and it is slightly positive. The four steels with the least absolute relative change for the c_{31} are all negative and with a maximum negative relative change betwen -0.3 % and -0.4 % for the c_{32} presented in Fig. 5.24. The last steel (HeclaATV) has a negative development for both the c_{31} and c_{32}, with a maximum negative relative change of approximately -0.4 % and -0.8 % respecitively.

Comparing the findings of the three different simulated relative sound velocities with the acousto elastic constants presented in Table 4.4 it is clear that the 8 steels can be grouped in three groups based on the simulations and the acoustoelastic constants. The three groups have been divided based on the slope of the relative change in the different sound velocities, longitudinal c_{33}, shear polarised parallel to applied tension c_{31}, and shear polarised perpendicular to applied tension c_{32}. Recall from Secs. 2.3 and 3.5 that the acoustic propagation direction have been perpendicular to the applied tension.

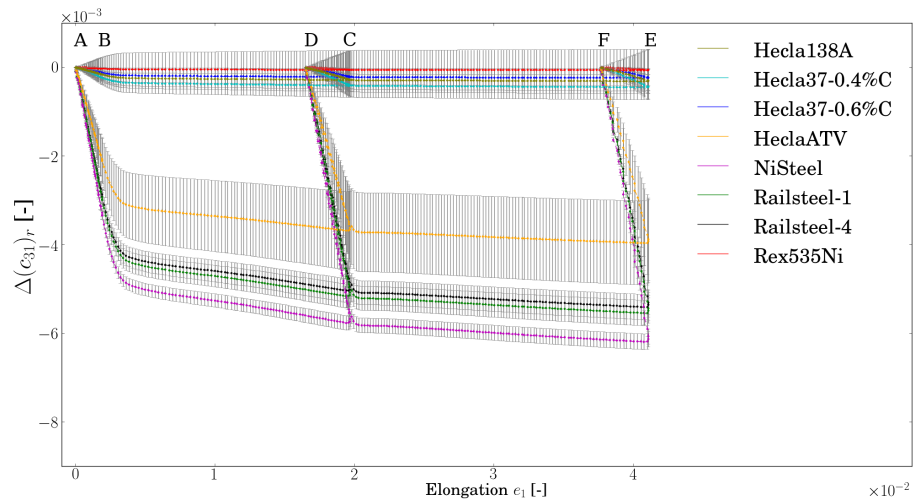**Figure 5.23:** Simulated relative sound velocity development of shear waves propagating perpendicular to-, and polarised parallel to the applied stress (c_{31}) based on elastic properties given in Table 4.4
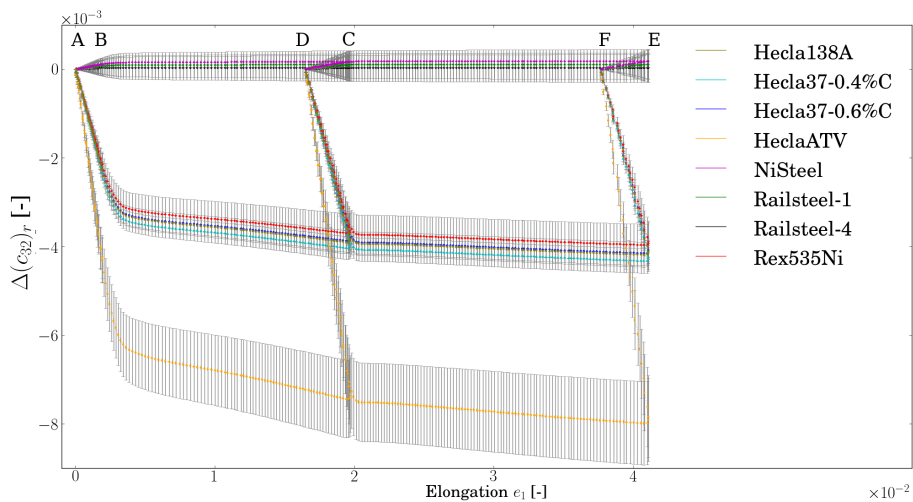
Figure 5.24: Simulated relative sound velocity development of shear waves both propagating and polarised perpendicular to the applied stress (c_{32}) based on elastic properties given in Table 4.4

Group 1 is the collection of steels that for increasing elongation e_1 have shown a decrease in c_{33} (denoted by $dc_{33}/de_1 < 0$), relative small, but negative, changes in c_{31} (denoted by $dc_{31}/de_1 \lesssim 0$), and a decrease in c_{32} (denoted by $dc_{32}/e_1 < 0$). Similarly Group 2 have shown a decrease in all of the sound velocities, i.e. $dc_{33}/de_1 < 0$, $dc_{31}/de_1 < 0$, and $dc_{32}/de_1 < 0$. Group 3 have shown an increase in c_{33} ($dc_{33}/de_1 > 0$), a decrease in c_{31} ($dc_{31}/de_1 < 0$), and relative small, but positive, changes in c_{32} ($dc_{32}/de_1 \gtrsim 0$). The development of the longitudinal sound velocity c_{33} can be seen in Fig. 5.22, while the shear sound velocities c_{31} and c_{32} can be seen in Figs. 5.23 and 5.24. The groups of steels together with the acoustoelastic constants have been presented in Table 5.6.

From these groups it can also be confirmed that steels with similar acousto elastic constants behave in similar manners. This is especially obvious when looking at the numerical value of the constants A and B within the different groups. These results will be further discussed in Sec. 7.6.

Table 5.6: 8 steels from Table 4.4 grouped by simulated behaviour of sound velocities toghether with Lamé and Landau & Lifshitz constants in GPa

Material	Lamé constants		Landau & Lifshitz constants		
	λ	μ	A	B	C
Group 1: $\frac{d}{de_1}(c_{33}) < 0$, $\frac{d}{de_1}(c_{31}) \lesssim 0$, $\frac{d}{de_1}(c_{32}) < 0$					
Hecla 37 (0.4 % C)	111 ± 1	82.1 ± 0.5	-44.3 ± 2.0	-282 ± 30	-179 ± 35
Hecla 37 (0.6 % C)	110.5 ± 1	82.0 ± 0.5	-41.8 ± 1.5	-261 ± 20	-67.0 ± 10
Hecla 138A	109 ± 1	81.9 ± 0.5	-44.3 ± 2.5	-265 ± 30	-162 ± 25
Rex 535 Ni steel	109 ± 1	81.8 ± 0.5	-42.3 ± 3.8	-240 ± 50	-87.5 ± 25
Group 2: $\frac{d}{de_1}(c_{33}) < 0$, $\frac{d}{de_1}(c_{31}) < 0$, $\frac{d}{de_1}(c_{32}) < 0$					
Hecla ATV austenitic	87 ± 2	71.6 ± 3	-25.0 ± 2.5	-552 ± 80	17.0 ± 10
Group 3: $\frac{d}{de_1}(c_{33}) > 0$, $\frac{d}{de_1}(c_{31}) < 0$, $\frac{d}{de_1}(c_{32}) \gtrsim 0$					
Nickle-steel S/NVT	109.0 ± 1	81.7 ± 0.2	-785 ± 7.0	-279 ± 6.9	-223 ± 21
Rail steel sample 1	115.8 ± 2.6	79.9 ± 1.8	-714 ± 19	-266 ± 27	18.0 ± 28
Rail steel sample 4	110.7 ± 2.5	82.4 ± 1.9	-724 ± 20	-254 ± 27	48.0 ± 28

5.7.3 Longitudinal and shear velocity ratios

As described in Sec. 2.7 the thickness dependence of the measured sound velocities presented in Sec. 5.6 can be removed by investigating the relative change of the ratio

5. EXPERIMENTAL AND THEORETICAL RESULTS

between the sound velocity of longitudinal and shear waves instead. To be able to compare these measurements with theoretically simulated values the relative change of the two ratios c_{33}/c_{31} and c_{33}/c_{32} have been calculated based on the simulated results presented in Sec. 5.7.1 above. Note that the theory predicts two different developments of the shear sound velocity based on their polarisation as shown in Sec. 5.7.2, while only one distinct development have been measured as presented in Sec. 5.6. This discrepancy will be further discussed in Sec. 7.6.1, however, both simulated alternatives have been presented here to be able to compare the simulation and measurement results. Fig. 5.25 shows the relative change in the ratio c_{33}/c_{31} for the 8 steels. For the Group 3 steels (Railsteel-1, Railsteel-4, and NiSteel) which have a positive relative change in c_{33} and negative relative change in c_{31}, the ratio c_{33}/c_{31} shows a larger maximum relative change (between approximately 0.6 % and 0.9 %) than the individual maximum absolute relative changes in c_{33} and c_{31} respectively and has "enhanced" the relative change as expected. For the Group 2 steel (HeclaATV) the relative change in both c_{33} and c_{31} are negative, but the relative change in c_{33} has a gentler slope in the elastic regions than c_{31}, and the relative change of the ratio is thus positive as seen in Fig. 5.25. Group 1 (Hecla37-0.4 % C, Hecla7-0.6 % C, Hecla138A, and Rex535Ni) also have a negative relative change in both c_{33} and c_{31}, however the relative change in c_{31} is much less prominent than in c_{33}, and thus the relative change in the ratio c_{33}/c_{31} is negative. For Group 1 and 2 the ratio between the longitudinal c_{33} and the shear c_{31} does not enhance the relative change from the respective individual relative change, but rather diminish the effect compared to the maximum relative change in either of the two individual sound velocities because both change in the same direction.

Fig. 5.26 is similar to Fig. 5.25, but shows the ratio c_{33}/c_{32}, where the shear sound velocity is polarised perpendicular to the applied tension. Comparing the relative change of c_{33} in Fig. 5.22 and c_{32} in Fig. 5.24 it is clear that the three groups experience relative sound velocity changes for both c_{33} and c_{32} with the same sign, and thus the relative change of the ratio is diminished compared to the maximum relative change in either of the two individual sound velocities. For the steels in Group 2 the relative change is positive, and $c_{33}{}'(e1) > c_{32}{}'(e1)$, thus leading to a positive relative change for the ratio c_{33}/c_{32}. For the steels in Group 1 and 3 the relative change is negative, and $c_{33}{}'(e1) < c_{33}{}'(e1)$, thus also leading to a positive relative change for the ratio c_{33}/c_{32}.
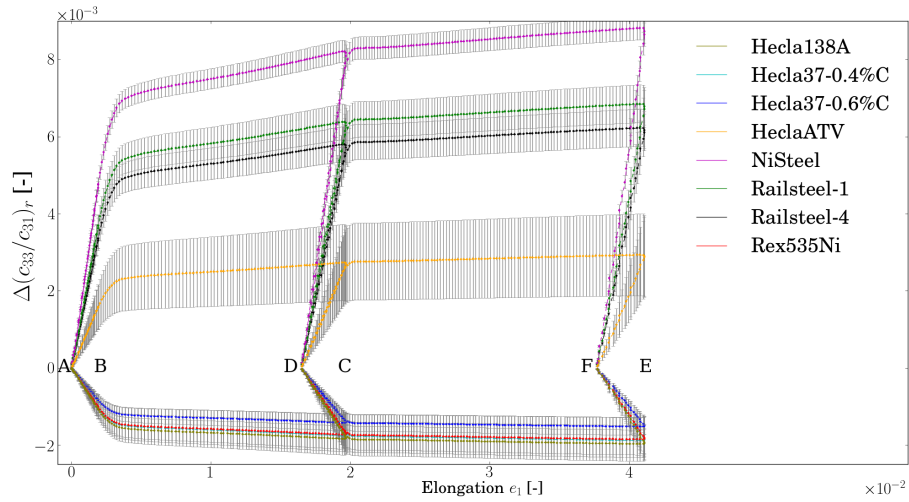
Figure 5.25: Simulated relative change of ratio between longitudinal (c_{33}) and shear sound velocity polarised parallel to applied stress (c_{31}) based on elastic properties given in Table 4.4
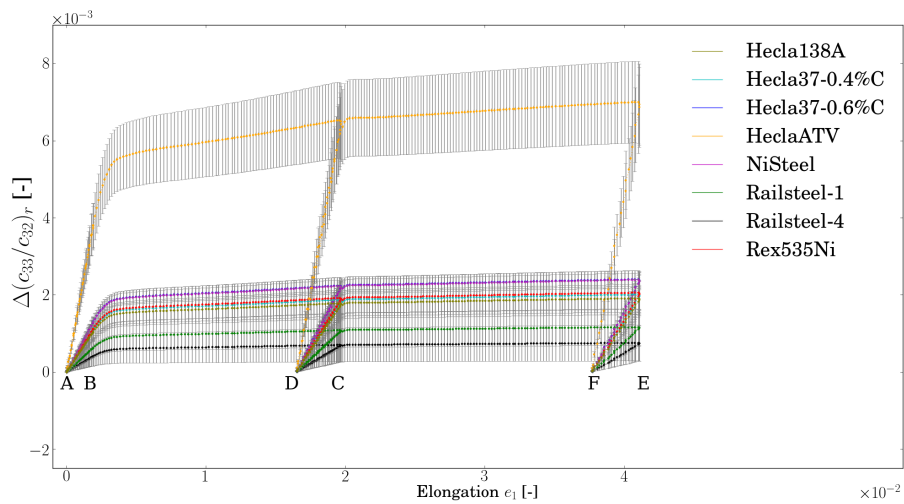
Figure 5.26: Simulated relative change of ratio between longitudinal (c_{33}) and shear sound velocity polarised perpendicular to applied stress (c_{32}) based on elastic properties given in Table 4.4

As seen from the measurement results presented in Sec. 5.6, Fig. 5.19 the measured longitudinal sound velocity experience a positive relative change, while the measured shear sound velocity experience a negative relative change, for increasing elastic deformation in the elastic regions (AB, CD, EF). This behaviour have also been seen for the steels in Group 3, for the longitudinal c_{33} and shear c_{31}. Thus only these steels and modes have been included when comparing the simulation results with the measurement results in Sec. 5.7.4.

5.7.4 Comparison between simulations and measurements

In Figs. 5.27 to 5.29 the simulated relative change in sound velocities c_{33}, c_{31}, and the ratio c_{33}/c_{31} respectively, for the Group 3 steels found in literature (see Table 5.6) have been plotted as solid lines togheter with the corresponding measurement quantities presented in Figs. 5.19 and 5.20. As seen in all of the figures there are similarities between the simulated behaviour (solid lines) and the measured behaviour for both the longitudinal sound velocity (denoted $c(L1, e_3)$ and $c(L2, e_3)$ in Fig. 5.27) and the sound velocity of the shear waves polarised parallel to the applied tension (denoted $c(S3, e_3)$ in Fig. 5.28). The measured relative change of the frequency (or sound velocity) ratios are denoted L1/S3 and L2/S3. Note that the measurements plotted here are the same as those presented together in Figs. 5.19 and 5.20 in Secs. 5.6 and 5.6.2. A more thorough discussion of these results have been done in Sec. 7.6.

It is noted that the predicted split of the unstressed shear sound velocity into the perpendicular polarised c_{31} and c_{32} which should experience different relative sound velocity change have not been seen in the measured and estimated sound velocity $c(S3, e_3)$. $c(S3, e_3)$ shows most resemblance with the c_{31} for the Group 3 steels, and c_{32} has thus not been compared in this section. The apparent discrepancy between the theory and the observed results has been discussed further in Sec. 7.6.1.
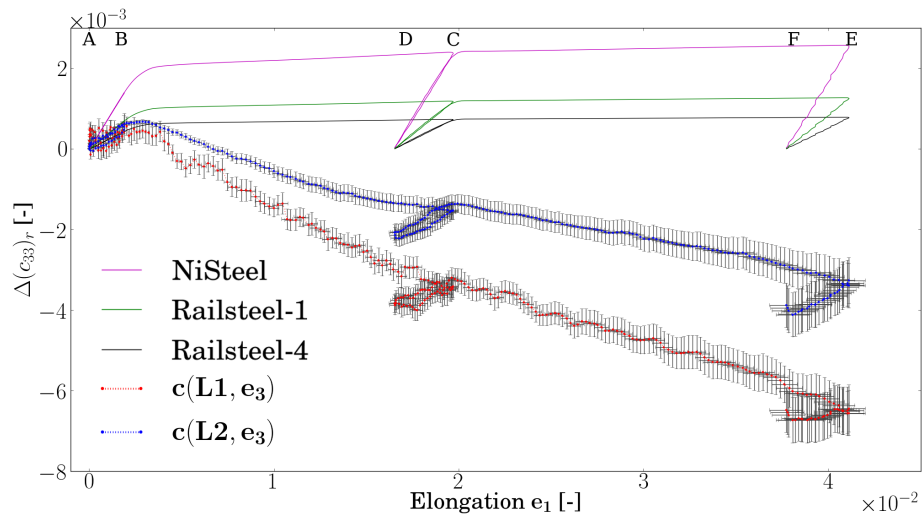
Figure 5.27: Comparison of relative sound velocity development of longitudinal waves measured ($c(L1, e_3)$ and $c(L2, e_3)$ from Fig. 5.19) and the simulated longitudinal sound velocity c_{33} for the Group 3 steels in Fig. 5.22
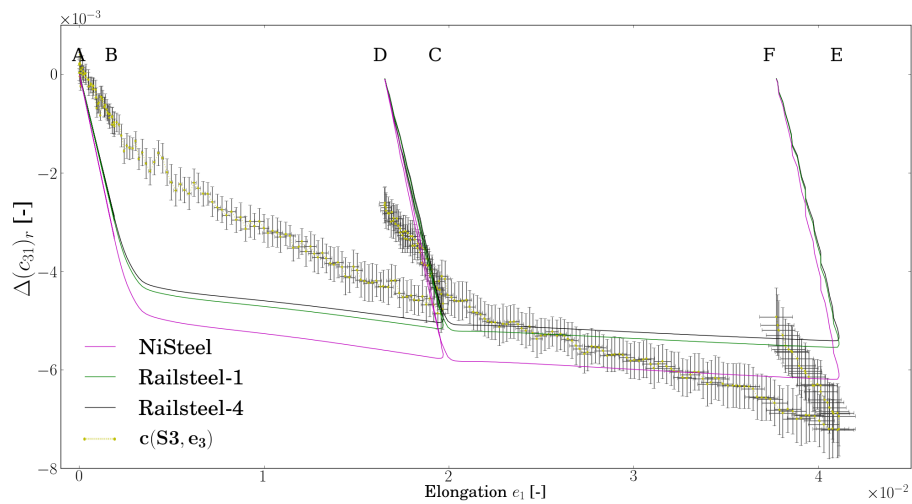
Figure 5.28: Comparison of relative sound velocity development of shear waves measured ($c(S3, e_3)$ from Fig. 5.19) and the simulated shear sound velocity c_{31} for the Group 3 steels in Fig. 5.23

141
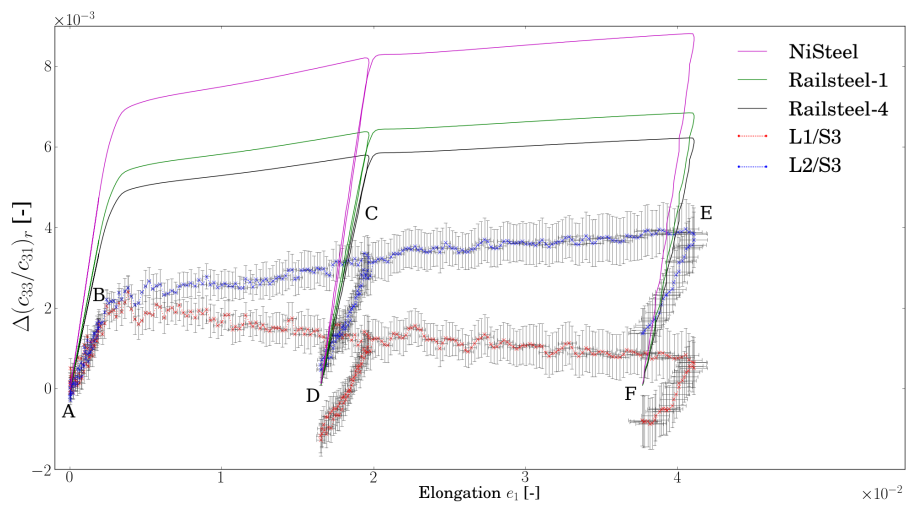
Figure 5.29: Comparison of relative change of the ratio between measured longitudinal and shear sound velocities (or resonance frequencies $L1/S3$ and $L2/S3$ from Fig. 5.20) and the simulated relative change of the ratio c_{33}/c_{31} for the Group 3 steels in Fig. 5.25

6

Uncertainty analysis

6.1 General

This section is based on the intrinsic uncertainties in the measurment equipment and the experimental measurement results presented in Ch. 5. It strives to identify, present and quantify the combined uncertainties related to each relevant measurement quantity. The uncertainty analysis has been done with reference to the document *Guide to the expression of uncertainty in measurement* known as the GUM [74]. The details of this document has not been presented here, but the relevant equations have been presented as they fit in to the subsequent order of this chapter.

Note that for convenience the calculation of propagated uncertainties has been done using the numerical computation library *Uncertainties: a Python package for calculations with uncertainties* [108]. A test has been run to verify that the computation library works as expected and the result from this has also been presented in Sec. 6.5. This means that although the combined uncertainty expressions derived in this chapter have not been used directly in the propagation of uncertainties presented in Ch. 5, they have been included here to better understand which intrinsic uncertainties contribute to the overall uncertainties. The input uncertainties used to estimate the combined uncertainties presented in Ch. 5 through the Python package have been presented in Tables 6.1, 6.4, 6.5, 6.7, 6.8, and 6.11, as well as resulting propagated uncertainties. In addition the propagated uncertainties for the sound velocity estimates and linear elastic moduli have also been presented in Tables 6.2 and 6.9.

6. UNCERTAINTY ANALYSIS

This chapter has been ordered based on the main result (i.e. relative change of frequency ratios and subsequent estimated sound velocities). The functional relationship of these results have been analysed with respect to contributing uncertainty factors. Each contributing factor has been analysed and broken down into its own constituent uncertainties.

The uncertainties presented in this chapter have been divided into three groups, namely the standard deviation of a measurand, the standard deviation of the mean of a measurand, and the combined standard uncertainty of a measurement result, and/or estimated results. The difference between these uncertainties are readily available in [74]. However, in the experience of the author the application of these different types of uncertainty measures might lead to some confusion if not explicitly explained. If the reader is familiar with the GUM [74] and the above mentioned uncertainty expressions he or she may skip the rest of this section and continue at Sec. 6.2.

The most fundamental uncertainty in a measurand quantity q is called the standard deviation σ_q and is estimated by the *experimental standard deviation* $s(q)$ of n independent observations q_k $(k = 1 \ldots n)$ under the same measurement conditions. This quantity characterises the dispersion of the observed values q_k about their mean $\bar{q}$ and is estimated by [74, Sec. 4]

$$\sigma_q^2 \approx s^2(q) = \frac{1}{n-1} \sum_{k=1}^{n} (q_k - \bar{q})^2. \tag{6.1}$$

The next level of uncertainty is closely related to the experimental standard deviation. However, instead of describing how widely spread one independent observation of a quantity may be from the mean value of that quantity (Eq. (6.1)), it quantifies how well the observed mean $\bar{q}$ of n independet observations estimates the expectation value μ_q of q (note that a barred variable signify the mean value over k measurments of that variable). Thus this uncertainty is called the *experimental standard deviation of the mean*, and it is estimated by [74, Sec. 4]

$$\sigma^2(\bar{q}) \approx s^2(\bar{q}) = \frac{s^2(q)}{n}, \tag{6.2}$$

where $s(q)$ is the experimental standard deviation estimating the standard deviation σ_q of the quantity q. The experimental standard deviation of the mean calculated by Eq.

(6.2) is a good approximation of the standard uncertainty $u(q_i)$ where $q_i = \bar{Q}_i$ is the estimate of an input quantity Q_i [74, Sec. 4]. That is

$$u(q_i) \approx s^2(\bar{q}_i). \tag{6.3}$$

The standard uncertainty $u(q_i)$ can also be obtained in other ways which have been treated in [74, Sec. 4].

Finally, when estimating a quantity based on other measured quantities it is necessary to propagate the uncertainty of the measured quantities to the estimated one. The uncertainty of the estimated value has been termed the *combined standard uncertainty*, and is denoted by $u_c(y)$ where $y = f(q_1, \ldots q_i)$ is the estimated quantity with the functional relation $f(q_1, \ldots q_i)$ depending on i input quantities q_i [74, Sec. 5]. Because the absolute value of the standard uncertainties may vary significantly between measurands the relative standard uncertainty, which is the standard uncertainty divided by the absolute value of the measurand as [74, Sec. 4]

$$u_r = \frac{u(y)}{|y|}, \tag{6.4}$$

have also been used in this work .

The combined standard uncertatinty, $u_c(y)$, of a measurement result is an unambiguous way to present the uncertainty, and has been used throughout this work where applicable. All uncertainties reported and plotted in this work have used the standard uncertainty (coverage factor $k_p = 1$) which has a confidence level of approximately 68.3 % if not stated otherwize [74]. For the uncertainties obtained from other works the original confidence level and probability distribution has been presented if available, before it has been converted to a standard uncertainty and used in this work. If no information about the confidence level was available it has been assumed that it was reported as a standard uncertainty of a normal distribution.

This chapter has been ordered by presenting the uncertainties related to the acoustic measurements and the estimated change in sound velocities first. Then the uncertainties related to the underlying measurement quantities of geometry and geometry change have been presented before any supporting measurement quantities like for example the estimated stress and linear elastic properties. Finally a few supporting tables have been included to summarise and describe the different uncertainties presented in this chapter.

6.2 Relative change in ratio of longitudinal and shear frequencies and/or sound velocities

The measured relative change of the ratio between longitudinal and shear sound velocities presented in Sec. 5.6.2 is a function of the longitudinal and shear resonance frequencies toghether with their unstressed reference values as seen from Eq. (2.125). The relative combined standard uncertainty according to [74] for both the relative frequency ratio and the relative sound velocity ratio can be expressed by

$$
\begin{aligned}
u_{cr}(\Delta(c_l/c_s)_r) \;\; &= \;\; \frac{u_c(\Delta(c_l/c_s)_r)}{|\Delta(c_l/c_s)_r|} = \frac{u_c(\Delta(f^{(n_l)}/f^{(n_s)})_r)}{|\Delta(f^{(n_l)}/f^{(n_s)})_r|} \\[2mm]
&= \; \Bigg[\left(\frac{u(f^{(n_l)})}{f^{(n_l)}} \right)^2 + \left(\frac{u(f^{(n_s)})}{f^{(n_s)}} \right)^2 + \left(\frac{u(f_0^{(n_l)})}{f_0^{(n_l)}} \right)^2 + \left(\frac{u(f_0^{(n_s)})}{f_0^{(n_s)}} \right)^2 \\[2mm]
&\quad 2\Bigg\{ \frac{u(f_0^{(n_l)})}{f_0^{(n_l)}} \frac{u(f^{(n_s)})}{f^{(n_s)}} r(f_0^{(n_l)}, f^{(n_s)}) + \frac{u(f^{(n_l)})}{f^{(n_l)}} \frac{u(f_0^{(n_s)})}{f_0^{(n_s)}} r(f^{(n_l)}, f_0^{(n_s)}) \\[2mm]
&\quad - \frac{u(f^{(n_l)})}{f^{(n_l)}} \frac{u(f^{(n_s)})}{f^{(n_s)}} r(f^{(n_l)}, f^{(n_s)}) - \frac{u(f_0^{(n_l)})}{f_0^{(n_l)}} \frac{u(f_0^{(n_s)})}{f_0^{(n_s)}} r(f_0^{(n_l)}, f_0^{(n_s)}) \Bigg\} \Bigg]^{1/2}
\end{aligned}
\tag{6.5}
$$

where the terms within the curly brackets {} are the covariance terms expressed with the correlation coefficient $r(x_i, x_j)$ between measurand x_i and x_j.

Each of the measured frequencies in Eq. (6.5) may have contributing uncertainty factors from the measurement system, the way they have been measured, and systematic contributions. This section aims to discuss the different contributions and present an estimate of the overall uncertainties in the estimated ratios.

The acoustic measurement system was set up with a sampling frequency of the resulting voltage from the acoustic pressure acting on the ring receiver (RX) of 15 Mhz during each acoustic shot. The relevant acoustic resonance frequencies lie between 300 and 800 kHz, which results in approximately 20 to 50 measurepoints of the RX-voltage (from the acoustic pressure) over the cycle of one sinusodial wave and a total of 900 measurepoints over the duration of interaction between the acoustic wave and the test specimen (90 μs). The extraction of the peak location in the FFT can be done to numerical precision and the uncertainty related to the numerical extraction of the resonance frequencies have thus been treated as negligible. However, the tail of the signal used to extract the resonance frequencies has a duration of 60 μs and the sampling frequency of the DAQ setup was 15 MHz. This yields a resolution in the

FFT frequency spectrum of Δf^{FFT} =16.7 kHz [66, ch. 9] as described in Sec. 3.5.1. This resolution is a measure of how close two distinct frequencies can be in the FFT frequency spectrum without merging into a single entity, and is inversly proportional to the length of the signal analysed and/or the number of sampling points within this signal. This resolution is sufficiently good to distinguish the resonance modes presented in Table 3.2. However, it is not good enough to distinguish the potential separation of shear resonance modes due to the effect of polarised particle motion as explained in Sec. 2.3, Eqs. (2.98) and (2.99). Thus the measured S3 resonance mode for a sufficiently large applied stress should be the combined effect of shear waves with both polarisation directions. This also means that the estimated shear sound velocity also will be the result of the combined effect of shear waves with both polarisation directions.

Among external sources of uncertainty, both acoustic and electromagnetic noise can affect the recorded acoustic pressure. Acoustic noise in the air surrounding the water tank has been assumed to be negligible because of the high attenuation of acoustic energy in air compared to the signal generated in the water tank. The tension machine in itself, as well as other acoustic noise propagating through the floor of the laboratory, can carry acoustic noise to the water tank which again will influence the recorded acoustic pressure. This noise should vary randomly, and thus by sampling consequtively and averaging over a number of samples, this effect should be minimised. The same applies for electromagnetic noise. The interference of eloctromagnetic noise on the cicuitry can also be mitigated by shielding the electronic circuits using a Faraday shield. Both the wiring and electronic circuits have been wrapped in aluminum foil and grounded. Some of the initially observed noise was effectively removed in this way. Other than these and possible other external factors, the uncertainties are related to signal excitation, propagation, response of target, signal capturing and internal electronic processing. The total uncertainty contribution from all these factors have been estimated by calculating the standard deviation over a set of acoustic shots done under close to the same conditions.

As described in Ch. 5 each test has been divided into a set of bins where relevant measurements have been grouped to be able to compare measured values across different test specimens. However, this benefit comes at a cost. Since the bin spans a small range of states, the standard deviation of the values in the bin will incorporate both the random measurement uncertainty of the measurand as well as actual variation due to change of measurement state. For linear data the arithmetic mean over the binned data

will represent a good approximation of an interpolated value at the midpoint of the bin. However, the standard deviation over each bin will be much larger for liner data than the actual uncertainty of the individual measurements. Thus the estimated experimental uncertainty for linear data will be larger than it actually is (i.e. a large portion of the estimated standard uncertainty over the bin is actually due to change of state). On the other hand, for data with large measurement uncertainties the measurepoints across the bin will look more stochastic. For this type of data the standard deviation over the bin will still incorporate both the measurement uncertainty and variation due to change of state. It can thus be used as an estimate for the upper limit of the measurement uncertainty of the binned measurement quantity. These bins span approximately 1s and include ∼40 acoustic shots. In this time the test specimen experienced a change in applied displacement of approximately 0.1 mm according to the description in Sec. 3.3. This corresponds to a variation of the stress state across the bins depending on its position in the load history. For the elastic regions the variation has a standard deviation across the bin of approximately 8 MPa (or 0.04 % elongation in the x_1-direction), while for the plastic region the standard deviation of the stress state is approximately 1 MPa (or 0.06 % elongation in the x_1-direction) across each bin. Note that the variation in measured elongation in the plastic regions are somewhat larger than in the elastic region even though the displacement velocity should be held constant by the control unit. This is probably an effect of the accuracy of the control system and the plastic response of the test specimens. The background for these values have been explained and further discussed in Sec. 6.4.1.2.

Because of the change in stress- / strain-state the sound velocity may change slightly across each bin. In addition, the test specimen will also experience a slight thinning of the sample which affects the resonance frequency across each bin (Eq. (2.121)). Thus the standard deviation of the measured resonance frequencies in each bin incorporate both the random measurement uncertainties, some variation due to thinning of the sample, and some variation due to actual change in sound velocity. Since this standard deviation includes both variation due to thinning and sound velocity change in addition to the random measurement uncertainties it has been assumed to be a good measure of the upper bound of uncertainty related to the unspecified random variations. The calculated standard uncertainty over each bin for the measured $f^{(n_l=1)}$ resonance frequencies

have been plotted in Fig. 6.1. This plot shows one coloured line for each test specimen, where each point represent the standard uncertainty $u(f^{(n_l=1)})$ for the individual bins. For the L1 resonance mode it can be seen that the standard uncertainty is less than approximately 80 Hz, which corresponds to a relative uncertainty, denoted by the subscript $_r$ (as in $u_r(f^{(n_l=1)})$ Eq. (6.4)), of approximately $\lesssim 0.02$ %. Fig. 6.2 shows the relative uncertainties based on the measured standard uncertainties presented in Fig. 6.1. Corresponding figures have also been made for the $f^{(n_l=2)}$ and $f^{(n_s=3)}$ resonance frequencies as well and these have been included in App. C.3, Figs. C.30, C.31, C.32, and C.33. The maximum observed standard uncertainties observed in these plots have been presented in Table 6.1.
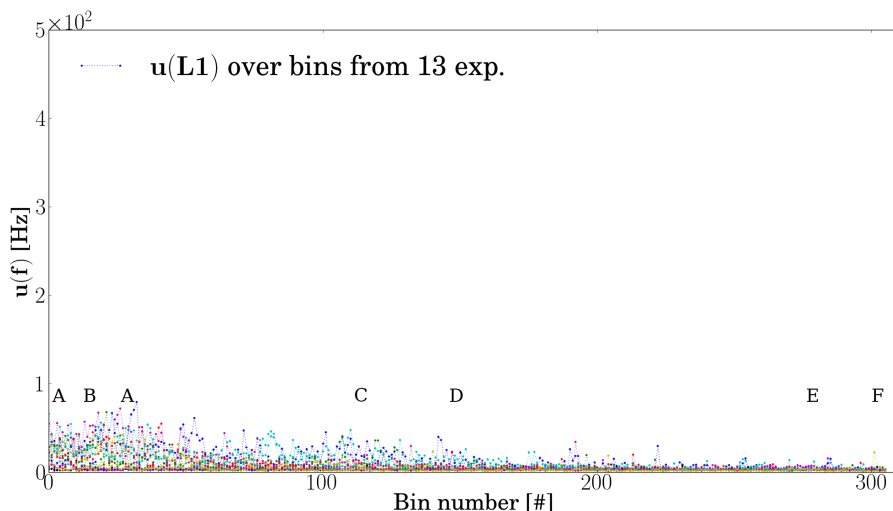
Figure 6.1: Standard uncertainty within each bin of the L1 resonance frequency throughout each of the 13 tests

Note that in the plots the short forms L1, L2, and S3 have been used to represent the frequencies $f^{(n_l=1)}$, $f^{(n_l=2)}$, and $f^{(n_s=3)}$ as introduced in Sec. 5.5. The subscript $_r$ represent in the context of uncertainties the relative uncertainty and follows the uncertainty symbol u, while for the above short forms it denotes the relative change (i.e. $L1_r = \Delta f_r^{(n_l=1)} \equiv \Delta f^{(n_l=1)}/f_0^{(n_l=1)}$ as introduced in Eq. (2.122)).

The best estimate of the upper bound of the uncertainties related to the acoustic measurements could have been taken as the standard deviation of the resonance frequencies in a bin where the displacement and force has been fixed. However, because the
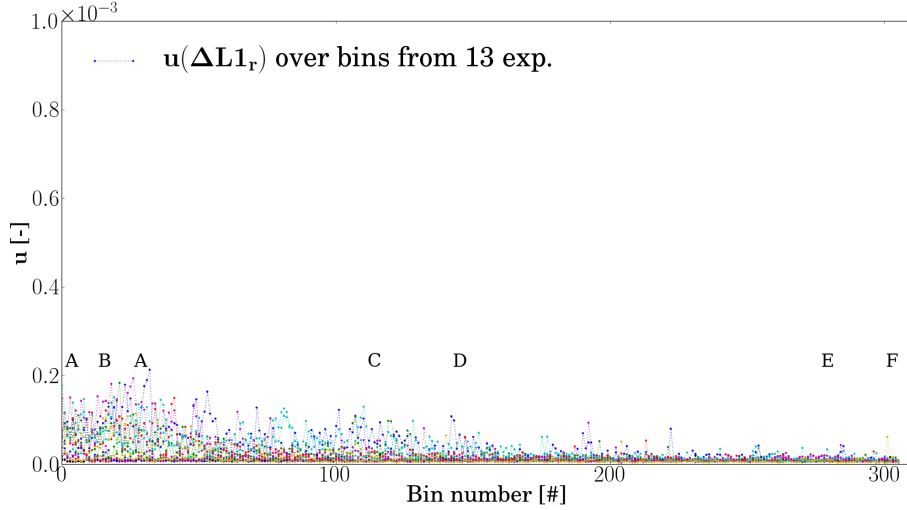
Figure 6.2: Standard uncertainty within each bin of the relative change in the L1 resonance frequency throughout each of the 13 tests

force and displacement vary in such a "static" configuration because of the fluctuations around the given set point in the integral control unit, the observed uncertainty in e.g. bin 30 (at zero force after the first unloading) has not been observed to be significantly lower than the uncertainty in a bin under dynamic deformation.

The systematic uncertainty contribution related to the beam effect described in Secs. 2.6.2 and 3.6.3.1, has been accounted for when presenting the estimated longitudinal sound velocity in Sec. 5.6, Fig. 5.17 (It has also been accounted for when considering the shear sound velocity $c(f^{(n_s=3)})$ in Fig. 5.18 by assuming that the correction factor $\eta^{(n_s=3)} = 1$). The systematic uncertainty estimated through Eq. (3.11) for the L1 mode has been caluclated to be an underprediction of approximately 5-6 %, while the L2 mode has been overpredicted with approximately 1-2 % (see Sec. 5.6). The uncertainty introduced in the absolute value of the sound velocity by correcting this systematic effect has been ignored since this work does not require the absolute value of the estimated sound velocities. Assuming that the beam effect is constant throughout the tests (argued in Sec. 3.5.1) this systematic uncertainty cancel out when looking at relative changes of the frequencies or sound velocities. Thus it has been ignored in the following, and only been included in Table 6.1 for completeness. This has been

discussed further in Sec. 7.4.1.

As described in Sec. 5.5 the absolute value of the unstressed resonance frequency for each mode can vary a lot across the test specimens (see Figs. 5.9, C.21, C.22). Since this work has investigated the relative change in sound velocity each resonance frequency has been divided by a reference frequency to calculate a relative change (see the equivalent Eq. (2.122) for relative sound velocity). This reference frequency can be arbitrarily chosen and is a pure mathematical operation that does not carry any uncertainty in itself. Thus it has been assumed that $u(f_0^{(n_l)}) = u(f_0^{(n_s)}) = 0$, and the only non-zero covariance term in Eq. (6.5) are the ones not including any of the reference frequency values. The reference frequency has for each test specimen and each resonance mode been chosen so that it is measured at the zero stress state. This happens in bin number 30, which has been controlled to be at the first zero stress state (without any plastic deformation) after the first unloading, and have thus been used as the reference frequency.

The uncertainties related to the individual test specimens have been discussed above. To increase the confidence in the observed results, 13 acoustic experiments have been performed under as close to identical conditions as practically reasonable. As described in Sec. 6.1 the averages over the relevant number of experimental measurements for any measurement quantity $(\bar{q}_i)$ are the values used when presenting results and when estimating derived results in Ch. 5.

Note that because the three relevant resonance frequencis of the first and second longitudinal mode $(f^{(n_l=1)}, f^{(n_l=2)})$, and the third shear mode $(f^{(n_s=3)})$, are all extracted from the same time signal of acoustic pressure. The uncertainties related to any external variation should thus be close to fully correlated since all of the extracted modes experience the same external influence. However, the uncertainty related to the actual propagation of the different modes in the test specimen may not be fully correlated. The results estimated based on the ratio between any two of the resonance modes have been presented with the correlated uncertainty. The correlation coefficient r has been estimated according to [74] as

$$r(q_i, q_j) = \frac{u(q_i, q_j)}{u(q_i)u(q_j)} \approx \frac{s(\bar{q}_i, \bar{q}_j)}{s(\bar{q}_i)s(\bar{q}_j)}. \qquad (6.6)$$

where the standard deviations have been calculated according to Eq. 6.1 and the co-
variance term has been calculated by [74]

$$s(\bar{q}_i, \bar{q}_j) = \frac{1}{n(n-1)} \sum_{k=1}^{N} (q_{i_k} - \bar{q}_i)(q_{j_k} - \bar{q}_j), \qquad (6.7)$$

for the quantity pairs q_i and q_j corresponding to the binned data of $f^{(n_l=1)}$ and $f^{(n_s=3)}$,
$f^{(n_l=2)}$ and $f^{(n_s=3)}$, and $f^{(n_l=1)}$ and $f^{(n_l=2)}$.

To investigate the contribution from correlation the combined relative uncertainty
$u_{cr}(f_i, f_j)$, where f_i is either $f^{(n_l=1)}$ or $f^{(n_l=2)}$ and f_j is either $f^{(n_s=3)}$ or $f^{(n_l=1)}$ (Eq.
6.5 with $u(f_0^{(n_l=1)}) = u(f_0^{(n_l=2)}) = u(f_0^{(n_s=3)}) = 0$) has been divided by the sum of
squares for the relative measurement uncertainty of the different resonance modes (i.e.
Eq. (6.5) as above with the correlations term $r(f_i, f_j) = 0$). This ratio has been plotted
in Fig. 6.3. The plot shows that the correlation between the frequencies may increase
or decrease the combined uncertainty compared to an assumption of not correlated
frequencies. However, as can be seen the negative contributions are less than approx-
imately 10 % and the positive contributions are less than approximately 20 % for all
of the three ratios investigated here. Thus an assumption of uncorrelated frequencies
would not have changed the uncertainty contribution significantly.
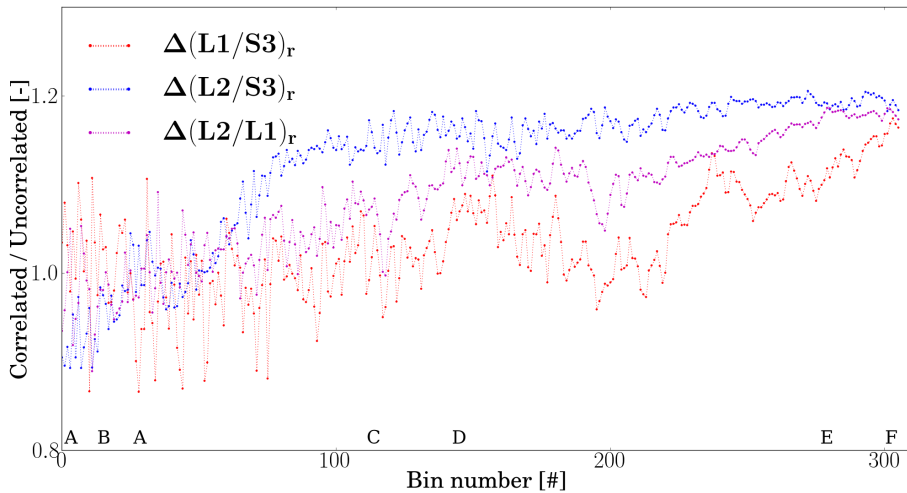
**Figure 6.3: Ratio of the relative combined uncertainty of the frequency ratios
with and without correlation between the three resonance modes L1, L2, and
S3.**
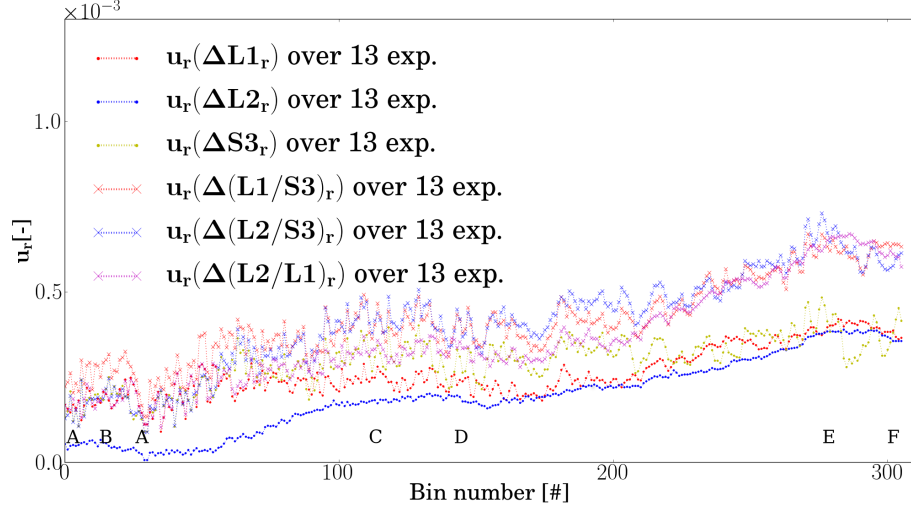
Figure 6.4: Relative combined uncertainty of the relative development of the three resonance modes L1, L2, and S3, and their ratios over the 13 acoustic experiments.

The maximum standard uncertainty per experiment (as shown in Figs. 6.1 and 6.2 for absolute and relative frequencies respectively) have been estimated as described in this section and is based on the absolute and relative frequency measurements from the 13 test specimens presented in Figs. 5.9 and 5.13 in Sec. 5.5 (L2 mode) and Figs. C.21 to C.24 in App. C.3 (L1 and S3 modes). Fig. 6.4 shows the experimental standard uncertainty over the 13 test specimens where acoustic measurements have been performed. The maximum of each uncertainty presented in this section together with the maximum of the standard uncertainty per experiment have been summarised in Table 6.1 for $f^{(n_l=1)}$, $f^{(n_l=2)}$, $f^{(n_s=3)}$, their relative change, and the relevant ratios.

In this work all result plots of the average over several experiments include the estimated standard uncertainty over the relevant experiments as dark grey error-bars (standard deviation of the mean). Those result plots which include several individual test specimens include the standard uncertainty of the values within each bin plotted as light grey error-bars.

From the uncertainty values presented in Table 6.1 it can be seen that the experimental standard uncertainty over the 13 test specimens are dominating the uncertainty contributions (i.e. the standard uncertainty over the 13 test specimens are close to

twice the maximum observed standard uncertainty within any of the individual test specimens, or more).

Table 6.1: Uncertainty in frequency measurements

Variable x_i	$\mu(x_i)$		$u(x_i)$		Confidence level [%]	$\frac{u(x_i)}{\|x_i\|}$ [%]	Based on
Instrumentation							
f^{FFT}	$\sim$300-800	kHz	-	Hz	68	negligible	
FFT resolution							
Δf^{FFT}	$\sim$300-800	kHz	16.7	kHz	68	2-6	
Systematic uncertainty related to the beam diffraction effect							
$f^{(n_l=1)}$	$\sim$371-375	kHz			68	$\sim$ -6	Fig. 3.9
$f^{(n_l=2)}$	$\sim$794-805	kHz			68	$\sim$ 2	Fig. 3.9
$f^{(n_s=3)}$	$\sim$645-654	kHz			68	$\sim$ 0	Fig. 3.9
Maximum observed standard uncertainty in the 13 individual relevant experiments							
$f^{(n_l=1)}$	$\sim$371-375	kHz	<80	Hz	68	<0.022	Figs. 6.1,6.2
$f^{(n_l=2)}$	$\sim$794-805	kHz	<52	Hz	68	<0.007	Figs. C.30,C.32
$f^{(n_s=3)}$	$\sim$645-654	kHz	<230	Hz	68	<0.036	Figs. C.31,C.33
Standard uncertainty over the 13 relevant experiments							
$f^{(n_l=1)}$	$\sim$371-375	kHz	<216	Hz	68	<0.058	Fig. C.21
$f^{(n_l=2)}$	$\sim$794-805	kHz	<615	Hz	68	<0.077	Fig. 5.9
$f^{(n_s=1)}$	$\sim$645-654	kHz	<389	Hz	68	<0.060	Fig. C.22
$f_0^{(n_l=1),(n_l=2),(n_s=3)}$	$\sim$371,794,645	kHz	0	Hz	100	0	see Sec. 6.3
$f_r^{(n_l=1)}$	1	-	<0.042	%	68	<0.042	Figs. 6.4,C.23
$f_r^{(n_l=2)}$	1	-	<0.039	%	68	<0.039	Figs. 6.4,5.13
$f_r^{(n_s=3)}$	1	-	<0.049	%	68	<0.049	Figs. 6.4,C.24
Standard combined uncertainty over the 13 relevant experiments							
$(f^{(n_l=1)}/f^{(n_s=3)})_r$	1	-	<0.067	%	68	<0.067	Figs. 6.4,C.25
$(f^{(n_l=2)}/f^{(n_s=3)})_r$	1	-	<0.073	%	68	<0.073	Figs. 6.4,C.26
$(f^{(n_l=2)}/f^{(n_l=1)})_r$	1	-	<0.067	%	68	<0.067	Figs. 6.4,C.27

Note that the term *uncertainty **in** individual relevant experiments* corresponds to the variation within one bin for one single experiment, while the term *standard uncertainty **over** relevant experiments* corresponds to the variation across all experiments for each bin number.

Recall that the $f^{(n_s=3)}$ resonance frequency consists of the contributions from both shear waves with particle motion polarised in parallel as well as perpendicular to the

applied tension, which have different sound velocity change dependencies (see Secs. 2.3 and 3.5.1). The uncertainty related to the contribution of the different particle motion polarisations will not affect the actual measured $f^{(n_s=3)}$ resonance frequency, and have thus not been considered in this work. This has been left to future studies. It is however noted that the spectral frequency resolution of 16.7kHz (see Sec. 3.5.1) only can be reduced by either increasing the length of the transient tail of the signal or by increasing the sampling frequency.

6.3 Sound velocity estimates

The associated relative combined standard uncertainty of the sound velocity in Eq. (2.121) can be expressed as [74]

$$\frac{u_c(c)}{|c|} = \sqrt{\left(\frac{u(f^n)}{f^n}\right)^2 + \left(\frac{u(l_3)}{l_3}\right)^2},$$

(6.8)

where c is either c_l or c_s, and the frequency ($f^{(n)} = f^{(n_l)}$, or $f^{(n)} = f^{(n_s)}$ correspondingly) and thickness measurement have been assumed to be independent since they are measured by two independent measaurement systems (the strain gauges or ARAMIS setup and the ART setup respectively). The thickness l_3 can be expressed by Eq. (2.123) and has the associated standard uncertainty [74]

$$\frac{u(l_3)}{|l_3|} = \sqrt{\left(\frac{u(L_3)}{L_3}\right)^2 + \left(\frac{e_3}{1+e_3}\right)^2 \left(\frac{u(e_3)}{e_3}\right)^2}$$

(6.9)

where the measurment of the original thickness and the elongation in the thickness direction have been assumed to be independent based on the same argument of independent measurement systems as above. The uncertainty in the thickness development has been discussed in Sec. 6.4.1.2 while the uncertainty of the original thickness has been discussed in Sec. 6.4.

Because of variations in the individual test specimens and the setup between the different tests the reference un-stressed frequency can vary across the test specimens. This will affect the absolute value of the calculated sound velocity and will introduce large experimental uncertainties. In addition the beam diffraction effect correction applied to the measured frequencies of the L1 and L2 resonance modes to align the two

different estimations of the unstressed longitudinal sound velocities also introduce uncertainties. This adjustment has only relevance for the determination of the absolute values of the longitudinal sound velocities. For all other measurement quantities it is either not relevant, or as is the case for relative measurements, is canceled out. By investigating the relative change in frequency or sound velocity the experimental variations caused by differences in initial, or reference, frequency can be removed. Although there are uncertainties associated with the determination of the reference frequency, the measurement data can be adjusted by an arbitrarily chosen reference frequency f_0^{ref} to align the relative frequency change with a known point on the load history curve as described in Sec. 6.2, this has been regarded as a pure mathematical operation and thus does not carrying any uncertainty.

The relative sound velocity of Eq. (2.122) is a function of three measurement quantities, where the referance value f_0 does not carry any uncertainty. Thus the assosiated relative combined standard uncertainty of the relative sound velocity becomes [74]

$$
\begin{aligned}
\frac{u_c(c_r)}{|c_r|} &= \sqrt{\left(\frac{u(f^n)}{f^n}\right)^2 + \left(\frac{u(f_0^{\text{ref}})}{f_0^{\text{ref}}}\right)^2 + \left(\frac{u(1+e_3)}{(1+e_3)}\right)^2} \\
&= \sqrt{\left(\frac{u(f^n)}{f^n}\right)^2 + \left(\frac{u(e_3)}{e_3}\right)^2}
\end{aligned}
\tag{6.10}
$$

The standard uncertainty for both the estimated relative and absolute sound velocities have been estimated through Eqs. (6.8) and (6.10) based on the average over relevant test specimens for the measured frequencies $f^{(n_s)}$ and $f^{(n_l)}$, the measured initial thickness L_3, and the thickness elongation e_3 measured by strain gauges. The estimated propagated standard uncertainty has been presented as dark grey errorbars in the result plots presented in Sec. 5.6. Fig. 6.5 shows the standard uncertainty in the estimated relative sound velocity change for the 13 test specimens including acoustic measurements presented in Figs. 5.19. The maximum of each uncertainty plotted here are the values reported in Table 6.2 for the relative sound velocity change $c_r(f^{(n_l=1)})$, $c_r(f^{(n_l=2)})$, $c_r(f^{(n_s=3)})$. The relative sound velocity change uncertainties are as described above (Eq. (6.10)) a combination of the propagated uncertainties of the measured relative frequency change (Fig. 6.4), the measured initial thickness (see Table 6.4), and the measured elongation e_3 (Fig. 6.7).
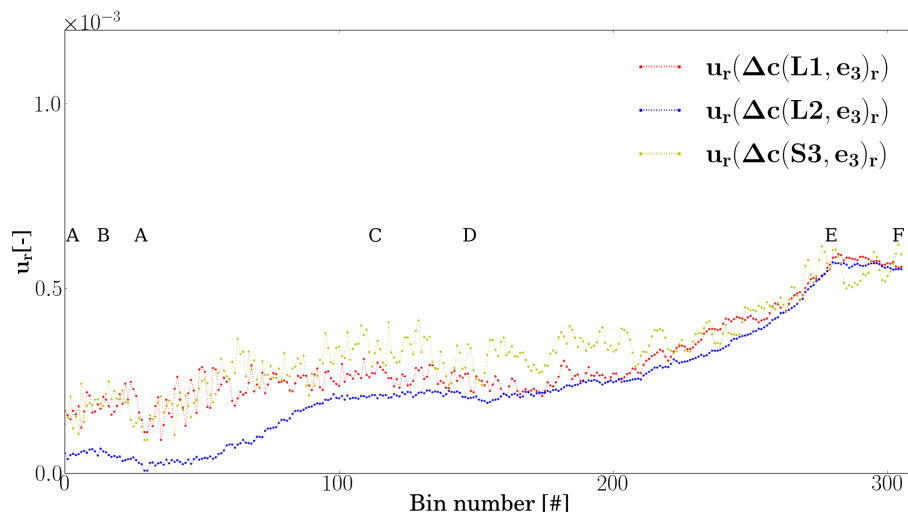
Figure 6.5: **Relative combined uncertainty of the relative development of the sound velocities based on the three resonance modes L1, L2, and S3, and the thickness development (elongation e_3) over the 13 acoustic experiments.**

Table 6.2: Standard combined uncertainties in estimated sound velocities

Variable x_i	$\mu(x_i)$		$u(x_i)$		Confidence level [%]	$\frac{u(x_i)}{\|x_i\|}$ [%]	Relevant Eq. #
$c(f^{(n_l=1)})$	$\sim$5870	m/s	<6.8	m/s	68	<0.12	(2.121),(3.7)
$c(f^{(n_l=2)})$	$\sim$5870	m/s	<6.4	m/s	68	<0.11	(2.121),(3.7)
$c(f^{(n_s=3)})$	$\sim$3230	m/s	<3.6	m/s	68	<0.11	(2.121)
$c_r(f^{(n_l=1)})$	1	-	<0.059	%	68	<0.059	(2.122)
$c_r(f^{(n_l=2)})$	1	-	<0.056	%	68	<0.056	(2.122)
$c_r(f^{(n_s=3)})$	1	-	<0.061	%	68	<0.061	(2.122)

Note that the uncertainty related to the ratio between $c(f^{(n_l=1)})$ and $c(f^{(n_s=3)})$, and $c(f^{(n_l=2)})$ and $c(f^{(n_s=3)})$, are the same as the uncertainties related to the corresponding frequency ratios presented in Table 6.1 because the expressions are identical (see Eq. (2.125)).

Note also that the sound velocities $c(f^{(n_l=1)})$ and $c(f^{(n_l=2)})$ where the resonance frequencies have been corrected for the beam effect do not include the uncertainty related to the calculated correction factor $\eta^{(n_l)}$ in Eq. (3.13). Since this work concentrates on the relative change of the sound velocity and not the absolute value it has not been deemed necessary to try to quantify the uncertainty related to the beam diffraction

correction, and thus it has been disregarded. This will also have an influence on the estimated uncertainties in the linear elastic moduli estimated based on the sound velocity in Table 5.5. This should however not be of any importance since the estimated linear elastic moduli have only been used to indicate the similarity of the currently used steel to those steel types already presented in literature (see Ch. 4).

For the shear sound velocity $c(f^{(n_l=2)})$ the uncertainty related to the contribution of the different particle motion polarisations (see Sec. 3.5.1) will not affect the actual estimates, similarly as for the measured $f^{(n_s=3)}$ resonance frequency. Thus it has not been considered in this work.

6.3.1 Temperature contribution

The acoustic sound velocities also depend on the temperature of the medium. To be able to quantify the change in sound velocities caused by temperature change during the tests, the temperature was measured before and after each acoustic test using a digital thermometer (see Table 3.1) with a resolution of $0.1°$ C.

From the measured data presented in Sec. 5.4, it is obvious that the temperature is close to constant throughout the test runs. The highest measured temperature difference over a test was $-0.4°$C. This was measured at one of the tests that have been removed from further evaluation because of missing displacement measurements. Thus the largest temperature difference measured for one of the samples which have been used in the evaluation of sound velocity change is $0.1°$C. This is the same as the digital thermometer resolution, and the distribution of the temperature uncertainty can be assumed to be rectangular. With a sound velocity - temperature dependency of ~ 0.02 %/°C (See Sec. 5.4 and [105]), this amounts to a relative uncertainty in the sound velocities of steel due to temperature difference ($< 0.1°$C) assuming a rectangular probability distribution of $\frac{0.02\%/°0.1°}{\sqrt{3}} \approx 0.0012$ % [74, Sec. 4], which has been regarded as insignificant, and thus ignored.

An empirical functional relationship between the unstressed longitudinal and shear sound velocities and the temperature have been presented by [105] as

$$c = a\,T^2 + b\,T + c \qquad (6.11)$$

with temperature T given in Kelvin. The coefficients a, b, c for two types of steels investigated in [105] have been reproduced in Table 6.3.

Table 6.3: Empirical coefficients for sound velocity dependence

Steel	Velocity	a	b	c
X14CrMoS17	c_l	$-2.1 \cdot 10^{-4}$	-0.73	6230
	c_s	$-7.2 \cdot 10^{-4}$	0.15	3258
X90CrMoV18	c_l	$-6.5 \cdot 10^{-4}$	-0.016	6032
	c_s	$-9.2 \cdot 10^{-4}$	0.41	3203

Reproduced from [105]

This yields a uncertainty contribution from any uncertainty in the temperature measurements less than [74]

$$u(c(T)) = \sqrt{(aT+b)^2} u(T) \tag{6.12}$$

For a temperature of 24°C (297 K) this yields $u(c_l(T)) = 0.79u(T)$ and $u(c_s(T)) = 0.06u(T)$ for the X14CrMoS17 steel, and $u(c_l(T))) = 0.21u(T)$ and $u(c_s(T)) = 0.13u(T)$ for the X90CrMoV18 steel. Assuming that these values are relevant for the current steel the propagated uncertainty is less than the uncertainty in the temperature measurement, which is less than the measured temperature change over the experiments. Thus this contribution has also been regarded as insignificant.

6.4 Test specimen geometry

One of the challenges in this work has been that the predicted changes in the sound velocities are very small (in the order of a few tenths of a percent) as seen in Secs. 5.6.2. To improve the statistical base of the resulting measurements and ensure repeatability of the experiment results a set of 41 test specimens have been tested under as close to the same conditions as practically reasonable. The first step to control the measurement conditions has been to obtain steel with the same geometry and material properties as described in Sec. 3.2.

This section discusses the uncertainties related to change in the geometry and derived measurands which depend on the geometry of the test specimen. The uncertainty related to the base measurements have been presented first while the relevant derived quantities have been discussed next.

6.4.1 Geometry change

As already presented in Sec. 6.3 the thickness l_3 depends on the initial thickness L_3 and the thickness elongation e_3 as given in Eq. (2.123) with the associated standard

relative uncertainty of Eq. (6.9). Similarly the width l_2 depends on the initial width L_2 and the elongation in the x_2-direction e_2 as

$$l_2 = L_2(1 + e_2).$$

(6.13)

and have the associated standard uncertainty [74]

$$\frac{u(l_2)}{|l_2|} = \sqrt{\left(\frac{u(L_2)}{L_2}\right)^2 + \left(\frac{e_2}{1 + e_2}\right)^2 \left(\frac{u(e_2)}{e_2}\right)^2}$$

(6.14)

while the current free length depends on a few more measurements as described in Sec. 3.2, Eq. (3.2). The associated standard uncertainty is

$$\frac{u(l_1^{free})}{|l_1^{free}|} = \sqrt{\left(\frac{u(L_1^{free})}{L_1^{free}}\right)^2 + \left(\frac{u(l_1^{g1})}{l_1^{g1}}\right)^2 + \left(\frac{u(l_1^{g2})}{l_1^{g2}}\right)^2 + \left(\frac{e_1}{1 + e_1}\right)^2 \left(\frac{u(e_1)}{e_1}\right)^2}.$$

(6.15)

The uncertainty in geometry change, and more specific the cross sectional area, is thus dependent on the initial geometry; free length L_1^{free}, width L_2 and thickness L_3, as well as the measured elongations in the three principal directions e_1, e_2, and e_3. The associated uncertainties in these measurement quantities have been discussed in this section.

6.4.1.1 Initial unstressed geometry

The uncertainty related to the variation in initial geometry between test specimens has been quantified by measurements of the physical dimensions by hand tools. This introduces, in addition to the variation across measurement points and across test specimens, uncertainties related to the actual measurement device. The length of each test specimen has been measured using a steel ruler, while the width and thickness was measured using a digital caliper and a micrometer caliper respecitvely. Although the readout of the measurement equipment is easy and inherent uncertainties in the readouts are well defined (presented in Table 6.4 under "Instruments"), these types of measurements are prone to systematic uncertaintes related to how the measurement equipment has been used by the user. To avoid this, each equipment has been calibrated against a calibration sample with known dimensions, and any systematic uncertainty has been corrected for (see Table 3.1 for name and make of calibration blocks and measurement

equipment). If any correction has been done, the uncertainty in the systematic correction has been assumed to be negligible for the dimensional measurement equipment. To estimate the variation in dimensions over the area where the acoustic signal has been focused, a set of thickness and width measurements distributed over the center of the specimen were taken in approximately the same area for each test specimen. Fig. 3.1 shows the approximate location of these measurements. The physical extent of the measurepoints can, in addition to the thickness of the test specimen at those locations, indicate how parallel the faces of the test specimen were. From Table D.1 and Fig. 3.1 it can be seen that the largest difference between the thickness on the left and right side was 0.04 mm (test no. 7). For a width of approximately 50 mm this corresponds to a deviation from parallel faces of $\theta = \arctan 0.04/50 \approx 0.046°$. In addition, all the tests were placed on a machined plane surface to visually inspect for any curvature in the test specimens. This was not observed, and it has been assumed that the surfaces were sufficiently plane and parallel. Any slight deviations in the order of what was observed and described above have been regarded as insignificant, and thus neglected.

In addition to the uncertainty in thickness and width measurement which propagate to other derived measurement quantities (see Sec. 5.3), the variation in dimensions between test specimens both before and after the tension test can help indicate how much of the uncertainty in the desired result quantities can be ascribed variation in the actual test specimens.

The length, width, and thickness measurements have been presented in Table D.1, while the experimental standard uncertainty have been summarised in Table 6.4.

The uncertainties related to the variation in material properties between test specimens and within each test specimen are hard to evaluate without damaging the test specimens. However, a good indication on how the material properties have varied across the test specimens can be evaluated based on the variation in deformation path between the test specimens. This has been discussed further in Sec. 6.4.4. However, it is worth noticing that the combined uncertainty for both relative frequency change and relative change of frequency ratios in Fig. 6.4, and for the relative change in sound velocity in Fig. 6.5, have their largest values at the end of the deformation path (located in sequence EF). Comparing the largest combined relative standard uncertainty of the frequencies $f_r^{(n_l=1)}$, $f_r^{(n_l=2)}$, $f_r^{(n_s=3)}$, ratios $(f^{(n_l=1)}/f^{(n_s=3)})_r$, $(f^{(n_l=2)}, f^{(n_s=3)})_r$, and sound velocities $c_r(f^{(n_l=1)})$, $c_r(f^{(n_l=2)})$, $c_r(f^{(n_s=3)})$ in Table 6.1 and 6.2 which have

Table 6.4: Uncertainties in measured unstressed geometry

Variable x_i	$\mu(x_i)$		$u(x_i)$		Confidence level [%]	$\frac{u(x_i)}{\|x_i\|}$ [%]
Instruments						
Micrometer caliper, L_3	7.50	mm	0.01	mm	100	0.08
Digital caliper, L_2	50	mm	0.01	mm	100	0.01
Steel ruler, L_1	600	mm	0.5	mm	100	0.05
Maximum observed standard deviation in individual test specimens (see Table D.1)						
L_3 at #18	7.49	mm	0.001	mm	68	0.21
L_2 at #2	49.89	mm	0.008	mm	68	0.15
L_1^{free} at #39	449	mm	0.05	mm	100	0.11
l_3 at #38	7.28	mm	0.019	mm	68	2.7
l_{2d} at #35	47.95	mm	0.18	mm	68	3.8
l_1^{free} at #39	467.	mm	0.05	mm	100	0.11
Standard uncertainty over 37 test specimens (from Table D.1)						
L_3	7.50	mm	0.001	mm	68	0.013
L_2	49.84	mm	0.004	mm	68	0.008
L_1	600	mm	0.03	mm	100	0.003
L_1^{free}	449.85	mm	0.03	mm	100	0.004
l_3	7.36	mm	0.003	mm	68	0.047
l_2	48.92	mm	0.032	mm	68	0.065
l_1	618.25	mm	0.22	mm	100	0.021
l_1^{free}	456.79	mm	2.4	mm	100	0.31

Note that the term *uncertainty **in** individual relevant experiments* corresponds to the variation within one bin for one single experiment, while the term *standard uncertainty **over** relevant experiments* corresponds to the variation across all experiments for each bin number.

standard relative uncertainties spanning from 0.039 % to 0.073 %, it is evident that much of this may be induced by variation in deformation path of the test specimens which has an observed standard uncertainty in the deformed thickness l_3 over all 37 test specimens of 0.047 % (Table 6.4).

6.4.1.2 Strain gauge measurements

Strain gauges have been used to measure the strain in all the principal directions (x_1, x_2, x_3). The gauges used were of the type YFLA-2 and YFLA-5, produced by Tokyo Sokki Kenkyujo Co. [101]. They have a very good temperature tolerance of

$\pm 0.85 (\mu m/m)/^{\circ}C$ [101]. However, the main contributing factor to uncertainties in the strain gauge measurements are related to alignment of the gauge with the desired principal strain direction, and how well the gauge was bonded to the specimen. Experienced laboratory personnel at DNV [109] evaluated this systematical uncertainty to be in the order of 2-4 % of the measured value. Note that uncertainty both in the orientation and in the bonding leads to under-prediction of the measured strain. This has not been included in the following calculations. The reason and any implication of this has been discussed in Sec. 6.4.1.3.

Fig. C.4 in App. C.2.1 shows the measured e_1 elongation from 7 strain gauges fastened to 6 individual test specimens. The experimental standard deviation across these 7 e_1 elongation measurements have been presented in Fig. 5.4 in Sec. 5.3. Fig. 6.6 shows the standard deviation of the elongation e_1 across each bin for the 7 strain gauge measurements. Note that the variation in measured elongation in the plastic regions are somewhat larger than in the elastic region. When comparing the standard deviation over each bin for the e_1-elongation with the standard deviation over the same bins for the x_1-displacement measured by the Instron machine shown in Fig. 6.12 in Sec. 6.4.4 it is clear that the standard deviations of the x_1-displacement has a close to constant value of ~ 0.04 mm throughout the tests (with exceptions at the position where the load history change from loading to unloading and vice versa, which have been discussed in Sec. 6.4.4), which indicate a constant displacement velocity. The observed increase in standard deviation in the e_1-elongation is probably an effect of the accuracy of the control system which might have more difficulties to control the needed applied force to produce the set displacement velocity when the response of the test specimens become plastic, and thus don't need any additional applied force to continue to deform the test specimen.

Fig. 6.7 shows the experimental standard uncertainty across the 18 test specimens including strain gauges based on the variation observed in Figs. C.4, C.5, and C.6 (App. C.2.1). As can be seen from the figure the experimental standard uncertainty of each of the elongations in the principal directions are small (<0.005 %) for the first 50 bins. This corresponds to the first elasic loading and unloading sequences (AB, BA), as well as the elastic part of the second loading sequence (AB), and the low standard uncertainty across the test specimens in this region indicate that the measured deformation of the test specimens were very similar before they where plastically deformed. The increase

in standard uncertainty towards bin number 100 indicate that the measured plastic deformation of the different test specimens are slightly different. This effect might have different origins. If for example the test specimens do not deform uniformely under plastic deformation the measured total elongation will be dependent on where the strain gauge is placed on the test specimen. Also, if the strain gauges are placed with slightly different angles off the principal axis to which it should be aligned, this will result in discrepancies in the measured elongation which will increase and become more apparent for larger deformations. This is thus an uncertainty related both to the measurement system and the response of the individual test specimen. The effect is also evident in Fig. C.4 where one can see that the measured elongation e_1 at the start of the second unloading (C) are at slightly different values. Fig. 6.7 then shows a flat area with no significant increase in standard uncertainty between bin number 130 and 180. This corresponds to the second elastic unloading (CD) and the elastic part of the third load sequence (DC). The experimental standard uncertainty increase towards bin number 280 corresponding to the plastic deformation CE whith the associated increasing spread in total measured elongation as observed at point E in C.4. Over the last 26 bins the standard uncertainty does not change significantly, which corresponds to the third, and last, elastic unloading.
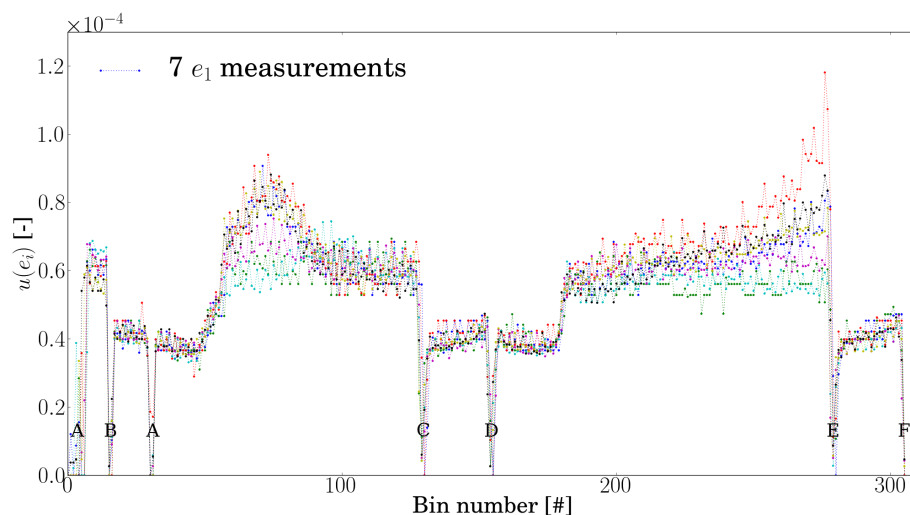
Figure 6.6: Standard deviation of e_1 elongation across each bin from 7 strain gauges on 6 test specimens
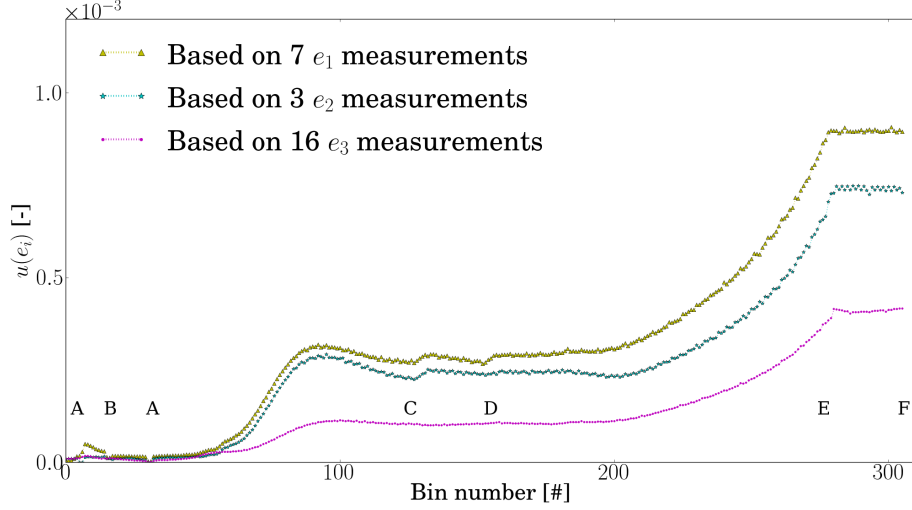
Figure 6.7: Standard uncertainty over the 18 test specimens were strain gauges have been included

Similar plots for the e_2- and e_3-elongations have been included in App. C.2.1, Figs. C.5, C.6, C.34, and C.35. The standard uncertainties related to strain gauge measurements have been listed in Table 6.5.

Table 6.5: Uncertainties related to strain gauge measurements

Variable x_i	$\mu(x_i)$		$u(x_i)$		Confidence level [%]	Based on
Strain gauges						
e_i	$\sim$0 - 4.1	%	$0.85 \cdot 10^{-5}$	%	68	[101]
Systematic						
e_i	$\sim$0 - 4.1	%	$\sim$-2–4	%	68	[109]
Maximum observed in individual relevant experiments						
e_1	0 - 4.1	%	<0.01	%	68	Fig. 6.6
e_2	-1.83 - 0	%	<0.005	%	68	Fig. C.34
e_3	-1.75 - 0	%	<0.005	%	68	Fig. C.35
Standard uncertainty over relevant experiments						
e_1	0 - 4.1	%	<0.09	%	68	Fig. 6.7
e_2	-1.83 - 0	%	<0.07	%	68	Fig. 6.7
e_3	-1.75 - 0	%	<0.04	%	68	Fig. 6.7

Table 6.6: Estimated Young's modulus and Poisson's ratio based on strain gauge measurements and adjusted for sytematic underprediction

	Systematic adjustment of elongation measurements [109]		
	0 %	2 %	4 %
Sequence	Estimated Young's modulus Y [GPa]		
1. loading	209	205	201
1. unloading	212	208	204
2. loading (elastic)	208	204	200

6.4.1.3 Systematic underestimation of elongation

As mentioned above an unquantified systematic underprediction of the measured elongation by strain gauges and the implication of leaving this contribution out will be discussed here. First it is noted that the measured elongations do not have any influence on the actual measured change in the ratio between longitudinal and shear sound velocity c_l/c_s, and not on any of the measurements in the unstressed state where $e_1 = e_2 = e_3 = 0$. What it does influence is the estimate of the magnitude of the applied stress, the Young's modulus and the Poisson's ratio, the theoretically estimated acoustoelastic effect, and the estimated change in sound velocities.

Recalling the estimated Young's moduli Y and Poisson's ratios ν presented in Table 5.2, these values have been estimated based on the actual measurement values without adjusting for any systematic uncertainty. If the measured elongations are adjusted by 2 % and 4 % respectively to compare the effect on the estimated Y, this yields the results presented in Table 6.6 (note that only the loadsequences without any plastic deformation have been included, AB, BA, and AB). The Young's modulus based on the estimated unstressed sound velocities (corrected for the beam effect) has been presented in Table 5.5 and was estimated to 214.1±0.4 GPa. This estimate is independent of the measured elongations, and one would expect the values based on either measured elongations and stresses or sound velocities should be comparable. The Young's moduli estimated without adjusting for the systematic uncertainty are closest to the Young's modulus based on estimated sound velocities, which might indicate that the underestimation might not be as large as indicated by [109]. Note that because the Poisson's ratio is a function of the relation between two measured elongations (see Eq. (2.105)) any relative adjustment percent will lead to an equal relative change in both measurands

which will not have any effect on the estimated value. The Poisson's ratio has thus not been included in this comparison.

Since the estimated stress and linear elastic properties have not been used for any other purposes than illustrating the load history and to validate that the current steel have elastic properties that are comparable to those steels reported in the literatur (see Ch. 4), it has been assumed that any adjustment to eliminate the systematic uncertainty in the strain gauge measurements will not have an impact on the conclusions of this work.

The influence on the theoretically estimated acoustoelastic effect has been plotted in Fig. 6.8 for the relative change in longitudinal sound velocity. The results based on the 0 %, 2 %, and 4 % adjustment is plotted with continuous, dashed and dotted lines respectively. Similar plots for the other theoretically estimated sound velocities and ratio's have been included in Figs. C.36 to C.37 in App. C.4. As can be seen, there is very little difference between the unadjusted and adjusted curves, much less than the uncertainty related to the second and third order elastic moduli (Figs. 5.22 to 5.26). It has thus been decided to use the unadjusted strain gauge measurements since they yield the Young's moduli Y that are closest to the one estimated based on unstressed sound velocities, and because any adjustment would not affect the conclusions.
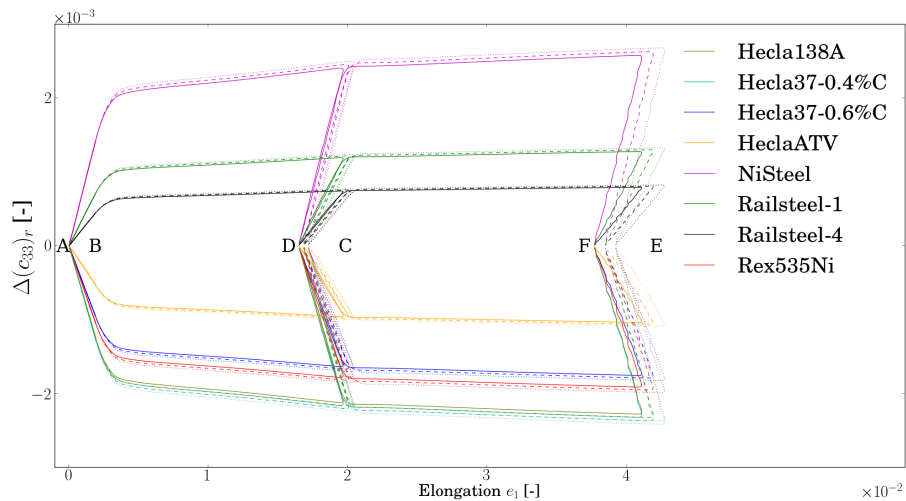
Figure 6.8: **Relative longitudinal sound velocity c_{33} development based on elastic properties given in Table 4.4 and the measured elastic strains with 0 %, 2 %, and 4 % adjustment for possible systematic underestimation**

6. UNCERTAINTY ANALYSIS

The elastic and plastic part of the total strain is calculated based on the relations in Eqs. (2.112) and (2.113). The associated standard uncertainties are thus [74]

$$\frac{u(e^e)}{|e^e|} = \sqrt{\left(\frac{u(F)}{F}\right)^2 + \left(\frac{u(y^{e_i})}{y^{e_i}}\right)^2} \tag{6.16}$$

and

$$\frac{u(e^p)}{|e^p|} = \sqrt{\left(\frac{u(e)}{e}\right)^2 + \left(\frac{u(e^e)}{e^e}\right)^2} \tag{6.17}$$

respectively where the uncertainty related to the generic linear regression slope of the stress-strain relations y^{e_i} (see Sec. 2.5.1) has been estimated as an experimental standard uncertainty of the linear regression slopes across the experiments including the relevant strain gauge measurements for each elastic loading and unloading sequence. The uncertainty related to the elastic and plastic elongation contributions has been plotted in Fig. 6.9. In this figure the three principal elongations e_1, e_2, and e_3 have been plotted using the markers $\triangle$, $\times$, and $\cdot$ respectively. The total elastic elongation has been plotted in black, while the elastic and plastic contributions have been plotted in blue and red respectively. For clarity it is notede that the curves marked with $\triangle$ lie above the corresponding curves marked with $\times$, which lie above the curves marked with $\cdot$. The black and red (total and plastic elongation) curves lies almost on top of eachother, while the blue (elastic) curves all lie almost on top of each other below the red and black curves. From this it is clear that the uncertainty in the estimated elastic elongation is much less than the uncertainties related to the total and/or plastic elongation measurements. The colours used when plotting the estimated contributions corresponds to the colours used in the figures on which the data is based (i.e. Figs. 5.8, C.8, and C.9). The black curves indicating the standard uncertainty in the total measured elongations e_i corresponding to the curves in Fig. 6.7. The maximum estimated uncertainty for the measured total, and the estimated elastic and plastic, elongations shown in Fig. 6.9, have been presented in tabulated form in Table 6.7.

Note that the maximum of the ranges reported for the plastic, and elastic elongations in Table 6.7 do not add up to the maximum of the total elongation perfectly. This is because the maximums have not been found at the exact same position in the load history, and thus may vary slightly.
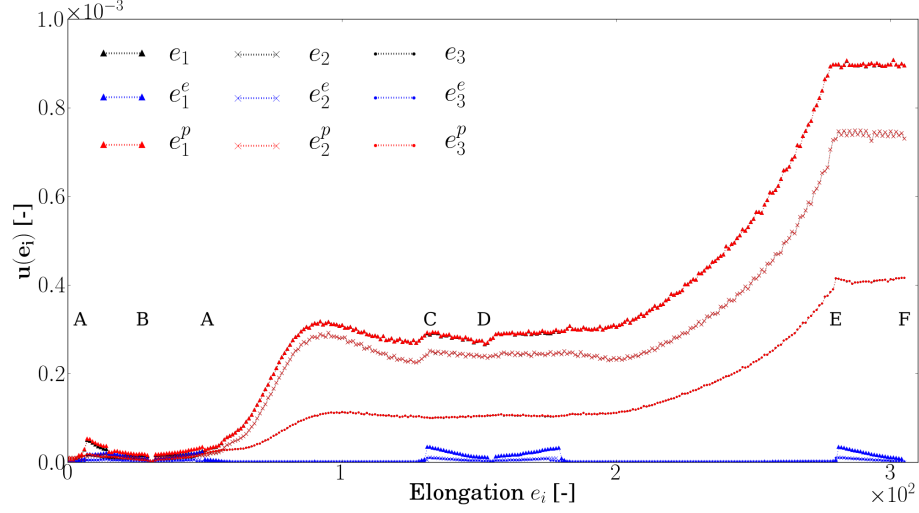
Figure 6.9: **Experimental standard uncertainty of total elongation and elastic and plastic contribution for the e_1, e_2, and e_3 elongations**

Table 6.7: Experimental standard uncertainty in estimated elastic and plastic contribution to total elongation from Fig. 6.9

Variable x_i	$\mu(x_i)$		$u(x_i)$		Confidence level [%]
e_1	0 - 4.1	%	<0.09	%	68
e_1^p	0 - 3.77	%	<0.09	%	68
e_1^e	0 - 0.35	%	<0.0035	%	68
e_2	-1.83 - 0	%	<0.08	%	68
e_2^p	-1.73 - 0	%	<0.08	%	68
e_2^e	-0.11 - 0	%	<0.0011	%	68
e_3	-1.75 - 0	%	<0.04	%	68
e_3^p	-1.64 - 0	%	<0.04	%	68
e_3^e	-0.11 - 0	%	<0.0011	%	68

6.4.1.4   ARAMIS

The photometric ARAMIS system has also been used to measure the geometric deformation as described in Sec. 3.6.2. The accuracy can be as good as 0.01 % strain according to the system description [107]. However, because of the limited experience of the author with this type of measurement system this work has evaluated the actual

achieved measurement uncertainty based on the results as described below.

One way to quantify this uncertainty is to calculate the standard deviation of the output strain field over a relevant area on the test specimen. This has been done over an area chosen to be a circle of diameter 20 mm in the center of the test specimen (at the location where the acoustic signal has been focused). The standard deviation of the ARAMIS calculated elongation e_{major} (in the x_1-direction) for 8 experiments has been plotted in Fig. 6.10. The variations in the level of standard deviation for the different test specimens are assumed to be a result of differences in the quality of the stochastic spray painted pattern applied to the face of the test specimens (see Fig. 3.11b). Compared to the uncertainty of the e_1 elongation measured by strain gauges shown in Fig. 6.6 it is obvious that the uncertainty in the ARAMIS measurements, which are approximately in the order of 0.05-0.2 %, are significantly larger than the uncertainty associated with the strain gauge measurements which are a full order of magnitude less (0.005-0.01 %).
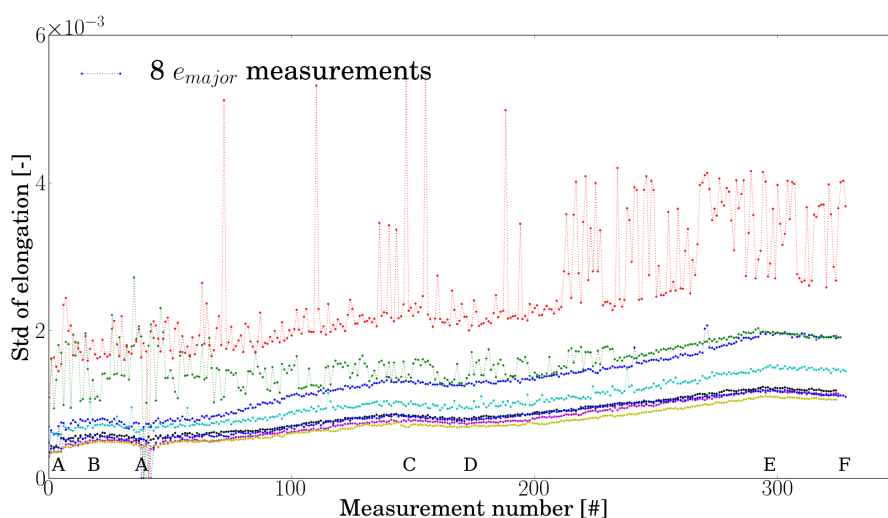
Figure 6.10: Standard deviation of e_{major} elongation over a circle of diameter 20 mm in the center of the test specimen for 8 ARAMIS measurements

Similar plots for the ARAMIS measured elongation in the x_2- and x_3-directions have been included in App. C.5, Figs. C.38 and C.39.

In addition to the inferior uncertainty associated with the ARAMIS measurements on a general basis, some of the tests run with the ARAMIS system resulted in very

Table 6.8: Uncertainties in measured geometry change by ARAMIS

Variable x_i	$\mu(x_i)$		$u(x_i)$		Confidence on	Based
ARAMIS system						
e_i	$\sim$0-4.5	%	0.01	%	68	[107]
Maximum observed in individual relevant experiments						
e_{major}	0-4.5	%	$\lesssim$0.5	%	68	Fig. 6.10
e_{minor}	-2-0	%	<0.2	%	68	Fig. C.38
e_z	-2-0	%	<0.5	%	68	Fig. C.39
Standard uncertainty over relevant experiments						
e_{major}	0-4.5	%	<0.06	%	68	Fig. C.11
e_{minor}	-2-0	%	<0.05	%	68 Fig. C.14	
e_z	-2-0	%	<0.04	%	68 Fig. C.17	

poor resolution in the stochastic spray painted pattern which has led to even larger variations of the ARAMIS calculated elongation within the relevant measurement area than shown in Fig. 6.10. These results have been deemed to poor to be included in evaluations in this work, and have thus been excluded (see Table 5.1). As argued in Sec. 5.3.1, the estimated stress versus strain/elongation relations and subsequent estimates of the Young's modulus Y and Poisson's ratio ν based on the ARAMIS elongation measurements do not fit accepted nominal values for steels, and it has thus been decided to exclude all the ARAMIS measurements from evaluation of any of the strain derived measurement quantities described in Sec. 3.6.3.

For reference the maximum standard uncertainty per experiment and the experimental standard uncertainty over the experiments have been presented in Table 6.8.

6.4.2 Linear elastic properties

The linear elastic properties Young's modulus Y and Poisson's ratio ν of the current steel can be estimated based on force measurements (or stress estimates) and elongation measurements according to Eqs. (3.19), and (2.105) respectively. The associated

uncertainty for the Young's modulus Y can thus be represented by [74]

$$\frac{u(Y)}{|Y|} = \left[\left(\frac{u(F)}{F} \right)^2 + \left(\frac{u(L_2)}{L_2} \right)^2 + \left(\frac{u(L_3)}{L_3} \right)^2 + \left(\frac{u(e_1^e)}{e_1^e} \right)^2 \right.$$
$$\left. + \left(\frac{e_2^p}{1 + e_2^p} \right)^2 \left(\frac{u(e_2^p)}{e_2^p} \right)^2 + \left(\frac{e_3^p}{1 + e_3^p} \right)^2 \left(\frac{u(e_3^p)}{e_3^p} \right)^2 \right]^{\frac{1}{2}} \qquad (6.18)$$

or assuming that the deformation is uniaxial and that the contraction in the transverse directions are biaxial (i.e. that $e_2 = e_3$ as in Eq. (3.15))

$$\frac{u(Y)}{|Y|} = \left[\left(\frac{u(F)}{F} \right)^2 + \left(\frac{u(L_2)}{L_2} \right)^2 + \left(\frac{u(L_3)}{L_3} \right)^2 + \left(\frac{u(e_1^e)}{e_1^e} \right)^2 \right.$$
$$\left. + 2 \left(\frac{e_2^p}{1 + e_2^p} \right)^2 \left(\frac{u(e_2^p)}{e_2^p} \right)^2 \right]^{\frac{1}{2}}. \qquad (6.19)$$

where F is the measured force recorded by the MessTek control unit with uncertainties presented in Sec. 6.4.4, L_2 and L_3 are the initial width and thickness respectively with uncertainties presented in Sec. 6.4.1.1, and e_i where $i = 1, 2, 3$ are the elongations measured by strain gauges with uncertainties presented in Secs. 6.4.1.2.

For Poisson's ratio the associated uncertainty can be estimated through Eq. (3.17) by [74]

$$\frac{u(\nu)}{|\nu|} = \sqrt{\left(\frac{u(e_1^e)}{e_1^e} \right)^2 + \left(\frac{u(e_2^e)}{e_2^e} \right)^2}$$
$$= \sqrt{\left(\frac{u(e_1^e)}{e_1^e} \right)^2 + \left(\frac{u(e_3^e)}{e_3^e} \right)^2}. \qquad (6.20)$$

By combining the standard uncertainty over the relevant experimental tests the combined standard uncertainty of the Young's modulus Y and Poisson's ratio ν have been estimated and presented in Table 6.9 for each of the elastic loading and unloading sequences (see Table 3.4). Note that the uncertainties presented here are based on measured values from the upper region of the elastic regions (i.e. where the estimated elongations are largest - close to point B, D, and F in Figs. 5.8, C.8, and C.9). This has been done because of the increase towards infinity in relative uncertainty as the estimated elastic elongations approach zero at point A (the unstressed state). This applies to all measurement quantities that at some stage might be close to zero. Thus, in this work it has been assumed that the relative uncertainty in this kind of measurements

Table 6.9: Standard combined uncertainties in estimated linear elastic constants

Variable x_i	$\mu(x_i)$		$u(x_i)$		Confidence level [%]	$\frac{u(x_i)}{|x_i|}$ [%]	Relevant Eq. #
1. loading sequence AB							
Y	209	GPa	2.6	GPa	68	1.2.	(3.14),(3.19)
$\nu(e_1, e_2)$	0.29	-	0.004	-	68	1.4	(2.105)
$\nu(e_1, e_3)$	0.31	-	0.004	-	68	1.4	(2.105)
1. unloading sequence BA							
Y	211	GPa	2.6	GPa	68	1.2	(3.14),(3.19)
$\nu(e_1, e_2)$	0.29	-	0.004	-	68	1.4	(2.105)
$\nu(e_1, e_3)$	0.28	-	0.004	-	68	1.4	(2.105)
2. loading sequence AB							
Y	208	GPa	2.5	GPa	68	1.2	(3.14),(3.19)
$\nu(e_1, e_2)$	0.28	-	0.004	-	68	1.4	(2.105)
$\nu(e_1, e_3)$	0.28	-	0.004	-	68	1.4	(2.105)
2. unloading sequence CD							
Y	185	GPa	2.2	GPa	68	1.2	(3.14),(3.19)
$\nu(e_1, e_2)$	0.31	-	0.004	-	68	1.4	(2.105)
$\nu(e_1, e_3)$	0.29	-	0.004	-	68	1.4	(2.105)
3. loading sequence DC							
Y	186	GPa	2.3	GPa	68	1.2	(3.14),(3.19)
$\nu(e_1, e_2)$	0.30	-	0.004	-	68	1.4	(2.105)
$\nu(e_1, e_3)$	0.29	-	0.004	-	68	1.4	(2.105)
3. unloading sequence EF							
Y	179	GPa	2.1	GPa	68	1.2	(3.14),(3.19)
$\nu(e_1, e_2)$	0.31	-	0.004	-	68	1.4	(2.105)
$\nu(e_1, e_3)$	0.30	-	0.004	-	68	1.4	(2.105)

can be estimated at a point where the absolute value is the largest. Applying this to the estimated relative uncertainty in Eqs. (6.18) or (6.19), and (6.20) leads to a relative standard uncertainty of the estimated Young's modulus Y of approximately 1.2 %, while for Poisson's ratio it is 1.4 %.

6.4.3   Stress estimates

Two stress estimates have been presented in this work. The uniaxial Lagrangian stress S_{11} and Cauchy stress σ_{11} which are related through Eq. (3.14). Their respective associated relative standard uncertainties can based on Eq. (3.14) be expressed as [74]

$$\frac{u(S_{11})}{|S_{11}|} = \sqrt{\left(\frac{u(F)}{F}\right)^2 + \left(\frac{u(L_2)}{L_2}\right)^2 + \left(\frac{u(L_3)}{L_3}\right)^2}, \tag{6.21}$$

and

$$\begin{aligned}
\frac{u(\sigma_{11})}{|\sigma_{11}|} &= \left[\left(\frac{u(F)}{F}\right)^2 + \left(\frac{u(L_2)}{L_2}\right)^2 + \left(\frac{e_2}{1+e_2}\right)^2 \left(\frac{u(e_2)}{e_2}\right)^2 \right. \\
&\quad \left. + \left(\frac{u(L_3)}{L_3}\right)^2 + \left(\frac{e_3}{1+e_3}\right)^2 \left(\frac{u(e_3)}{e_3}\right)^2 \right]^{\frac{1}{2}}.
\end{aligned} \tag{6.22}$$

Similar to the calculation of the Young's modulus the Cauchy stress can be obtained assuming that $e_2 \approx e_3$ (see Figs. 5.5 and 5.6). Thus the Cauchy stress can be estimated as a function of both e_2 and e_3, or of e_2 or e_3 individually. This has been done, and the propagated uncertainties have been estimated based on Eq. (6.22) and plotted in Fig. 6.11. Recognising the relative constant standard uncertainty for the bins below point C and point E as the part of the load history where the test specimens deform plastically (and thus do not experience much change in the applied force), it is obvious that the uncertainty in the stress estimate is less during plastic deformation than during elastic deformation. The maximum levels of standard uncertainty in the estimated stress have been estimated based on Fig. 6.11 for both the elastic and plastic part of the load history, and have been presented in Table 6.10. Although these uncertainties have not been used in this work, they have been included for reference since the stress can be used as input in the acoustoelastic theory as described in Sec. 2.3.

Table 6.10: Standard combined uncertainty in Cauchy stress over relevant experiments

Variable x_i	$\mu(x_i)$		$u(x_i)$		Confidence level [%]
σ_{11}^{e}	0-630	MPa	<9	MPa	68
σ_{11}^{P}	0-630	MPa	<1	MPa	68
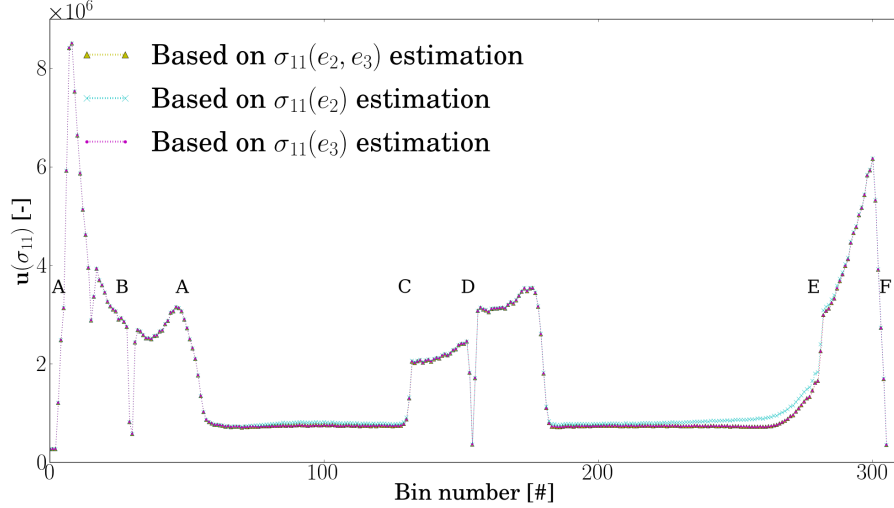
Figure 6.11: Propagated uncertainty of estimated σ_{11} based on measurement and uncertainty values from force F, and the combination of or the individual elongations e_2 and e_3

6.4.4   Tension machine

Even though the steel is from the same production batch there will always be variations of the material between the test specimens, but also within each test specimen. These variations will mainly affect the deformation path of the test specimens. The deformation paths (force and displacement) have been recorded by the MessTek control unit during each test. However, beacuse of slightly different initial conditions and the fact that the tests are dynamic makes it difficult to ensure that each measurepoint of the deformation path of any given test specimen has an exact corresponding measurepoint at any of the other test specimens. The results have been binned to be able to compare measured values across different test specimens, as described in Sec. 3.4 and discussed in Sec. 6.2.

The tension force and displacement of the Instron tension machine has been recorded as voltage signals by the MessTek controll unit. The force and displacement voltage signals have been sampled at a frequency of 10 Hz throughout each test. This sample rate was so slow that random variations in the voltage signal over the measurement caused by electric disturbances and fluctuations in the control system were small compared to the voltage change between two measurements. This ensures that both the

175

displacement and force measurements are monotonically increasing or decreasing during elastic loading / unloading respectively with approximately linear behaviour between measurepoints. However, when the test specimen starts to plastically deform the tension machine continue to deform the test specimen displacement controlled while the applied force stays approximately the same. Thus the test specimen experience large displacement without a corresponding increase in the applied force as it did in the elastic regime. Thus, random variations in the force voltage will start to be significant compared to the actual change in force between two measurepoints. However, the displacement change linearly both in the elastic and the plastic region (with the current setup of the control unit). This property makes the displacement ideal as a reference measurement to which all other measurements can be related to be able to combine them at a later stage.

The displacement measurement x_1 is not a good measurement to estimate any of the desired results related to change in sound velocity as mentioned in Sec. 5.2. However, because of its close relation to both the force/stress in the steel sample and the strain state of the sample, that it behaves linearly throughout the tests, and that it is one of the two entities the tension machine control the load history by, it is an important measurement quantity. The uncertainty in the actual value of the displacement is however not that important as long as the relative measurements along the deformation path or across the different test specimens do not vary significantly. As described in Ch. 5, the measurements have been grouped in bins spanning approximately 0.1 mm of displacement (or 1 s). Fig. 6.12 shows the standard deviation of measured displacement in the 306 bins for 37 test specimens. This shows that the standard deviation within each bin is close to constant at ∼0.04 mm for all bins and tests. Assuming linear behaviour of the displacement within each bin spanning ∼0.1 mm, the mean value of each bin should be half way between the minimum and maximum value, and all values should be within approximately ±0.05 mm defining the whole bin. This implies that the displacement control moves at a constant speed and is accurate relative to itself across the whole load history as well as across the different test specimens. The 6 distinct dips in this plot (point A,B,C,D,E,F) indicate that the variation in displacement over the current bin is close to zero, and corresponds to the locations where the control system holds the current displacement and force constant between changes from a loading to an unloading sequence or vice versa. The standard deviation of displacement here is

<0.01 mm (based in the data shown in Fig. 6.12), and can be used as an estimate of how well the system controls a static displacement. Note that the readout from the control system will be more accurate when the system is dynamically loaded than during static loading (either displacement of force controlled) because of fluctuations around a specified set value in the control unit. Fig. 6.13 is a similar plot showing the standard deviation of measured force in each of the 306 bins. The same dips corresponding to where the tension machine holds the current position and force is clearly visible in this plot as well. In addition, there are two areas where the standard deviation is close to zero (0) for a longer period of time (spanning several consequtive bins over the sequence BC and CE). These identify areas where the force does not change significantly over the span of a bin and corresponds to where the test specimen deformes plastically (i.e. no significant additional force is needed for the test specimen to continue to deform. Based on this it is possible to deduce that in the elastic loading/unloading sequences the force changes relatively constant so that the standard deviation over the measurements in a bin is between 3 kN and 4 kN, while where the test specimen deformes plastically, the force changes less such that the standard deviation over a bin is <1kN. Note also that these plots shows the standard deviation across each bin and not the standard uncertainty.
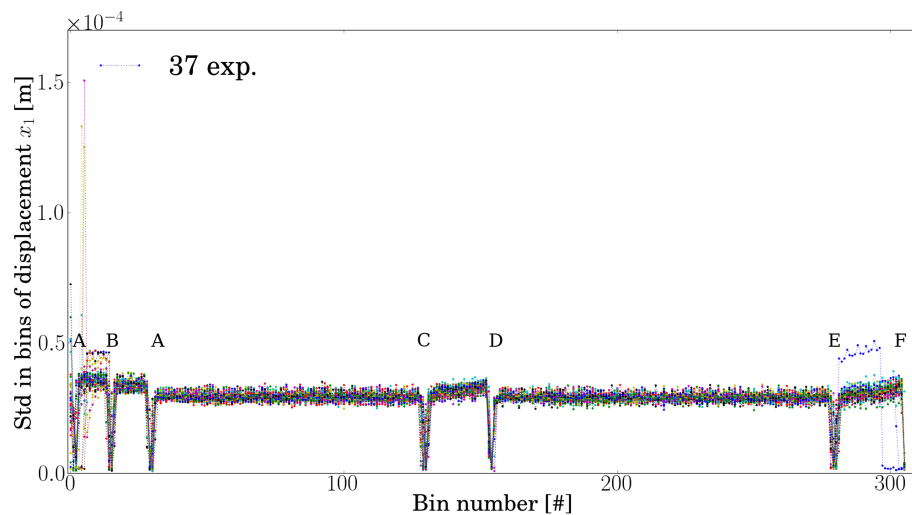
Figure 6.12: Standard deviation of the recorded displacement voltage (x_1) from the Instron machine within each bin
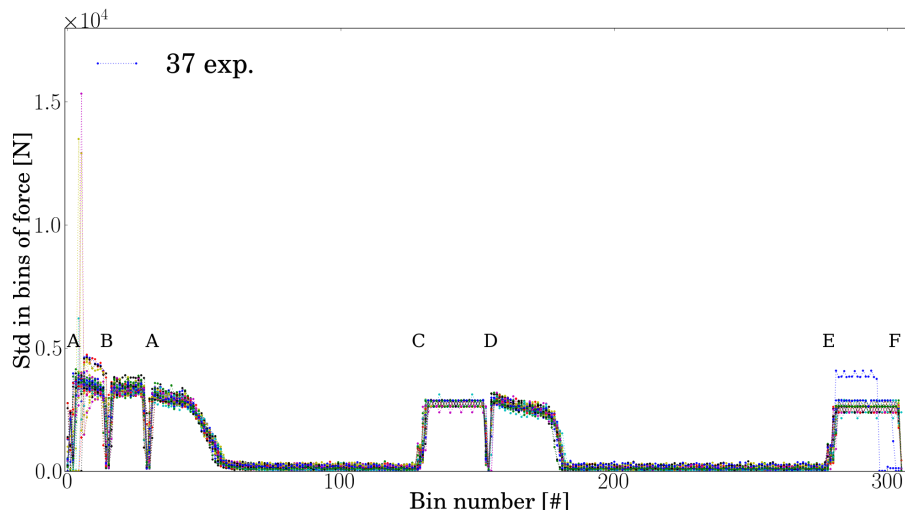
Figure 6.13: Standard deviation of the recorded force voltage (F) from the Instron machine within each bin

For all the different type of measurements a simultaneous reading of the displacement and force voltages have been recorded, with the exception of the acoustic (ART) measurements. Because of limitations of input channels on the DAQ in the acoustic setup, only a concurrent displacement voltage has been recorded. The ART measurements have been sampled at a frequency of approximately 40 Hz (i.e. 40 individual acoustic shots have been performed per second). For each of the acoustic shots/measurements the acoustic signal has been sampled at a frequency of 15 MHz by the DAQ, while simultaneously recording the displacement voltage at the same sampling frequency. At this high sampling rate random electric noise becomes observable over the acoustic shot / measurement period (90 μs). This can be seen in Fig. 3.7 b). The mean recorded displacement voltage over the acoustic interaction period (reference signal + tail) has been used to correlate the acoustic measurements to the concurrent force or other measurement quantities. The observed standard deviation in recorded displacement over the acoustic shot is less than approximately 0.008 mm. This is only 1/5 of the magnitude of the almost constant standard uncertainty over each bin of 0.04 mm shown above. Since the displacement voltage recorded by the acoustic setup and the MessTek are in fact the same voltage signal, the observed uncertainty across each bin from the MessTek displacement voltage recording does in fact include the uncertainty observed

over each acoustic shot. Thus the uncertainty observed across the acoustic shot has been disregarded when propagating uncertainties related to the displacement voltage reading for the acoustic measurements.

Since the reference displacement voltage behaves in a monotonically linear fashion, the relation between the recorded displacement voltages for different acoustic shots and the corresponding force can be extracted by linear interpolation from the displacement and force voltages recorded by Instron. The recorded displacement has as explained in Sec. 3.4 been used to relate the acoustic measurements to the other measurement quantities.

The Instron machine has been calibrated with respect to force (see App. B). The uncertainties in the force measurements are presented in Table 6.11. This force has been used to estimate the stress state of the test specimens, and to estimate the linear elastic properties of the current steel as described in Sec. 3.6.3, and the propagation of the related uncertainties have been discussed in Secs. 6.4.2 and 6.4.3.

The displacement output has not been calibrated since it incorporates the movement of the machine, the clamping wedges, and deformation of the test specimen itself. The uncertainty in the displacement reading is not vital for any further evaluation of estimated quantities and has not been evaluated beyond what has been described above, except as a measure of how well the deformation path of the different test specimens match each other. The standard uncertainty (see Eq. (6.2)) of the displacement and force over the 37 experiments have been plotted in Figs. 6.14 and 6.15 based on the recorded data from the individual tests shown in Figs. C.1 and C.2. The maximum observed uncertainty has been presented in Table 6.11. Recall that the standard uncertainty over n experiments is related to the variation of the mean over all the experiments and is inversely proportional to the number n of experiments. Thus this experimental standard uncertainty over the 37 tension experiments are less than the uncertainty within an individual experiment.
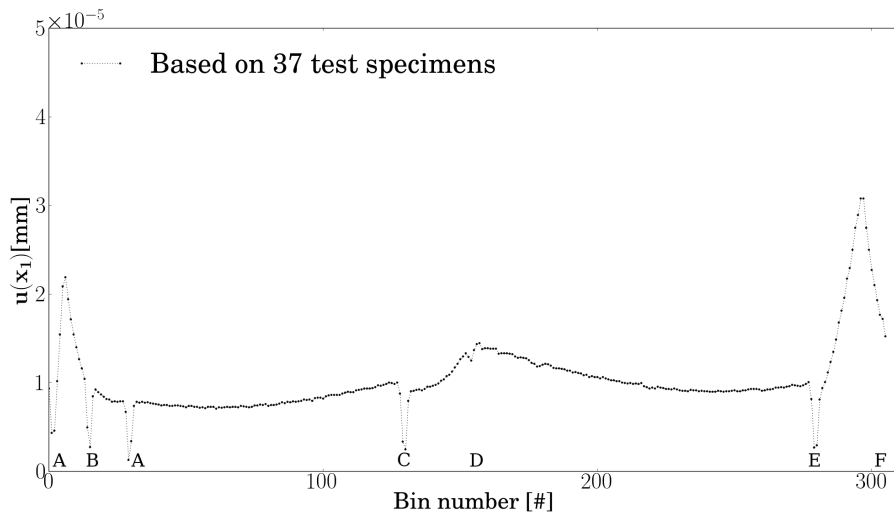
Figure 6.14: Standard uncertainty over 37 test specimens of the recorded displacement voltage (x_1) from the Instron machine
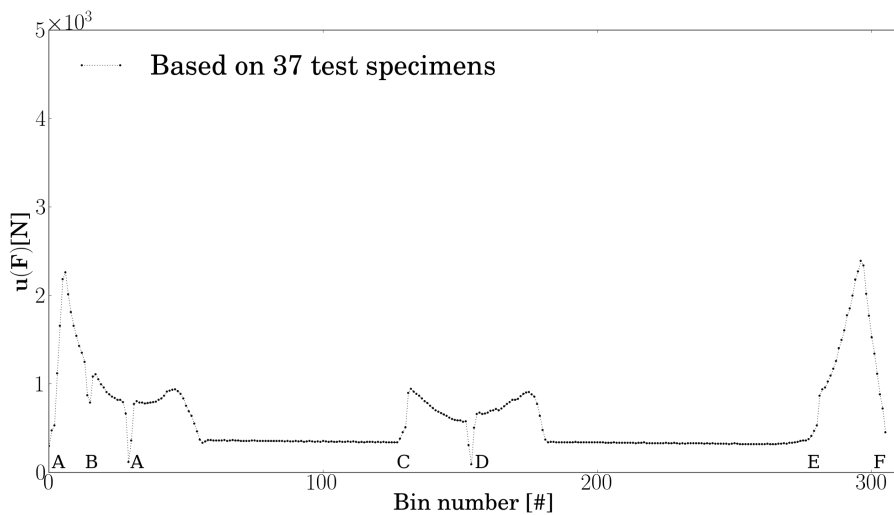
Figure 6.15: Standard uncertainty over 37 test specimens of the recorded force voltage (F) from the Instron machine applied in the $x - 1$-direction

Table 6.11: Uncertainties related to tension machine

Variable x_i	$\mu(x_i)$		$u(x_i)$		Confidence level [%]	$\frac{u(x_i)}{\lvert x_i \rvert}$ [%]	Based on
Instron/MessTek							
x_1^{Instron}	$\sim$0-22	mm	NA	-	-	-	-
F	$\sim$20-250	kN	-	%	68	<0.7	App. B
Maximum observed in relevant experiments							
x_1^{ART}	0-20	mm	$\sim$0.008	mm	68	-	similar data as shown in Fig. 3.7 b)
x_1	0-20	mm	<0.05	mm	68	-	Fig. 6.12
F^e	0-250	kN	$\sim$3-4	kN	68	-	Fig. 6.13
F^p	0-250	kN	<1	kN	68	-	Fig. 6.13
Standard uncertainty over relevant experiments							
x_1	0-20	mm	<0.03	mm	68	-	Fig. 6.14
F	0-250	kN	$\lesssim$2	kN	68	-	Fig. 6.15

Where x_1^{ART} and x_1^{Instron} denote the displacement measured by the Instron voltage recorded by the acoustic setup and the MessTek control unit respectively, while F^e and F^p denotes force measurements in the elastic and plastic region respectively.

Note that the term *uncertainty **in** individual relevant experiments* corresponds to the variation within one bin for one single experiment, while the term *standard uncertainty **over** relevant experiments* corresponds to the variation across all experiments for each bin number.

6.5 Simulation - uncertainty evaluation

No second or third order elastic constants have been available for the currently used construction steel. However, to be able to compare the measured values with the theory, the second and third order elastic constants for 8 steels found in the literature [39] [44] [46] have been used as presented in Sec. 5.7.4. The second order, Lamé constants λ and μ can be estimated based on estimated Young's modulus Y from the measured stress-strain relation, and the Poisson's ratio ν related to the contraction in the x_2- and x_3-direction compared to the elongation in the x_1-direction as done in Sec. 5.3.1. It has also been assumed that the uncertainty in the elastic constants presented in Table 4.2 and 4.3 from the above mentioned literature corresponds to a standard uncertainty (i.e. a coverage factor $k_p = 1$).

The propagation of these uncertainties through Eqs. (2.92), (2.93), (2.94), and (2.97), (2.98), (2.99) is complex, and to avoid rigorous derivation of uncertainty budgets a more convenient approach has been used. A numerical computation library called

Uncertainties: a Python package for calculations with uncertainties which utilise linear error propagation theory [108], has been used to propagate the stated uncertainties. To verify that the computation library works a case for the Railsteel (sample 4) from [46] has been run where all the lower and upper bound of different combinations of nominal values and stated uncertainties ($k_p = 1$) have been combined when calculating the sound velocity change. That is; the three values $\lambda - u(\lambda)$, λ, and $\lambda + u(\lambda)$ for the input parameter λ have been combined with the same three value variations for μ, A, B, C, and ρ resulting in 729 variations. The nominal, maximum and minimum resulting sound velocity changes from this variation have been compared to the calculations using the Python package *Uncertainties* [108]. The result of this comparison has been plotted in Fig. 6.16 where the gray lines are the estimates based on the varied combinations of inputs. This shows that the uncertainty package calculates uncertainties on the same scale as the variation of input does. As can be seen from Fig. 6.16 the uncertainty estimated based on the Python package is less than the variation seen between the maximum and minimum from the parameter variation. This is as espected as it is more unlikely that the estimated parameters are combined in such a way as to maximise or minimise the effect of the combination. The nominal value plotted in Fig. 6.16 is the same as already shown for Railsteel-4 in Fig. 5.22, including the propagated uncertainties using the Python package.
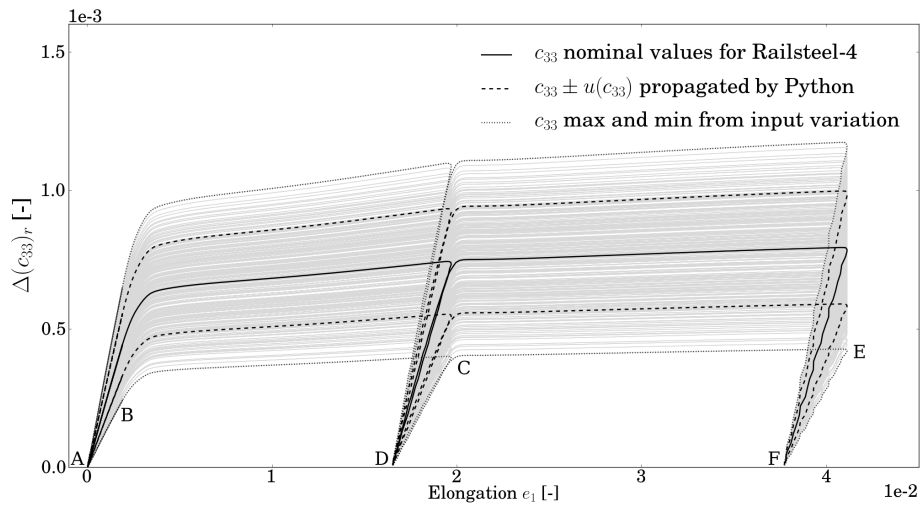
Figure 6.16: Uncertainty propagation in calculation of relative longitudinal sound velocity change for Railsteel (sample 4) (see Table 4.4) using the python package *Uncertainties* and by varying the input parameters as described in Sec. 6.5.

7

Discussion

In this chapter the relevant measurement results are discussed, together with a comparison between the measurements and the predicted theoretical results. Together with the actual measurement results this forms the basis for the overall conclusions summarised in Ch. 8.

7.1 Tension test results

Sec. 5.2 presents the load history and displacement pattern for each of the 37 test specimens that form the basis of the experimental investigation performed in this study. As can be seen in Fig. 5.1 the displacement behaviour of all the 37 test specimens are close to identical for the given load history. Based on the similarity of the initial geometry it is evident from Fig. 5.1 that all the 37 test specimens have a very similar deformation response for the axial elongation (in x_1-direction) when subjected to the applied load history. From this it is reasonable to assume that all the test specimens are subjected to approximately the same history of stress/strain levels. Thus the acoustoelastic effect measured in any of the test specimens should experience the same level of pre-stress and be comparable across the test specimens. The fact that all the test specimens have been subjected to the same load history and deformation response is a requirement to be able to statistically evaluate and compare measurements from all of the test specimens.

7.2 Elongation and true stress

There are mainly two reasons why the strain/elongation and stress development throughout the test sequences have been measured. The first reason is related to how the

7. DISCUSSION

measured acoustoelastic effect can be compared with results from the theory presented in Ch. 2. As shown in Eqs. (2.91) and (2.95) the predicted change in sound velocity is a function of either applied e_1-elongation (axial) or true stress. The other reason, which has been argued to be obsolete, is to be able to calculate the sound velocity across the test specimen based on the measured resonance frequencies. The resonance frequencies are dependent on the actual thickness at the moment of each resonance frequency measurement, which can be estimated based on the measured elongation in the thickness direction (elongation in the x_3-direction). Thus the estimated sound velocities are also dependent on the actual thickness of the test specimen. However, because of the removal of the thickness dependence by investigating the development of the ratio between resonance frequencies as described in Sec. 2.7, the elongation measurements are not actually needed to be able to measure the effect predicted by the acoustoelastic theory. Nevertheless resulting sound velocity estimates gives valuable additional information of the acoustic behaviour and have been included in this work.

In addition, two second-order elastic moduli may be estimated from the relations between different elastic elongation and stress measurements as described in Secs. 2.4 and 3.6.3.3.

Two different approaches have been used to measure local elongation of the test specimens in the x_1-, x_2-, and x_3-direction. As described in Sec. 3.6.1 one of the approaches was to use strain guages adhered to specified relevant locations on the test specimens. These strain gauges have given good average measurements in one direction over the area of their physical extent at the location where they are fastened. The measured elongation and estimated stress from several strain gauges in the x_1-, x_2-, and x_3-direction on different test specimens have been presented in Figs. 5.4 to 5.7. With the approximately uniform geometry of the test specimens and homogeneous displacement the elongation measured at one specific location should be a good estimate for the elongation in the same direction at any other point on the test specimen. By varying the location of placement of the strain gauges and comparing the results for all the relevant tests, as done in the figures mentioned above, this has been shown to be a reasonable assumption. The estimated values for the elastic moduli Young's modulus Y and Poisson's ratio ν based on the elongation and stress measurements from the strain gauge setup have been presented in Table 5.2. They have also been estimated

based on the estimated sound velocities in the unstressed state (Table 5.5) which shows reasonable good coherence with the estimates based on elongation measurements and values reported in the literature (Table 4.4). This also corroborate the method used to estimate the sound velocities including the beam diffraction correction (discussed in Sec. 7.5). As discussed in Sec. 6.4.1.2 the strain gauges have an assumed associated systematical underprediction error related to the orientation of placement and bonding of the strain gauge on the test specimens. Experienced laboratory personelle at DNV estimate this underprediction to be in the order of 2-4 % of the measured elongation [109]. However, the calculated elastic moduli Y and ν based on the uncorrected elongation measurements (see Table 6.6) are closer to those estimated based on estimated unstressed sound velocities in Table 5.5, and they fit reasonably well with the second-order elastic moduli for other steels presented in Table 4.5. The implication of disregarding the systematic error in the strain gauge measurements have been presented in Table 6.6 in Sec. 6.4.1.2. It is evident from Eq. (2.105) that the estimated Poisson's ratio is not significantly affected if one assumes that the same order of magnitude of error appears both for the axial (e_1) as well as the transverse (e_2, e_3) elongations. For the estimation of Young's modulus in Eq. (3.19) the true stress is a function of elongation in both the transverse directions (e_2, e_3). Because the effect of underprediction of e_2 and e_3 on the stress is much less than the effect on the e_1 elongation (see Sec. 6.4.3), and thus the Young's modulus is overpredicted by close to the same amount as the e_1 elongation is underpredicted.

From Eqs. (2.121) and (2.122) it is also evident that both the absolute and relative sound velocity changes are affected by an underprediction in e_3 elongation values. The change in ratio between longitudinal and shear sound velocities (Eq. (2.124)), or its relative change (Eq. (2.125)), is however not affected by this underprediction of the elongations. It should however be noted that since the results presented in this work are plotted against the measured elongations the plotted points might have a horisontal shift in the order of up to 4 % of their elongation value. This one-sided tentative additional uncertainty in the presented elongation measurements has not been included in the error bars of the plotted elongations in this work.

Without documentation on the actual underprediction, the relative good fit with other steel data, and the fact that the accuracy of the absolute elongation values does

not influence on the measured effect of acoustoelasticity for the ratios between longitudinal and shear sound velocities, it has been decided to use the uncorrected elongation measurements from the strain gauges when presenting the results from this work.

The other approach to stress and strain measurements was a photometric measurement technique called ARAMIS (Sec. 3.6.2), which gives a two-dimensional strain field in the x_1-x_2-plane on the surface of the test specimens. Based on this 2D strain field a thickness reduction strain in the x_3-direction was also estimated by the ARAMIS software (see Sec. 3.6.2 for details). The measurement results from the ARAMIS setup have been shown in Figs. C.10 to C.19 in App. C.2.2. The estimated values for the elastic moduli Young's modulus Y and Poisson's ratio ν based on the ARAMIS measurements have been presented in Table 5.3. When comparing these elastic moduli with the ones estimated based on strain gauge measurements in Table 5.2 and the ones for steels presented by other authors in Table 4.5, the ARAMIS measurements result in estimated values which differ considerably from the values which are commonly accepted as reasonable values for steel types. The values of $\nu(e_3) > 0.5$ estimated based on the ARAMIS estimated e_3-elongation are in fact unphysical since $\nu \in \{-1, 0.5\}$ [13]. In addition, the maximum measured uncertainty of the ARAMIS measurements are considerably larger than the corresponding uncertainties in the strain gauges (see Table 6.8 in Sec. 6.4.1.4). Based on these considerations the ARAMIS measurements have only been included for reference in App. C.2.2, and all relevant conclusions are thus based on the measured elongations by strain gauges.

7.3   Temperature

As argued both in Secs. 5.4 and 6.3.1 the relative uncertainty in the sound velocity due to temperature difference is ~0.0006 % for the actual measurements performed in this study. This is two to three orders of magnitude less than the actual observed sound velocity change (which is in the order of 0.1 % for the elastic ranges, AB, CD and EF in Fig. 5.19). The sound velocity of both longitudinal and shear waves are also negatively correlated with increasing temperature [105], which can not explain the different sign of the sound velocity change observed for the longitudinal and shear sound velocity. Thus, any temperature contribution has been assumed to be negligible in this work.

7.4 Acoustic resonance

Comparing the different acoustic resonance frequencies (the L1, L2, and S3 mode) across the different test specimens shows that there is a large spread in the measurements (See Fig. 5.9 in Sec. 5.5 and Figs. C.21, and C.22 in App. C), both across the tests as well as within some of the tests. By grouping the acoustic shots in bins as described in Sec. 3.4 (Table 3.4) it is possible to investigate the mean behaviour across the number of test specimens. The result of this has been presented in Figs. 5.10, 5.11, and 5.12. By comparing the relative change instead of the absolute values the variability is further reduced as can be seen in Fig. 5.14. From this, it can be seen that there is a similar resonance frequency response in all of the test specimens as a function of applied elongation. As an increase in frequency corresponds either to an increase in sound velocity, or a reduction in the thickness of the specimen, according to Eq. (2.121), it is difficult from the relative change in resonance frequencies (Fig. 5.14) alone to draw any conclusions to whether the change in resonance frequencies are related to sound velocity change or thickness change. However, examining the elastic loading and unloading regions below approximately 0.2 % (AB), 2 % (CD), and 4 % (EF) applied elongation e_1, it is evident that the S3 resonance frequency changes in a negative manner compared to the opposite positive change of the L1 and L2 resonance frequencies. This can not be attributed to the change of thickness, and as such must be related to a corresponding change in sound velocity. Because of the obvious difference in behaviour of the longitudinal and shear resonance frequencies it is possible to eliminate the thickness dependency as described in Sec. 5.6.2.

Fig. 5.20 shows a clear dependency between the applied elastic elongation level and the measured ratio of longitudinal (L1 and L2) and shear (S3) resonance frequencies. The L1/S3 or L2/S3 ratio shows a linear dependency on the applied elongation e_1 with a relative change of just above 0.2 % over the elastic loading regions AB, CD, and EF. In the plastic regions the L1/S3 and L2/S3 ratio have much less dependence on the applied elongation e_1, and the two ratios also show different sign of the slope of the relative change during plastic deformation. This discrepancy in the behaviour of the two ratios has been further discussed in Sec. 7.4.1.

The relative change in L1/S3 and L2/S3 frequency ratios are independent of the thickness and is thus only related to the change in sound velocity as a function of the

189

applied elongation level. Based on this finding it is evident that the ART method is capable of measuring a systematic significant effect of acoustoelasticity as function of applied uniaxial stress/elongation. The systematic significance has been discussed in more detail in Sec. 7.7 where the results from this work has been reviewed in light of the objective of this study.

7.4.1   Beam effect

Theoretically, the longitudinal sound velocity giving rise to both the longitudinal resonance frequencies (mode L1 and L2) should be the same, and thus it could be argued that the development of the L1/S3 and L2/S3 frequency ratios should be equal. This is obvious not true from both Figs. 5.14 and 5.20. Recalling the beam effect discussed in Sec. 2.6.2, the different resonance modes will be shifted either up or down in frequency. This effect depend on angle of incidence compared to the resonance frequencies created by waves propagating perpendicular to the interfaces of the rectangular test specimen. The L1 resonance mode measured for the different ART tests has been shifted downwards in frequency by approximately 4.5 %. Conversely the measured L2 mode has been shifted upwards in frequency by approximately 1.5 %, while the S3 mode has no significant systematic shift caused by the beam effect (see Figs. 2.10 and 3.9). If the beam diffraction effect is constant throughout the tests it will fall out of the relative change relations. However, if the frequency shift depends on the thickness and/or stress state, or other factors that vary throughout the load history, it may have lead to a more complex relation that will not fall out of the relative change relations. Thus, it is concievable that the discrepancy between the L1/S3 and L2/S3 ratios seen in Fig. 5.20 is due to the beam effect not beeing constant throughout the tests. According to Eq. (2.121) the ratio L2/L1 should ideally have 0 relative change throughout the tests, and this discrepancy may simlilarly be an effect of the downward- and upward-shift of the L1 and L2 modes respectively. The beam diffraction effect has been investigated by other authors [92][93][96][97] (see Sec. 2.6.2), but its influence on the acoustoelasticity has not been within the scope of this work (with the exception of correcting the initial estimated longitudinal sound velocity as described in Sec. 3.6.3.1).

7.5   Sound velocity change

The longitudinal and shear sound velocities and their corresponding relative change can be calculated based on the measured resonance frequency and the measured thickness change as described in Sec. 5.6. The acoustoelastic effect predicts changes in the longitudinal and polarised shear sound velocities as a function of the applied deformation or stress level. The relative change in sound velocities are predicted to be different for both different propagation directions and different particle motion directions. This effect of velocity changes of longitudinal and shear waves for an isotropic hyperelastic material subjected to either compression or tension has been proved by several authors for many polycrystalline materials including both aluminium and steel (see [32] [44] [39] and Sec. 1.4). The observed change in the sound velocities presented in Sec. 5.6 corroborates thus these earlier works, as well as confirm the capability of the currently applied measurement method to measure the acoustoelastic effect. However, the uncertainties associated with the estimation of actual sound velocities, or their relative change, are very much dependent on the uncertainties related to the initial thickness and/or its development (Sec. 6.3). As such the uncertainties in the sound velocity measurements are much larger than those associated with the ratio of longitudinal and shear sound velocities where the thickness dependence fall out. Because of the thickness independence of the relative change of sound velocity ratio (Eq. (2.125)), or conversely of resonance frequencies, this ratio is a more accurate method of measauring the acoustoelastic effect than by measuring the relative change of the individual sound velocities. Thus it has been selected as the main measurement result to investigate the capability of measuring the acoustoelastic effect by the ART methodology.

It is also noted that a beam diffraction correction of the estimated initial sound velocities of the L1 and L2 resonance modes as shown in Fig. 5.17 can be done to mitigate the shift in estimated longitudinal sound velocities based on the beam diffraction effect described in 3.6.3.1. This way of correcting for the beam diffraction effect has not, in the knowledge of the author, been done before. The beam diffraction effect will however not affect the relative change in sound velocities if the same correction factor $\eta^{(n_l)}$ in Eq. (3.11) is applicable throughout the tests. However, it is noted that this might not be the case and further investigation and inclusion of the beam effect presented in Sec. 2.6.2 are needed to adequately account for the changing resonance thicknesses.

The good coherence between the linear elastic moduli estimated based on elongation measurements (Table 5.2) and based on estimated longitudinal and shear sound velocities for the unstressed configuration (Table 5.5) also corroborate the method used to estimate these sound velocities (including the beam diffraction correction).

7.6   Comparison of experiments and simulation

Figs. 5.22 to 5.26 shows a large variety in simulated acoustoelastic responses based on the reported third-order elastic constants from 8 steel types found in literature (see Table 4.4). Figs. 5.27 to 5.29 show the same simulated acoustoelastic development for the three steel types (Group3 in Table 5.6) that have the same type of sound velocity development for both longitudinal and shear modes overlayed with the measured acoustoelastic development of the current steel type used in this work ("Bright rectangular steel bar S235JRG2C+C" [79]). It is evident that the measured developments are similar to several of the theoretical development curves, however, it is also evident that one can not assume a certain behaviour of a relevant steel type without extensive experimental testing to establish the acoustoelastic constants. Looking at the spread in L1/S3 and L2/S3 ratios (Figs. C.25 and C.26), this may also indicate that the acoustoelastic effect may be slightly different for different test specimens from the same production batch (e.g. spatial variation in third-order elastic constants for one steel type). Establishing the necessary third-order elastic constants through extensive testing is impractical for most inspection situations where the steel under investigation may be from several production batches, and even different manufacturors. Based on the relative concurrence of the acoustoelastic behaviour across the test specimen seen in this work, it might be possible to establish an acoustoelastic relation based on simple tension tests for the relevant steel. As can be seen from the three different groups of steels with similar magnitude third order elastic constants presented in Table 5.6, the results from the theoretically simulated behaviour presented in Sec. 5.7.2 are similar for the steels within each group. Although it is not possible to establish the correct theoretical relation between a relative change in sound velocities (or the ratio between sound velocities) and an applied elongation through such a simple tension test, it might nevertheless provide a sufficiently good empirical relation for the steel under investigation as done by Gaschi in 2009 [64] as mentioned in Sec. 1.4. This is an area that needs

further investigation of many more steel types to be able to categorize the steels which behave in such a manner that this approach is applicable.

Note also that the benefit of using the ratio between the longitudinal and shear sound velocities/frequencies to remove the thickness dependency is most prominent when the longitudinal and shear sound waves experience opposing changes in relative sound velocity change. It is conceivable that in the case where the longitudinal and shear sound velocity change with the approximately the same relative magnitude and sign, the benefit of making the measurement thickness independent may be opposed by diminishing measured change in the ratio c_l/c_s.

The observed variation in the measured relative sound velocity change for the different test specimens from the same production batch, with a magnitude in the order of the acoustoelastic effect, indicate that local variation of the second- and third-order elastic parameters may also be present within each test specimen of the investigated steel. This indicates that it might be difficult to experimentally determine second- and third-order elastic parameters which are reliable and relevant for arbitrary measurement points on a given steel. A more generic apporach may be to rather rely on empirically established relations between the applied stress/strain and relative change in L1/S3 or L2/S3 ratios for the relevant steel, and statistical analysis of independent measurements.

7.6.1 Polarisation of shear waves

One particular area of discrepancy between the theory and the current measurements that has not been discussed yet is the seamingly missing predicted effect of different sound velocity change of the shear waves polarised (i.e. with particle motion) parallel (c_{31}, Eq. (2.98)) and perpendicular (c_{32}, Eq. (2.99)) to the applied tension (i.e. for $\sigma_{11} \neq 0$ and $e_1 \neq 0$). This effect has been proved by other authors (see [32], [44], and [39] and Sec. 1.4) and shown in the simulations of the different steel types in Figs. 5.23 and 5.24 respectively. As argued in Sec. 3.5, waves of all polarisation directions (uniform circular distribution) should be excited in the test specimen, leading to an equal amount of vertically polarised shear waves (SV) polarised in the direction of- as well as perpendicular to- the applied tension. However, the measured relative change of the shear sound velocity shows a similar behaviour as the simulated sound velocities for the shear waves polarised in parallel to the applied tension for the Group 3 steels (see

7. DISCUSSION

Tbl. 5.6) as shown in Fig. 5.28. Thus it has been assumed in this work that the shear wave with particle motion polarised in parallel with the applied tension has the most dominating sound velocity change, and thus dominate the contribution to the sound velocity induced relative change in the S3 resonance mode. This is also in concordance with the observations reported in e.g. [32], [44], and [39], where the shear sound velocity polarised in parallel with the applied stress experience a larger relative magnitude of change in sound velocity that the shear wave polarised perpendicular to the applied stress. The difficulty in distinguishing the potential different resonance peaks of shear waves polarised in parallel or perpendicular to the applied stress is discussed below.

For all the steels compared in Figs. 5.23 and 5.24, the simulated change in sound velocity for the shear waves polarised parallel to the tension is different in magnitude to the shear waves polarised perpendicular to the applied tension, and some times also with opposite sign of change [32] [44] [39]. This is also the effect utilised in the bifurcation measurements presented in e.g. [50] mentioned in Sec. 1.4. If the currently tested steel specimens exhibit the same behaviour one would expect the even distribution of shear wave polarisations of the un-stressed S3 resonance frequency to split into two destinct peaks for a sufficiently large applied stress (i.e. $\sigma_{11} \neq 0$ and $e_1 \neq 0$). This split of a resonance peak in the frequency spectrum, corresponding to two perpendicularly polarised shear waves (parallel and perpendicular to the applied tension) propagating perpendicular to the applied tension across the thickness of the test specimen, must be sufficiently large to be detected by the FFT algorithm. However, for the small changes in the resonant frequencies as have been measured in this work (approximately -0.2 % over the elastic ranges AB, CD, and EF - corresponding to approximately -1 kHz), the potential splitting of the S3 frequency spectrum peaks are to close to each other for the FFT algorithm to distinguish them (i.e. from Sec. 3.5.1 the FFT of the current recorded signal has a spatial frequency resolution of 16.7 kHz compared to the potential split of less than 1 kHz). For the Group 3 steels (having the most similar simulated velocity change behaviour compared to the currently used steel) the maximum simulated change in c_{31} is between -0.3 % and -0.6 %, while the maximum change in c_{32} is positive and an order of magnitude less (between 0 and 0.05 %). This corresonds to a frequency change of approximately -2 to -4 kHz for the waves polarised parallel to the applied tension (c_{31}), and approximately +0 to + 0.3 kHz for the waves polarised perpendicular to the applied tension (c_{32}). Although the FFT algorithm can determine the peak position of

the resonance peak to numerical precision, it is less adequate to distinguish two nearby peaks as the full width at half maximum value of the S3 peak is approximately 40 kHz. See Fig. 7.1 and the shear resonance frequency peak at approximately 660 kHz. For reference, dark blue lines indicate the measurements at the start of the test while increasing warmth through lighter blue, green, and yellow tones signify measurements along the load history, finally reaching bright red at the end of the test. As the full width at half maximum is approximately 10 times the expected difference in resonance peaks of the waves propagating at the respective sound velocities c_{31} and c_{32}, it has been assumed that the S3 resonance peak is actually a superposition of the two shear wave resonance peaks. Thus the measured S3 peaks are probably measured at some frequency value in-between the frequencies corresponding to the individual polarised waves. The development of the S3 resonance measured in this study is thus probably the combined effect of shear waves polarised both perpendicular and parallel to the applied tension. Note that if it is assumed that the Group 3 steels are a good representation of the current steel, this means that the measured relative change in the S3 resonance should be somewhere between the simulated change in c_{31} with a maximum between -0.3 % and -0.6 %, and the maximum simulated relative change in c_{32} between 0 and 0.05 %. The maximum relative change observed in the elastic regions AB, CD, EF is in the order of -0.2 %, which fits well with this assumption for the Group 3 steels.

Even though the different polarisation directions in the worst case could behave in a way that cancel out the acoustoelastic effect, the measured shear resonance will still be important because of its capability of making the acoustoelastic response through the ratio of longitudinal and shear resonance frequencies independent of thickness change. Its also has the ability to enhance the relative change where shear and longitudinal waves have opposite development behaviour, which can be used in an empirical calibration of the acoustoelastic effect for a relevant test specimen material as earlier mentioned was done in [64]. The effect of excited polarisation of shear waves, and algorithms and hardware able to distinguish them, should be further investigated in future work.

7.7   Results compared to the literature

The objective of this work is to investigate the possibility for using a non-contact acoustic measurement system measuring the cross-thickness resonance frequencies across a
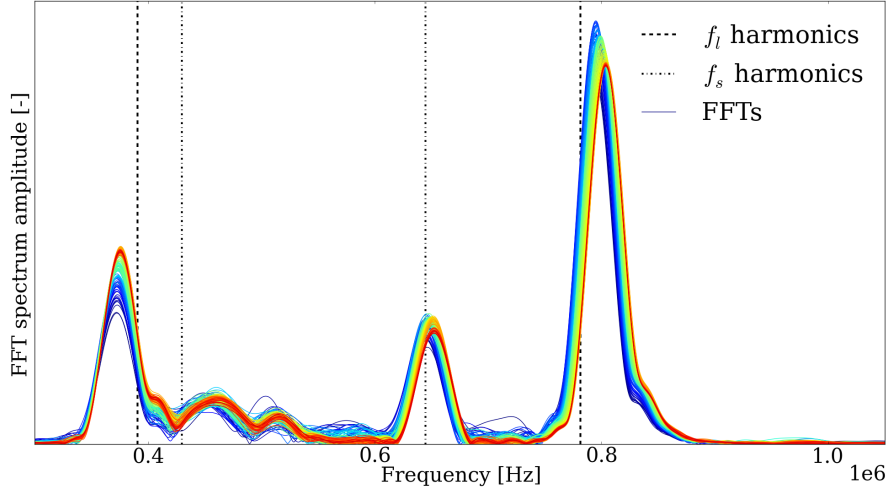
Figure 7.1: FFT spectrum development of test specimen # 32 throughout the load history. Dark blue signify the start of the load history, while increasing warmth through lighter blue, green, and yellow tones signify measurements along the load history, finally reaching bright red at the end of the test.

steel plate to detect changes in material properties at very high stresses. The investigated method used in this work relates the measured resonance frequencies and changes therein to changes in the compressional sound wave velocity, c_l , and/or the shear sound wave velocity, c_s, which have been shown in the literature to depend on the stress state of the steel as mentioned in Sec. 1.4 e.g. [32], [44], and [39]. The measurement methods used in the literature presented in Sec. 1.4 commonly utilise a system of transducers bonded directly to the test specimen (see e.g. [61], [67], [64]), although there are examples of setups using non-contact methods (e.g. [52] utilising longitudinal pressure waves with a frequency of 12.5 MHz to excite the test specimen). However, in their 2009 paper [68], Kim and Hong studied a non-contact setup utilising oblique incidence of longitudinal waves and mode-conversion and time of flight (TOF) of a pulse-echo system to measure the sound velocity of both c_l and c_s in the test specimen. They noted that the method was limited by the resolution and sensitivity necessary to generate the high-frequency ultrasound needed to detect small changes in TOF.

The currently applied measurement method utilise the same phenomenon of mode-conversion to excite both longitudinal and shear waves in the specimen by an incoming longitudinal pressure wave. The excited waves reflect within the specimen and transmitt

longitudinal pressure waves which propagate back toward the transducer system including information on the cross-thickness resonance frequencies of both longitudinal and shear waves. This work has shown that the acoustic resonance technology is capable of measuring small changes in these resonance frequencies. The accuracy of the measured resonance frequencies is limited by the stochastic uncertainty in resonance modes which has been estimated to be in the order of <0.02 % for the two longitudinal modes L1 and L2 and <0.04 % for the shear mode S3 (see Sec. 6.2, Table 6.1). Note that the spatial resolution of the FFT limiting the ability to distinguish two resonance frequencies in close proximity as discussed in Sec. 7.4.1 means that the stochastic variation in the measured S3 mode is related to the determination of the possibly combined FFT peak. Combining the longitudinal and shear resonance modes to measure the relative change in the c_l/c_s ratio removes the thickness dependency as described in Sec. 2.7. This is a plane wave theory simplification, and because of the beam diffraction effect the c_l/c_s ratio may not be entirely thickness independent (see Secs. 2.6.2, 5.6.2, and 7.4.1). The propagated stochastic uncertainty in the ratio has been estimated to be in the order of $\lesssim 0.07$ % (Sec. 6.2, Table 6.1), which is less than the maximum measured relative change over the elastic regions AB, CD and EF of ~ 0.2 % (see Sec. 5.6.2 Fig. 5.20). Although the maximum stochastic uncertainty is approximately 35 % of the maximum measured relative velocity ratio change, it has been shown that the experimental mean is changing in a non-stochastic manner throughout the loadhistory of the test specimen. Even though the uncertainty of one measurement is too high to be able to estimate the stress state, the measurement method has been regarded sufficiently accurate when comparing several consequtive measurements to measure a systematic significant effect of acoustoelasticity as function of applied uniaxial stress/elongation over the elastic range of the steel applied in this work. The relative change in the estimated mean value over the 13 acoustic test specimens for the sound velocities $c(f^{(n_l=1)}, e_3)$, $c(f^{(n_l=2)}, e_3)$, and $c(f^{(n_s=3)}, e_3)$ are in the order of $\lesssim 0.08$ % for the two longitudinal estimates, and $\lesssim 0.2$ % for the shear estimate respectively (see Sec. 5.6). However, eventhough these relative changes are in the order of the changes measured for the c_l/c_s ratio, they ared dependent on the e_3 measurements and its related uncertainty. Thus, to avoid the actual need of performing thickness measurements, it is convenient to remove this dependency by using the c_l/c_s ratio (see Secs. 5.6 and 6.3).

7. DISCUSSION

The result of this work has shown the capability of a non-contact acoustic measurement method to measure predicted and previously confirmed effects of the acoustoelastic theory (e.g. [32], [44], and [39]), both for longitudinal and shear sound velocity development. It has also shown how the acoustoelastic effect can be measured with a thickness independent quantity by combining opposite development of the longitudinal and shear sound velocity and their ratio c_l/c_s (i.e. (2.124)). This is an important development with respect to industrial use where sufficiently accurate thickness measurements may be difficult to obtain.

One challenge identified by the current work has been the large diversity of the acoustoelastic behaviour for different steels. This has been suggested by the simulation of the theory using second- and third-order elastic constants for different steel types presented in the literature. The simulations indicate that steels with similar second-order elastic constants may have third-order elastic constants resulting in very different simulated behaviour of the longitudinal and shear sound velocities. Although the steel used in this work seems to change according to one class of steel types where at least one of the shear modes have a negative sound velocity development while the longitudinal pressure mode have a positive change under tensional loads, which will increase the measured relative change of the c_l/c_s ratio (i.e. $\Delta \left(\frac{c_l}{c_s} \right)_r$ in Eq. (2.125)), other steels may behave in a manner that instead reduce the measured relative change of this ratio. For industrial application it is important to understand the mechanism which distinguish different steels to either enhance the measured relative change by utilising the c_l/c_s ratio, or where this actually reduce the measured relative change.

7.7.1 Potential industrial application of results

As this work has been performed utilising an existing ART measurement system developed for inline inspection of pipelines it is natural to view the results in light of this application.

It has been observed that steels with small variations of the second order elastic parameters (λ and μ) may have significantly different third order elastic parameters (A, B, and C) result in significantly different dependencies of the sound velocities on the applied elongation/stress state (see Sec. 5.7.2 and Table 5.6). Accurately determined elastic properties are needed to estimate the stress dependency on the acoustic sound velocities, as well as an unstressed reference state to be able to estimate the relative

change in the sound velocities, is needed to estimate the stress state. As such, this renders a single measurement of resonance frequencies incapable of determining the elongation/stress state in steel.

However, by performing a set of uniaxial tension tests it might be possible to establish a relevant empiric dependency between the applied elongation/stress and the relative change in ratio of longitudinal and shear resonance frequencies for a relevant isotropic steel. This dependency is independent of the thickness of the sample / measurement object. Thus, if the sound velocity - stress dependency has a sufficiently significant variation over the elastic deformation range, it may be possible to use ART to estimate the uniaxial elastic elongation/stress state at a specific location given an established reference measurement for an unstressed state. Continous monitoring of the stress level at a given location where the measurement system can be installed permanently and operated continuously may thus be a potential industrial application.

For in-line inspections using an ART pipeline inspection gauge (PIG) it is not possible to establish the above mentioned reference measurements for an unstressed state of already installed pipelines. However, using statistical methods two potential applications have been identified:

- With N independent sensors measuring around the circumference of the pipeline it may be possible to establish the mean resonance ratio c_l/c_s response around the cross-section of the pipeline. By comparing consequtive sets of circumferential measurements in the axial direction, one should be able to identify any circumferential location with a consistent significant deviation from the circumferential mean over a finite axial length. This would then indicate an area with hoop strain/stress consentration compared to the surrounding areas, and could together with the thickness measurements identify a corroded area where the hoop stress level is close to the structural capacity. This method requires the pipeline to be operated at operating pressure, so that the steel is subjected to the critical dominating hoop-stress, to be able to identify the relevant critical areas.

- Another application may be to identify locations along the pipeline where excessive strains/stresses are localised due to global buckling of the pipeline. Where the pipeline is subjected to bending the cross-section of the pipeline will be subjected to a range of stress states ranging from compressive stress on the inside of the bend, through a state of zero stress in the midle of the pipeline, to a tensional stress on

the outside of the bend. Thus, by comparing the circumferential measurements along the axis of the pipeline it should be possible to identify areas where the pipeline has been subjected to global buckling. This method require the pipeline to be run at low operating pressure so that the axial stress is the dominating stress.

For the current steel investigated it is also noted that the shear frequency decrease under increasing applied elastic stress (Figs. 5.12 and 5.18). However, when the specimen start to plastically deform the shear resonance frequency has been observed to increase. This indicates that the thickness-reduction, giving rise to an increase in measured frequency (Eq. (2.120)), under plastic deformation is larger than any negative change in sound velocity according to the acoustoelastic effect. Thus, if the load is known to be stable or increasing together with an observed increase in the measured shear resonance frequency, this might indicate that the elastic limit has been exceeded for the current steel. Such considerations might thus be used as an indication if the material has seen plastic deformation during the measurement period.

7.8 Change of Young's modulus

The experimental work performed in this study has revealed an, to the author, unexpected effect where the Young's moduls Y changes significantly after the test specimens were plastically deformed (in the order of -15 % for 4.5 % axial elongation). This was not expected with reference to e.g. [29, ch. 10.5]. However, similar observations have been reported in the literature before in e.g. [110], [111], and [112]. The current observation has been presented in Sec. 5.3.1 and discussed here. Although the observation discussed in this section is not within the objective of this work it is an interesting physical behaviour that the author have not found readily discussed in current literature. Thus this section have been included for reference.

Repeated testing of steel samples from a common construction steel "Bright rectangular steel bar S235JRG2C+C" [79] have shown a consistent reduction of the Young's modulus as a function of applied plastic elongation. It has been observed that the relation between applied stress (calculated from force and cross sectional elongation) and elongation in the x_1-direction (measured by strain gauges and ARAMIS) does not

follow the same slope for all elastic loading/unloading sequences. In the elastic regime before first yield (plastic deformation) the slope of the stress-elongation curve yields a Young's modulus (Y) (estimated from linear regression) of approximately 210 GPa, which fits well with the other unstressed steels presented in the literature (see e.g. Table 4.5). However, after the test specimens have been plastically deformed, the next unloading at approximately 2 % e_1 elongation yields a Young's modulus of $\sim$185 GPa, while the last unloading at $\sim$4 % e_1 elongation yields a Young's modulus as low as $\sim$179 GPa (see Table 5.2). This is a lowering of the Young's modulus of approximately -12 % and -15 % respectively (The uncertainty in the estimated Y has been estimated to be approximately 1.2 % in Sec. 6.4.2). This effect was not expected, and while it could concievably be an effect of degredation in the strain gauges used to measure the deformation, the independent photometric ARAMIS measurements showed a similar reduction in estimated Y (see Table 5.3). Note that the ARAMIS measurements have not been used in any evaluations done in this work due to high uncertainties related to the absolute value of the strain measurements. However, eventhough the absolute values have a large uncertainty, the decrease in estimated Y still corroborate the corresponding results based on the strain gauge measurements. This effect was not anticipated, however, the author has found similar observations reported in literature (see for example [110], [111], and [112]).

Since the acoustic sound velocity in solids can to the first order of approximation be expressed as (from Eqs. (2.97), (2.98), and (2.99))

$$c_l = \sqrt{\frac{\lambda + 2\mu}{\rho_0}} = \sqrt{\frac{Y(1-\nu)}{\rho_0(1+\nu)(1-2\nu)}} \tag{7.1}$$

$$c_s = \sqrt{\frac{\mu}{\rho_0}} = \sqrt{\frac{Y}{2\rho_0(1+\nu)}}. \tag{7.2}$$

A significant decrease in the Young's modulus Y should result in a corresponding decrease of the sound velocities given that ρ_0 and ν do not change significantly. Note that a change in the Young's modulus Y does not affect the ratio of c_l and c_s as

$$\left(\frac{c_l}{c_s}\right)^2 = \frac{1-\nu}{2(1+\nu)}. \tag{7.3}$$

Thus this ratio removes the uncertainty associated with the change in Young's modulus.

7. DISCUSSION

These equations show that both the longitudinal and shear sound velocities depend on the square root of the Young's modulus. This imply that a -12 % and a -15 % decrease in Young's modulus should respectively result in a -6 % and -8 % decrease in both the longitudinal and shear sound velocities (if the Poisson's ratio ν and the density ρ_0 are unchanged). Including a 3.5 % positive change in the Poisson's ratio ν (see change in mean values of $\nu(e_2)$ and $\nu(e_3)$ from 1. loading to 3. unloading in Table 5.2) does not contribute to more than approximately 1 % positive change in the longitudinal sound velocity. Using the maximum change in $\nu(e_2)$ from Table 5.2 of approximately 11 % change contribute approximately to a 4 % increase. For the shear sound velocity the contributions are in the order of -1 % for the same increases in Poisson's ratio.

The maximum decrease in sound velocity observed is in the order of -0.6 % (see Fig. 5.22), a full order of magnitude lower than the above values for both the shear and longitudinal sound velocities. Thus the corresponding decrease in density should be in the order of approximately -10 % to -15 % to account for the decrease in Young's modulus. This corresponds to an decrease in density ρ_0 of approximately 1000 kg/m^3, which is assumed to be highly unlikely. It is noted that the densities of the test specimens before and after the tests have unfortunately not been measured in this work.

conversely, the estimated linear elastic moduli as a function of change in the estimated sound velocity have been presented in Table 5.5. The maximum estimated change in the Young's modulus in Table 5.5 is approximately -1 %, which is significantly lower than the observed change of -15 %.

The lack of a corresponding velocity change based on the observed change in Youngs modulus are very interesting and deserve further investigation. As the industry commonly assumes that any unloading after a plastic deformation follows the initial elastic response [29, ch. 10.5], this reduction in Young's modulus Y might have impact on structural analysis of materials that have seen large plastic deformations [113]. However this has not been a part of this work and is highly recommended for further investigation.

8

Conclusions

8.1 Summary

The main conclusions of this work have been presented in short form in this section, while more details can be found in Sec. 8.2

This work has shown that the ART can be used to measure variation in sound velocities across a rectangular steel specimens subjected to uniaxial tension with statistically significant accuracy under controlled laboratory conditions as presented in Sec. 5.6. The measurement results also show reasonable reseamblance with numerical simulations of the acoustoelastic effect for a collection of steels presented in the literature as shown in Sec. 5.7.4. Based on these findings the main objective of this work has been achieved by showing that a linear dependecy of the measured quantity (c_l/c_s or $f^{(n_l)}/f^{(n_s)}$ in Fig. 5.20) with respect to the applied elastic deformation e_1^e of the current steel test specimens can be measured with statistically significant accuracy by the ART method. The obtained linear dependency was measured to be approximately a 0.25 % relative change in the c_l/c_s ratio over the elastic deformation range $e_1^e \in \{0, 0.3\,\%\}$. In the elastic loading sequence ABAB the standard uncertainty in the measured c_l/c_s ratio were less than 0.04 % corresponding to a relative standard uncertainty of approximately 16 %.

The main contribution of this work to the scientific field of the acoustoelastic effect and the application thereof has been to show the possibility of using a non-contact broadband measurement technique (ART) to accurately measure relative change in both longitudinal and shear sound velocities (Sec. 5.6). This has then been used to show

how these sound velocities depend on the stress state in a uniaxially tensioned rect-angular steel test specimen, as predicted by the acoustoelastic theory (Sec. 2.3). It has also been shown that the measurement quantity $f^{(n_l)}/f^{(n_s)}$ yields a thickness in-dependent measure of the acoustoelastic effect. This may be important for industrial applications where good quality thickness measurements may be impractical to perform.

8.2 Detailed conclusions

This work includes two different aspects. The main part consists of a controlled labo-ratory experimental setup described in Ch. 3, where uniaxial tension has been applied to rectangular test specimens while measuring the acoustic resonance frequencies across their thickness. The acoustoelastic theory presented in Sec. 2.3 predicts small changes in the acoustic sound velocities of acoustic waves propagating in a hyperelastic isotropic solid subjected to changing levels of stress. The experiments have been performed to investigate how accurately the currently applied acoustic measurement system (ART) is able to measure the predicted changes in the acoustic sound velocities. Based on these measurements it has been an objective of this work to investigate if the measured changes can be related consistently to the applied stress state. To corroborate the ex-perimental results a set of simulations have been done to simulate the expected changes in the sound velocities according to the acoustoelastic theory based on acoustoelastic parameters for steels found in the literature presented in Ch. 4. The main conclusions based on the discussion in Ch. 7 are presented in this section.

The acoustic resonance frequencies have been measured on 13 test specimens as they have been exposed to a predefined load history. For the tested steel "Bright rectangu-lar steel bar S235JRG2C+C" [79] the first and second harmonic longitudinal resonance frequencies (L1 and L2) and the third harmonic shear resonance frequency (S3) have shown a consistent and systematic development with a clear linear dependency on the applied elongation/stress while the test specimen deformed elastically. Although the measured relative changes in resonance frequencies show a significant variation across the 13 test specimens where acoustic measurements have been performed, the experi-mental mean shows a consistent development in the resonance frequencies. The negative

relative change in the S3 resonance mode can only be related to a change in the shear sound velocity c_s (and not thickness reduction), confirming the predicted acoustoelastic effect. By including measurements of the thickness change it has also been shown that part of the relative change in longitudinal resonance modes also relates to a change in the longitudinal sound velocity c_l (see Fig. 5.19).

The test specimens have been deformed uniaxially well into the plastic regime with intermediate elastic unloading sequences. The three elastic loading and unloading sequences (marked by AB, CD, and EF in the result figures) show a linear dependency of the L1, L2, and S3 resonance frequencies. The elastic loading sequences (i.e. $e_1^e \in \{0, 0.3\,\%\}$) corresponds to a relative change in the resonance frequencies of approximately 0.1 % for the longitudinal resonance frequencies, and -0.1 % for the shear resonance frequencies. However, during plastic deformation both longitudinal and shear resonance modes have experienced a relative increase.

It is not possible to determine how much of the relative changes in the resonance frequencies are due to thickness reduction and how much is caused by the acoustoelastic effect based on the individual resonance frequency measurements alone. This work has shown that the ratio between measured longitudinal and shear resonance frequencies (L1/S3 and L2/S3) can be used to minimize/remove the effect of change in sample thickness during uniaxial loading of the rectangular test specimens (see Eq. 2.125). In addition, if the longitudinal and shear sound velocities have opposing relative change development over the elastic loading sequences (AB, CD, EF) these ratios will also increase the maximum estimated value of relative change as shown in Fig. 5.20 compared to Fig. 5.19. The ratio of longitudinal and shear sound velocities ($c_l/c_s = f^{(n_l)}/f^{(n_s)}$) of waves travelling across the sample is independent of the thickness according to Eq. 2.125, and thus the uncertainty contribution from changing thickness is effectively removed in this way when evaluating the acoustoelastic effect (see Sec. 7.4. An additional benefit of using the ratio between resonance frequencies of different sound velocities, specifically when they have opposing development of change depending on the applied elongation/stress state, is that the measured elongation/stress dependency will be increased compared to the dependency of each individual resonance frequency (which also will be more affected by the quality of thickness measurements). For the elastic loading sequences (AB, CD, EF) an applied elastic elongation $e_1^e \in \{0, 0.3\,\%\}$ results in a relative change in the L1/S3 and L2/S3 ratios of approximately 0.25 % as can be seen in

Fig. 5.20. For the part of the load sequences where the test specimen deform plastically (BC, CE) the measured relative change in the L1/S3 and L2/S3 ratios are significantly less prominent than during elastic deformation, approximately -0.2 % and 0.2 % respectively over approximately 3.8 % of plastic elongation (e_1^p). The relative change of the L1/S3 ratio shows a negative development during plastic deformation while for L2/S3 the relative change is positive. This difference has been discussed in Sec. 7.4.1.

The experimental combined standard uncertainty over the 13 test specimens of the two thickness independent frequency ratios (L1/S3 and L2/S3) has been estimated to have their highest value in the order of 0.07 % at the end of the load history (see Sec. 6.2). Compared with the maximum difference in relative change measured over the elastic load sequences of approximately 0.25 %, this corresponds to a relative standard uncertainty of 28 %. At this point late in the load history much of the variation across the test specimens may be influenced by differences in the plastic response. Looking at the experimental combined standard uncertainty in the elastic regions before first yield (loading sequence ABA in Fig. 6.4), the maximum combined standard uncertainty is less than 0.04 %. This corresponds to approximately a relative standard uncertainty of 16 %. Thus, for the collection of the 13 tests including acoustic resonance measurements, it has been shown that the currently applied measurement technique is capable of measuring a significant effect of the acoustoelastic effect in the current steel during elastic loading.

For the estimated sound velocities and their estimated relative change the positive relative changes in the estimated longitudinal sound velocities have been observed to be just less than 0.06 % and 0.08 % for the $c(f^{(n_l=1)}, e_3)$ and $c(f^{(n_l=2)}, e_3)$ respectively (see Fig. 5.19). Both $c(f^{(n_l=1)}, e_3)$ and $c(f^{(n_l=2)}, e_3)$ have an estimated experimental standard uncertainty of approximately 0.06 % (at the end of the test shown in Fig. 6.5). Comparing the standard uncertinaties in Fig. 6.5 and the observed relative change in sound velocities in Fig. 5.19, this yields a relative experimental standard uncertainty $(u(x)/|x|)$ of 100 % and 75 % for the respective maximum measured elastic longitudinal sound velocity change for $c(f^{(n_l=1)}, e_3)$ and $c(f^{(n_l=2)}, e_3)$ respectively. Within the ABA load sequence, the standard uncertainties are 0.03 % and 0.01 % for $c(f^{(n_l=1)}, e_3)$ and $c(f^{(n_l=2)}, e_3)$. This yields a relative experimental standard uncertainty of 50 % and 17

% for $c(f^{(n_l=1)}, e_3)$ and $c(f^{(n_l=2)}, e_3)$ respectively. Only the latter can give estimates in relative changes that are comparable in accuracy to the ratios L1/S3 and L2/S3 as described above, but $c(f^{(n_l=2)}, e_3)$ is dependent on good quality measurements of the thickness change, which is impractical in most industry applications. Thus the L1/S3 and L2/S3 ratios are more applicable for the investigated application.

It is also noted that during the loading sequence deforming the test specimens plastically (BC and CE), the estimated longitudinal sound velocity as well as the shear sound velocity have a decreasing development. The acoustoplastic effect has not been within the scope of this work, however, it is noted that; during plastic deformation the estimated sound velocities experience close to the same negative change (-0.7 % for $c(L1, e_3)$, -0.4 % for $c(L2, e_3)$, and -0.6 % for $c(S3, e_3)$ shown in Fig. 5.19) wich result in the slight relative decrease and increase for the L1/S3 and L2/S3 ratio already mentioned and shown in Fig. 5.20.

The beam effect described in Sec. 2.6.2 and discussed in Sec. 7.4.1 has been assumed to be constant throughout the tests, and will thus fall out when comparing relative change of the L1/S3 and L2/S3 ratios. However, if this assumption is valid, the two ratios should have the same development throughout the load history. This is contradictory to the developement shown in Fig. 5.20. This work has shown (Fig. 5.20) that such an effect is not that prominent for the two ratios (L1/S3 and L2/S3) during elastic loading when the acoustoelastic effect is opposite for the longitudinal and shear sound waves. However, during plastic deformation (BC and CE) all the sound velocities experience close to the same negative relative change, and thus the ratios L1/S3 and L2/S3 do not experience the same prominent change as during elastic deformation. The observed discrepancy between the L1/S3 and L2/S3 ratios observed during plastic deformation (Fig. 5.20) may thus possibly be attributed to the beam effect as discussed in Sec. 7.4.1.

The methodology developed to correct for the beam diffraction effect has successfully been utilised in the unstressed state. Further investigation is needed to understand its dependency on thickness change, and how it may be used to correct for the beam diffraction effect throughout the load history of similar tests.

8. CONCLUSIONS

Even though steels of similar composition and crystal structure have third-order elastic constants of the same magnitude, the acoustoelastic effect can vary significantly between them. This work has shown that the investigated steel "Bright rectangular steel bar S235JRG2C+C" [79] has a similar acoustoelastic response as the simulated results of three steels (Group 3 in Tbl. 5.6) reported in the literature. However, other steels show significantly different acoustoelastic behaviour, even having opposite signs of relative change in some of the simulated sound velocities shown in Figs. 5.22, 5.23, and 5.24.

9

Further work

As stated in the conclusion the ART can be used to measure a significant variation in resonance frequencies across a rectangular steel specimen subjected to uniaxial tension in a laboratory setup. This is a first step to investigate the potential for an existing ultrasonic wall thickness measurement technology that is also applicable for determining locations in steel pipelines with a high stress and/or strain state. To reach a level where the technology can be qualified for such applications the technology and the measured response need to be further investigated. This section presents identified areas of research that need to be investigated.

It has been recognised through this work that both longitudinal and shear waves are excited in the steel specimen for a normal beam incidence. This is related to the distribution of incident angles because of the transducer radiating with a finite beam angle between 4° and 13° for different frequencies as described in Sec. 2.6.2. This study has identified one easily recognised shear resonance mode with the current experimental setup, namely the 3rd harmonic (S3). According to the acoustoelastic theory (Sec. 2.3, Eq. (2.68)) the shear wave speed in an isotropic medium under uniaxial load is dependent on the polarisation of the particle motion of the shear wave. Since, as discussed in Sec. 7.4.1, the current experimental setup excite shear waves with an even distribution of polarisations in all directions (circular symmetry), it has been assumed that an equal amount of shear waves polarised both perpendicular and parallel to the applied stress is excited. Because of the developmental differences of the resonance frequency based on the polarisation of the particle motion (in the order of 0.05 % and -0.6 % for particle motion perpendicular and parallel to the applied tension respectively for

the Group 3 steels in Figs. 5.23 and 5.24) the measured S3 shear resonance frequency should thus split in two peaks differing by less than approximately 4 kHz. This is, as discussed in Sec. 7.4.1, one order of magnitude less than the frequency resolution of the FFT spectrum as discussed in Sec. 7.6.1, and the resonance peak is thus most likely a superposition of the contributing effect from the two potential different polarisations of the shear waves. To account for this superposition further work should investigate the effect of polarisation and look into the possibility of designing the transducer setup in such a way as to be able to control the polarisation of excited shear waves.

The evident discrepancy between the ratio of the two longitudinal resonance modes (L1 and L2) to the shear resonance mode (S3), and its dependence on the applied plastic elongation and/or thickness reduction might also be an area of further investigation. If this is a consistent effect which can be explained by the theory behind the beam diffraction effect (e.g. [92] [93] [96] [97]), it could add valuable information to an inspection application.

The seemingly large theoretical variety of sound velocity changes shown in Sec. 5.7.2, and thus, resonance frequency change due to applied elongation/stress for different classes of steel types should be investigated. More specifically further work should look into the possibility of establishing a characteristic mean resonance-response for a specific steel through simple uniaxial testing. This kind of classification can also establish which class of steels have longitudinal and shear sound velocities that behave in such a way that they enhance the measured relative change in the c_l/c_s ratio as discussed in Sec. 7.7.

The uncertainties related to the currently used experimental setup have been discussed in Ch. 6. Future work may be able to reduce some of these uncertainties by considering alternative setups. It may for example be possible to reduce the uncertainty in the measured acoustic resonance frequencies across different tests by using a more accurate rig to position the transducer in the exact same relative position to the test specimen for each test. Another example may be to carefully control the incident angle and with better characterisation of the beam angle it might be possible to control the amount of shear waves with a certain particle motion polarisation. In this way it might be possible to excite shear waves with particle motion in a predominate direction either

in parallel or perpendicular to the applied tension, and thus control which shear mode to be dominant.

The current experimental setup used a rectangular test specimen with a thickness to width ratio of $7.5/50 = 0.15$, assuming it behaved as an infinite plate. The effect of this assumption should be investigated. For industrial application to pipelines it is also important to investigate the effect of a plate with curvature, i.e. how the resonance modes behave in a pipe shell as a function of the pipe radius.

Another area of investigation is the influence of a bi-axial stress state. The investigation of this work have focused on uni-axial stress states, but a pipline subjected to internal pressure, temperature gradients, residual stress from installation, etc. will have a combination of hoop and axial stresses. It is important to include the effect of a bi-axial stress state to increase the confidence in real-world measurements.

The above mentioned fields of study are intended to gain knowledge about the acoustic response at any, but nevertheless at one specific, location. However, there may be a lot of information and knowledge gained by looking at the collective measurement data from a distribution of measurement points over the object under investigation. For the ART method already developed for pipelines one should look into already established measurement data and apply the methodology developed in this work to examine distributed measurements. The thickness independence increases the possible application of this method to combine measurements at neighbouring locations to extract information about the distributed strain/stress state of a pipeline. Both concentration of strain/stress around corrosion defects under operation as well as the difference in strain/stress state over the cross section where the pipeline has been subjected to bending are examples of areas that could be further investigated, and where the industry would benefit from more knowledge.

Finally, the conundrum related to the relatively large observed decrease in Young's modulus with increasing plastic strain and the lack of a corresponding decrease in sound velocity needs more study. Note also that the test specimens have not been loaded after the tests were run (i.e. after a latency) to check if any relaxation effects could be observed to restore the Young's modulus. The observed effect with respect to

the decreasing Young's modulus has been outside the scope of this work, but it is an interesting observation that would benefit from future studies.

References

[1] P.J. Withers and H.K.D.H. Bhadeshia. **Residual stress. Part 1 - Measurement techniques**. *Materials Science and Technology*, **17**(4):355–365, April 2001.

[2] P.J. Withers and H.K.D.H. Bhadeshia. **Residual stress. Part 2 - Nature and origins**. *Materials Science and Technology*, **17**(4):366–375, April 2001.

[3] F. A. Kandil, J. D. Lord, A. T. Fry, and P. V. Grant. **A Review of Residual Stress Measurement Methods - A Guide to Technique Selection**. Technical report, Queens Road, Teddington, Middelsex, TW11 0LW, UK, 2001.

[4] J. Krautkrämer and H. Krautkrämer. *Ultrasonic Testing of Materials*. Springer, Berlin, Heidelberg, New York, January 1983.

[5] J. D. N. Cheeke. *Fundamentals and Applications of Ultrasonic Waves, Second Edition*. CRC Press, June 2012.

[6] Halfwave AS. **Halfwave Homepage**. `http://www.halfwave.com/`, Last viewed 2014-01-03.

[7] Å. A. Olsen, J. Jacobsen, T. M. H. Skar, P. Norli, Å. Bergh, N.-O. Negård, and S. Låg. **Acoustic thickness measurements using gas as a coupling medium**. US Patent no.: 7975548. July 2011.

[8] Å. A. Olsen, J. Jacobsen, T. M. H. Skar, P. Norli, Å. Bergh, N.-O. Negård, and S. Låg. **Detection of ingress of water in an intermediate layer using acoustic resonance technology**. US Patent no.: 8011227. September 2011.

[9] G. Waag, L. Hoff, and P. Norli. **Air-coupled thickness measurements of stainless steel**. arXiv e-print 1210.0428, oct 2012.

[10] G. Maze, J. L. Izbicki, J. Ripoche, A. Nagl, H. Uberall, and K. B. Yoo. **Transient acoustic scattering from layers and plates**. *The Journal of the Acoustical Society of America*, **80**(1):295–301, July 1986.

[11] C. C. H. Guyott and P. Cawley. **The measurement of through thickness plate vibration using a pulsed ultrasonic transducer**. *The Journal of the Acoustical Society of America*, **83**(2):623–631, February 1988.

[12] A. Norris. **Finite-Amplitude Waves in Solids**. In M. F. Hamilton and D. T. Blackstock, editors, *Nonlinear Acoustics*, Nonlinear Acoustics, pp. 263–277. Acoustical Society of America, 1998.

[13] A. Ben-Menahem and S. J. Singh. *Seismic Waves and Sources*. Springer, Berlin, Heidelberg, New York, 1981.

[14] L. Brillouin. **Les tensions de radiation; leur interprétation en mécanique classique et en relativité**. *J. Phys. Radium*, **6**(11):337–353, 1925.

[15] F. D. Murnaghan. **Finite Deformations of an Elastic Solid**. *American Journal of Mathematics*, **59**(2):235–260, April 1937.

[16] D. S. Hughes and J. L. Kelly. **Second-Order Elastic Deformation of Solids**. *Physical Review*, **92**(5):1145, December 1953.

[17] C. Truesdell. **General and exact theory of waves in finite elastic strain**. *Archive for Rational Mechanics and Analysis*, **8**(1):263–296, January 1961.

[18] R. A. Toupin and B. Bernstein. **Sound Waves in Deformed Perfectly Elastic Materials. Acoustoelastic Effect**. *The Journal of the Acoustical Society of America*, **33**(2):216–225, February 1961.

[19] R. N. Thurston and K. Brugger. **Third-Order Elastic Constants and the Velocity of Small Amplitude Elastic Waves in Homogeneously Stressed Media**. *Physical Review*, **133**(6A):A1604, March 1964.

[20] F. Birch. **The Effect of Pressure Upon the Elastic Parameters of Isotropic Solids, According to Murnaghan's Theory of Finite Strain**. *Journal of Applied Physics*, **9**(4):279–288, 1938.

[21] S. Tang. **Wave propagation in initially-stressed elastic solids**. *Acta Mechanica*, **4**(1):92–106, March 1967.

[22] R. W. Ogden. *Non-Linear Elastic Deformations*. Dover Publications, Inc., Mineola, New York, 1997.

[23] R. W. Ogden. **Incremental Statics and Dynamics of Pre-Stressed Elastic Materials**. In M. Destrade, G. Saccomandi, F. Pfeiffer, F. G. Rammerstorfer, J. Salençon, B. Schrefler, and P. Serafini, editors, *Waves in Nonlinear Pre-Stressed Materials*, **495** of *CISM Courses and Lectures*, pp. 1–26. Springer Vienna, 2007.

[24] A. Norris. **Small-on-Large Theory with Applications to Granular Materials and Fluid/Solid Systems**. In M. Destrade, G. Saccomandi, F. Pfeiffer, F. G. Rammerstorfer, J. Salençon, B. Schrefler, and P. Serafini, editors, *Waves in Nonlinear Pre-Stressed Materials*, **495** of *CISM Courses and Lectures*, pp. 27–62. Springer Vienna, 2007.

[25] Z. Abiza, M. Destrade, and R.W. Ogden. **Large acoustoelastic effect**. *Wave Motion*, **49**(2):364–374, March 2012.

[26] D. Roylance. **Yield and Plastic Flow**. Massachusetts Institute of Technology. http://ocw.mit.edu/courses/materials-science-and-engineering/3-11-mechanics-of-materials-fall-1999/modules/yield.pdf, October 2001, last viewed 2012-03-27.

[27] M. Kobayashi. **Ultrasonic nondestructive evaluation of microstructural changes of solid materials under plastic deformation - Part I. Theory**. *International Journal of Plasticity*, **14**(6):511–522, 1998.

[28] M. Kobayashi, S. Tang, S. Miura, K. Iwabuchi, S. Oomori, and H Fujiki. **Ultrasonic nondestructive material evaluation method and study on texture and cross slip effects under simple and pure shear states**. *International Journal of Plasticity*, **19**(6):771–804, June 2003.

[29] A.J.M Spencer. *Continuum Mechanics*. Dover Publications, Inc., Mineola, New York, 2004.

[30] J. Achenbach. *Wave Propagation in Elastic Solids*. Elsevier, Amsterdam, January 1984.

[31] M. A. Biot. **The Influence of Initial Stress on Elastic Waves**. *Journal of Applied Physics*, **11**(8):522–530, August 1940.

[32] R. H. Bergman and R. A. Shahbender. **Effect of Statically Applied Stresses on the Velocity of Propagation of Ultrasonic Waves**. *Journal of Applied Physics*, **29**(12):1736, 1958.

[33] R. N. Thurston. **Determination of Nonlinear Properties from the Velocity of Small-Amplitude Waves in Statically Stressed Crystals**. *The Journal of the Acoustical Society of America*, **38**(5):926, 1965.

[34] Y.-H. Pao and U. Gamer. **Acoustoelastic waves in orthotropic media**. *The Journal of the Acoustical Society of America*, **77**(3):806–812, 1985.

[35] D. R. Bland. *Nonlinear dynamic elasticity*. Blaisdell Waltham, 1969.

[36] A. C. Eringen and E. S. Suhubi. *Elastodynamics*, **2**. Academic press New York, 1974.

[37] LD Landau and EM Lifshitz. *Theory of Elasticity, 3rd ed.* Pergamon Press, Oxford, UK, 1986.

[38] D. I. Crecraft. **Ultrasonic Wave Velocities in Stressed Nickel Steel**. *Nature*, **195**(4847):1193–1194, September 1962.

[39] D.I. Crecraft. **The measurement of applied and residual stresses in metals using ultrasonic waves**. *Journal of Sound and Vibration*, **5**(1):173–192, January 1967.

[40] R. P. Espinola and P.C. Waterman. **Ultrasonic Interferometer for the Measurement of the Temperature Dependence of Elastic Constants**. *Journal of Applied Physics*, **29**(4):718–721, 1958.

[41] N. P. Cedrone and D. R. Curran. **Electronic Pulse Method for Measuring the Velocity of Sound in Liquids and Solids**. *The Journal of the Acoustical Society of America*, **26**(6):963–966, 1954.

[42] D.I. Crecraft. **Ultrasonic measurement of stresses**. *Ultrasonics*, **6**(2):117–121, April 1968.

[43] Gilbert Everett Doan. *The Principles of Physical Metallurgy*. McGraw-Hill book Company, Incorporated, New York, 1935.

[44] R. T. Smith, R. Stern, and R. W. B. Stephens. **Third-Order Elastic Moduli of Polycrystalline Metals from Ultrasonic Velocity Measurements**. *The Journal of the Acoustical Society of America*, **40**(5):1002–1008, 1966.

[45] R.T. Smith. **Stress-induced anisotropy in solids—the acoustoelastic effect**. *Ultrasonics*, **1**(3):135–147, July 1963.

[46] D. M. EGLE AND D. E. BRAY. **Measurement of acoustoelastic and third-order elastic constants for rail steel**. *The Journal of the Acoustical Society of America*, **60**(3):741–744, 1976.

[47] A. N. GUZ', F. G. MAKHORT, O. I. GUSHCHA, AND V. K. LEBEDEV. **Theory of wave propagation in an elastic isotropic body with initial deformations**. *Soviet Applied Mechanics*, **6**(12):1308–1313, December 1970.

[48] A. N. GUZ', F. G. MAKHORT, O. I. GUSHCHA, AND V. K. LEBEDEV. **Theory underlying the determination of initial stresses from the results of ultrasonic measurements**. *Soviet Applied Mechanics*, **7**(6):676–679, June 1971.

[49] O. I. GUSHCHA AND F. G. MAKHORT. **Acoustic method of determining biaxial residual stresses**. *International Applied Mechanics*, **12**(10):1010–1013, 1976.

[50] F. BACH AND V. ASKEGAARD. **General stress-velocity expressions in acoustoelasticity**. *Experimental Mechanics*, **19**(2):69–75, February 1979.

[51] H. FUKUOKA, H. TODA, AND T. YAMANE. **Acoustoelastic stress analysis of residual stress in a patch-welded disk**. *Experimental Mechanics*, **18**(7):277–280, July 1978.

[52] M. P. SCOTT, D.M. BARNETT, AND D.B. ILIC. **The Nondestructive Determination of Residual Stress in Extruded Billets from Acoustoelastic Measurements**. In J. DEKLERK AND B. R. MCAVOY, editors, *1979 Ultrasonics Symposium*, pp. 265–268, New Orleans, LA, IEEE Group on Sonics and Ultrasonics, Sept. 26 – 28 1979.

[53] J. FRANKEL, W. SCHOLZ, G. CAPSIMALIS, AND W. KORMAN. **Residual Stress Measurement in Circular Steel Cylinders**. In B. R. MCAVOY, editor, *Ultrasonics Symposium Proceedings*, pp. 1009–1012, Atlanta, Georgia, IEEE Group on Sonics and Ultrasonics, Oct. 31 – Nov. 2 1983.

[54] R. B. KING AND C. M. FORTUNKO. **Determination of in-plane residual stress states in plates using horizontally polarised shear waves**. *Journal of Applied Physics*, **54**(6):3027, 1983.

[55] DIXON V. V. MISHAKIN, S. AND M. D. G. POTTER. **The use of wide band ultrasonic signals to estimate the stress condition of materials**. *Journal of Physics D: Applied Physics*, **39**(21):4681–4687, 2006.

[56] N. YE. NIKITINA, A. V. KAMYSHEV, V. A. SMIRNOV, A. V. BORSHCHEVSKII, AND YU. M. SHARYGIN. **Determination of axial and circumferential stresses in the wall of a closed tube via an ultrasonic method using the acoustoelasticity effect**. *Russian Journal of Nondestructive Testing*, **42**(3):185–189, March 2006.

[57] N.YE. NIKITINA, A.V. KAMISHEV, S.V. KAZACHEK, AND N.A. MIRONOV. **Evaluation of biaxial stress in pipelines by ultrasonic nondestructive method**. In *Proceedings of the XIX Session of the Russian Acoustical Society*, Nizhny Novgorod, Sept. 24 – 28 2007.

[58] N. YE. NIKITINA, A. V. KAMYSHEV, AND S. V. KAZACHEK. **Application of the acoustoelasticity phenomenon in studying stress states in technological pipelines**. *Russian Journal of Nondestructive Testing*, **45**(12):861–866, April 2010.

[59] G. C. JOHNSON. **Acoustoelastic theory for elastic–plastic materials**. *The Journal of the Acoustical Society of America*, **70**(2):591–595, 1981.

[60] G. C. JOHNSON. **On the Applicability of Acoustoelasticity for Residual Stress Determination**. *Journal of Applied Mechanics*, **48**(4):791, 1981.

[61] T. DAAMI, M. TOURATIER, AND L. CASTEX. **Effect of plastic deformation on the acoustoelastic response of some materials**. *Experimental Mechanics*, **27**(4):333–337, December 1987.

[62] M. KOBAYASHI. **Ultrasonic nondestructive evaluation of microstructural changes of solid materials under plastic deformation - Part II. Experiment and simulation**. *International Journal of Plasticity*, **14**(6):523–535, 1998.

[63] M. KOBAYASHI. **Analysis of deformation localization based on proposed theory of ultrasonic wave velocity propagating in plastically deformed solids**. *International Journal of Plasticity*, **26**(1):107–125, January 2010.

[64] S. GACHI, F. BELAHCENE, AND F. BOUBENIDER. **Residual stresses in AA7108 aluminium alloy sheets joined by friction stir welding**. *Nondestructive Testing and Evaluation*, **24**(3):301, 2009.

[65] G. MAZE, J. L. IZBICKI, AND J. RIPOCHE. **Resonances of plates and cylinders: Guided waves**. *The Journal of the Acoustical Society of America*, **77**(4):1352–1357, April 1985.

[66] S. W. Smith. *The scientist and engineer's guide to digital signal processing*. For more information visit the book's website at: www.DSPguide.com, 1997, Last viewed 2013-08-16.

[67] T. Sato, W. Ma, H. Ninoyu, K.-Y. Jhang, and Y. Kosugi. **Estimation of the stress state inside metals using stress perturbing waves and probe waves**. *NDT & E International*, **26**(3):119–126, June 1993.

[68] N. Kim and M. Hong. **Measurement of axial stress using mode-converted ultrasound**. *NDT & E International*, **42**(3):164–169, April 2009.

[69] B. A. Auld. *Acoustic fields and waves in solids*, **vol. 2**. Wiley New York, 1973.

[70] J. Lubliner. *Plasticity Theory - Revised Edition (PDF)*. http://www.scribd.com/doc/21551320/Plasticity-Theory-Jacob-Lubliner - previously published by Pearson Education, Inc., Berkley, 2006, Last viewed 2013-08-15.

[71] S. Eldevik, Å. A. F. Olsen, and P. Lunde. **Sound velocity change owing to the acousto-elastic/plastic effect in steel measured using Acoustic Resonance Technology (ART)**. In *34th Scandinavian Symposium on Physical Acoustics*, Geilo, Norway, The Norwegian Physical Society, jan 31 – feb 2 2011.

[72] S. Eldevik, F. Prieur, and P. Lunde. **Measuring stress-state of gas pipeline**. Poster at conference, European Gas Technology Conference (EGATEC), Paris, France, may 30 – 31 2013.

[73] S. Eldevik and P. Lunde. **Measurement of non-linear acoustoelastic effect in steel**. Presentation at conference, 36th Scandinavian Symposium on Physical Acoustics, The Norwegian Physical Society, Geilo, Norway, feb 3 – 6 2014.

[74] JCGM. **JCGM 100:2008 Evaluation of measurement data — Guide to the expression of uncertainty in measurement (GUM)**. http://www.bipm.org/utils/common/documents/jcgm/JCGM_100_2008_E.pdf, 2008.

[75] G. Waag. **Beam diffraction effect**. Halfwave AS and Høgskolen i Buskerud og Vestfold, Norway. Personal communication, 2013.

[76] M. Aanes. **Beam diffraction effect**. Dept. of Physics and Technology, University of Bergen, Norway. Personal communication, 2013.

[77] Charles Henry Edwards and David E. Penney. *Calculus with Analytic Geometry*. Prentice-Hall International, 5th edition, 1999.

[78] Y. Ling. **Uniaxial true stress-strain after necking**. *AMP Journal of Technology*, **5**:37–48, 1996.

[79] Norsk Stål. **Produkt katalog**. http://www2.norskstaal.no/varekatalog/, Last viewed 2012-03-29.

[80] S. C. Cowin and M. M. Mehrabadi. **Anisotropic Symmetries of Linear Elasticity**. *Applied Mechanics Reviews*, **48**:247, 1995.

[81] S. Burns. **Negative Poisson's Ratio Materials**. *Science*, **238**(4826):551–551, October 1987.

[82] R. Lakes. **Foam Structures with a Negative Poisson's Ratio**. *Science*, **235**(4792):1038–1040, February 1987.

[83] F. D. Murnaghan. *Finite deformation of an elastic solid*. Wiley, New York, 1951.

[84] A. Rusinek, J. A. Rodríguez-Martínez, J. R. Klepaczko, and R. B. Pęcherski. **Analysis of thermo-visco-plastic behaviour of six high strength steels**. *Materials & Design*, **30**(5):1748–1761, May 2009.

[85] J. Gozzi. *Plastic Behaviour of Steel - Experimental investigation and modelling*. PhD thesis, Luleå University of Technology, Luleå, Sweeden, 2011.

[86] M. Kobayashi. **Theoretical study of acoustoelastic effects caused by plastic anisotropy growth**. *International Journal of Plasticity*, **3**(1):1–20, 1987.

[87] Y.-H. Pao. **Theory of Acoustoelasticity and Acoustoplasticity**. In J. D. Achenbach and Y. Rajapakse, editors, *Solid mechanics research for quantitative non-destructive evaluation*, pp. 257–273. Springer Netherlands, January 1987.

[88] H. P. Myers. *Introductory solid state physics*. Taylor & Francis (London), 1997.

[89] L. E. Kinsler, A. R. Frey, A. B. Coppens, and J. V. Sanders. *Fundamentals of Acoustics, 4th edition*. Wiley-VCH, New York, 2000.

[90] PCT. **PCT Homepage**. http://www.pct-ltd.co.uk/, Last viewed 2012-03-29.

[91] P. Norli. **Characterization of Near Field Transducer 1**. Technical report, DNV - MTPNO366 - Acoustic Resonance Technology, Høvik, Norway, 2008 - CONFIDENTIAL.

[92] K.D. Lohne, M. Vestrheim, and P. Lunde. **Ultrasonic signal transmission in plates - Study of a steel plate immersed in water**. In *31th Scandinavian Symposium on Physical Acoustics*, Geilo, Norway, The Norwegian Physical Society, jan 27 − 30 2008.

[93] K.D. Lohne, P. Lunde, and M. Vestrheim. **Measurement and 3D simulations of ultrasonic directive beam transmission through a water-immersed steel plate**. In *34th Scandinavian Symposium on Physical Acoustics*, Geilo, Norway, The Norwegian Physical Society, jan 31 − feb 2 2011.

[94] M. Aanes, K.D. Lohne, P. Lunde, and M. Vestrheim. **Finite element analysis of acoustic beam interactions with a plate at normal incidence. Comparison with a 3D angular spectrum method and measurements.** In *34th Scandinavian Symposium on Physical Acoustics*, Geilo, Norway, The Norwegian Physical Society, jan 31 − feb 2 2011.

[95] M. Aanes, K.D. Lohne, P. Lunde, and M. Vestrheim. **Normal incidence ultrasonic beam transmission through a water-immersed plate using a piezoelectric transducer. Finite element modeling, angular spectrum method and measurements.** In *19th International Congress on Sound and Vibration*, Vilnius, Lithuania, The International Institute of Acoustics and Vibration (IIAV), jul 8 − 12 2012.

[96] M. Aanes, K.D. Lohne, P. Lunde, and M. Vestrheim. **Ultrasonic beam transmission through a water-immersed plate at oblique incidence using a piezoelectric source transducer. Finite element - angular spectrum modeling and measurements**. In *Ultrasonics Symposium (IUS), 2012 IEEE International*, pp. 1972–1977, Dresden, Germany, Oct 7 − 10 2012.

[97] G. Waag, L. Hoff, and P. Norli. **Model for thickness measurements of steel plates using half-wave resonances**. In *Ultrasonics Symposium (IUS), 2012 IEEE International*, pp. 2438–2441, Dresden, Germany, oct 7 − 10 2012.

[98] Instron. **Instron Homepage**. http://www.instron.se/, Last viewed 2012-03-29.

[99] MessTek. **MessTek Homepage**. http://messtek.com/, Last viewed 2012-03-29.

[100] C. Husvik. **Gain, bandwidth and noise in prototype RX/TX system**. Technical report, DNV - MTPNO366 - Acoustic Resonance Technology, Høvik, Norway, 2008 - CONFIDENTIAL.

[101] Ltd. TML Tokyo Sokki Kenkyujo Co. **TML Homepage - Products - Strain gauge**. http://www.tml.jp/e/product/strain_gauge/index.html, Last viewed 2013-08-18.

[102] **ARAMIS Homepage**. GOM mbH. http://www.gom.com/metrology-systems/system-overview/aramis.html, Last viewed 2012-03-29.

[103] T. Oliphant and SciPy development community. **Numpy and Scipy Documentation**. http://docs.scipy.org/doc/, 1997, Last viewed 2013-08-16.

[104] Python Software Foundation. **Python Documentation**. http://www.python.org/doc/, 1997, Last viewed 2013-08-16.

[105] K. Nowacki and W. Kasprzyk. **The Sound Velocity in an Alloy Steel at High-Temperature Conditions**. *International Journal of Thermophysics*, **31**(1):103–112, November 2009.

[106] GOM mbH, Mittelweg 7-8, D-38106 Braunschweig, Germany. *ARAMIS User Information - Hardware, Rev. aramis_hw-2lt-4-5-5lt-12-hs-adjustable_en_rev-a*, May 2011.

[107] GOM mbH, Mittelweg 7-8, D-38106 Braunschweig, Germany. *ARAMIS User Manual - Software, Rev. aramis-v6-3_1st_en_rev-a*, May 2011.

[108] E. O. Lebigot. **Uncertainties: a Python package for calculations with uncertainties**. http://pythonhosted.org/uncertainties/, Last viewed 2013-04-29.

[109] E. Habberstad. **Systematic uncertainty in strain gauge measurements**. Det Norske Veritas. Personal communication, 2013.

[110] H. Kim, M. Kimchi, N. Kardes, and T. Altan. **Effects of variable elastic modulus on springback predictions in stamping advanced high-strength steels (AHSS)**. *Steel Res Int*, pp. 628–33, 2011.

[111] C. Nikhare. **A Numerical Approach on Reduction of Young's Modulus During Deformation of Sheet Metals**. *Modeling and Numerical Simulation of Material Science*, **02**(01):1–13, 2012.

REFERENCES

[112] Guoshuang Shui, Yue-Sheng Wang, and Fei Gong. **Evaluation of plastic damage for metallic materials under tensile load using nonlinear longitudinal waves**. *NDT & E International*, **55**:1–8, April 2013.

[113] SIMULIA. **SIMULIA Abaqus FEA 6.12 User's manual**. With installation of program: `http://www.3ds.com/products-services/simulia/portfolio/abaqus/`, 2012.

[114] P. Lunde. **PHYS374 - Theoretical acoustics**. University of Bergen, Dept. of Physics and Technology, Norway. Lecture notes. 2013.

Appendix A

Detailed derivations

A.1 Lagrangian and Eulerian strain

This section is a reproduction of an excerpt from the lecture notes given in [114].

Using Fig. 2.2 the separation between two material points P and Q in the reference configuration can be described by the vector

$$d\mathbf{X} = (dX_1, dX_2, dX_3) \tag{A.1}$$

and correspondingly between the same material points p and q in the current configuration as

$$d\mathbf{x} = (dx_1, dx_2, dx_3). \tag{A.2}$$

The absolute distance between the material points can be taken as the absolute magnitude of these vectors and are

$$dS \equiv |d\mathbf{X}| = \sqrt{d\mathbf{X} \cdot d\mathbf{X}} = \sqrt{dX_m dX_m}, \qquad m = 1, 2, 3 \tag{A.3}$$

$$ds \equiv |d\mathbf{x}| = \sqrt{d\mathbf{x} \cdot d\mathbf{x}} = \sqrt{dx_i dx_i}, \qquad i = 1, 2, 3 \tag{A.4}$$

where the summation convention over repeated indices is used. Looking at the difference between the square of these two quantities yields

$$(ds)^2 - (dS)^2 = dx_i dx_i - dX_m dX_m, \qquad m, i = 1, 2, 3. \tag{A.5}$$

For the Lagrangian description where $\mathbf{x} = \mathbf{x}(\mathbf{X}, t)$ and by using the chain rule Eq. (A.5)

A. DETAILED DERIVATIONS

becomes

$$
\begin{aligned}
(ds)^2 - (dS)^2 &= dx_i dx_i - dX_m dX_m \\
&= \frac{\partial x_i}{\partial X_k} dX_k \frac{\partial x_i}{\partial X_l} dX_l - dX_m dX_m \\
&= \left(\frac{\partial x_i}{\partial X_k} \frac{\partial x_i}{\partial X_l} - \delta_{kl} \right) dX_k dX_l \\
&= 2 E_{kl} dX_k dX_l
\end{aligned}
\tag{A.6}
$$

where

$$
E_{kl} \equiv \frac{1}{2} \left(\frac{\partial x_i}{\partial X_k} \frac{\partial x_i}{\partial X_l} - \delta_{kl} \right)
\tag{A.7}
$$

is the Lagrangian finite strain tensor defined in Eq. (2.15) [29], and δ_{kl} is the Kronecker delta. Correspondingly using the Eulerian description where $\mathbf{X} = \mathbf{X}(\mathbf{x}, t)$ this becomes

$$
\begin{aligned}
(ds)^2 - (dS)^2 &= dx_m dx_m - dX_i dX_i \\
&= dx_m dx_m - \frac{\partial X_i}{\partial x_k} dx_k \frac{\partial X_i}{\partial x_l} dx_l \\
&= dx_k dx_l \delta_{kl} - \frac{\partial X_i}{\partial x_k} \frac{\partial X_i}{\partial x_l} dx_k dx_l \\
&= 2 e_{kl} dx_k dx_l
\end{aligned}
\tag{A.8}
$$

where

$$
e_{kl} \equiv \frac{1}{2} \left(\delta_{kl} - \frac{\partial X_i}{\partial x_k} \frac{\partial X_i}{\partial x_l} \right)
\tag{A.9}
$$

is the Eulerian finite strain tensor defined in Eq. (2.15) [29]. To get the Lagrangian and Eulerian strain tensors in terms of displacement we use the displacement introduced in Eq. (2.3) on component form as

$$
u_i = x_i - X_i.
\tag{A.10}
$$

The partial derivatives of Eq. (A.7) for the Lagrangian description becomes

$$
\frac{\partial x_i}{\partial X_k} = \frac{\partial u_i}{\partial X_k} + \delta_{ik},
\tag{A.11}
$$

and from Eq. (A.9) for the Eulerian description

$$
\frac{\partial X_i}{\partial x_k} = \delta_{ik} - \frac{\partial u_i}{\partial x_k}.
\tag{A.12}
$$

Substituting with the relevant indices yields

$$
\begin{aligned}
E_{kl} &= \frac{1}{2}\left[\left(\frac{\partial u_i}{\partial X_k}+\delta_{ik}\right)\left(\frac{\partial u_i}{\partial X_l}+\delta_{il}\right)-\delta_{kl}\right] \\
&= \frac{1}{2}\left(\frac{\partial u_i}{\partial X_k}\frac{\partial u_i}{\partial X_l}+\frac{\partial u_l}{\partial X_k}+\frac{\partial u_k}{\partial X_l}+\delta_{ik}\delta_{il}-\delta_{kl}\right) \\
&= \frac{1}{2}\left(\frac{\partial u_l}{\partial X_k}+\frac{\partial u_k}{\partial X_l}+\frac{\partial u_i}{\partial X_k}\frac{\partial u_i}{\partial X_l}\right)
\end{aligned} \tag{A.13}
$$

and

$$
\begin{aligned}
e_{kl} &= \frac{1}{2}\left[\delta_{kl}-\left(\delta_{ik}-\frac{\partial u_i}{\partial x_k}\right)\left(\delta_{il}-\frac{\partial u_i}{\partial x_l}\right)\right] \\
&= \frac{1}{2}\left(\delta_{kl}-\delta_{ik}\delta_{il}+\frac{\partial u_l}{\partial x_k}+\frac{\partial u_k}{\partial x_l}-\frac{\partial u_i}{\partial x_k}\frac{\partial u_i}{\partial x_l}\right) \\
&= \frac{1}{2}\left(\frac{\partial u_l}{\partial x_k}+\frac{\partial u_k}{\partial x_l}-\frac{\partial u_i}{\partial x_k}\frac{\partial u_i}{\partial x_l}\right)
\end{aligned} \tag{A.14}
$$

which are the exact Lagrangian and Eulerian strain tensors presented in Eq. (2.16).

A.2   Constitutive relation

Recalling the stress power densities of Eq. (2.30) it can be shown that [22, ch. 3.5.1-2]

$$
\mathrm{tr}(\mathbf{S}\dot{\mathbf{F}}) = J\,\mathrm{tr}(\boldsymbol{\sigma}\boldsymbol{\Sigma}). \tag{A.15}
$$

From the restriction on the strain-energy density function W imposed in Eq. (2.32) defining a conjugate stress and strain tensor pair, it can be shown that several such conjugate pairs exist [22, ch. 3.5.2]. For the purpose of this work only the Lagrangian strain $\mathbf{E}$ defined in Eqs. (2.15) and (2.16) and its conjugate, the 2nd Piola-Kirchhoff stress tensor defined as [29, ch. 9.5][22, ch. 4.2.6]

$$
\mathbf{T} = \mathbf{S}(\mathbf{F}^{-1})^T \tag{A.16}
$$

are included here. This leads to the relation between the stress power densities as [22, ch. 3.5.2]

$$
\mathrm{tr}(\mathbf{S}\dot{\mathbf{F}}) = \mathrm{tr}(\mathbf{T}\dot{\mathbf{E}}). \tag{A.17}
$$

Using the same argument as when developing the constitutive relation between $\mathbf{S}$ and $\mathbf{F}$ in Eq. (2.36) it is clear that [22, ch. 4.3.1]

$$
\mathbf{T} = \frac{\partial W}{\partial \mathbf{E}}(\mathbf{E}). \tag{A.18}
$$

The further restriction that the strain-energy density function W should be objective leads to [22, ch. 5.1.1]

$$W(\mathbf{F}) = W(\mathbf{E}). \tag{A.19}$$

Combining Eqs. (A.16), (A.18), and (A.19) with the constitutive relation of Eq. (2.36) yields

$$\mathbf{S} \equiv \frac{\partial W}{\partial \mathbf{F}}(\mathbf{F}) = \mathbf{T}\mathbf{F}^T = \frac{\partial W}{\partial \mathbf{E}}(\mathbf{E})\mathbf{F}^T, \tag{A.20}$$

and thus

$$\frac{\partial W}{\partial \mathbf{F}}(\mathbf{F}) = \frac{\partial W}{\partial \mathbf{E}}(\mathbf{E})\mathbf{F}^T \tag{A.21}$$

A.3   Small-on-large

The objective of Sec. 2.2.2 is to derive the equation of motion for an additional disturbance $\mathbf{u}^{(1)}$ in terms of the intermediate deformation $\mathbf{u}^{(0)}$. Recalling the Lagrangian law of motion in Eq. (2.46) rewritten in terms of the small-on-large coordinate vectors $\mathbf{x}'$ as

$$\text{Div}\,\mathbf{S} = \rho_0 \ddot{\boldsymbol{\chi}}(\mathbf{X}, t), \tag{A.22}$$

where $\mathbf{x}' = \boldsymbol{\chi}(\mathbf{X}, t)$, we first investigate the right-hand side of the equation. The total displacement of the material points can be described by Eq. (2.47) as

$$\mathbf{u} = \mathbf{u}^{(0)} + \mathbf{u}^{(1)}, \tag{A.23}$$

and the initial static and additional dynamic displacement in Eq. (2.48)

$$\mathbf{u}^{(0)} = \mathbf{x} - \mathbf{X}, \qquad \mathbf{u}^{(1)} = \mathbf{x}' - \mathbf{x}, \tag{A.24}$$

A.3.1   Time dependent part of the Lagrangian law of motion

First we look at the time dependent part of the Lagrangian law of motion in Eq. (A.22). Rearranging the total displacement given by Eqs. (A.23) and (A.24) yields the right-hand side of Eq. (A.22) as

$$\begin{aligned}
\rho_0 \ddot{\mathbf{x}}' &= \rho_0 \frac{\partial^2}{\partial t^2}(\mathbf{u}^{(0)} + \mathbf{u}^{(1)} + \mathbf{X}) \\
&= \rho_0 \frac{\partial^2 \mathbf{u}^{(1)}}{\partial t^2}
\end{aligned} \tag{A.25}$$

under the assumption that both the unstressed state B_0 and the initial deformation state B_t are static and thus $\partial^2/\partial t^2(\mathbf{X}) = \partial^2/\partial t^2(\mathbf{u}^{(0)}) = 0$ [24]. This is the time dependent term of the small-on-large additional deformation that appears as the right-hand side of Eq. (2.62).

A.3.2 Expansion of partial derivatives in X

In our further consideration of the left-hand side of the Lagrangian law of motion in Eq. (A.22) an expansion of partial derivatives with respect to X_j in x_j has been used. This has been done to be able to divide the space dependent part of the Lagrangian law of motion (Eq. (2.62)) into one part related to the static displacement $u_k^{(0)}$ and one part related to the additional dynamic displacement $u_k^{(1)}$ as done in Sec. A.3.4.

Using the chain rule, and changing the variable through the total displacement in Eqs. (A.23) and (A.24) the partial derivatives of Eq. (2.62) can be expanded in terms of the static displacement $u_k^{(0)}$ as [24]

$$
\begin{aligned}
\frac{\partial}{\partial X_j} &= \frac{\partial}{\partial x_k}\frac{\partial x_k}{\partial X_j} = \frac{\partial}{\partial x_k}\frac{\partial}{\partial X_j}\left(X_k + u_k^{(0)}\right) \\
&= \frac{\partial}{\partial x_j} + \frac{\partial u_k^{(0)}}{\partial X_j}\frac{\partial}{\partial x_k} \\
&= \frac{\partial}{\partial x_j} + \frac{\partial u_k^{(0)}}{\partial x_j}\frac{\partial}{\partial x_k} + \cdots \\
&= \frac{\partial}{\partial x_j} + u_{k,j}^{(0)}\frac{\partial}{\partial x_k} + \cdots
\end{aligned}
\tag{A.26}
$$

A.3.3 Expansion of S

Considering the left-hand side of Eq. (A.22) we first look at how S_{ji} from Eq. (2.55) can be expressed by the shorter form in Eq. (2.56). Replacing the Lagrangian strain tensor E_{kl} with the expansion given in Eq. (A.13) yields

$$
\begin{aligned}
S_{\beta q} &= \left(\frac{\partial u_\alpha}{\partial X_q} + \delta_{\alpha q}\right)\left[\frac{1}{2}C_{\alpha\beta kl}\left(\frac{\partial u_l}{\partial X_k} + \frac{\partial u_k}{\partial X_l} + \frac{\partial u_r}{\partial X_k}\frac{\partial u_r}{\partial X_l}\right)\right. \\
&\quad + \frac{1}{3!}\left\{\frac{1}{4}C_{\alpha\beta klmn}\left(\frac{\partial u_l}{\partial X_k} + \frac{\partial u_k}{\partial X_l} + \frac{\partial u_r}{\partial X_k}\frac{\partial u_r}{\partial X_l}\right)\left(\frac{\partial u_n}{\partial X_m} + \frac{\partial u_m}{\partial X_n} + \frac{\partial u_s}{\partial X_m}\frac{\partial u_s}{\partial X_n}\right)\right. \\
&\quad + \frac{1}{4}C_{ij\alpha\beta mn}\left(\frac{\partial u_j}{\partial X_i} + \frac{\partial u_i}{\partial X_j} + \frac{\partial u_r}{\partial X_i}\frac{\partial u_r}{\partial X_j}\right)\left(\frac{\partial u_n}{\partial X_m} + \frac{\partial u_m}{\partial X_n} + \frac{\partial u_s}{\partial X_m}\frac{\partial u_s}{\partial X_n}\right) \\
&\quad + \left.\frac{1}{4}C_{ijkl\alpha\beta}\left(\frac{\partial u_j}{\partial X_i} + \frac{\partial u_i}{\partial X_j} + \frac{\partial u_r}{\partial X_i}\frac{\partial u_r}{\partial X_j}\right)\left(\frac{\partial u_l}{\partial X_k} + \frac{\partial u_k}{\partial X_l} + \frac{\partial u_r}{\partial X_k}\frac{\partial u_r}{\partial X_l}\right)\right\} + \cdots\right] \\
&\approx \frac{1}{2}C_{q\beta kl}\left(\frac{\partial u_l}{\partial X_k} + \frac{\partial u_k}{\partial X_l}\right) \\
&\quad + \frac{1}{2}C_{q\beta kl}\frac{\partial u_r}{\partial X_k}\frac{\partial u_r}{\partial X_l} \\
&\quad + \frac{1}{2}C_{\alpha\beta kl}\left(\frac{\partial u_k}{\partial X_l}\frac{\partial u_\alpha}{\partial X_q} + \frac{\partial u_l}{\partial X_k}\frac{\partial u_\alpha}{\partial X_q} + \frac{\partial u_r}{\partial X_k}\frac{\partial u_r}{\partial X_l}\frac{\partial u_\alpha}{\partial X_q}\right) \\
&\quad + \frac{1}{3!}\left\{\frac{1}{4}C_{q\beta klmn}\left(\frac{\partial u_k}{\partial X_l}\frac{\partial u_m}{\partial X_n} + \frac{\partial u_k}{\partial X_l}\frac{\partial u_n}{\partial X_m} + \frac{\partial u_l}{\partial X_k}\frac{\partial u_m}{\partial X_n} + \frac{\partial u_l}{\partial X_k}\frac{\partial u_n}{\partial X_m} + \mathcal{O}^3 + \mathcal{O}^4\right)\right. \\
&\quad + \frac{1}{4}C_{ijq\beta mn}\left(\frac{\partial u_i}{\partial X_j}\frac{\partial u_m}{\partial X_n} + \frac{\partial u_i}{\partial X_j}\frac{\partial u_n}{\partial X_m} + \frac{\partial u_j}{\partial X_i}\frac{\partial u_m}{\partial X_n} + \frac{\partial u_j}{\partial X_i}\frac{\partial u_n}{\partial X_m} + \mathcal{O}^3 + \mathcal{O}^4\right) \\
&\quad + \frac{1}{4}C_{ijklq\beta}\left(\frac{\partial u_i}{\partial X_j}\frac{\partial u_k}{\partial X_l} + \frac{\partial u_i}{\partial X_j}\frac{\partial u_l}{\partial X_k} + \frac{\partial u_j}{\partial X_i}\frac{\partial u_k}{\partial X_l} + \frac{\partial u_j}{\partial X_i}\frac{\partial u_l}{\partial X_k} + \mathcal{O}^3 + \mathcal{O}^4\right) \\
&\quad + \left.\mathcal{O}^3 + \mathcal{O}^4 + \mathcal{O}^5\right\} + \cdots
\end{aligned}
\tag{A.27}
$$

Neglecting third order terms ($\mathcal{O}^3$) and higher in $\partial u_i/\partial X_j$ and introducing the short form given in Eq. (2.57)

$$
M_{ijklmn} = C_{ijklmn} + C_{ijln}\delta_{km} + C_{jnkl}\delta_{im} + C_{jlmn}\delta_{ik},
\tag{A.28}
$$

it can be shown through rigorous expansion and grouping of the terms in Eq. (A.27) that it can be written as [22][23]

$$
S_{ji} = C_{ijkl}\frac{\partial u_k}{\partial X_l} + \frac{1}{2}M_{ijklmn}\frac{\partial u_k}{\partial X_l}\frac{\partial u_m}{\partial X_n} + \frac{1}{3}M_{ijklmnpq}\frac{\partial u_k}{\partial X_l}\frac{\partial u_m}{\partial X_n}\frac{\partial u_p}{\partial X_q} + \cdots
\tag{A.29}
$$

which is the form used in Eq. (2.56).

A.3.4   Space dependent part of the Lagrangian law of motion

Considering the left-hand side of Eq. (A.22) this can be expanded with use of the expansions in Eqs. (A.26) and (A.29) as

$$
\begin{aligned}
\frac{\partial S_{ji}}{\partial X_j} &\approx \frac{\partial S_{ji}}{\partial x_j} + u_{p,j}^{(0)} \frac{\partial S_{ji}}{\partial x_p} \\
&\approx C_{ijkl}\left(\frac{\partial^2 u_k}{\partial x_j \partial x_l} + u_{q,l}^{(0)} \frac{\partial^2 u_k}{\partial x_j \partial x_q} + u_{q,lj}^{(0)} \frac{\partial u_k}{\partial x_q} \right) \\
&\quad + u_{p,j}^{(0)} C_{ijkl}\left(\frac{\partial^2 u_k}{\partial x_p \partial x_l} + u_{q,l}^{(0)} \frac{\partial^2 u_k}{\partial x_p \partial x_q} + u_{q,lp}^{(0)} \frac{\partial u_k}{\partial x_q} \right) \\
&\quad + \frac{1}{2} M_{ijklmn}\Bigg\{ \left(\frac{\partial^2 u_k}{\partial x_j \partial x_l} + u_{q,l}^{(0)} \frac{\partial^2 u_k}{\partial x_j \partial x_q} + u_{q,lj}^{(0)} \frac{\partial u_k}{\partial x_q} \right)\left(u_{m,n} + u_{r,n}^{(0)} u_{m,r} \right) \\
&\qquad\quad + \left(u_{k,l} + u_{q,l}^{(0)} u_{k,q} \right)\left(\frac{\partial^2 u_m}{\partial x_j \partial x_n} + u_{r,n}^{(0)} \frac{\partial^2 u_m}{\partial x_j \partial x_r} + u_{r,nj}^{(0)} \frac{\partial u_m}{\partial x_r} \right) \Bigg\} \\
&\quad + u_{p,j}^{(0)} \frac{1}{2} M_{ijklmn}\Big\{ \cdots \Big\} \\
&\quad + \cdots
\end{aligned}
\tag{A.30}
$$

where the short form $u_{m,n}^{(0)} \equiv \partial u_m^{(0)}/\partial x_n$ has been introduced.

If we now assume that the total stress S_{ij} related to the total displacement displacement u_k can be split into two contributions, one which is caused by the initial static displacement $u_k^{(0)}$, denoted $S_{ji}^{(0)}(u_k^{(0)})$, and one which is related to the additional dynamic displacement $u_k^{(1)}$, denoted $S_{ji}^{(1)}(u_k^{(0)}, u_k^{(1)})$ yields

$$
\frac{\partial S_{ji}(u_k)}{\partial X_j} = \frac{\partial S_{ji}^{(0)}(u_k^{(0)})}{\partial X_j} + \frac{\partial S_{ji}^{(1)}(u_k^{(1)})}{\partial X_j}.
\tag{A.31}
$$

Recalling the Lagrangian form of the Cauchy's first law of motion (Eq. (2.24)) without body forces ($\mathbf{b} = 0$) and where the initial deformation of B_t is in equilibrium (i.e. that the body is at rest ($\dot{\mathbf{x}} = 0$)) ensure that

$$
\frac{\partial S_{ji}^{(0)}}{\partial X_j} = 0.
\tag{A.32}
$$

Thus, expanding the total displacement as $u_k = u_k^{(0)} + u_k^{(1)}$ and disregarding any term in Eq. (A.30) that solely depends on $u_k^{(0)}$ (justified by reasoning that only the initial displacement $u_k^{(0)}$ contributes alone to $S_{ij}^{(0)}$ as well as any contribution to $S_{ij}^{(1)}$ must be caused by an additional displacement $u_k^{(1)}$) when the the initial state B_t is in equilibrium.

A. DETAILED DERIVATIONS

Assuming further that third order or higer terms in $u_{m,n}^{(1)}$ are insignificant leads to the simplification of Eq. (A.30) as

$$
\begin{aligned}
\frac{\partial S_{ji}}{\partial X_j} &\approx \frac{\partial S_{ji}}{\partial x_j} + u_{p,j}^{(0)} \frac{\partial S_{ji}}{\partial x_p} \\
&\approx C_{ijkl}\left(\frac{\partial^2 u_k^{(1)}}{\partial x_j \partial x_l} + u_{q,l}^{(0)}\frac{\partial^2 u_k^{(1)}}{\partial x_j \partial x_q}\right) + u_{p,j}^{(0)} C_{ijkl}\left(\frac{\partial^2 u_k^{(1)}}{\partial x_p \partial x_l}\right) \\
&\quad + \frac{1}{2}M_{ijklmn}\left\{\frac{\partial^2 u_k^{(1)}}{\partial x_j \partial x_l}u_{m,n}^{(0)} + u_{k,l}^{(0)}\frac{\partial^2 u_m^{(1)}}{\partial x_j \partial x_n}\right\} \\
&= \left(C_{ijkl} + C_{ijkq}u_{l,q}^{(0)} + C_{ipkl}u_{j,p}^{(0)}\right)\frac{\partial^2 u_k^{(1)}}{\partial x_j \partial x_l} \\
&\quad + \frac{1}{2}\left(C_{ijklmn} + C_{ijln}\delta_{km} + C_{jnkl}\delta_{im} + C_{jlmn}\delta_{ik}\right)\left\{\frac{\partial^2 u_k^{(1)}}{\partial x_j \partial x_l}u_{m,n}^{(0)} + u_{k,l}^{(0)}\frac{\partial^2 u_m^{(1)}}{\partial x_j \partial x_n}\right\} \\
&= \left(C_{ijkl} + C_{ijkq}u_{l,q}^{(0)} + C_{ipkl}u_{j,p}^{(0)}\right)\frac{\partial^2 u_k^{(1)}}{\partial x_j \partial x_l} \\
&\quad + \frac{1}{2}\Big\{C_{ijklmn}(u_{m,n}^{(0)} + \delta_{km}\delta_{ln}u_{k,l}^{(0)}) + C_{ijln}(u_{k,n}^{(0)} + \delta_{ln}u_{k,l}^{(0)}) + C_{jnkl}(u_{i,n}^{(0)} + \delta_{ik}\delta_{ln}u_{k,l}^{(0)}) \\
&\quad\quad + C_{jlmn}(\delta_{ik}u_{m,n}^{(0)} + \delta_{ik}\delta_{km}\delta_{ln}u_{k,l}^{(0)})\Big\}\frac{\partial^2 u_k^{(1)}}{\partial x_j \partial x_l} \\
&= \Big(C_{ijkl} + \delta_{ik}C_{jlqr}u_{q,r}^{(0)} + C_{rjkl}u_{i,r}^{(0)} + C_{irkl}u_{j,r}^{(0)} + C_{ijrl}u_{k,r}^{(0)} + C_{ijkr}u_{l,r}^{(0)} \\
&\quad\quad + C_{ijklmn}u_{m,n}^{(0)}\Big)\frac{\partial^2 u_k^{(1)}}{\partial x_j \partial x_l} \\
&= B_{ijkl}\frac{\partial^2 u_k^{(1)}}{\partial x_j \partial x_l} \tag{A.33}
\end{aligned}
$$

where

$$
B_{ijkl} = C_{ijkl} + \delta_{ik}C_{jlqr}u_{q,r}^{(0)} + C_{rjkl}u_{i,r}^{(0)} + C_{irkl}u_{j,r}^{(0)} + C_{ijrl}u_{k,r}^{(0)} + C_{ijkr}u_{l,r}^{(0)} + C_{ijklmn}u_{m,n}^{(0)}. \tag{A.34}
$$

Combining the time and space dependent part of the Lagrangian law of motion Eq. (A.22) can thus be written as a linear equation for the additional disturbance $\mathbf{u}^{(1)}(\mathbf{x}, t)$ through Eqs. (A.25) and (A.33) as [24]

$$
B_{ijkl}\frac{\partial^2 u_k^{(1)}}{\partial x_j \partial x_l} = \rho_0 \frac{\partial^2 u_i^{(1)}}{\partial t^2}, \tag{A.35}
$$

which is the form used in Eq. (2.62).

A.4 Expansion of sound velocities

With the effective elastic moudli B_{ijkl} of Eq. (A.34) and the elastic moduli of Eqs. (2.71) and (2.72) for a hyperelastic isotropic material as [12]

$$
\begin{aligned}
C_{ijkl} &= \lambda\delta_{ij}\delta_{kl} + 2\mu I_{ijkl}, &\text{(A.36)}\\
C_{ijklmn} &= 2C\delta_{ij}\delta_{kl}\delta_{mn} + 2B(\delta_{ij}I_{klmn} + \delta_{kl}I_{mnij} + \delta_{mn}I_{ijkl})\\
&\quad +\frac{1}{2}A(\delta_{ik}I_{jlmn} + \delta_{il}I_{jkmn} + \delta_{jk}I_{ilmn} + \delta_{jl}I_{ikmn}), &\text{(A.37)}
\end{aligned}
$$

the longitudinal sound velocity c_{33} in Eq. (2.90) can be expanded using the uniaxial homogeneous displacements in Eq. (2.79). The results of this expansion have been presented in [25], and the detail of this expansion is shown here to complement this result. Note that the symbol ρ is used for the undeformed density in [25] while it is subscripted with 0 in this work for consistency. Note also that the first index of c_{ij} is 3 in this work, while 2 in [25]. This is related to the selected propagation direction perpendicular to the tension, which for an isotropic material is interchangeable.

Thus, for a longitudinal sound wave with propagation direction perpendicular to the applied tension (in this work denoted c_{33} as described in Sec. 2.3) can on use of

$$
u_{i,j}^{(0)} = \begin{cases} e_i & \text{for} & i = j \\ 0 & \text{for} & i \neq j \end{cases}
\tag{A.38}
$$

and $e_2 = e_3$, be expanded in e_1 as

$$
\begin{aligned}
\rho_0 c_{33}^2 &= B_{3333}\\
&= C_{3333}\\
&\quad + C_{3311}u_{1,1}^{(0)} + \cancel{C_{3312}u_{1,2}^{(0)}} + \cancel{C_{3313}u_{1,3}^{(0)}} + \cancel{C_{3321}u_{2,1}^{(0)}} + C_{3322}u_{2,2}^{(0)} + \cancel{C_{3323}u_{2,3}^{(0)}}\\
&\quad + \cancel{C_{3331}u_{3,1}^{(0)}} + \cancel{C_{3332}u_{3,2}^{(0)}} + C_{3333}u_{3,3}^{(0)} + \cancel{C_{1333}u_{3,1}^{(0)}} + \cancel{C_{2333}u_{3,2}^{(0)}} + C_{3333}u_{3,3}^{(0)}\\
&\quad + \cancel{C_{3133}u_{3,1}^{(0)}} + \cancel{C_{3233}u_{3,2}^{(0)}} + C_{3333}u_{3,3}^{(0)} + \cancel{C_{3313}u_{3,1}^{(0)}} + \cancel{C_{3323}u_{3,2}^{(0)}} + C_{3333}u_{3,3}^{(0)}\\
&\quad + \cancel{C_{3331}u_{3,1}^{(0)}} + \cancel{C_{3332}u_{3,2}^{(0)}} + C_{3333}u_{3,3}^{(0)} + C_{333311}u_{1,1}^{(0)} + \cancel{C_{333312}u_{1,2}^{(0)}} + \cancel{C_{333313}u_{1,3}^{(0)}}\\
&\quad + \cancel{C_{333321}u_{2,1}^{(0)}} + C_{333322}u_{2,2}^{(0)} + \cancel{C_{333323}u_{2,3}^{(0)}} + \cancel{C_{333331}u_{3,1}^{(0)}} + \cancel{C_{333332}u_{3,2}^{(0)}} + C_{333333}u_{3,3}^{(0)}\\
&= C_{3333} + (C_{3311} + C_{333311})e_1 + (C_{3322} + C_{333322})e_2 + (5C_{3333} + C_{333333})e_3
\end{aligned}
\tag{A.39}
$$

227

A. DETAILED DERIVATIONS

$$
\begin{aligned}
&= \lambda + 2\mu + (\lambda + 2C + 2B)e_1 + (6\lambda + 10\mu + 4C + 8B + 2A)e_2 \\
&= \lambda + 2\mu + \left[(\lambda + 2C + 2B) - \frac{\lambda}{2(\lambda + \mu)}(6\lambda + 10\mu + 4C + 8B + 2A) \right] e_1 \\
&= \lambda + 2\mu + \frac{(\lambda + \mu)(\lambda + 2C + 2B) - \lambda(3\lambda + 5\mu + 2C + 4B + A)}{(\lambda + \mu)} e_1 \\
&= \lambda + 2\mu + \frac{-2\lambda^2 - 4\lambda\mu - \lambda A - 2\lambda B + 2\mu B + 2\mu C}{(\lambda + \mu)} e_1 \\
&= \lambda + 2\mu - \frac{2\lambda(\lambda + 2\mu) + \lambda A + 2(\lambda - \mu)B - 2\mu C}{(\lambda + \mu)} e_1 \\
&= \lambda + 2\mu + a_{33}e_1
\end{aligned}
\tag{A.40}
$$

where a_{33} is the acoustoelastic coefficient related to effects from third order elastic constants used in Eq. (2.92). Similarly it can be shown that

$$
\rho_0 c_{3k}^2 = \mu + a_{3k}e_1, \quad k = 1, 2
\tag{A.41}
$$

This section has thus shown the method of expansion of the sound velocities as a function of the initial elongation of a homogeneous uniaxial deformation for an hyperelastic isotropic material. The expansion of the other acoustoelastic coefficients are not explicitly done here but follows imediately from the expansion of B_{1313} and B_{2323}. Note also that higher order acoustoelastic coefficients can be included by including higher order terms in the expansion of B_{ijkl} shown in App. A.3.4. Abiza et al. [25] have shown that the acoustoelastic coefficients, b_{ij}, related to effects from fourth order elastic constants (E, F, G, H) may also be important for some cases. Although they have not been applied in this work, they have been included here for completeness together with the corresponding expressions for the sound velocities.

$$
\rho_0 c_{33}^2 = \lambda + 2\mu + a_{33}e_1 + b_{33}e_1^2, \qquad \rho_0 c_{3k}^2 = \mu + a_{3k}e_1 + b_{3k}e_1^2, \quad k = 1, 2
\tag{A.42}
$$

$$
\begin{aligned}
b_{33} = {}& -\frac{\lambda\mu(\lambda + 2\mu)}{(\lambda + \mu)^2} - \frac{\lambda(2\lambda^2 - \mu^2)}{2(\lambda + \mu)^3}A - \frac{3\mu(3\lambda^2 + 3\lambda\mu + \mu^2)}{(\lambda + \mu)^3}B - \frac{\mu(3\lambda^2 + 4\lambda\mu + 3\mu^2)}{(\lambda + \mu)^3}C \\
& -\frac{\lambda^2}{4(\lambda + \mu)^3}A^2 - \frac{2(3\lambda^2 + 2\lambda\mu + 2\mu^2)}{(\lambda + \mu)^3}B^2 - \frac{2\mu^2}{(\lambda + \mu)^3}C^2 - \frac{5\lambda^2 + 2\lambda\mu + 2\mu^2}{2(\lambda + \mu)^3}AB \\
& -\frac{3\lambda^2 + 2\lambda\mu + 6\mu^2}{(\lambda + \mu)^3}BC - \frac{\lambda^2 + 2\mu^2}{2(\lambda + \mu)^3}AC + \frac{3\lambda(\lambda - 2\mu)}{2(\lambda + \mu)^2}E + \frac{3\lambda^2 + 4\mu^2}{(\lambda + \mu)^2}F \\
& +4\left[1 + \frac{\lambda^2}{(\lambda + \mu)^2} \right] G + \frac{12\mu^2}{(\lambda + \mu)^2}H
\end{aligned}
\tag{A.43}
$$

$$b_{31} = b_{13} - \gamma - \frac{3\kappa\mu^2}{(\lambda+\mu)^2} \tag{A.44}$$

$$b_{32} = -\frac{\lambda\mu^2}{(\lambda+\mu)^2} + \frac{\lambda(3\lambda^2-\mu^2)}{4(\lambda+\mu)^3}A - \frac{3\mu(3\lambda^2+2\lambda\mu+\mu^2)}{2(\lambda+\mu)^3}B - \frac{\mu^3}{(\lambda+\mu)^3}C - \frac{\lambda^2}{8(\lambda+\mu)^3}A^2$$

$$-\frac{3\lambda^2+2\lambda\mu+2\mu^2)}{2(\lambda+\mu)^3}B^2 - \frac{2\lambda^2+\lambda\mu+\mu^2)}{2(\lambda+\mu)^3}AB - \frac{\mu^2}{(\lambda+\mu)^3}(A+2B)C - \frac{3\lambda\mu}{2(\lambda+\mu)^2}E$$

$$+\frac{\mu^2}{(\lambda+\mu)^2}F + \left[2 + \frac{\lambda^2}{(\lambda+\mu)^2}\right]G \tag{A.45}$$

where b_{13} is

$$b_{13} = 6\mu + \frac{9(\lambda+2\mu)}{8(\lambda+\mu)}A + \frac{9\mu}{2(\lambda+\mu)}B - \frac{\lambda^2}{16(\lambda+\mu)^3}A^2 - \frac{3\lambda^2+2\lambda\mu+\mu^2}{2(\lambda+2\mu)^3}B^2$$

$$-\frac{5\lambda^2+2\lambda\mu+2\mu^2)}{8(\lambda+\mu)^3}AB - \frac{\mu^2}{4(\lambda+\mu)^3}(A+4B)C + \frac{3\mu(\lambda+2\mu)}{4(\lambda+\mu)^2}E \tag{A.46}$$

$$+\frac{\mu^2}{(\lambda+\mu)^2}F + \left[2 + \frac{\lambda^2}{(\lambda+\mu)^2}\right]G$$

A. DETAILED DERIVATIONS

Appendix B

Calibration certificates

KALIBRERINGSBEVIS

Version 3.22

Certificate of calibration

Nr./*No.:* CALDNV-0098-A/2013

DET NORSKE VERITAS AS
Section: Materials Laboratory, TNTNO715.

Delivery address: Veritasveien 1, 1363 Høvik, Norway
Postal address: P. O. Box 300, 1323 Høvik, Norway.
Phone : +47 67579900   Fax   : +47 67579911

Side/*Page: 1 of   6*
Måleprotokoll/*Ref. to records:*
71580106

I dog sted for kalibrering/*Date and place of calibrations:* 15 Jan 2013 at DNV,Høvik	Bevisets utstedelsesdato/*Date of issue:* 16. jan. 2013
Kalibrering utført av/*Calibration done by:* Erik Habberstad *Erik Habberstad*	Ansvarlig/ *Responsible:* Bjørn Engh

CALIBRATION OF TENSILE/COMPRESSION TESTING MACHINE

Client

TNTNO715
HØVIK

Equipment Calibrated and its Identification

Universal testing machine

Manufacturer	: Instron Ltd. England
Model	: A 25100-1001
Serial No.	: H 0554
Rated capacity	: 300 kN
Year of manufacture	: 1995
Force indicator system	: Messtek, Dyn. Reg. Version 7.4 Type MT2A/16, Ser No. 10742

Reference instruments used

Proving ring	200kN	Wazau	MBM DZ	83002
Proving ring	600kN	Wazau	MBM DZ	78066
Displacement transducer	12 mm	Heidenhain	MT 12	12319199G
Displacement display	-	Heidenhain	283 481 01	5402314 R11

KALIBRERINGSBEVIS
Certificate of calibration

Certificate No.: CALDNV-0098-A/2013

Traceability

The force reference normal was calibrated at SP, Borås, with traceability to mass and gravitational acceleration.

Calibration method

The calibration was carried out according to DNV NTANO715 Internal Service Instruction: ISI-NTANO-CAL-04: KALIBRERING AV PRØVEMASKINER FOR STREKK- OG/ELLER TRYKKBELASTNING.
(Calibration of testing machines for tension- and/or compression force) which embraces EN ISO 7500-1. The force reference normal was loaded by the calibrated machine in series with its force measuring device.

Calibration uncertainty

The measurement uncertainty has been calculated for each load step according to the document EA-4/02 and includes:

- Uncertainty of the force reference, including long and short term effects.
- Uncertainty in mass and local gravity in case reference force was realized by masses.
- Uncertainty due to temperature variations.
- Uncertainty of the force reference indicator.
- Uncertainty of the calibration method.
- Measurement resolution of the calibrated machine.
- Variations of the repeated measurements at the same force level.

The expanded relative measurement uncertainty, U, is shown for each load step in the column "Relative uncertainty U, k=2". It is reasonable to assume that for each load step, the force indicated on the machine, subtracted the shown relative accuracy error, with 95% probability, will not deviate more from the true force than the stated relative uncertainty. This provided that the machine has not changed since the calibration and is operated the same way and under the same conditions as during the calibration.

Calibration environment

The temperature is given in the result table for each calibrated range.

Range classification and detailed results

Machine range data		Machine range class assignment		
Range	Scale division	Range	Largest relative resolution (%)	ISO/DNV class
300kN Tension	0,01 kN	20 - 300 kN	0,050	1 / 1
300kN Compression	0,01 kN	20 - 300 kN	0,050	1 / 1

Calibration results

The result tables and error diagrams are shown for each calibrated range on the next pages. The error calculation methods and the maximum permissible errors for each machine class are shown in the Appendix.

Cal. Date: **Instron 300 kN**

15.01.2013 **Ser. no.: H0554 Sense: -55.0 kN/V Offset: 22,6 kN**

Calibrated range 300 kN Tension		Temp. 17,4 C Software: Y120926b		
Reference: WAZAU 200kN tension WAZAU 600kN tension				

Force rel. 0 on calibrated equipment kN	Force rel. 0 on calibration normal kN	Relative Accuracy Error	Relative Repeatability Error	Relative Uncertainty U, k=2
		----------- % of applied force -----------		
20	20,0875	-0,44	0,56	1,1
60	60,2311	-0,38	0,13	0,40
100	100,419	-0,42	0,094	0,39
120	120,513	-0,43	0,031	0,38
200	199,614	0,19	0,26	0,78
250	249,400	0,24	0,28	0,78
300	299,139	0,29	0,13	0,63

Mean of zero errors after load cycles (kN):   0,00

Largest relative resolution (%):   0,050

Largest relative zero error after load cycles. (% of force range):   -0,013

Class assignments for the range: EN ISO 7500-1-Class = 1. DNV CAL011-Class = 1.

Legend: Accuracy error (%) — Repeatability error (%) — Uncertainty U, k=2 (%)

Cal. Date:	**Instron 300 kN**
15.01.2013	**Ser. no.: H0554 Sense: -55.0 kN/V Offset: 22,6 kN**

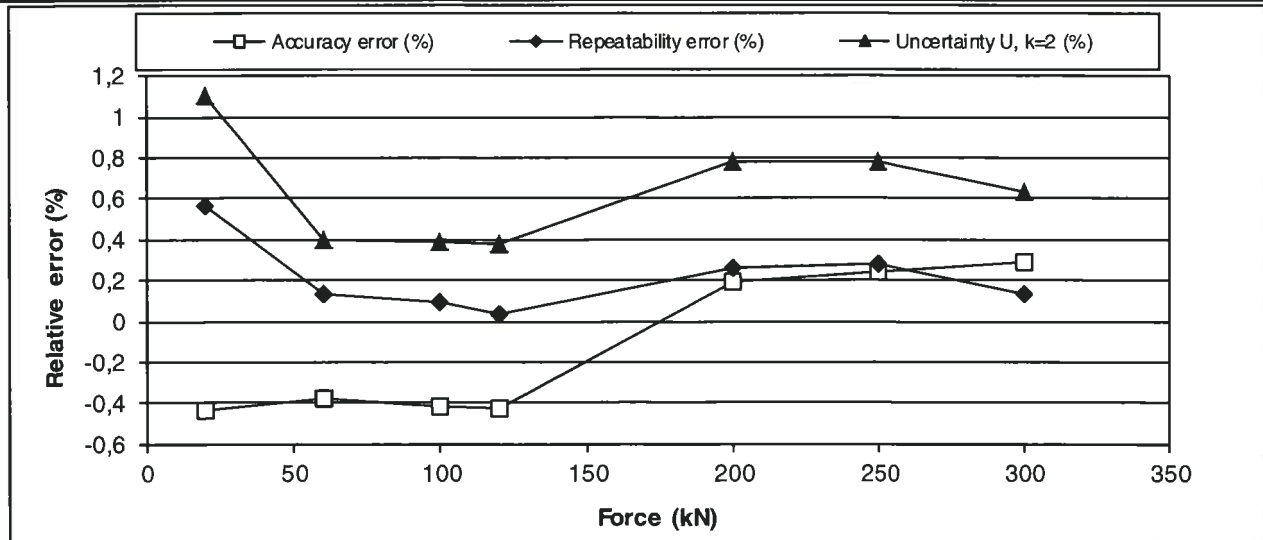| Calibrated range 300 kN Compression	Temp. 18 C	Software: Y120926b

Reference: WAZAU 200kN compression WAZAU 600kN compression

Force rel. 0 on calibrated equipment kN	Force rel. 0 on calibration normal kN	Relative Accuracy Error	Relative Repeatability Error	Relative Uncertainty U, k=2
		----------- % of applied force -----------		
20	20,0301	-0,15	0,76	1,4
60	60,2942	-0,49	0,063	0,43
100	100,655	-0,65	0,056	0,41
120	120,803	-0,66	0,094	0,42
200	201,426	-0,71	0,085	0,41
250	251,968	-0,78	0,068	0,37
300	302,508	-0,83	0,057	0,34

Mean of zero errors after load cycles (kN):	**0,00**
Largest relative resolution (%):	**0,050**

Largest relative zero error after load cycles. (% of force range):	**-0,013**

Class assignments for the range: EN ISO 7500-1-Class = 1. DNV CAL011-Class = 1.
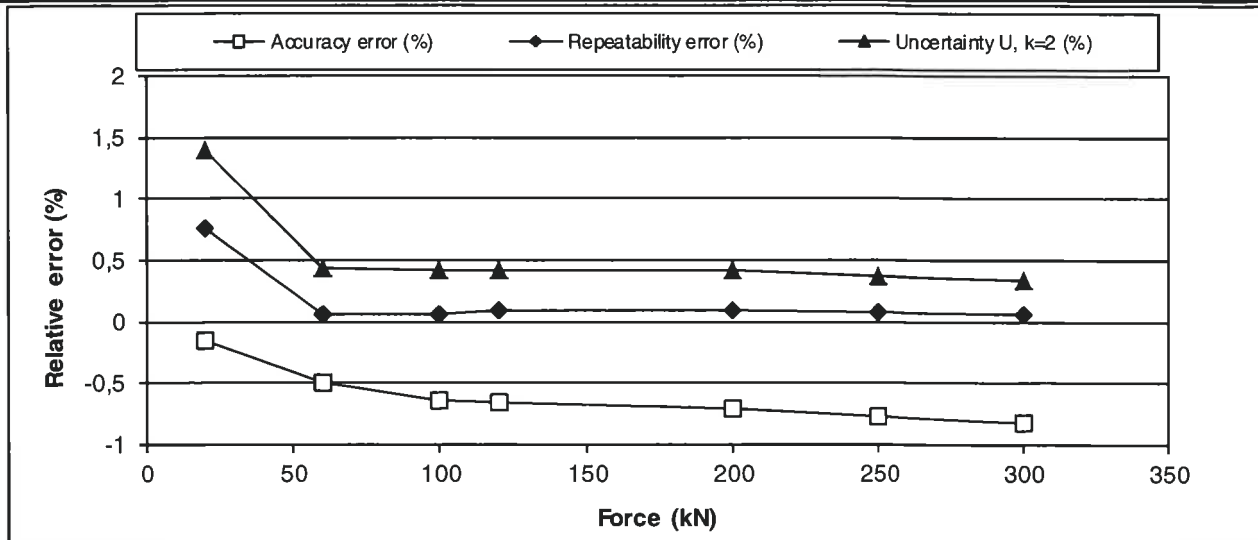
APPENDIX

CALCULATION OF ERRORS

The errors shown in the table(s) are calculated from 3 force applications with increasing loads and 3 applications with decreasing loads:

Relative accuracy error (q):

$$q = \frac{F_i - \overline{F}}{\overline{F}} \, x \, 100 \, \%$$

Relative repeatability error (b):

$$b = \frac{F_{max} - F_{min}}{\overline{F}} \, x \, 100 \, \%$$

where

F_i	=	force reading on the indicator on the testing machine
$\overline{F}$	=	arithmetic mean value of the force read on the force reference.
F_{max}	=	highest force read on the force reference.
F_{min}	=	lowest force read on the force reference.

NOTE:

A negative q means that the indicator on the machine shows too low value

A positive q means that the indicator on the machine shows too high value

TESTING MACHINE CLASS ACCORDING TO EN ISO 7500-1

An additional requirement to the below table is that the assigned machine class can not be better than the class assigned to the reference load cell during its last calibration.

Class of Machine	Maximum permissible error, %				
	Accuracy q	Repeatability b	Reversibility[1)] V	Zero f_0	Relative resolution a
0,5	±0,5	0,5	±0,75	±0,05	0,25
1	±1,0	1,0	±1,5	±0,1	0,5
2	±2,0	2,0	±3,0	±0,2	1,0
3	±3,0	3,0	±4,5	±0,3	1,5

3) The verification of reversibility shall only be carried out on request (see 6.4.8 EN ISO 7500-1)

TESTING MACHINE CLASS ACCORDING TO DNV CAL 011

In this alternative to the EN ISO 7500-1 class assignment, the accuracy error, q, is increased by the relative expanded uncertainty in the applied force, U_f k=2, while the class assigned to the reference load cell is not considered. This alternative accuracy error is calculated as $q' = \sqrt{(q^2 + U_f^2)}$. The class is then determined according to the above table using q' instead of q. As the U_f also includes uncertainties for the reference load cell during the last and previous calibrations, temperature effects and the indicating instrument, DNV regards this as a more adequate way of determining the accuracy error.

- oOo –

B. CALIBRATION CERTIFICATES

Appendix C

Figures

C.1   Instron measurements

Figs. C.1 and C.2 shows the recorded Instron displacement x_1 from the 37 individual test specimens which is the basis for the experimental average presented in Figs. 3.4 and 3.5 in Sec. 3.3.
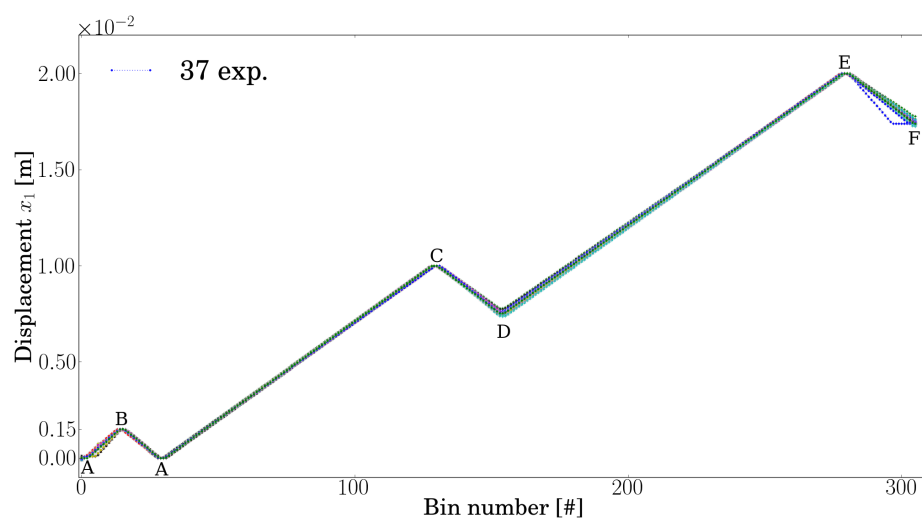
Figure C.1: Recorded x_1 displacement in 306 predefined bins for the 37 test specimens

Fig. C.3 shows the results from the 37 individual test specimens which is the basis for the experimental average presented in Fig. 5.3 in Sec. 5.2.
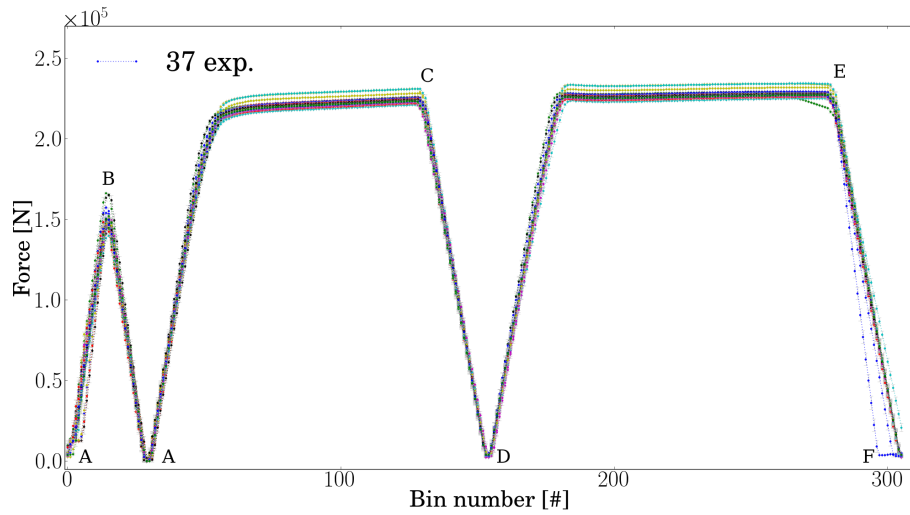
Figure C.2: Recorded applied force in x_1-direction in 306 predefined bins for the 37 test specimens
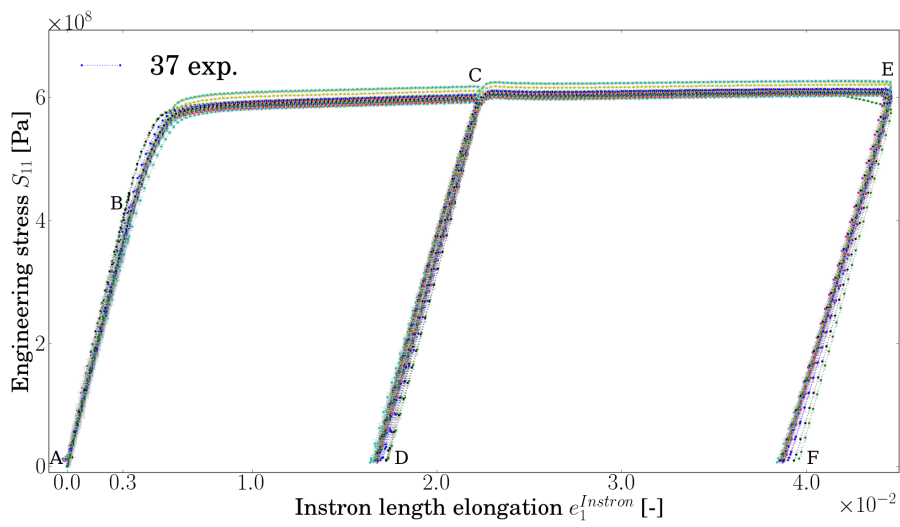
Figure C.3: Average of calculated engineering stress S_{11} and elongation $e_1^{Instron}$ in 306 predefined bins

C.2 Geometrical change

C.2.1 Stress and strains from strain gauge measurements

Figs. C.4 to C.6 shows the measured strain from individual strain gauges placed on a variety of test specimens. These plots are the basis of the reported experimental average presented in Sec. 5.3, Figs. 5.4, 5.5, and 5.6 respectively.
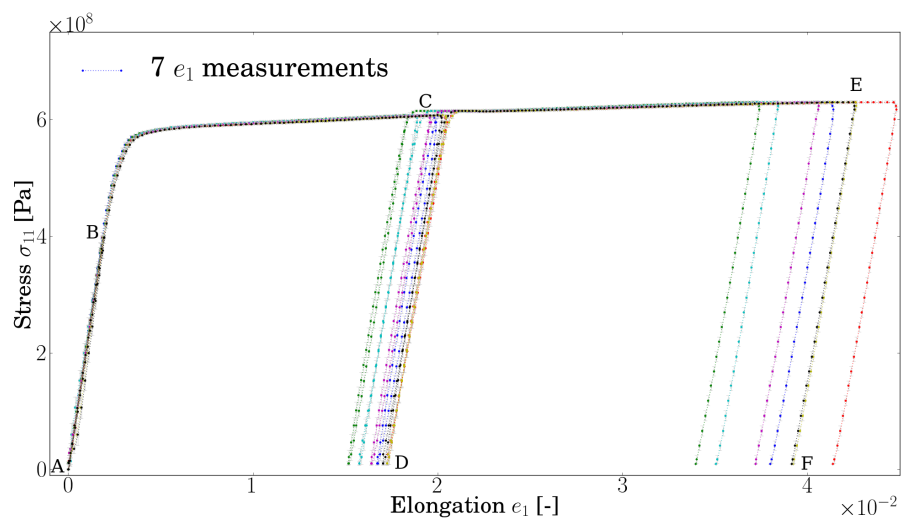
Figure C.4: Measured e_1 elongation from 7 strain gauges on 6 test specimens plotted against σ_{11}
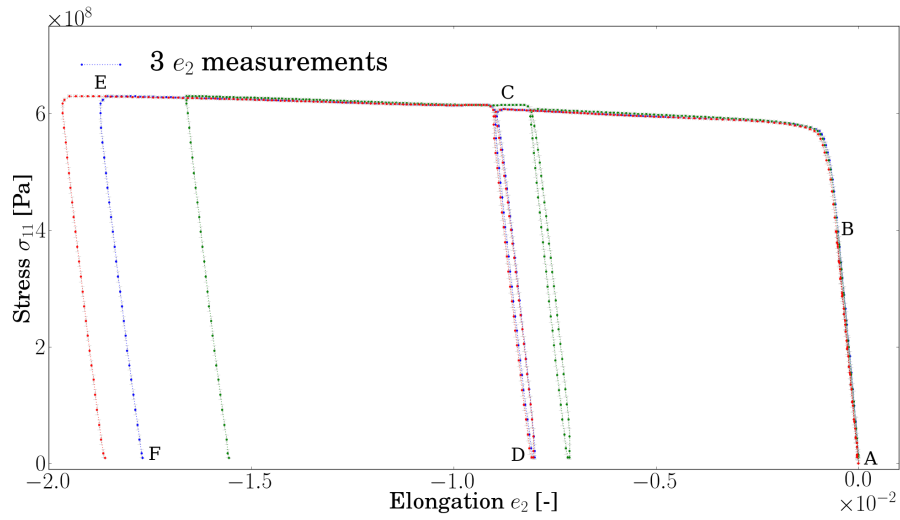
Figure C.5: Measured e_2 elongation from 3 strain gauges on 2 test specimens plotted against σ_{11}
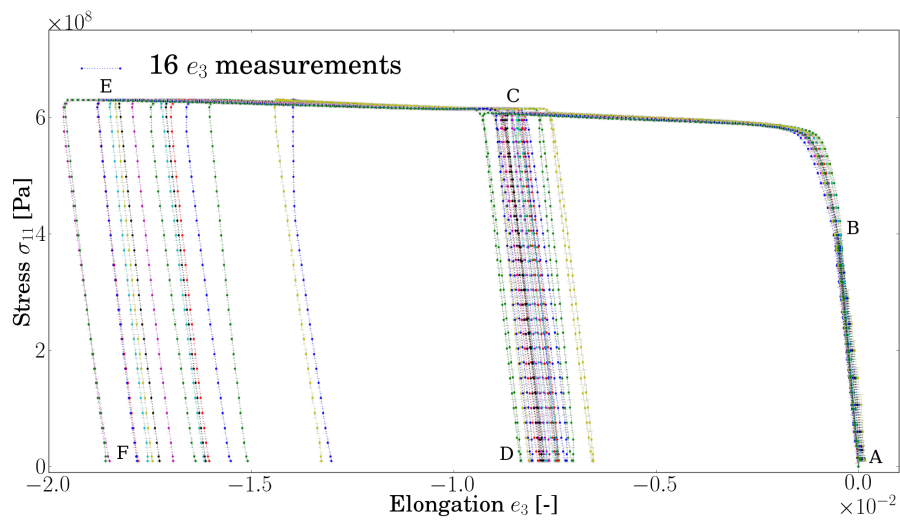
Figure C.6: Measured e_3 elongation from 16 strain gauges on 13 test specimens plotted against σ_{11}

Fig. C.7 shows the ratio between stresses estimated by assuming the Poisson's effect is valid and either of the two transverse elongations e_2 or e_3 and the stresses estimated based on both of the transverse elongations. The symmetry of this plot can be explained by investigating the ratios from Eq. 3.16 as

$$\frac{(1-e_2)(1-e_3)}{(1-e_2)^2} = \frac{(1-e_2)}{(1-e_3)}, \qquad \text{and} \qquad \frac{(1-e_2)(1-e_3)}{(1-e_3)^2} = \frac{(1-e_3)}{(1-e_2)} \qquad \text{(C.1)}$$

where it is easily seen that the first ratio is the inverse of the second ratio. The figure include all the possible combinations of $\sigma_{11}(e_2, e_3)$, $\sigma_{11}(e_2)$, and $\sigma_{11}(e_3)$ from the only two test specimens where strain gauges for all the principal directions (i.e. e_1, e_2, and e_3) were included (i.e. experiments #14 and #17).
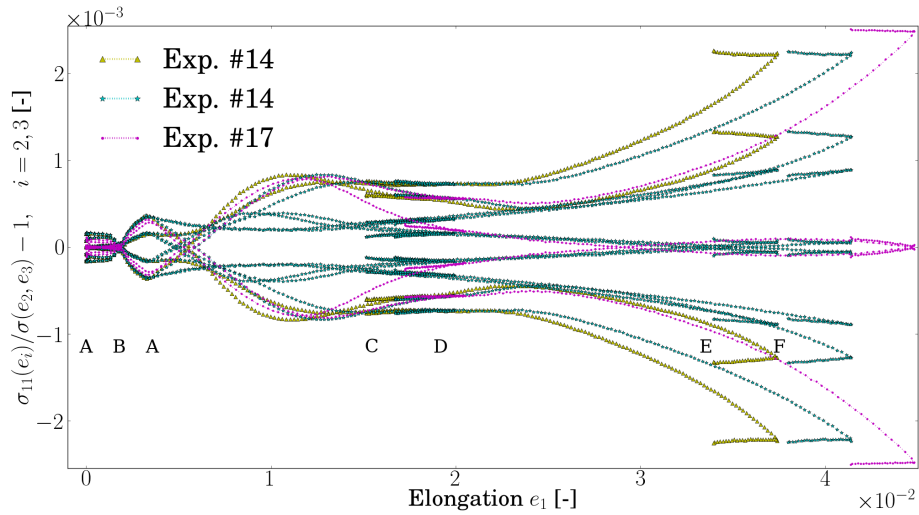
Figure C.7: Ratio between σ_{11} stress estimated by e_2 or e_3 (Eq. (3.15)) and σ_{11} stress estimated by e_2 and e_3 (Eq. (3.14))

Figs. C.8 and C.9 shows the elastic and plastic part of the total measured elongation in the x_2- and x_3-direction respectively. The corresponding plot for the elongation in the x_1-direction have been explained in Sec. 5.3 and shown in Fig. 5.8.
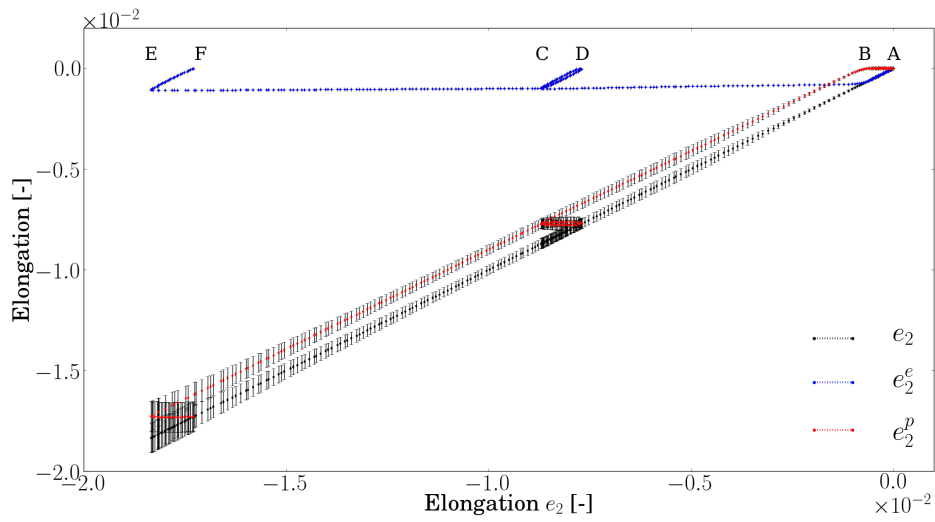
Figure C.8: Elastic and plastic elongation (e_2^e, e_2^p) plotted against total measured elongation e_2
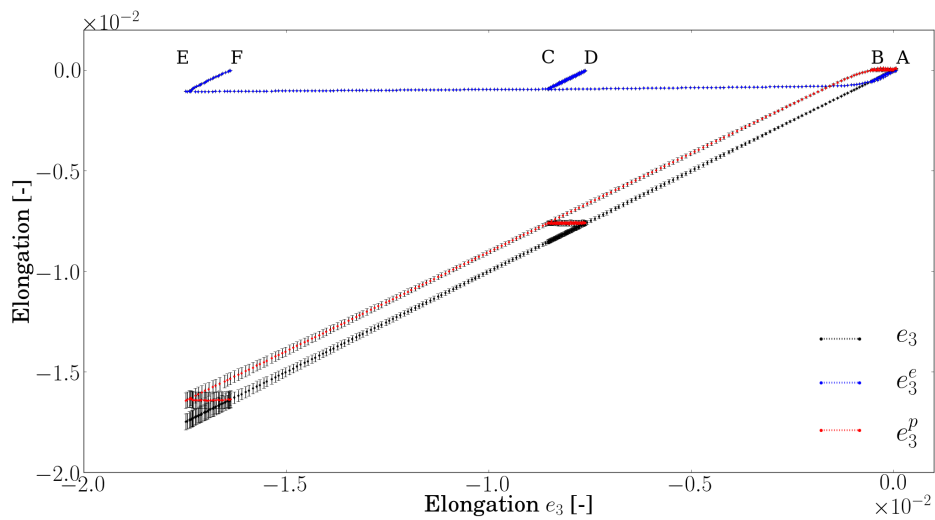
Figure C.9: Elastic and plastic elongation (e_3^e, e_3^p) plotted against total measured elongation e_3

C.2.2 ARAMIS stress and strains

As explained in Sec. 5.3.1 the ARAMIS results were deemed too uncertain to use in this work. Thus the results from the ARAMIS measurements have only been included here for reference. The plots below corresponds to those presented and explained in Secs. 5.3 and C.2.1 for the strain gauge measurements.
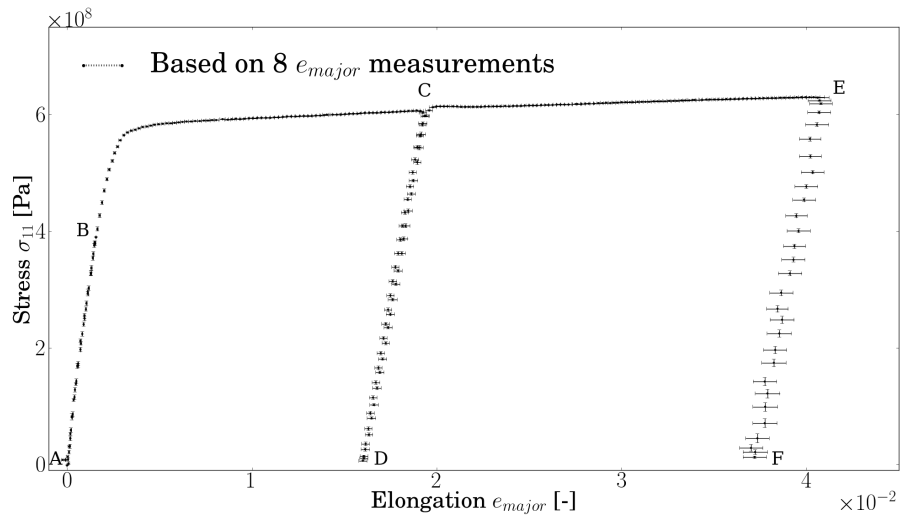
Figure C.10: Average of e_{major} strain over 8 test specimens
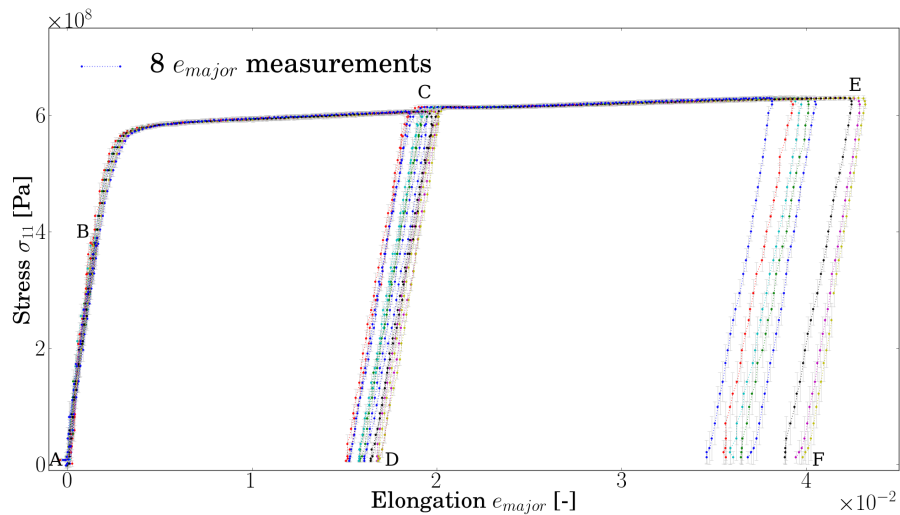
Figure C.11: Measured e_{major} strain
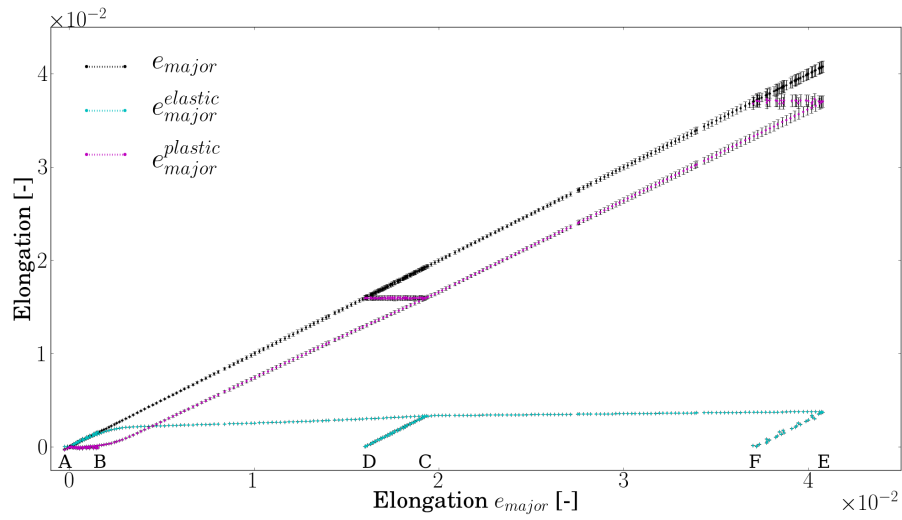
Figure C.12: Elastic and plastic elongation (e^e_{major}, e^p_{major}) plotted against total measured elongation e_{major}
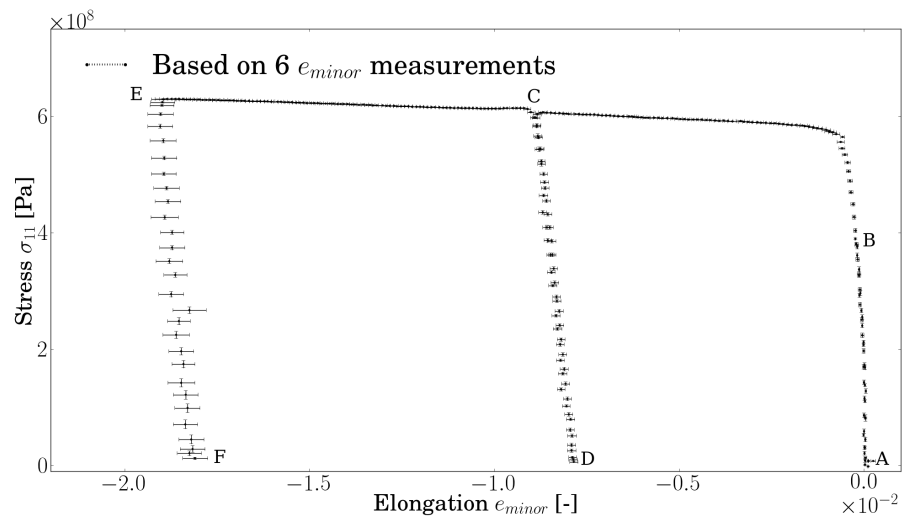
Figure C.13: Average of e_{minor} strain over 6 test specimens
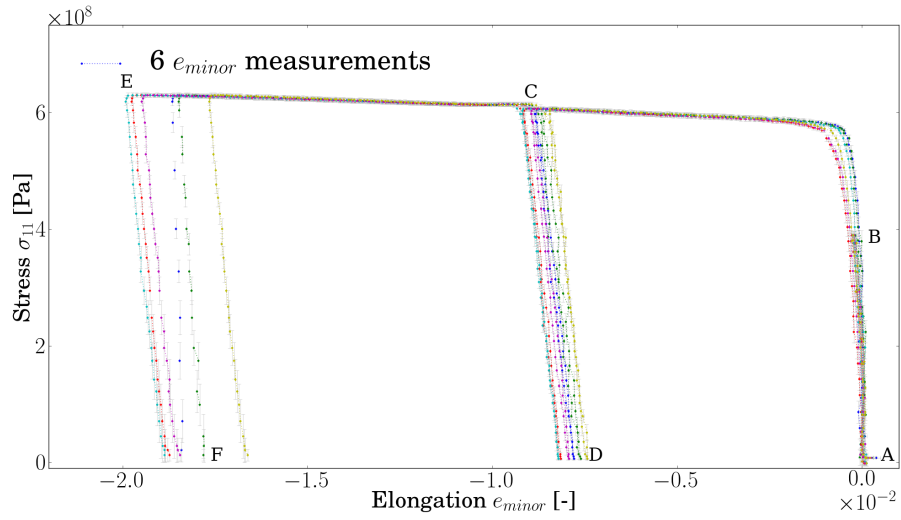
Figure C.14: Measured e_{minor} strain
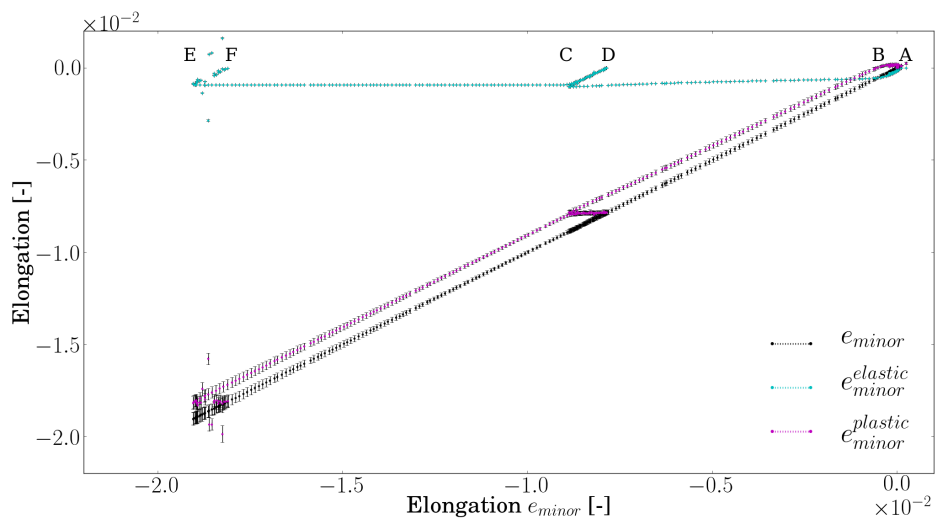
Figure C.15: Elastic and plastic elongation ($e_{minor}^{e}, e_{minor}^{p}$) plotted against total measured elongation e_{minor}
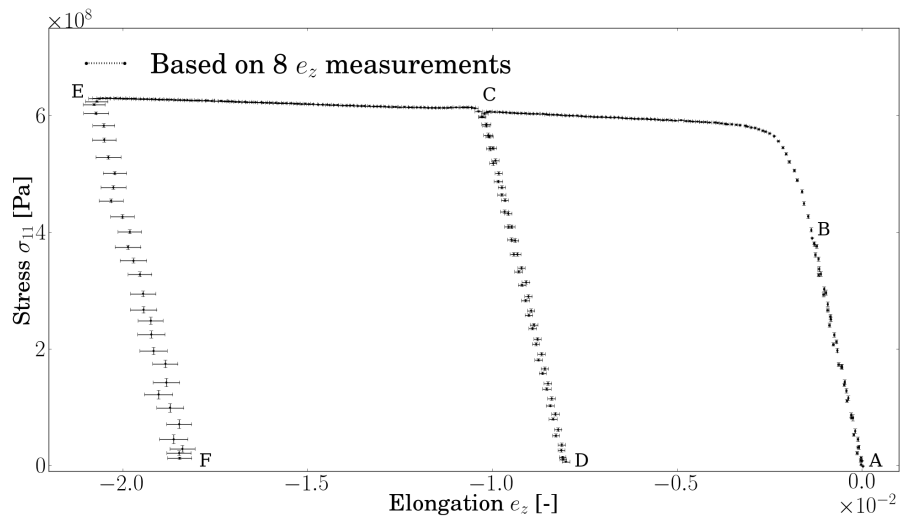
Figure C.16: Average of e_z strain over 8 test specimens
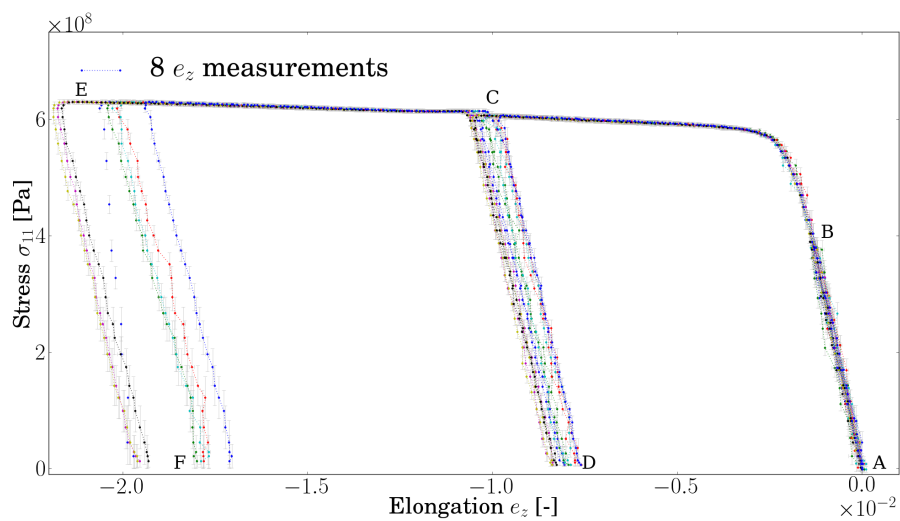
Figure C.17: Measured e_z strain
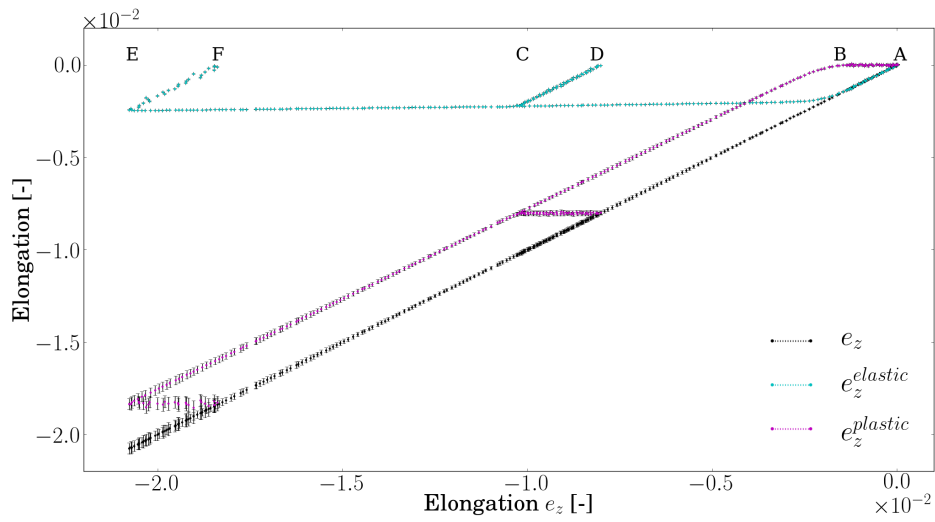
Figure C.18: Elastic and plastic elongation (e_z^e, e_z^p) plotted against total measured elongation e_z
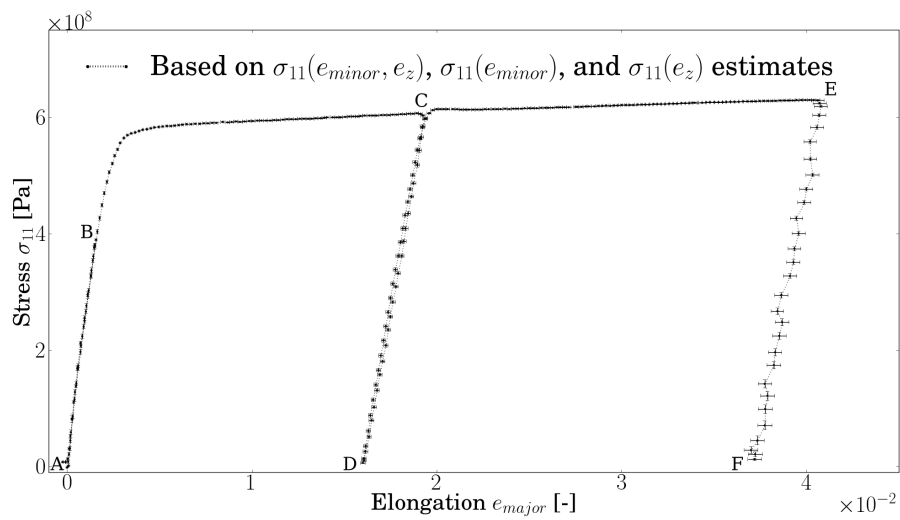
Figure C.19: Average of σ_{major} stress and e_{major} strain based on measured contraction strains (e_{minor} and e_z)
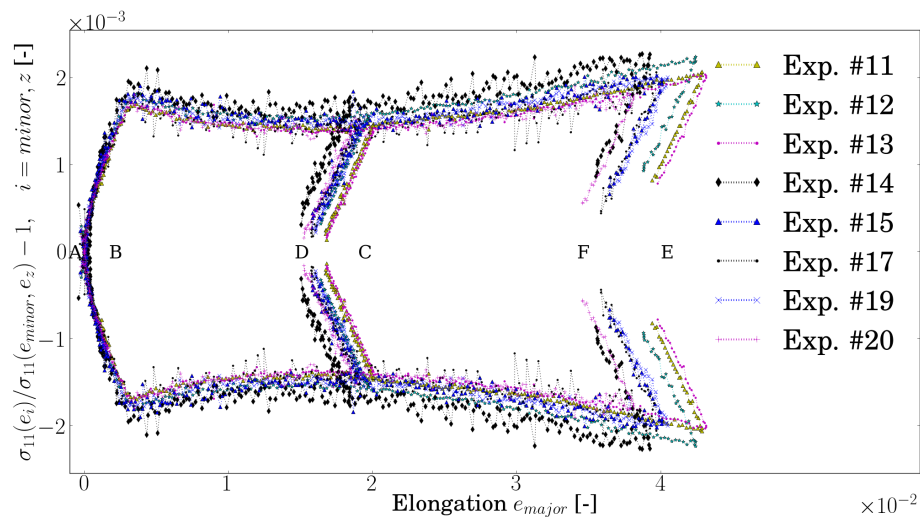
Figure C.20: Ratio between σ_{major} stress estimated by e_{minor} or e_z (Eq. (3.15)) and σ_{major} stress estimated by e_{minor} and e_z (Eq. (3.14))

C.3 ART

Figs. C.21 and C.22 shows the development of recorded frequencies for the L1 and S3 mode in the 13 individual test specimens and corresponds to the plot of the L2 mode presented in Fig. 5.9. The experimental average over these measurements have been presented in Figs. 5.11 and 5.12.
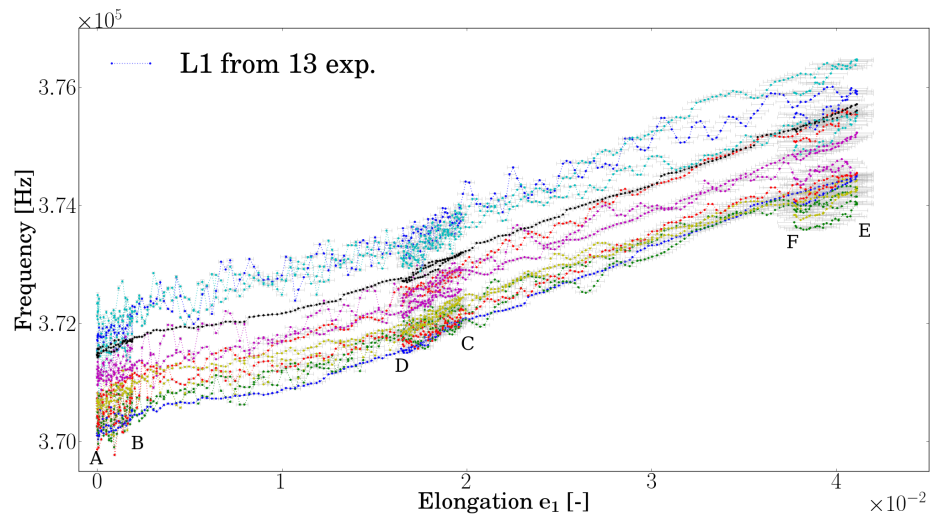
Figure C.21: Resonance frequency for the L1 mode
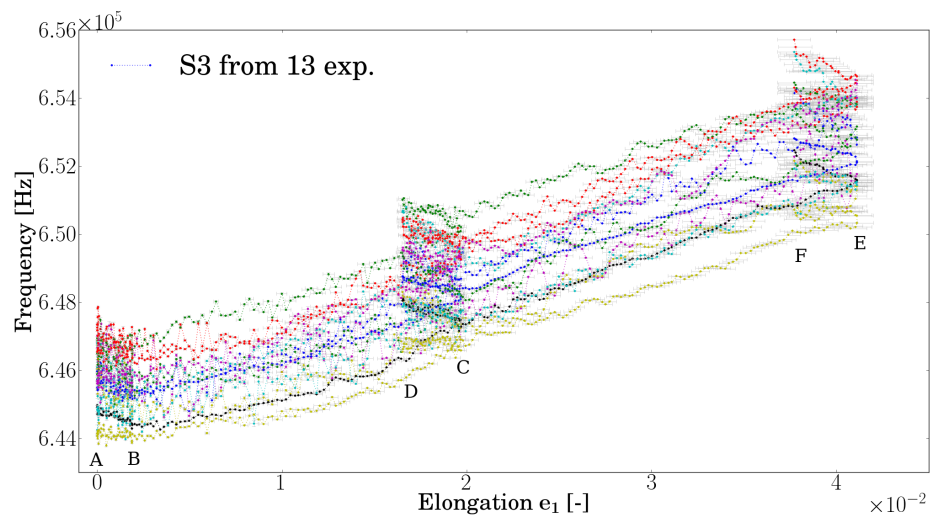
Figure C.22: Resonance frequency for the S3 mode

Based on the L1 and S3 resonance frequencies in Figs. 5.11 and 5.12, their relative change have been calculated and shown in Figs. C.23 and C.24. This is the basis for the experimental average presented in Figs. 5.14.
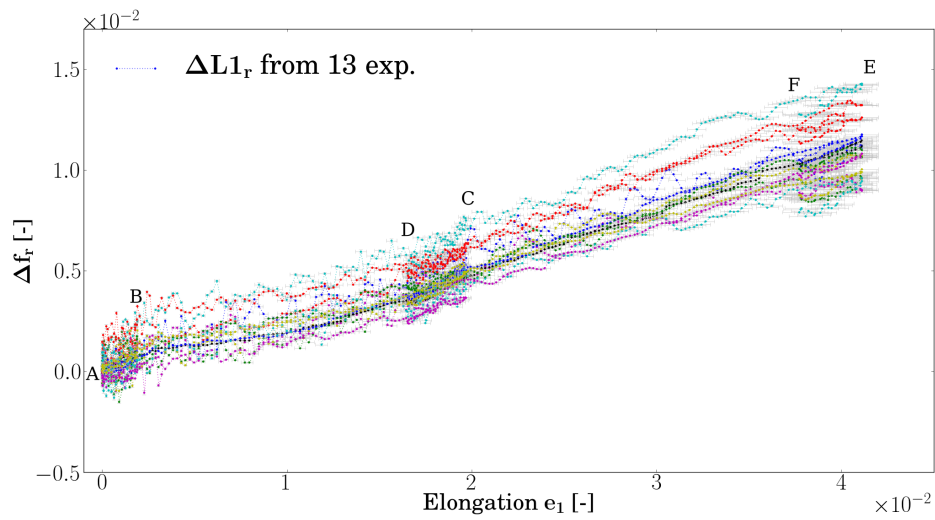
Figure C.23: Relative resonance frequency change for the L1 mode
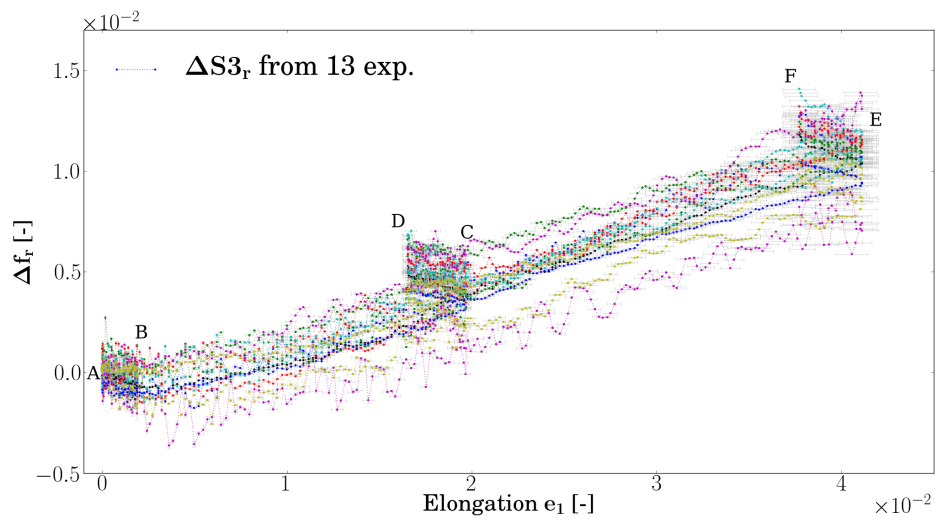
Figure C.24: Relative resonance frequency change for the S3 mode

The relative change of the ratio between the longitudinal modes L1 or L2 and the shear mode S3 are the main results discussed in this work, and have been presented in Sec. 5.6.2, Fig. 5.20. To illustrate the spread across the 13 acoustic tests the individual ratios have been included here in Figs. C.25 to C.27.
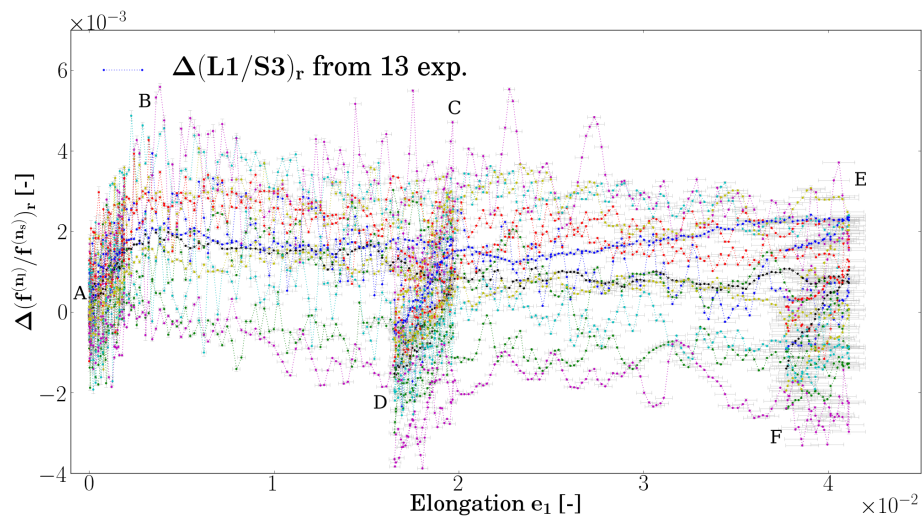
Figure C.25: Relative change in ratio of resonance mode L1 and S3
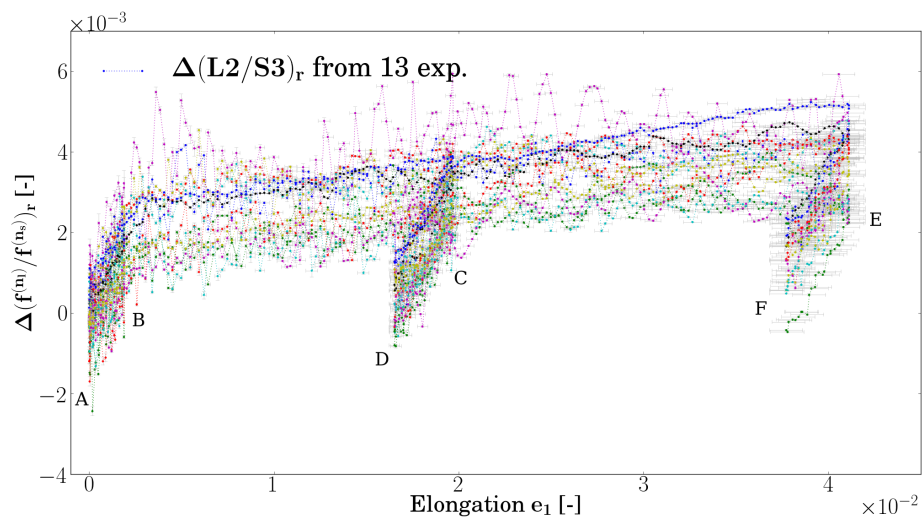
Figure C.26: Relative change in ratio of resonance mode L2 and S3
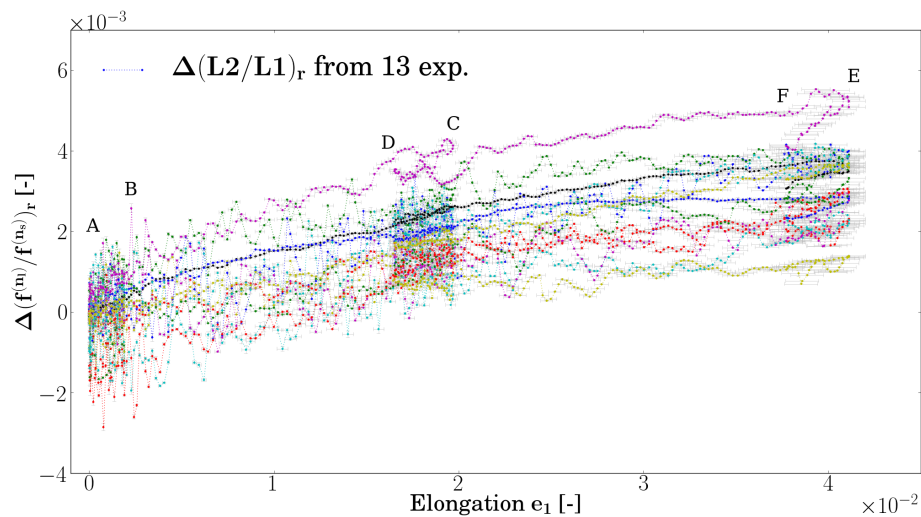
Figure C.27: Relative change in ratio of resonance mode L2 and L1

C.4 Simulation

Because of differences in the reported density and Lamé constants of the different steel types simulated the absolute magnitude of the simulated initial unstressed sound velocities have a relative large variation (as already shown for the longitudinal sound velocity in Sec. 5.7.1 Fig. 5.21). See Table. 4.1 and 4.4, and Eq. (2.97) for the relation between the parameters and the initial unstressed sound velocity. The absolute magnitude of the simulated shear sound velocities have thus just been included here for reference (Figs. C.28 and C.29), and corresponds to Fig. 5.21 for the simulated longitudinal sound velocity. The initial unstressed sound velocity of the steel applied in this work have been measured to be approximately 3230 m/s, which fits reasonably well with the main part of the steels presented here.
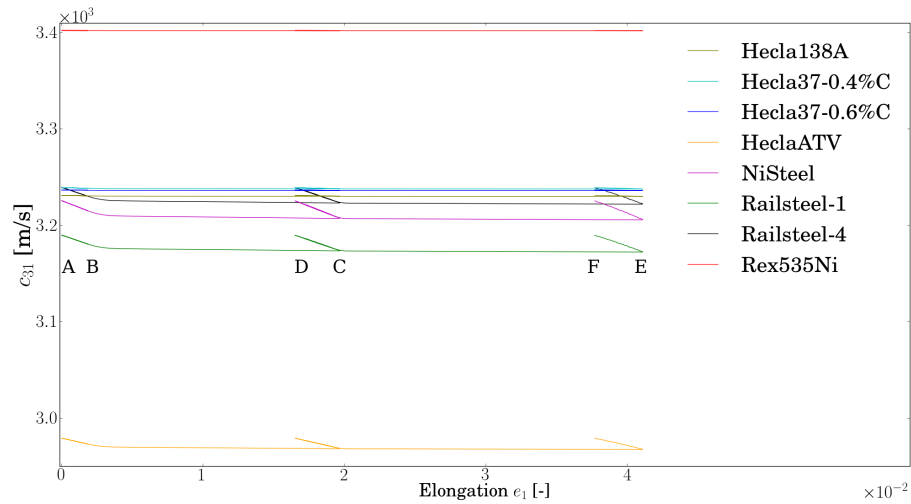
Figure C.28: Simulated sound velocity development of shear waves propagating perpendicular to-, and polarised parallel to the applied stress (c_{32}) based on elastic properties given in Table 4.4
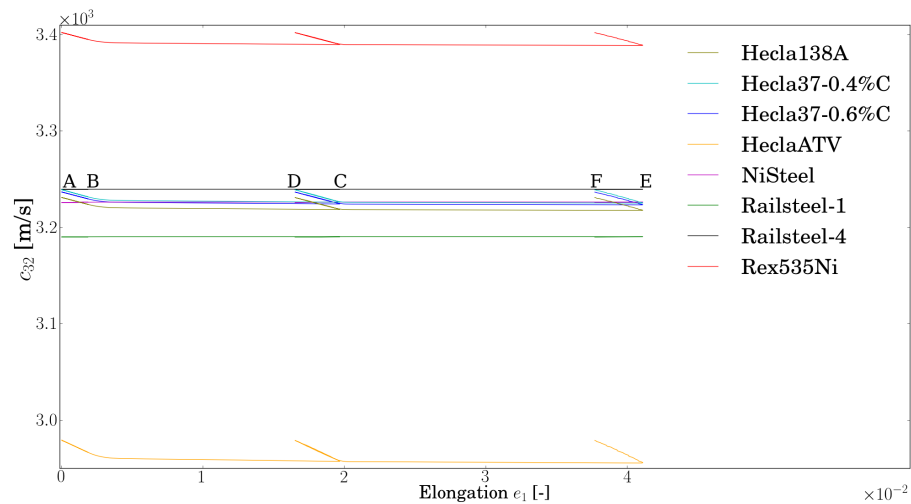
Figure C.29: Simulated sound velocity development of shear waves propagating perpendicular to-, and polarised perpendicular to the applied stress (c_{32}) based on elastic properties given in Table 4.4

C.5 Uncertainty

The figures presented in this section is used as basis for some of the results presented in the uncertainty chapter (Ch. 6).

Figs. C.30, C.31, C.32, and C.33 are basis for the uncertainties realted to each measurement bin of the measured L2 and S3 resonance mode frequencies and their relative change respectively, and corresponds to Figs. 6.1 and 6.2 presented in Sec. 6.2 for the L1 resonance mode. The maximum within these plots have been presented in Table 6.1.
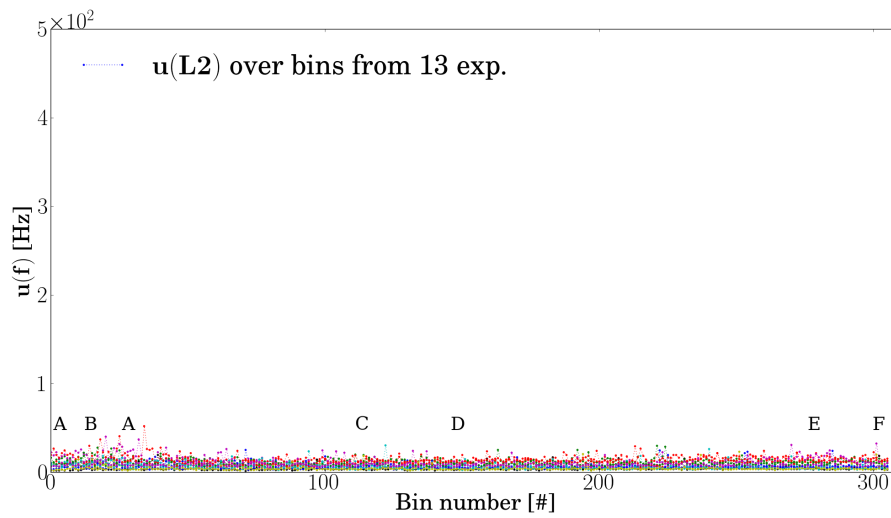
Figure C.30: Standard uncertainty within each bin of the L2 resonance frequency throughout each of the 13 tests
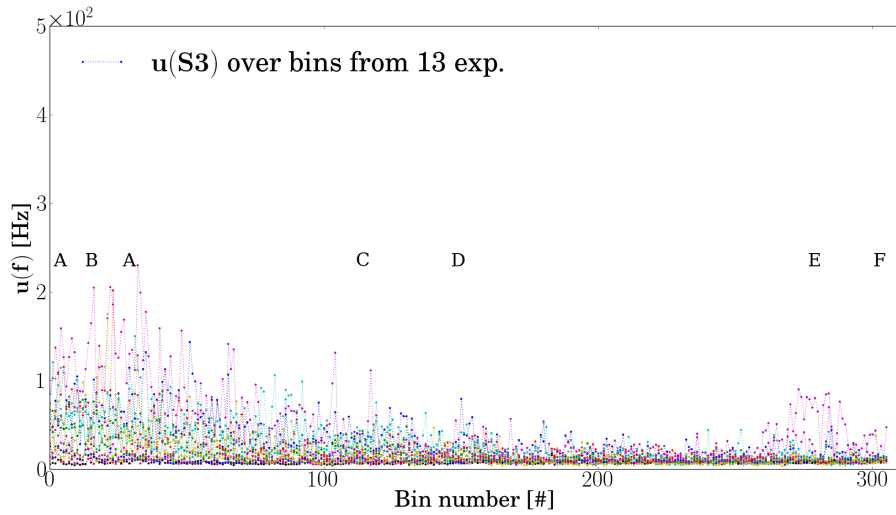
Figure C.31: Standard uncertainty within each bin of the S3 resonance frequency throughout each of the 13 tests
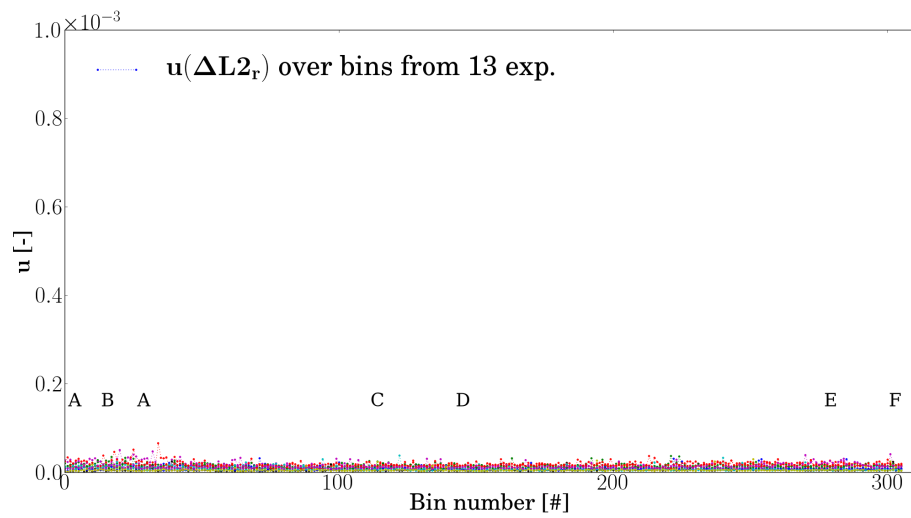
Figure C.32: Standard uncertainty within each bin of the relative change in the L2 resonance frequency throughout each of the 13 tests
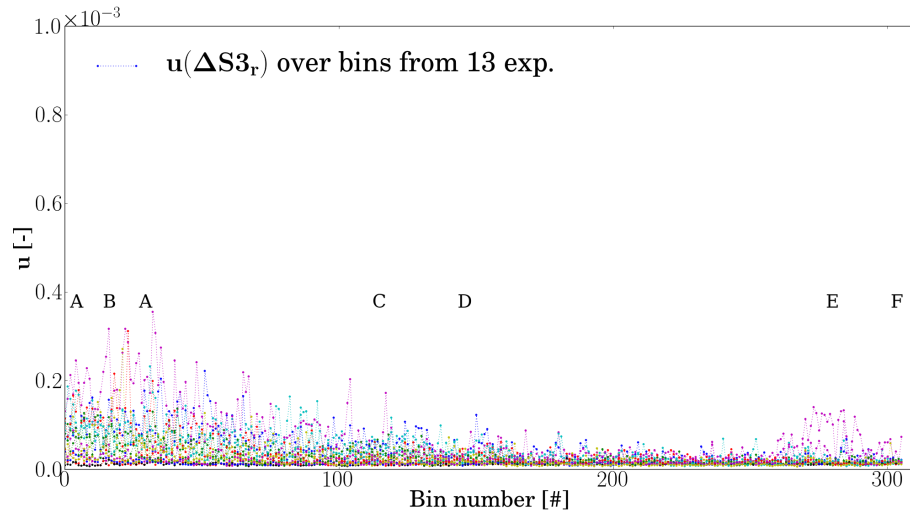
Figure C.33: Standard uncertainty within each bin of the relative change in the S3 resonance frequency throughout each of the 13 tests

Figs. C.34 and C.35 corresponds to Fig. 6.6 discussed in Sec. 6.4.1.2.
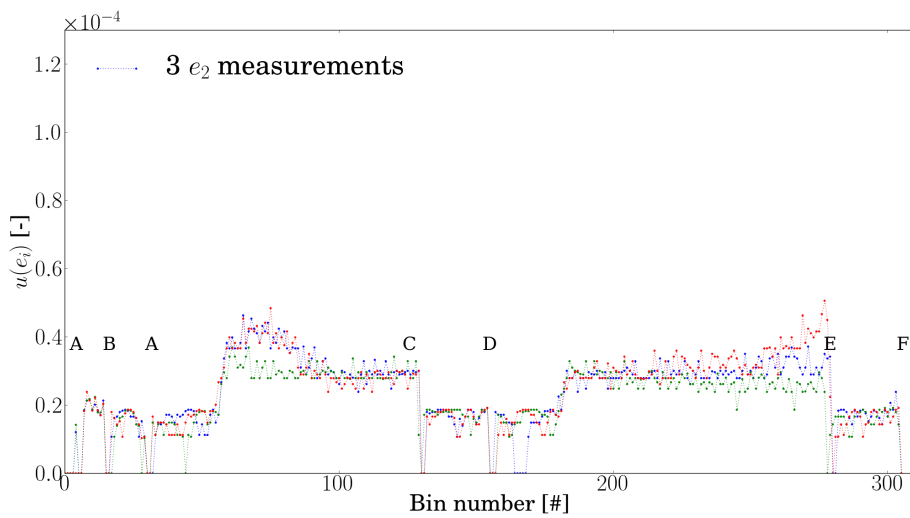
Figure C.34: Standard deviation of e_2 elongation across each bin from 3 strain gauges on 2 test specimens
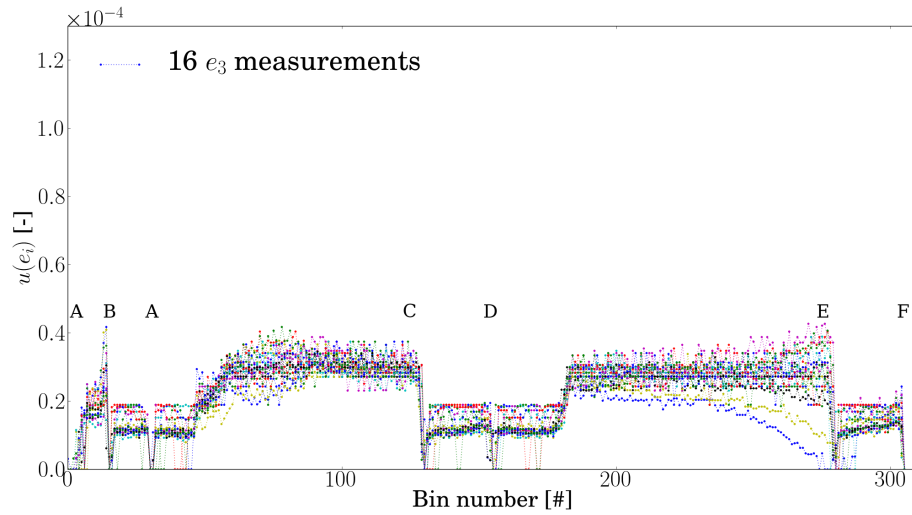
Figure C.35: Standard deviation of e_3 elongation across each bin from 16 strain gauges on 13 test specimens

Figs. C.36 and C.37 corresponds to Fig. 6.8 discussed in Sec. 6.4.1.2 relating to the possible systematic underprediction of the strain gauge measurements.
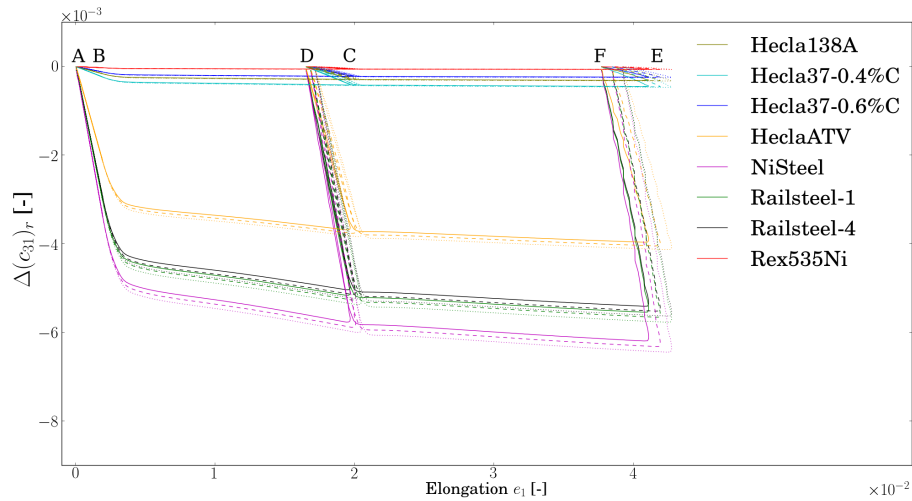
Figure C.36: Relative shear sound velocity development of shear waves propagating perpendicular to the applied stress and polarised parallel to the applied stress c_{31} based on elastic properties given in Table 4.4 and the measured elastic strains with 0%, 2%, and 4% adjustment for possible systematic underestimation.
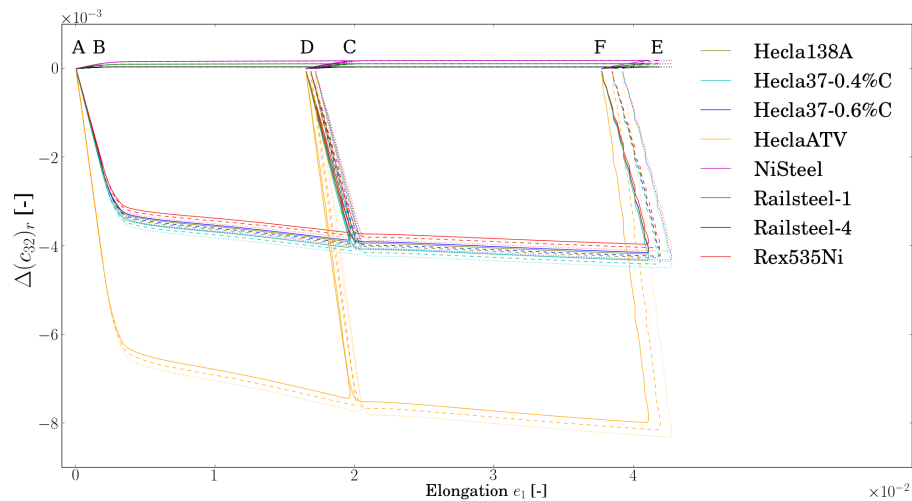
Figure C.37: Relative sound velocity development of shear waves propagating perpendicular to the applied stress and polarised perpendicular to the applied stress c_{32} based on elastic properties given in Table 4.4 and the measured elastic strains with 0%, 2%, and 4% adjustment for possible systematic underestimation.

Figs. C.38 and C.39 corresponds to Fig. 6.6 discussed in Sec. 6.10.
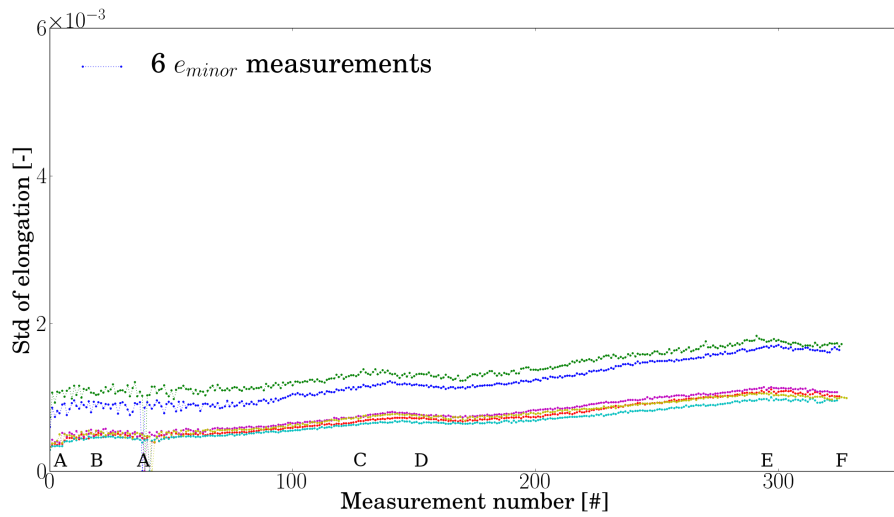
Figure C.38: Standard deviation of e_{minor} elongation over a circle of diameter 20 mm in the center of the test specimen for 6 ARAMIS measurements
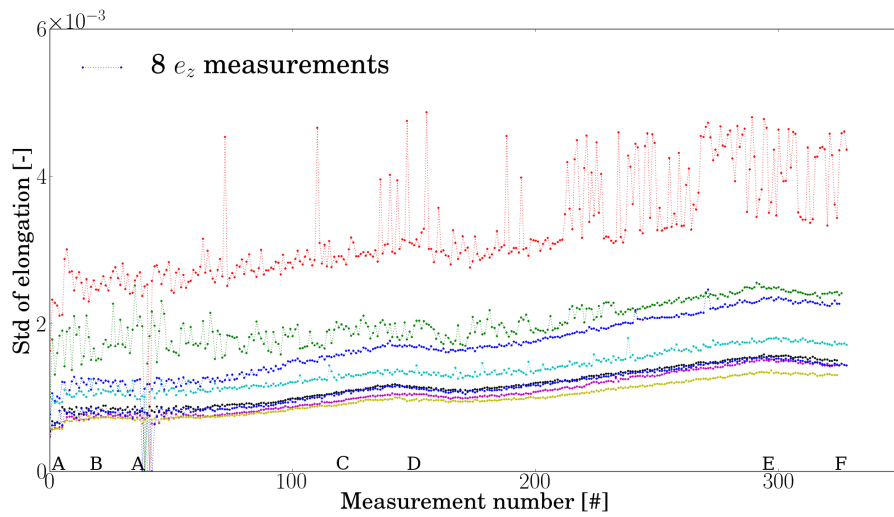
Figure C.39: Standard deviation of e_z elongation over a circle of diameter 20 mm in the center of the test specimen for 8 ARAMIS measurements

Appendix D

Tables

D.1 Thickness, width, and length measurement of the test specimens

The length (l_1), width (l_2), and thickness (l_3) measurement of the test specimens before and after the tests have been measured as described in Sec. 3.2, and the results have been presented in Table D.1. The first column include the test specimen number, and whether ART, ARAMIS, and/or strain gauges (denoted sg) measurements have been performed during the test (when no type is specified the test have been done without ART or ARAMIS measurments - i.e. only MessTek recording Instron displacement and force).

Table D.1: Length (l_1), width (l_2), and thickness (l_3) measurement of the test specimens

Test Type	Variable	1	2	3	4	5	6	7	8	9		mean [mm]	std [mm]	Relative std [%]
1	L_3	7.5	7.49	7.51	7.51	7.51	7.52	7.52	7.52	7.5		7.51	0.011	0.14
-	l_3	7.34	7.33	7.35	7.35	7.35	7.38	7.38	7.39	-		7.36	0.022	0.29
	L_2	49.85	49.88	49.86	49.83	49.82	49.82	49.83	49.85	49.86		49.84	0.021	0.04
	l_2	48.9	48.91	48.97	48.93	49.02	48.82	48.83	48.78	-		48.90	0.081	0.17
	L_1	599	l_1	-	l_1^{g1}	75.5	l_1^{g2}	76	L_1^{free}	447.5	l_1^{free}	-		
2	L_3	7.52	7.52	7.52	7.51	7.5	7.5	7.5	7.52	7.52		7.51	0.010	0.13
-	l_3	7.35	7.33	7.33	7.32	7.3	7.31	7.29	7.31	7.35		7.32	0.021	0.29
	L_2	49.98	49.95	49.96	49.86	49.88	49.85	49.85	49.86	49.82		49.89	0.058	0.12
	l_2	49.01	48.66	48.55	48.68	48.8	48.56	48.56	48.54	48.6		48.66	0.155	0.32
	L_1	600	l_1	623	l_1^{g1}	73.5	l_1^{g2}	76	L_1^{free}	450.5	l_1^{free}	473.5		
3	L_3	7.5	7.5	7.5	7.5	7.5	7.51	7.51	7.51	7.5		7.50	0.005	0.07
sg	l_3	7.35	7.35	7.37	7.37	7.37	7.38	7.36	7.38	7.41		7.37	0.018	0.25
	L_2	49.94	49.88	49.89	49.88	49.91	49.89	49.9	49.89	49.92		49.90	0.020	0.04
	l_2	49.01	48.95	49.01	49.03	49.03	48.97	49	49.04	49.07		49.01	0.036	0.07
	L_1	600	l_1	617	l_1^{g1}	75	l_1^{g2}	75	L_1^{free}	450	l_1^{free}	467.0		
4	L_3	7.5	7.5	7.5	7.51	7.51	7.51	7.51	7.52	7.52		7.51	0.008	0.10

Continue on next page...

Test Type	Variable	1	2	3	4	5	6	7	8	9			mean [mm]	std [mm]	Relative std [%]
sg	l_3	7.38	7.36	7.38	7.37	7.38	7.39	7.38	7.4	7.4			7.38	0.013	0.18
	L_2	49.84	49.84	49.83	49.86	49.83	49.89	49.89	49.86	49.87			49.86	0.023	0.05
	l_2	49.12	49.08	49.15	49.12	49.01	49.01	49.04	48.96	48.79			49.03	0.110	0.22
	L_1	600	l_1	618	l_1^{g1}	73	l_1^{g2}	76	L_1^{free}	451	l_1^{free}	469.0			
5	L_3	7.51	7.52	7.5	7.5	7.51	7.49	7.5	7.5	7.52			7.51	0.010	0.14
sg	l_3	7.37	7.38	7.36	7.36	7.36	7.35	7.36	7.36	7.38			7.36	0.010	0.14
	L_2	49.87	49.85	49.82	49.88	49.86	49.84	49.83	49.83	49.86			49.85	0.020	0.04
	l_2	49	48.96	48.85	48.88	48.97	48.91	49.05	48.98	48.94			48.95	0.062	0.13
	L_1	600	l_1	617	l_1^{g1}	72	l_1^{g2}	75	L_1^{free}	453	l_1^{free}	470.0			
6	L_3	7.49	7.49	7.5	7.5	7.5	7.51	7.51	7.51	7.51			7.50	0.008	0.11
sg	l_3	7.37	7.34	7.35	7.37	7.36	7.39	7.37	7.38	7.42			7.37	0.023	0.32
	L_2	49.86	49.86	49.89	49.88	49.84	49.85	49.85	49.83	49.82			49.85	0.022	0.04
	l_2	49.14	49.14	49.13	49.09	48.87	48.85	48.79	48.79	48.87			48.96	0.157	0.32
	L_1	600	l_1	618	l_1^{g1}	73.5	l_1^{g2}	76	L_1^{free}	450.5	l_1^{free}	468.5			
7	L_3	7.52	7.53	7.52	7.51	7.51	7.49	7.49	7.51	7.52			7.51	0.014	0.18
sg	l_3	7.4	7.39	7.4	7.38	7.38	7.37	7.37	7.39	7.41			7.39	0.014	0.19
	L_2	49.84	49.85	49.88	49.86	49.82	49.82	49.82	49.82	49.87			49.84	0.024	0.05
	l_2	49.01	49.06	49.12	49.06	49.06	49.07	48.93	48.97	48.84			49.01	0.087	0.18
	L_1	600	l_1	618	l_1^{g1}	73	l_1^{g2}	75	L_1^{free}	452	l_1^{free}	470.0			
8	L_3	7.52	7.52	7.51	7.51	7.5	7.49	7.49	7.5	7.51			7.51	0.011	0.15
sg	l_3	7.4	7.4	7.4	7.38	7.37	7.38	7.37	7.35	7.39			7.38	0.017	0.23
	L_2	49.84	49.86	49.86	49.85	49.88	49.88	49.84	49.86	49.85			49.86	0.015	0.03
	l_2	49.1	49.04	49.05	49.02	49.1	48.95	49.05	49.07	48.87			49.03	0.074	0.15
	L_1	600	l_1	618	l_1^{g1}	73.5	l_1^{g2}	75.5	L_1^{free}	451	l_1^{free}	469.0			
9	L_3	7.49	7.49	7.5	7.51	7.51	7.52	7.52	7.52	7.5			7.51	0.012	0.16
sg	l_3	7.36	7.37	7.36	7.37	7.39	7.39	7.41	7.38	7.36			7.38	0.017	0.23

Continue on next page. . .

D.1 Thickness, width, and length measurement of the test specimens

Test Type	Variable	1	2	3	4	5	6	7	8	9			mean [mm]	std [mm]	Relative std [%]
	L_2	49.82	49.82	49.82	49.81	49.87	49.81	49.81	49.84	49.88			49.83	0.027	0.05
	l_2	48.93	49	48.98	49	49.03	49.06	49	48.99	48.9			48.99	0.048	0.10
	L_1	600	l_1	618	l_1^{g1}	73	l_1^{g2}	76	L_1^{free}	451	l_1^{free}	469.0			
10	L_3	7.51	7.51	7.51	7.5	7.5	7.49	7.49	7.5	7.51			7.50	0.008	0.11
sg	l_3	7.38	7.38	7.39	7.38	7.36	7.38	7.38	7.37	7.39			7.38	0.009	0.13
	L_2	49.87	49.85	49.86	49.83	49.86	49.81	49.85	49.86	49.88			49.85	0.021	0.04
	l_2	49.03	49.01	49.05	49.11	49.11	49.06	49.03	49.04	49.02			49.05	0.037	0.07
	L_1	600	l_1	618	l_1^{g1}	74	l_1^{g2}	75.5	L_1^{free}	450.5	l_1^{free}	468.5			
11	L_3				7.51				7.51	7.51			7.51	0.000	0.00
aramis	l_3				7.37				7.39	7.36			7.37	0.015	0.21
	L_2	49.87				49.83			49.83	49.84			49.84	0.019	0.04
	l_2	49.05				48.89			48.89	48.87			48.93	0.084	0.17
	L_1	600	l_1	618	l_1^{g1}	73.5	l_1^{g2}	76	L_1^{free}	450.5	l_1^{free}	468.5			
12	L_3				7.51				7.5	7.48			7.50	0.015	0.20
aramis	l_3				7.35				7.39	7.35			7.36	0.023	0.31
	L_2	49.85				49.88				49.86			49.86	0.015	0.03
	l_2	48.98				48.91				48.97			48.95	0.038	0.08
	L_1	600	l_1	618	l_1^{g1}	74	l_1^{g2}	76	L_1^{free}	450	l_1^{free}	468.0			
13	L_3				7.5				7.49	7.51			7.50	0.010	0.13
aramis	l_3				7.36				7.37	7.36			7.36	0.006	0.08
	L_2	49.84				49.85				49.83			49.84	0.010	0.02
	l_2	49.04				48.98				48.9			48.97	0.070	0.14
	L_1	600	l_1	618	l_1^{g1}	74	l_1^{g2}	76	L_1^{free}	450	l_1^{free}	468.0			
14	L_3				7.5				7.5	7.51			7.50	0.006	0.08
aramis	l_3				7.37				7.37	7.37			7.37	0.000	0.00
sg	L_2	49.86				49.88				49.88			49.87	0.012	0.02

Continue on next page. . .

Test Type	Variable	1	2	3	4	5	6	7	8	9			mean [mm]	std [mm]	Relative std [%]
	l_2	48.97				49.08				48.92			48.99	0.082	0.17
	L_1	600	l_1	618	l_1^{g1}	74	l_1^{g2}	76	L_1^{free}	450	l_1^{free}	468.0			
15	L_3				7.51				7.5	7.52			7.51	0.010	0.13
aramis	l_3				7.36				7.35	7.39			7.37	0.021	0.28
	L_2	49.83				49.83				49.88			49.85	0.029	0.06
	l_2	48.92				48.9				49.05			48.96	0.081	0.17
	L_1	600	l_1	618	l_1^{g1}	74	l_1^{g2}	76	L_1^{free}	450	l_1^{free}	468.0			
16	L_3				7.5				7.51	7.5			7.50	0.006	0.08
aramis	l_3				7.4				7.38	7.35			7.38	0.025	0.34
	L_2	49.96				49.95				49.91			49.94	0.026	0.05
	l_2	48.9				49.06				48.97			48.98	0.080	0.16
	L_1	600	l_1	618	l_1^{g1}	74	l_1^{g2}	76	L_1^{free}	450	l_1^{free}	468.0			
17	L_3				7.5				7.5	7.5			7.50	0.000	0.00
aramis	l_3				7.36				7.35	7.37			7.36	0.010	0.14
sg	L_2	49.84				49.87				49.89			49.87	0.025	0.05
	l_2	48.86				49.03				48.98			48.96	0.087	0.18
	L_1	600	l_1	618	l_1^{g1}	74	l_1^{g2}	76	L_1^{free}	450	l_1^{free}	468.0			
18	L_3				7.49				7.48	7.51			7.49	0.015	0.20
aramis	l_3				7.35				7.38	7.36			7.36	0.015	0.21
	L_2	49.87				49.85				49.82			49.85	0.025	0.05
	l_2	49.1				48.93				48.87			48.97	0.119	0.24
	L_1	600	l_1	618	l_1^{g1}	74	l_1^{g2}	76	L_1^{free}	450	l_1^{free}	468.0			
19	L_3				7.49				7.5	7.51			7.50	0.010	0.13
aramis	l_3				7.36				7.35	7.36			7.36	0.006	0.08
	L_2	49.86				49.86				49.84			49.85	0.012	0.02
	l_2	49				48.94				48.95			48.96	0.032	0.07

Continue on next page. . .

D.1 Thickness, width, and length measurement of the test specimens

Test Type	Variable	1	2	3	4	5	6	7	8	9			mean [mm]	std [mm]	Relative std [%]
	L_1	600	l_1	618	l_1^{g1}	74	l_1^{g2}	76	L_1^{free}	450	l_1^{free}	468.0			
20	L_3				7.5				7.49	7.5			7.50	0.006	0.08
aramis	l_3				7.37				7.37	7.35			7.36	0.012	0.16
sg	L_2	49.89				49.86				49.85			49.87	0.021	0.04
	l_2	49.05				49.1				48.86			49.00	0.127	0.26
	L_1	600	l_1	618	l_1^{g1}	74	l_1^{g2}	76	L_1^{free}	450	l_1^{free}	468.0			
21	L_3				7.51				7.5	7.51			7.51	0.006	0.08
art	l_3				7.38				7.35	7.4			7.38	0.025	0.34
	L_2	49.86				49.85				49.88			49.86	0.015	0.03
	l_2	48.78				49.01			49.02				48.94	0.136	0.28
	L_1	600	l_1	618	l_1^{g1}	74	l_1^{g2}	76	L_1^{free}	450	l_1^{free}	468.0			
22	L_3				7.49				7.5	7.49			7.49	0.006	0.08
art	l_3				7.37				7.35	7.38			7.37	0.015	0.21
	L_2	49.82				49.81				49.83			49.82	0.010	0.02
	l_2	48.81				49			49.06				48.96	0.131	0.27
	L_1	601	l_1	618	l_1^{g1}	74.5	l_1^{g2}	76	L_1^{free}	450.5	l_1^{free}	467.5			
23	L_3				7.49				7.49	7.49			7.49	0.000	0.00
art	l_3				7.38				7.34	7.37			7.36	0.021	0.28
	L_2	49.87	49.87	49.81	49.83	49.89	49.85	49.89	49.82	49.85			49.85	0.029	0.06
	l_2	48.78	48.97	48.97	48.99	49.06	49.01	49.03	49.02				48.98	0.086	0.18
	L_1	600	l_1	618	l_1^{g1}	74.5	l_1^{g2}	76	L_1^{free}	449.5	l_1^{free}	467.5			
24	L_3				7.49				7.49	7.5			7.49	0.006	0.08
art	l_3				7.38				7.35	7.39			7.37	0.021	0.28
	L_2	49.85				49.82				49.85			49.84	0.017	0.03
	l_2	48.72				49.08			49.11				48.97	0.217	0.44
	L_1	600	l_1	618	l_1^{g1}	74	l_1^{g2}	76	L_1^{free}	450	l_1^{free}	468.0			

Test Type	Variable	1	2	3	4	5	6	7	8	9		mean [mm]	std [mm]	Relative std [%]
25	L_3				7.5				7.51	7.51		7.51	0.006	0.08
art	l_3				7.38				7.35	7.39		7.37	0.021	0.28
	L_2	49.82				49.82				49.81		49.82	0.006	0.01
	l_2	48.83				49.05			49.05			48.98	0.127	0.26
	L_1	600	l_1	618	l_1^{g1}	74	l_1^{g2}	76	L_1^{free}	450	l_1^{free}	468.0		
26	L_3				7.49				7.5	7.5		7.50	0.006	0.08
aramiss	l_3				7.37				7.36	7.38		7.37	0.010	0.14
	L_2	49.82				49.86				49.82		49.83	0.023	0.05
	l_2	48.89				49.01				48.98		48.96	0.062	0.13
	L_1	600	l_1	617	l_1^{g1}	75	l_1^{g2}	76	L_1^{free}	449	l_1^{free}	466.0		
27	L_3				7.51				7.52	7.51		7.51	0.006	0.08
aramiss	l_3				7.39				7.4	7.4		7.40	0.006	0.08
	L_2	49.84				49.84				49.86		49.85	0.012	0.02
	l_2	49.02				49.11				49.06		49.06	0.045	0.09
	L_1	600	l_1	615	l_1^{g1}	75	l_1^{g2}	75	L_1^{free}	450	l_1^{free}	465.0		
28	L_3				7.49				7.49	7.48		7.49	0.006	0.08
aramiss	l_3				7.37				7.38	7.35		7.37	0.015	0.21
	L_2	49.84				49.84				49.85		49.84	0.006	0.01
	l_2	49.04				49.06				48.77		48.96	0.162	0.33
	L_1	600	l_1	617	l_1^{g1}	74	l_1^{g2}	76	L_1^{free}	450	l_1^{free}	467.0		
29	L_3				7.49				7.5	7.49		7.49	0.006	0.08
aramiss	l_3				7.33				7.37	7.35		7.35	0.020	0.27
sg	L_2	49.83				49.85				49.83		49.84	0.012	0.02
	l_2	48.93				48.89				48.97		48.93	0.040	0.08
	L_1	600	l_1	617	l_1^{g1}	76	l_1^{g2}	75	L_1^{free}	449	l_1^{free}	466.0		
30	L_3				7.49				7.5	7.51		7.50	0.010	0.13

D.1 Thickness, width, and length measurement of the test specimens

Test Type	Variable	1	2	3	4	5	6	7	8	9		mean [mm]	std [mm]	Relative std [%]
aramiss	l_3				7.36				7.37	7.36		7.36	0.006	0.08
sg	L_2	49.81				49.83				49.87		49.84	0.031	0.06
	l_2	49.08				48.95				48.9		48.98	0.093	0.19
	L_1	600	l_1	618	l_1^{g1}	76	l_1^{g2}	75	L_1^{free}	449	l_1^{free} 467.0			
31	L_3				7.5				7.51	7.51		7.51	0.006	0.08
art	l_3				7.42				7.24	7.37		7.34	0.093	1.27
	L_2	49.85				49.84				49.82		49.84	0.015	0.03
	l_2	48.88				49.18				49.04		49.03	0.150	0.31
	L_1	600	l_1	618	l_1^{g1}		l_1^{g2}		L_1^{free}	-	l_1^{free} -			
32	L_3				7.5				7.5	7.51		7.50	0.006	0.08
art	l_3				7.39				7.33	7.38		7.37	0.032	0.44
sg	L_2	49.85				49.82				49.82		49.83	0.017	0.03
	l_2	48.4				49.16				49.07		48.88	0.415	0.85
	L_1	600	l_1	618	l_1^{g1}		l_1^{g2}		L_1^{free}	-	l_1^{free} -			
33	L_3				7.5				7.49	7.51		7.50	0.010	0.13
art	l_3				7.39				7.3	7.39		7.36	0.052	0.71
	L_2	49.8				49.85				49.83		49.83	0.025	0.05
	l_2	48.78				49.11				49.06		48.98	0.178	0.36
	L_1	600	l_1	618	l_1^{g1}		l_1^{g2}		L_1^{free}	-	l_1^{free} -			
34	L_3	7.48	7.48	7.49	7.49	7.5	7.51	7.51	7.51	7.52		7.50	0.015	0.19
art	l_3	7.35	7.37	7.36	7.37	7.37	7.38	7.38	7.38	7.35		7.37	0.012	0.16
sg	L_2	49.81	49.81	49.84	49.81	49.82	49.81	49.82	49.88	49.81		49.82	0.023	0.05
	l_2	48.93	49.05	49.15	49.01	49.1	49.03	49.03	49.02	49.1		49.05	0.064	0.13
	L_1	600	l_1	618	l_1^{g1}		l_1^{g2}		L_1^{free}	-	l_1^{free} -			
35	L_3				7.49				7.48	7.51		7.49	0.015	0.20
art	l_3				7.37				7.17	7.35		7.30	0.110	1.51

Test Type	Variable	1	2	3	4	5	6	7	8	9		mean [mm]	std [mm]	Relative std [%]
	L_2	49.89				49.82				49.84		49.85	0.036	0.07
	l_2	45.83				49.01				49.03		47.96	1.842	3.84
	L_1	600	l_1	623	l_1^{g1}		l_1^{g2}		L_1^{free}	-	l_1^{free}	-		
36	L_3				7.5				7.5	7.48		7.49	0.012	0.15
art	l_3				7.39				7.31	7.37		7.36	0.042	0.57
	L_2	49.81				49.79				49.83		49.81	0.020	0.04
	l_2	48.68				49.02				49.09		48.93	0.219	0.45
	L_1	600	l_1	618	l_1^{g1}	75.5	l_1^{g2}	75	L_1^{free}	449.5	l_1^{free}	467.5		
37	L_3				7.5				7.5	7.52		7.51	0.012	0.15
art	l_3				7.39				7.26	7.38		7.34	0.072	0.99
	L_2	49.81				49.83				49.79		49.81	0.020	0.04
	l_2	48.91				48.96				49.03		48.97	0.060	0.12
	L_1	600	l_1	620	l_1^{g1}	76	l_1^{g2}	75	L_1^{free}	449	l_1^{free}	469.0		
38	L_3				7.5				7.5	7.5		7.50	0.000	0.00
art	l_3				7.39				7.06	7.4		7.28	0.193	2.66
sg	L_2	49.83				49.81				49.8		49.81	0.015	0.03
	l_2	46.83				49.07				49.02		48.31	1.279	2.65
	L_1	600	l_1	620	l_1^{g1}	75	l_1^{g2}	76	L_1^{free}	449	l_1^{free}	469.0		
39	L_3	7.49	7.48	7.49	7.5	7.51	7.51	7.51	7.49	7.52		7.50	0.013	0.18
art	l_3	7.36	7.36	7.37	7.37	7.38	7.37	7.39	7.28	7.35		7.36	0.032	0.43
sg	L_2	49.81	49.82	49.79	49.79	49.82	49.81	49.8	49.79	49.8		49.80	0.012	0.02
	l_2	48.76	48.28	48.82	48.89	48.94	49.02	49.12	49.01	48.86		48.86	0.243	0.50
	L_1	601	l_1	619	l_1^{g1}	76	l_1^{g2}	76	L_1^{free}	449	l_1^{free}	467.0		
40	L_3				7.5				7.5	7.49		7.50	0.006	0.08
art	l_3				7.36				7.33	7.33		7.34	0.017	0.24
sg	L_2	49.84				49.8				49.79		49.81	0.026	0.05

D.1 Thickness, width, and length measurement of the test specimens

Test Type	Variable	1	2	3	4	5	6	7	8	9			mean [mm]	std [mm]	Relative std [%]
	l_2	48.7				49.04				59.79			52.51	6.307	12.01
	L_1	600	l_1	619	l_1^{g1}	75	l_1^{g2}	76	L_1^{free}	449	l_1^{free}	468.0			
41	L_3				7.49				7.49	7.5			7.49	0.006	0.08
art	l_3				7.37				7.26	7.35			7.33	0.059	0.80
	L_2	49.82				49.82				49.81			49.82	0.006	0.01
	l_2	48.35				48.98				48.72			48.68	0.317	0.65
	L_1	600	l_1	620	l_1^{g1}	76	l_1^{g2}	75.5	L_1^{free}	448.5	l_1^{free}	468.5			